Multi-impact behavior of composite structures : experimental and numerical approach

Ayoub Soufri

Ayoub Soufri. Multi-impact behavior of composite structures : experimental and numerical approach. Mechanics of materials [physics.class-ph]. Université Bourgogne Franche-Comté, 2023. English. NNT : 2023UBFCK038 . tel-04584744

THÈSE DE DOCTORAT DE L'ÉTABLISSEMENT UNIVERSITÉ BOURGOGNE FRANCHE-COMTÉ

PRÉPARÉE À L'UNIVERSITÉ DE BOURGOGNE

Ecole doctorale n° 37

Sciences Physiques pour l'Ingénieur et Microtechniques (SPIM)

Doctorat de Mécanique

Par

M. SOUFRI Ayoub

MULTI-IMPACT BEHAVIOR OF COMPOSITE STRUCTURES : EXPERIMENTAL AND NUMERICAL APPROACH

Thèse présentée et soutenue à Nevers, le 25 septembre 2023

Composition du Jury :

Mme Xiao-Jing GONG	Professeure des universités, ICA Toulouse	Présidente
Mme Emmanuelle ABISSET-CHAVANNE	Professeure des universités, ENSAM Bordeaux	Rapporteuse
M Peter DAVIES	Ingénieur de recherche, IFREMER Brest	Rapporteur
M Julien BERTHE	Ingénieur de recherche, ONERA Lille	Examinateur
M Bruno MARTIN	Professeur des universités, ISAT Nevers	Directeur de thèse
M Christophe BOUVET	Professeur des universités, ISAE-SUPAERO	Encadrant de thèse
M Ameur CHETTAH	Maître de conférences, ISAT Nevers	Encadrant de thèse
M Benoît PIEZEL	Maître de conférences, ISAT Nevers	Encadrant de thèse

Acknowledgement

This work is the result of nearly three years of effort. I started from scratch, developing and constructing a compressed air cannon, conducting experimental tests, and validating a numerical model. During this time, I also enrolled in an engineering school and shared my passion for science with the cannon's visitors. I must acknowledge the immense assistance I received from numerous individuals who supported me at every level.

I would like to express my heartfelt gratitude to my thesis supervisors : Ameur, Benoit, Bruno and Christophe. Your guidance, involvement, and confidence were invaluable. Ameur, I am especially grateful for your unwavering trust in me, for believing in my abilities, and for suggesting and helping me to teach future engineers. Thank you for protecting and promoting this project, and for always pushing me to move forward. Benoit, I extend my thanks for your professionalism, availability, and dedication to this project. Bruno, thank you for your motivating words, your belief in my capabilities, and your adept handling of difficult situations. Christophe, I cannot express enough gratitude for everything you have done for me throughout this thesis. In the language of soccer, which you love, I would say : "thank you for being the FC Barcelona to the Messi that I am." I am immensely thankful for all the technical expertise and knowledge you have shared with me.

I would like to express my gratitude to the members of the jury. In particular, I would like to thank Ms. Emmanuelle ABISSET-CHAVANNE and Mr. Peter DAVIES for reviewing my thesis during the summer vacations. I would also like to thank Ms. Xiao-Jing GONG and Mr. Julien BERTHE for accepting to examine my work, for attending my defense and for the time devoted to our exchanges.

Thanks to the members of the DRIVE laboratory, to its director Sidi-Mohammed for his guidance and support to the PhD students, my thesis would not have succeeded without your involvement. I would also like to thank Martine, the laboratory secretary, for her cheerfulness and good croissant, and wish you a pleasant retirement.
Thanks to the lab technical staff, Regis for his discipline and the physical effort involved in assembling, manufacturing and calibrating the cannon. Thanks to Sylvain, for providing me with everything I needed to develop the cannon. Thanks to Alain for the good times spent together machining some part of the cannon and talking about the history of Morocco and France. I would like to extend my warmest thanks to all the PhD students for the enjoyable time we spent together.
Thanks to the ISAT teaching team, to Ali Kribèche and Ali El-Hafidi for the trust they showed me during my second and third years, allowing me to teach last and penultimate year engineering students and supervise them during their PFEs.

Grateful recognition to the French Ministry of Higher Education and Research, the doctoral school (SPIM, ED37) and the Burgundy region for funding the thesis and all the materials needed to manufacture the cannon and composite plates. Thanks

to the Institut Clément Ader (ICA, CNRS UMR 5312) for the use of the computing mesocenter CALMIP.

I dedicate this PhD thesis to my beloved family :
Her Majesty, my mother, the joy of my heart. I won't forget anything ; your unconditional love and countless sacrifices and prayers have shaped the person I am today.
To my father, l'hajj Et-taibi, this work is the result of your sacrifices for my education. No dedication could be eloquent enough to express what you truly deserve.
Zineb, I am forever grateful for your endless love and for being my anchor in both the calm and stormy seas of life ; your patience, understanding, and sacrifices have allowed me to fully immerse myself in this pursuit of knowledge. To all my brothers and sisters, my deepest affection and gratitude, I wish you and your childrens a happy life !

Ayoub

Abstract :

Composite materials are widely used in the transportation field due to their high specific mechanical properties. However, during their life cycle, they can undergo significant degradation of their mechanical properties when subjected to impact loading. Impact-induced damage occurs in various forms, such as fiber breakage, matrix cracking, fiber/matrix decohesion and delamination. The study of the impact behavior of composite structures has attracted considerable attention in the literature. However, these studies generally relate to the case of a single impact or repeated impacts. Few studies have focused on the case of multiple impacts, even though these are closer to actual service conditions, as in the case of falling hailstones or the projection of external objects such as road gravels, bird strikes, etc. In this thesis, we present robust experimental and numerical methods for in-situ and post-mortem monitoring of damage following the various possible impact cases : single-impact, repeated, sequential, simultaneous impacts, etc. The first phase of the project involved the development of a unique "compressed air cannon" test bench. Then, a dialogue (experimental tests-numerical computations) was ensured to better understand the phenomena involved in multi-impact cases, to finally reach the maximum performance of composite materials.

Keywords : Multi-impact ; impact ; composite structures ; experimental and numerical approach ; compressed air cannon ; discrete ply model.

Résumé :

Les matériaux composites sont largement utilisés dans le domaine des transports en raison de leurs propriétés mécaniques spécifiques élevées. Cependant, au cours de leur cycle de vie, ils peuvent subir une dégradation significative de leurs propriétés mécaniques lorsqu'ils sont soumis à des chargements d'impacts. Les dommages induits par des impacts se manifestent sous différentes formes telles que la rupture des fibres, la fissuration matricielle, la décohésion fibres/matrice et le délaminage. L'étude du comportement aux impacts des structures composites a suscité une attention importante dans la littérature. Cependant, ces études se rapportent généralement au cas d'un seul impact ou d'impacts répétés. Peu de travaux se sont intéressés au cas d'impacts multiples, même s'ils sont plus proches des conditions réelles de service, comme dans les cas de chute de grêlons ou de projection d'objets externes tels que les gravillons présents sur les routes, les impacts d'oiseaux, etc. Dans cette thèse, nous présentons des méthodes expérimentales et numériques robustes pour le suivi in-situ et post-mortem des endommagements suite aux différents cas d'impacts possibles : mono-impact, impacts répétés, séquentiels, simultanés, etc. Ce travail a consisté dans un premier temps à développer un banc d'essai unique « canon à air comprimé ». Ensuite, un dialogue (essais expérimentaux-calculs numériques) a été assuré afin de mieux comprendre les phénomènes en jeu dans les cas de multi-impacts, pour finalement atteindre les performances maximales des matériaux composites.

Mots-clés : Multi-impacts ; impact ; structures composites ; approche expérimentale et numérique ; canon à air comprimé ; discrete ply model.

List of Figures

Acronyms :

- **AE :** Acoustic Emission
- **ANELFA :** Association Nationale d'Études et de Lutte contre les Fléaux Atmosphériques
- **ASME :** American Society of Mechanical Engineers
- **ASTM :** American Society for Testing and Materials
- **BVID :** Barely Visible Impact Damage
- **CAI :** Compression After Impact
- **CAC :** Compressed Air Cannon
- **CDM :** Continuum Damage Mechanics
- **CFRP :** Carbon Fiber Reinforced Polymer
- **DIC :** Digital Image Correlation
- **DPM :** Discrete Ply Model
- **FAA :** Federal Aviation Administration
- **FE :** Finite Element
- **FEA :** Finite Element Analysis
- **FEMB :** Finite Element Model Builder
- **FFT :** Fast Fourier Transform
- **FILs :** Fully Isotropic Laminates
- **FRF :** Frequency Response Function
- **FOD :** Foreign Object Debris
- **FPS :** Frames Per Second
- **FPZ :** Fracture Process Zone
- **FVF :** Fiber Volume Fractions
- **HSC :** High Speed Camera
- **HVI :** High Velocity Impact
- **ICA :** Independent Component Analysis
- **IR :** Infrared
- **LEFM :** Linear Elastic Fracture Mechanics
- **LVI :** Low Velocity Impact
- **MIP :** Multi-impact Parameter
- **NDT :** Non-Destructive Testing
- **NI :** National Instruments
- **PCA :** Principal Component Analysis
- **SEM :** Scanning Electron Microscope

- **SERR :** Strain Energy Release Rate
- **SSR :** Solid State Relay
- **SVD :** Singular Value Decomposition
- **TTL :** Transistor-Transistor Logic
- **UD :** Unidirectional
- **UI :** Ultrasonic Inspection
- **VCCT :** Virtual Crack Closure Technique

General introduction

Figure 1 – Illustration of certain impact and multi-impact cases : (a) Hail-induced damages to a car body (1), (b) hailstones of different sizes, (c) impact damage caused by falling down an A350-900 central wing box strut, (d) Airbus A320 nose hit by hail on takeoff (2).

Over the past five decades, fiber-reinforced composites have found increasing application in the primary structures of a variety of flight vehicles, from small unmanned aircraft to space launch vehicles. The proportion of structural weight comprised of composite materials has grown significantly, surpassing 50% since the construction of the Boeing 787 Dreamliner and then the Airbus A350 XWB. This expansion in the use of composites has been mainly driven by the demand for weight reduction, stealth capabilities for military aircraft and cost concerns in the commercial aviation sector. Moreover, by leveraging composites' lightweight nature, durability, and versatility, we can significantly decrease energy consumption, lower greenhouse gas emissions, minimize waste generation and actively participate in the ecological transition. Composites also offer the advantage of adaptable directional properties, which improve structural performance, and can incorporate actuators and sensors, enabling the development of multi-functional structures.

If composite materials are increasingly used as structural components, their structural integrity must be ensured under different types of loading. One of the most common types of loading to which composite structures may be subjected during their life-cycle is impact, or more generally multi-impact, see figure 1. For example, in the case of external object projection, hail impact, gravel impact or bird strikes, etc. In the literature, the case of a single impact is widely studied, whereas in reality the most general case is that of several impacts (which includes simultaneous, delayed or repeated impacts, and even that of a single impact when two impacts are sufficiently distant to avoid interaction between one another). This study is primarily motivated by the distinction between the different impact and multi-impact configurations and the difference between the damage generated in each case and the phenomena involved, to gain a more comprehensive understanding of the different impact loadings and their criticality.

To carry out this study, a test bench was needed to control simultaneity, the number of impacts and the distance between impacts, which are essential input parameters for the study of multi-impacts. Given the scarcity of this type of test bench, we opted for developing it ourselves in the DRIVE laboratory. We then proceeded to its instrumentation to enable a detailed understanding of the phenomena involved both during and after impacts, the calibration of the cannon was a necessary step to improve its repeatability and enable us to obtain the most reliable results possible.

The second stage of the project involved manufacturing the composite plates and carrying out the various multi-impact tests. We then proceeded to analyze the data from these different tests, which is not an obvious task as the number of impacts increases. We therefore decided to move on to the third stage of the project, which involved using a numerical model to refine our understanding of the phenomena involved, by validating the model's results on simple impact cases that are easier to follow experimentally. Once this was accomplished, we moved on to 2 impacts, 3 impacts, etc. up to 5 impacts. Each time, a dialogue between experiment and numerical modelling was ensured to pinpoint the most influential parameters. Several configurations were remade or added to confirm the remarks made using the numerical model, just as several calculations were launched to verify, one by one, the configurations tested experimentally and then others that exceeded our experimental limits, such as controlling the time lag between impacts to within a tenth of a millisecond.

This is a complete project, from the design of the test bench to the validation of the numerical model and the various experimental tests. During this work, we used classical impact monitoring methods such as C-scans, plate displacement and impact force monitoring, and obtained more encouraging results than in the literature with our thermal camera analysis. In addition, we developed a number of concepts relating to multi-impacts, distinguished the different cases of possible multi-impacts to homogenize the key words used in the literature, and precisely defined the role of the most important parameters.

The originality of this work lies in clearly distinguishing between the different cases and the corresponding damage and phenomena involved in the various possible cases of impacts and multi-impacts, studying the influence of parameters not yet studied, such as the spatial and temporal lag between impacts, and assessing the importance of other parameters commonly used in the literature in a multi-impact case. The concept of virtual testing is widely used in this manuscript, with frequent back and forth between experimental and numerical investigations after designing the compressed air cannon, as shown in the diagram below :

This thesis is divided into five chapters, each of which compares experimental and numerical results, and presents the most relevant results on a case-by-case basis. It is therefore important to follow the summary table presented at the beginning of the third chapter to follow the sequence of results. The five chapters present in general terms :

- **Chapter 1 :** Literature review, to synthesize the research done so far, provide a comprehensive and critical overview of current insights and tools on impact and multi-impact, cite our research in relation to others and highlight the originality of this work.
- **Chapter 2 :** To present in detail the development of the "compressed air cannon" test bench, from its design phase through its calibration, homologation and automation to the operational phase.
- **Chapter 3 :** Present the tools and methods used in single-impact cases, verify the consistency between the various experimental tools used and the reliability of the DPM, summarize the various phenomena involved in the case of a single impact and the influence of the various single-impact parameters.
- **Chapter 4 :** Defining the key differences between the single-impact and multi-impact cases, comparing a single-impact case with cases belonging to multi-impact configurations, primarily the simultaneous impact case and the sequential impact case, concluding on the relevance of taking simultaneous cases into account, and the multitude of phenomena that can be brought into account in this particular multi-impact case.
- **Chapter 5 :** study in detail the case of simultaneous impacts, define and study the influence of multi-impact parameters, highlight the role played by classic impact parameters in the case of multi-impacts and finally study the special case of impacts that are both simultaneous and repeated.

At the end, we conclude with a review of the research carried out on this subject, the various tools and methods used, the relevance of this study and its various perspectives.

Table of Contents

CHAPTER 1 : LITERATURE REVIEW

1. Literature review

Introduction

The purpose of this literature review chapter is to examine and analyze existing research on the behavior of composite structures under impact and multi-impact conditions. This chapter aims to provide a comprehensive understanding of the various factors that influence the response of composite materials when subjected to impact loading, including the types of damage mechanisms that can occur and the structural performance degradation over multiple impact events. By reviewing relevant studies and analyzing the findings, this chapter will contribute to the knowledge and understanding of the impact behavior of composite structures, informing the subsequent chapters on experimental and numerical investigations. Ultimately, the goal is to enhance the design and analysis of composite structures, ensuring their optimal performance and durability in real-world applications where impacts and multi-impacts are potential concerns. The aim of this chapter is also to situate our research in relation to what has already been done, and to justify the use of the new testing methods, damage monitoring and data analysis presented in the following chapters. Particular attention will be devoted to multi-impact cases, and to the experimental and numerical advances made to date in relation to the impact damage tolerance design concept.

1.1. Impact and multi-impact behavior of composite materials

1.1.1. Overview

Composite materials are widely used in the field of transportation because of their high specific mechanical properties. However, during their life cycle, they may undergo significant mechanical properties degradation when are subjected to impact loading. In the literature, numerous studies have focused on single point isolated or repeated impact events, but few deal with composite laminate subjected to multi-impact, simultaneous or sequential impacts, even if these test configurations are closer to real service conditions, in the case of falling hailstones or the projection of external objects such as gravel on the road, tire debris, etc. Compared with a single point impact, a synergistic effect from stress waves interaction induced by different projectiles modifies the overall response of the structure.

Composite materials are frequently exposed to impact loadings by foreign objects during manufacturing, service and maintenance operations (3). For example, the projection of external objects such as road gravel during take-off or landing, hailstones, bird strikes or falling tools during manufacturing or maintenance operations. These

Figure 1.1 – Bird Strike risk, a flock of birds surrounding an airplane (4).

impacts can be of low/medium/high velocity and low/medium/high energy depending on their nature (5). The induced impact damage comes in various forms such as fiber breakage, matrix cracking, fiber/matrix debonding and delamination (6). Composite structures are particularly susceptible to the foreign impact loads because of their poor properties in the through thickness direction (7).

Consequently, the problem of impact-induced damage has attracted considerable attention in the literature ((5), (8), (9)). However, these studies generally relate to the case of an isolated impact at a single point or repeated impacts ((10), (11), (12)). Although, in real scenarios, many structures are potentially exposed to multi-impact loading. Recently, researchers have been more interested in the case of multi-impact by distinguishing between sequential and simultaneous impacts on composite structures ((7), (13), (14), (15)), where the difference is linked to the stress wave interaction (constructive or destructive interference). Generally, two impacts are considered simultaneous when stress and shock wave interaction is expected (15) and sequential when the time-hit interval is sufficiently long to avoid synergistic effects from stress waves interaction (16). These studies are considering high energy/velocity impacts on fiberglass composites ((7), (13), (14)) or short fibre reinforced composites (15). We note that, the high velocity impact regime is characterized by a very short impact time with dilatational wave dominated response, while the intermediate velocity impact is characterized by a short impact time with flexural and shear wave dominated response (5).

Compared with single point impact, the overall structural response in multi-impact loading is modified due to a more complex damage mechanism activated by the interaction of damage induced by different projectiles (7), even if these impacts are in damaged (14) or undamaged regions (15) (in order to manage or avoid the interaction of local effects). The combined effects of the interaction between cracks propagation, stress waves (especially the reflected tensile waves) and complex bending effects (leading to high local tensile stress and out-of-plane shear effects) is observed to govern the fracture mechanisms and the damage extent (15).

This study will focus on the behavior of a composite laminate, with unidirectional carbon fibers and an epoxy matrix, under multiple low-medium velocity and low-medium energy multi-site simultaneous or sequential impacts. For this purpose, a five-stage compressed air cannon was designed and constructed for the multi-impact series of experiments. This test setup will allow us to approximate real service conditions to study the structural integrity of a composite subjected to simultaneous or sequential multi-site impacts. Thus, it is possible to control various parameters such as the number of impacts, their location, time delay, velocity and impact energy. To better understand the interaction between multiple impacts, finite element models are used to predict the damage developing in composite structures. This allows us to model other multi-impact configurations and to distinguish the most critical ones. During the numerical modeling, a dialogue between tests and calculations is ensured in order to validate the performances of the models and to show the role of "Virtual Testing" in reducing the costs of test campaigns and increasing the understanding of the different damage mechanisms to reach the maximum performances of composite materials.

For definition, an impact is a collision between two bodies which results in energy dissipation by elastic deformation (small vibratory shocks) or plastic without violent crushing of the overall structure in an extremely short time, of the order of a few ms (hence the difference with the crash). Generally, a projectile of a given mass, geometric shape, direction, velocity and nature of material hits a structure in an impact zone producing contact, waves and material behavior. There are several types of impact depending on their energies and velocities. Generally, an impact is distinguished by its velocity/energy pair (see the subsection 1.1.2. Parameters influencing the impact response of composites), which leads to the accumulation of several types of damage up to macroscopic failure.

For more than 4 decades, the impact of composite structures remains a preoccupation of researchers and industrialists in order to meet safety requirements in terms of accidental risks. This accidental risk can represent :

- **Ground impact :** during maintenance, manufacturing or assembly operations, through the fall of tools. The associated energy is of the order of a few tens of J (16). In addition, we mention the impact of the effects of an explosion on an industrial site, the impact of gravel on an aerodrome or on a car runway or ballast (railroad), the impact of debris from foreign objects encountered on runways, commonly called FOD (Foreign Object Debris) (16) or even fragments of explosive warheads in the military field.

- **Impact at altitude :** like birdstrike, feared by aircraft pilots, is taken into account by aircraft manufacturers since birdstrikes can have dramatic consequences, especially when they affect the integrity of the propulsion system. The birdstrike on the radome area of the B737 of the Turkish Airlines flight TK2004 in 2015 illustrates perfectly these remarks (17). Figure 1.1 shows the risk of multiple impacts in this type of situation, rather than a single impact.
- **Slamming impact :** most offshore structures, including offshore wind turbines, ships, etc., experience impulsive pressure loads due to slamming in rough waves.
- **Hail impacts :** the aeronautical certification texts (as EASA CS-23) indicate a probability law for the size of hailstones. These texts propose a Gaussian law whose maximum value is a diameter of 55 mm and an average diameter of 16 mm. Aeronautical structures exposed to this type of impact must be able to withstand the impact of a hailstone of exceptional size and repeated impacts of medium-sized hailstones in order to be certified. The energies involved are between 30 and 900 J for a real velocity of about 175 m/s (16).

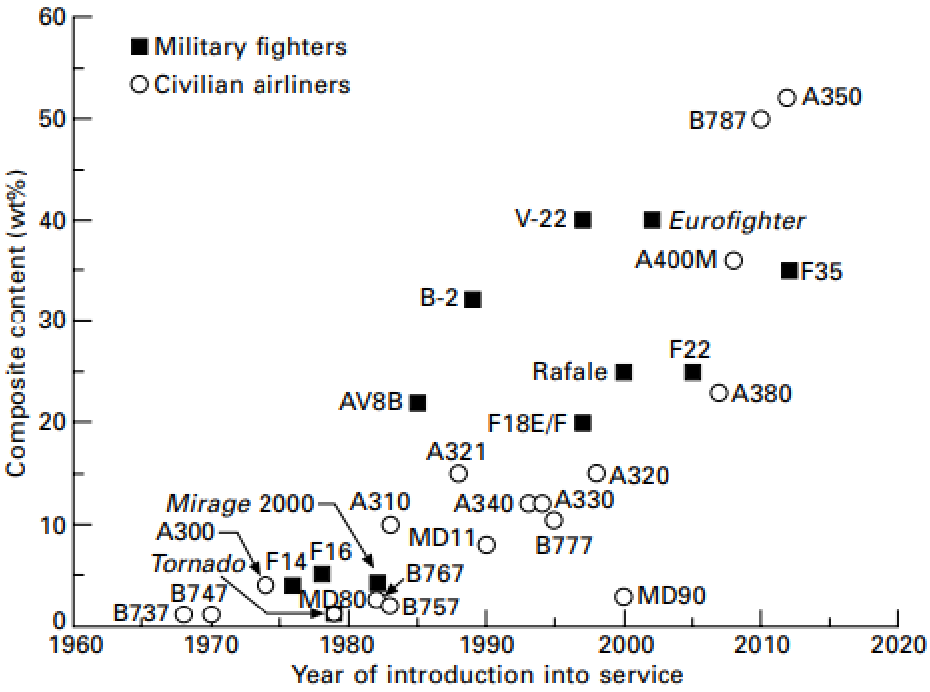

Figure 1.2 – Percentage in advanced composites (by mass) on civil and military aircraft (18).

Composite materials remain a concern regarding these different types of impacts because they have the particularity, often, of not being marked in case of low energy impacts, in case of fall of a part during an assembly/disassembly operation for example.

As the impact force is transmitted between the fibers, the defect can be confined within the structure in the form of delamination, fiber pull-out or other defects. These defects are generally invisible to visual inspection and considerably reduce the mechanical properties of the impacted structure, up to -70% according to Davies and Olsson (19).

In practice, structures are exposed to several repeated impacts or impacts at the same time. For example, impact of a group of birds, of several gravels or ballasts, fall of a part several times during the assembly operations, etc. However, the literature does not yet precisely define each type of impact configuration.

In aeronautics, despite the existence of over 120,000 materials, less than a hundred different materials are used in the fuselage and engines of airplanes. The four main materials are aluminum alloys, fiber-polymer composites (especially carbon-glass-epoxy), titanium alloys, and high-strength steels ; these materials represent over 80% of the mass in most commercial and military aircraft (18), where they are increasingly used, see figure 1.2. Composites are present in almost all the fuselage, wing, ailerons, vertical stabilizer and horizontal stabilizer, etc. They constitute almost 80% of the structure by volume and 50% by mass. The impact damage tolerance of composite structures is one of the three types of requirements of the European standard JAR 25.571 that an aircraft must withstand without structural failure until the damage (irreversible process that leads to the appearance of local defects) is detected during inspection operations, this is due to the fact that polymer matrix composites are known to be very sensitive to out-of-plane loads. Moreover, impacts on composite structures are particularly critical because they can strongly decrease the residual strength without leaving any visible mark on the outer surface, that is why we aim to conduct a study at low and medium energies, to spread the study on several types of application cases on any type of means of transport (bicycle, car, plane, etc.). To ensure that our tests are as precise as possible, we need to be able to control the time and space lag between impacts and the number of impacts, in addition to the classic impact parameters (velocity, energy, diameter, etc.).

In this thesis, depending on the detectability of damages, we will focus on all the domains from B to E (Figure 1.3), to study the impact behavior of composites in transportation areas where inspection is regular, but with an inevitable time interval between inspections. To extend this work, post-impact loading in compression (compression after impact CAI) can be used to monitor material residual strength ((8),(9)) performed according to several standards : Airbus AITM 1-0010 (20), Boeing BSS 7260 (21), SACMA SRM 2R-94 (22) and ASTM D7137/D7137M (23). In this work, we simply repeat the most critical configurations to assess the residual strength of composite materials after multiple impacts.

To differentiate between the first two domains we use the notion of the smallest damage detectable during an inspection designated by a damage detectability threshold BVID (Barely Visible Impact Damage, figure 1.4), but which can still decrease the compressive strength of a plate by 58% (24) or more according to Davies and Olsson (70%) (19). The exceeding of this threshold is detected by inspection procedures : non-

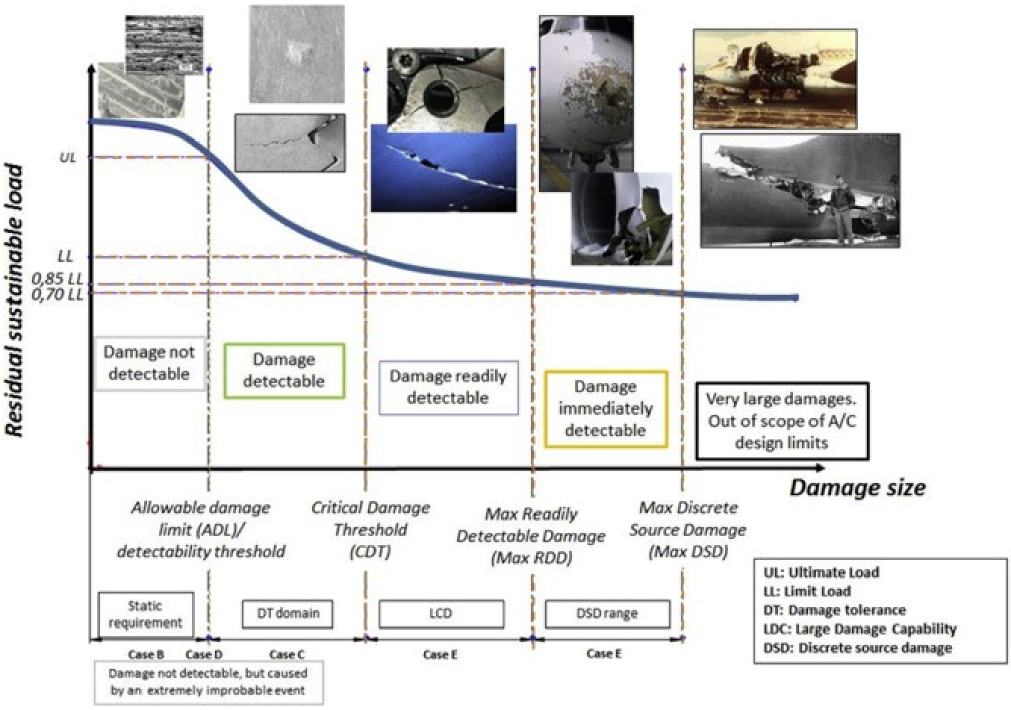

Figure 1.3 – Load to be supported by a composite structure according to the size of the damage (25).

destructive ultrasonic testing or generally (for economical reasons (26)) visual checks based on permanent indentation (27) which must not exceed certain values (or rather, below these values we cannot guarantee detection of defects) : some authorities accept a permanent indentation value of 0.3 mm (28), or 1 mm (29). Others specify the conditions for acquisition or inspection, 0.25-0.50 mm at a distance of 1.5 m with given lighting conditions (30), etc. The standards are such that for a permanent indentation less than BVID, the structure must be able to support the extreme loads, while for a value greater than or equal to BVID, only the limit loads are required (figure 1.4 (31)).

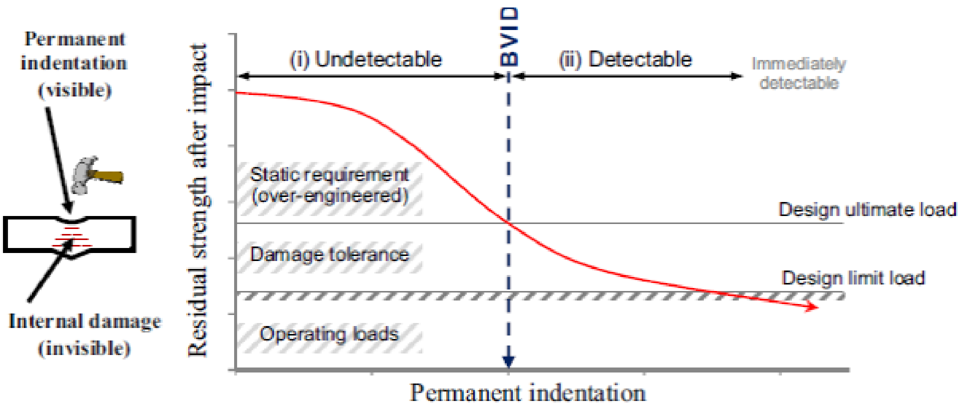

Figure 1.4 – Design by impact damage tolerance. (31)

Incremental impact tests are used by the industry to determine the impact energy

at which the BVID is reached. After each impact of the incremental test, the plate is removed from its mounting system to measure the indentation depth, another plate is used for the next increment. The different indentation depths are analyzed in order to choose, for single impact tests, an energy lower than the BVID, an energy equivalent to the BVID and an energy greater than the BVID. (32).
The BVID is fixed by Airbus at a depth of 0.3 mm for an unlimited duration inspection and inspection distance of 50 cm, and at 1.3 mm for an inspection of 30 seconds per panel at a distance of one meter (33).

The parameters to be considered during impact testing are : maximum impactor displacement, absorbed energy, permanent indentation depth, delaminated surface and residual properties such as compression after impact (CAI) (34).

1.1.2. Parameters influencing the impact response of composites

The damages shown previously in Figure 1.3 strongly depend on several parameters, among which we can cite :

— **The pair (Velocity/Energy) :** Material impact is generally classified into ((21), (7)) : low-velocity regimes (high mass), intermediate-velocity regimes, high/ballistic-velocity regimes (small mass), and hyper-velocity regimes. Serge Abrate discusses the work done in this area in his book "Impact engineering of composite structures" (5) and defines the impact regimes by considering the ratio between the impactor velocity and the transverse compression wave velocity and the maximum deformation up to failure in that direction. Indeed, an impact triggers elastic waves that propagate from the impact point (35). Material damping and energy diffusion associated with the propagation of two- or three-dimensional waves lead to a decrease in the influence of the corresponding waves. The response is therefore either governed by the wave propagation or by the impactor velocity. For example, high velocity is characterized by fiber rupture induced by penetration, and low velocity by matrix delamination and cracking. A small-mass impact at high velocity can lead to a higher degree of local loading with a corresponding increase in damage for an equivalent impact energy. Thus, for impact times of the order of the time required for waves to traverse the thickness, the response is mainly dominated by three-dimensional wave propagation. For longer impact

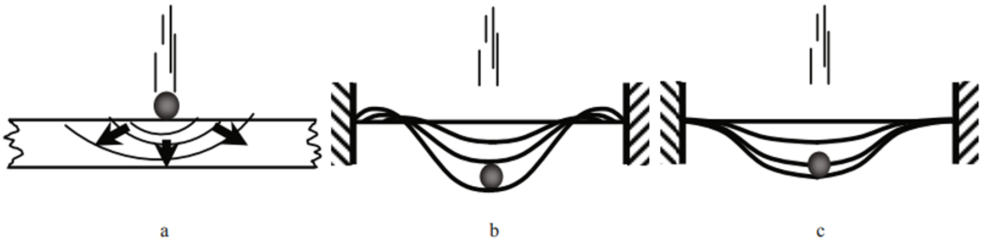

Figure 1.5 – Impact categories according to the velocity of the projectile. (a) High velocity, (b) Intermediate velocity, (c) Low velocity (5).

times, the response is first governed by bending and shear waves, and for times much longer than the time required for these waves to reach the limits of the plate, the lowest vibration mode of the impactor-plate system predominates. The resulting response is quasi-static in the sense that deformation and load have the same relationship as in a static case.

As illustrated in Figure 1.5 : (c) Low Velocity Impact (LVI) results from conditions arising from tool drops, which typically occur at speeds less than 10 m/s, where there is an equivalence between the two loading modes (impact/static indentation) since the response time of the impacted structure is long enough for the deformation waves associated with the impact to propagate and be reflected at the boundaries of the target. The response is close to quasi-static behavior, meaning that the position and type of boundary conditions play an important role in the phenomena involved (5). Davies and Robinson (36) stated that during low-velocity impact, a cylindrical region below the impactor undergoes a uniform compressive strain (ϵ_c) as the stress waves propagate through the plate. This can be mathematically expressed as :

$$\epsilon_c = \frac{\text{impactor velocity}}{\text{speed of sound in the material}} \tag{1.1}$$

Gravel and foreign debris on roads and airports are considered to fall under the regime of intermediate velocity impact and medium energy, figure 1.5(b). Intermediate impact events occur in the range of 10 m/s to 50 m/s, where the response time is short, and the target response is dominated by vibration modes. This is a transient situation between the low velocity/energy and high velocity configurations. Figure 1.5(a), high velocity impact (ballistic) is usually the result of small arms fire or explosive shell fragments. The response to high velocity impact is dominated by the propagation of a deformation wave through the thickness of the material, in which the structure does not have time to react, leading to localized damage. The effects of boundary conditions can be ignored because the impact occurs before the stress waves reach the boundary (5).

— **The mass of the projectile :** It is evident that the size of the plate and the boundary conditions influence the response shown in Figure 1.5(c), but less the response shown in Figures 1.5(a) and 1.5(b). The load, deflection, and deformations are out-of-phase during a low-mass impact, whereas they are more or less in phase during a high-mass impact. Moreover, due to more localized deflection, small-mass impactors cause higher impact loads and earlier damage initiation than large-mass impactors with the same kinetic energy. Studies on the influence of impactor mass (38) show that low-mass impactors cause much larger delaminations than high-mass impactors, as shown in Figure 1.6. These results demonstrate also that the response and damage are influenced by the duration of the impact, not just the impact energy.

Hosur et al. (41) note that not only energy but also velocity and mass are decisive factors affecting the response of a laminate. A low mass and high velocity have a more severe effect than high mass and low velocity.

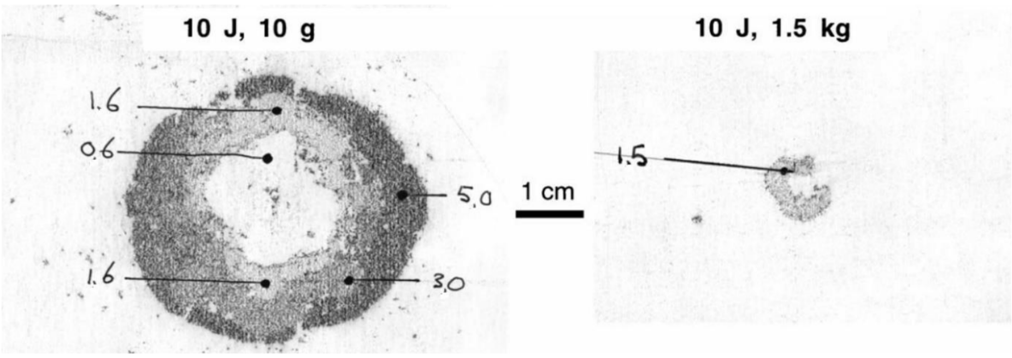

Figure 1.6 – Influence of impactor mass (of a 10 J impact with low and high mass), HTA/6376C carbon/epoxy laminate, handwritten delamination depth (38).

- **The nature and shape of the projectile :** Mitrevski et al. (44), in their work to evaluate the effect of the projectile shape on the impact of composite structures, conclude that the larger the projectile radius, the larger the delaminated area. Conversely, the smaller the impactor radius, the more localized the contact area, resulting in fiber failure before plate bending. Comparing a hemispherical, conical, and ogival impactor, the hemispherical impactor generates less permanent indentation, making it harder to detect defects and therefore more dangerous. Therefore, spherical projectile shapes can be used in our experimental tests using multi-compressed air cannons. To ensure repeatability, it is preferable to use surface-treated steel to reduce variability.

- **Boundary conditions of the target :** In the case of low velocity impacts, where the contact time is long enough so the structure can react, the boundary conditions modify the structure's response to the impact. Indeed, the permitted movements of the structure will not be the same, and thus the clamped plates will be less likely to deflect than the simply supported plates at the edges. The absorbed elastic energy is lower, and therefore the target will be damaged more quickly. At high velocity, the boundary conditions can be ignored, see Figure 1.5 a.

- **The material :** Carbon fibers are the most common in aeronautics, although the impact strengths of glass and aramid are higher than those of carbon, due to the progressive rupture mode of these fibers compared to the brittle fracture of carbon fibers. Kevlar fibers have the greatest energy absorption capacity (45). Therefore, the choice of Carbon/Epoxy composites over other composites to address the multi-impact problem can be justified. The experimental and numerical methods developed during this work can subsequently be considered for application to other composites, such as glass/epoxy or bio-composites, etc.

- **Thickness of the composite :** Several experimental studies conclude that impact behavior is related to geometric parameters such as the thickness of the composite. Indeed, Ulven et al. (46) concluded from their tests on carbon/epoxy composite plates of thicknesses 3.2 and 6.5mm at high speeds, that thin plates, therefore more flexible, absorb less energy than thick ones and consequently, transverse damage is more significant in thick plates, while longitudinal damage is almost the same. On the other hand, the thicker the plate, the higher its resistance to perforation since the projectile has more material to penetrate.

  G. Caprino and V. Lopresto (47), using the layering $[(0°/-45°/0°/45°/90°)]_s$, show that the thicker the plate, the greater its flexural stiffness and the lower the permitted deflection, the dominant failure modes are thus induced by shear at the impact face, unlike thin plates whose onset of failure occurs on the opposite face of the impact.

  Alcock et al. (48) show the existence of a nonlinear relationship between the thickness of the specimen and the energy absorbed by different composite specimens, but the thicker the specimen, the more energy absorbed, as shown in Figure 1.7.

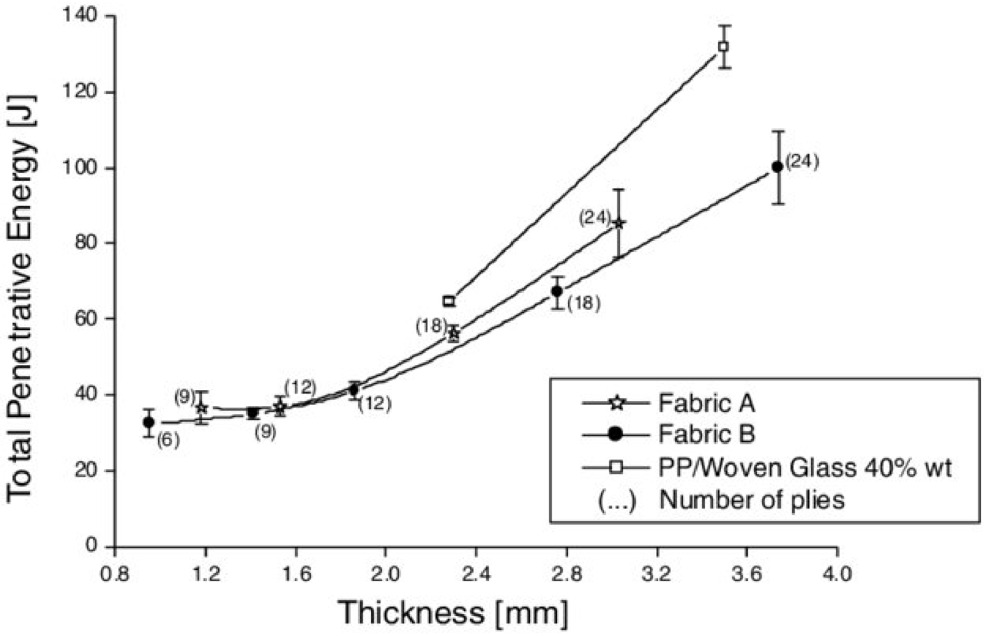

Figure 1.7 – Impact energy absorbed as a function of composite thickness (48).

- **Stacking sequence :** Hosur et al. (41) have performed impact tests on different stacking sequences. The delaminated surfaces change depending on the layering chosen. The maximum damage is observed in layers with maximum orientation difference (90°) such as 0/90 or +45/-45.

  H.B. Mokhtar (10) performed impact tests after 85% wet aging at 70°C on three types of laminates : Fully isotropic 24 laminates, Fully isotropic 18 laminates and $[45/90/-45/0]_s$. She noted that the damaged area, according to the C-scan results, is constant for $[45/90/-45/0]_s$ and FILs 24, while the damaged area increases linearly for FILs 18 and the impact damage is generally lower for FILs 24 than for $[45/90/-45/0]_s$. The stacking sequence determines the structure of the stiffness matrix (42) :

- Symmetry : There is no membrane-flexure coupling in the case of symmetric laminates. Moreover, symmetric laminates do not show a tendency to warp due to deformations (contractions) induced during the cooling process following the implementation process (42).
- Fiber orientations : The choice of fiber orientation is a compromise that improves in-plane shear stiffness at the expense of some loss of longitudinal stiffness. The in-plane modulus is maximum at θ=0, while the shear modulus is maximum at $\theta = \pm 45$, figure 1.8. Therefore, most laminates contain these two orientations plus others to respond to different loading directions. Generally, the composite is balanced ; it contains as many layers oriented along θ as -θ.

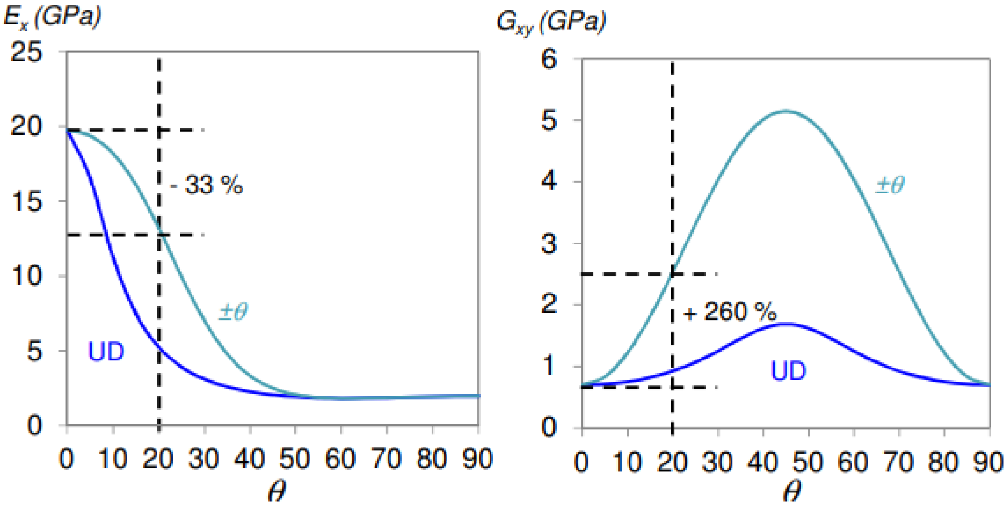

Figure 1.8 – Variations of elastic moduli according to the fiber orientation in a UD composite (42).

Additionally, in laminated composites, delamination occurs between successive plies of different orientations due to differences in their bending stiffness. Fuoss et al. (figure 1.9) show that the damage size increases significantly when the angle between two successive plies is less than 30° or greater than 75°.

Furthermore, Hosur et al. (41) observed that in many cases, the maximum damage occurs between plies with maximum differences in fiber orientation, such as 0/90 and +45/-45.

In general, impact damage increases with depth until the maximum size is reached (starting from the impacted face). The maximum delamination

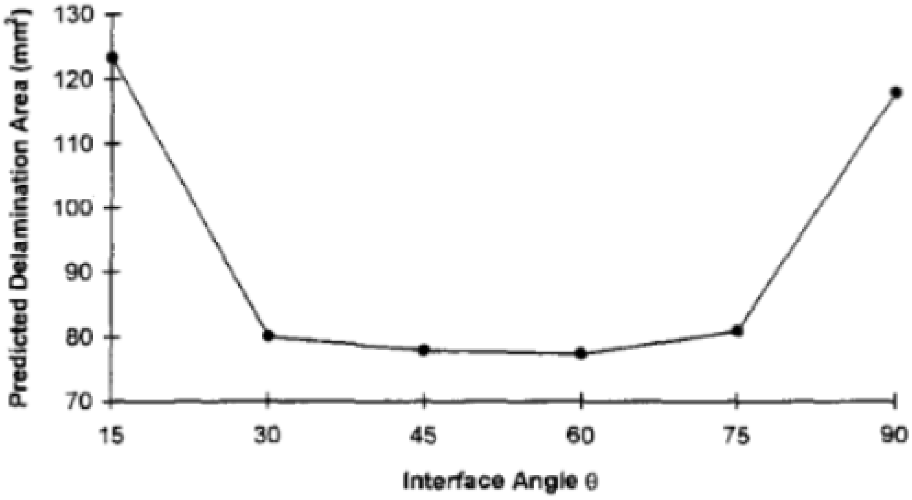

Figure 1.9 – Delamination area as a function of differences in angle between successive plies under a 7.5 kN load (43).

occurs in the layers near the non-impacted face, at about 75 to 85% of the thickness of the impacted surface.

— **Draping manufacturing :** The use of prepreg material is justified whenever maximum performance is desired for the composite part to be produced. Its advantages include control of the reinforcement/resin weight percentage, handling of a single product, and increased safety and hygiene (50). It is preferable to store the semi-finished product at -18°C in a plastic bag (50). To remove it from storage, it should be gradually brought to 20°C while protecting it from the ambient air (50). The plies are then cut and stacked with the desired fiber orientation. Once the plate is manufactured, we must perform a quality control check to ensure that we have not generated a concentration of defects during production.

However, several studies that investigate the effect of preloads on the impact behavior of composites do not observe major differences between a loaded and an unloaded specimen ((44), (49), (52)).

1.1.3. Damage mechanisms

Due to the heterogeneity of their structure, there is no single mechanism damage of composites but several types of damage that differ in nature and mode of development (54), figure 1.10.

The first internal damage to be triggered is usually matrix cracking, which then causes delamination initiations at the upper and lower interfaces of the concerned ply (55). Later, fiber failure occurs due to compression and local stress concentration around the indentation or due to extensional bending deformation (56). As a result, the overall failure process in composites is often considered as an accumulation process of different types of damage (57), see figure 1.11.

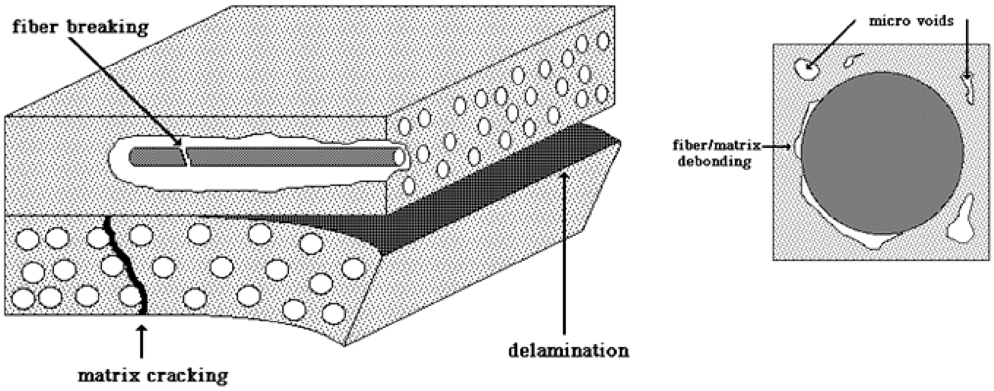

Figure 1.10 – Damage mechanisms of a laminated composite (53).

Matrix cracking :

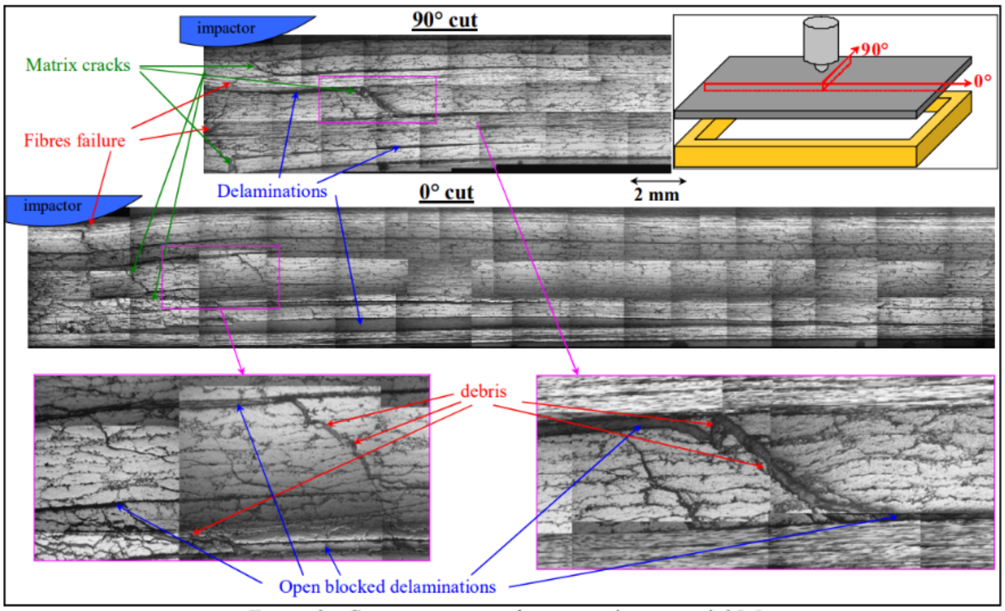

Figure 1.11 – illustration of damage types : micrographic sections after an impact at 25 J (55).

Matrix cracking is the primary failure mode due to impact resulting from the difference in properties between the matrix and fibers (58). Figures 1.12 on the left and right show the complex matrix cracking system that forms after impact using two different mechanisms :

- Shear-induced cracking primarily develops under the impact zone in the center of the plate (Figure 1.12), inclined at 45° to the normal direction to the interfaces (55)
- Cracking due to transverse tensile stresses observed in the lower structure plies.

In thick plates (stiffer in bending), the first type of cracking is initiated first, while in thin plates, cracking due to transverse tensile stresses predominates (59).

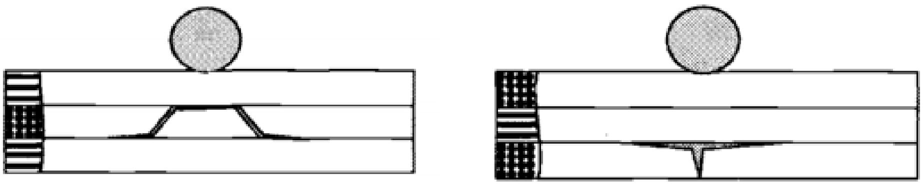

Figure 1.12 – Matrix cracking : dominated by shear (left), tension (right) (56).

Delamination :

Delamination corresponds to local decohesion between adjacent layers of different orientations, linked to a significant concentration of shear stresses that generally initiates in the lower interface of the plies (60). Delamination is generally considered as the result of a difference in bending stiffness between adjacent plies ; therefore, the plies will separate under out-of-plane load as they deform differently. The propagation of delamination can lead to the ruin of the composite structure (53), even if this is not generally the case in impact. Delamination is the main mode of damage in composite structures and one of the main defects of unidirectional laminates is out-of-plane failure, due to both a three-dimensional stress field and the presence of couplings between out-of-plane and in-plane failure modes (cracking in plies) (113). A physical explanation of this interaction is proposed by M. Renault (111) and schematized by C. Bouvet (79) in figure 1.13.

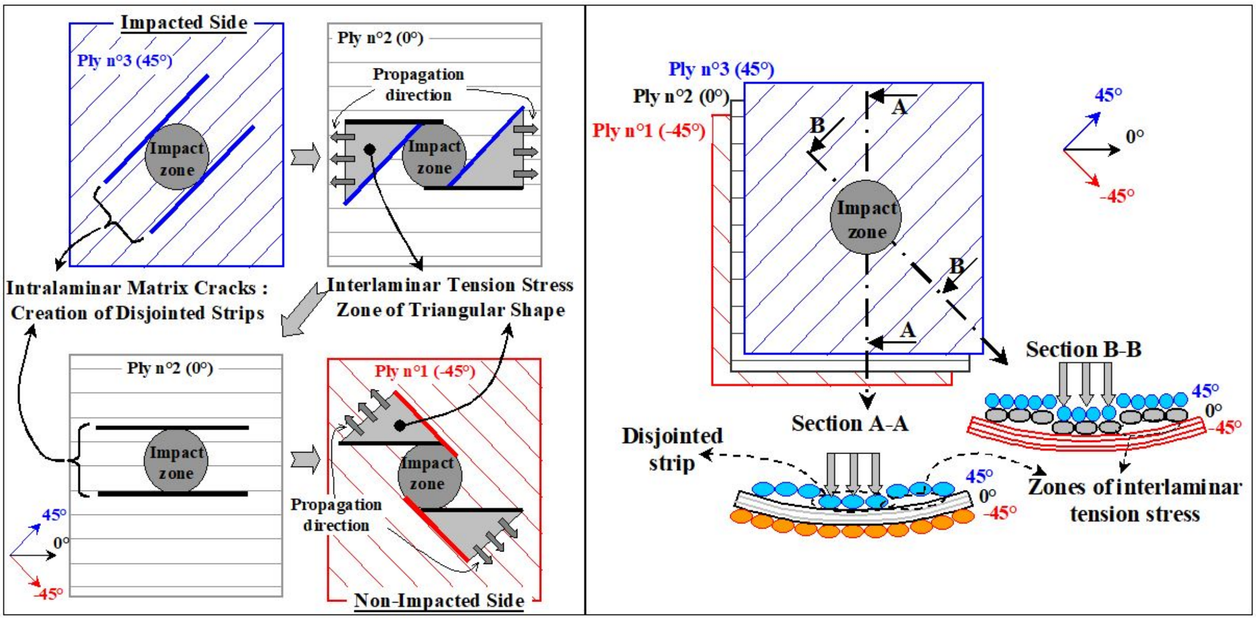

-a- -b-

Figure 1.13 – Formation mechanism of delaminations (a) and interface tension stress zones (b) (79).

Several delamination propagation modes can be distinguished depending on the mode of solicitation of the sub-laminates on either side of the crack ; it should be noted that, in practice, delamination results from a combination of these modes. This combination depends on both the material type, stacking sequence, and solicitations (61) :

- Mode I or opening mode (Figure 1.14 left), which is the most critical, then mode II and finally mode III (62), where the crack propagates locally under the effect of a traction load at the crack tip.
- Mode II or sliding mode (Figure 1.14 middle) where the crack propagates by shear 1-2 of the interface, and the two plies slide relatively to each other in the propagation direction.
- Mode III or tearing mode (Figure 1.14 right) where ply sliding occurs in the out-of-plane direction.

Each mode of propagation can be associated with a strain energy release rate (SERR) G per unit area of cracked zone, which can be traced back to the energy required for propagating a crack within the material in the context of a linear elastic fracture mechanics (LEFM) approach. A critical SERR, G_c, refers to the value of energy release rate required for crack propagation, this energy is dissipated to propagate the Fracture Process Zone (FPZ), and depends on several parameters such as the stacking sequence, fiber/matrix couple, manufacturing method, fiber volume fractions (FVF), etc. (100). If :

- $G < G_c$: not enough energy to drive the extension of the crack.
- $G = G_c$: critical moment for stable crack extension.
- $G > G_c$: unstable crack extension.

ASTM has created standards or is working on standards to measure G_c under a variety of loading conditions (71) : the ASTM standard for mode I loading (ASTM D5528) uses the double cantilever beam (DCB) test to measure the pure mode I fracture toughness (G_{Ic}). The End Notch Flexure (ENF) test is used for pure mode II fracture toughness (G_{IIc}). The mixed-mode bending (MMB) test is an ASTM standard (ASTM D6671) that can measure fracture toughness over a wide range of combinations of Mode I and Mode II loading. For pure mode III, the Edge Crack Torsion Test (ECT) can be used to measure fracture toughness.

A diagram of damage from impact on a quasi-isotropic laminate is presented in Figure 1.15. Eve O. (53) shows that the position of delaminations within the thickness seems to depend on the loading, the thickness of the material, the size of the damage and the depth of the indentation. He conducted tests on bi-axial specimens (subjected to combined tension and compression stresses) by increasing the volume of damage in the impact zone, which showed that delaminations propagated in the first half of the thickness (impacted face). Furthermore, the delamination presents a spiral pattern that rotates around the center of impact, and the main direction of the delamination coincides with the fiber orientation in the lower ply (64).

In the case of a structure subjected to an impact, the mode of crack propagation depends mainly on the impact velocity. For velocities lower than ten meters per second,

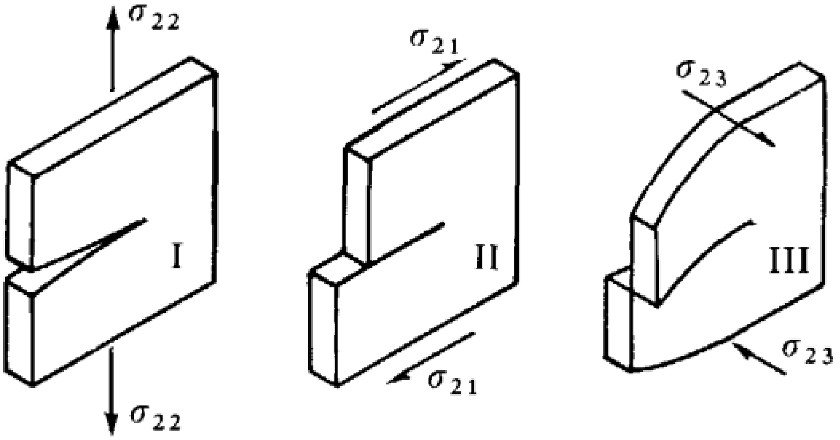

Figure 1.14 – Delamination fracture modes (100).

the specimen behaves globally like a plate subjected to a three-point bending stress. The plies of the laminate then start to slide against each other during the plate's deflection, resulting in a delamination crack propagation mode mainly in mode II. On the other hand, during a high-velocity impact, the damage is dominated by wave propagation effects that induce crack propagation modes in mode I at the impact point and mode II around it (56).

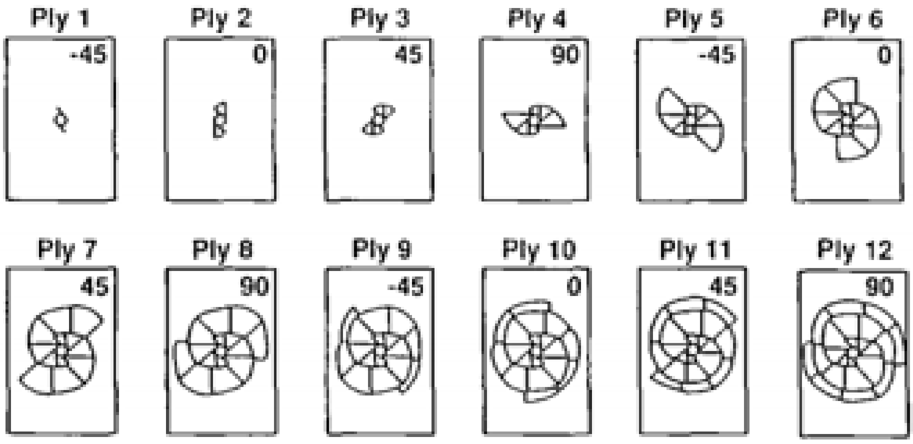

Figure 1.15 – Schematic of impact-damaged delaminations through the thickness of a $[-45/0/45/90]_{3s}$ plate (63).

Fiber breakage :

Even though this type of damage may not necessarily appear during low energy impact and this type of damage usually occurs later than delamination (and therefore after matrix cracking), fiber rupture can still occur on the impact surface due to compression and concentration of local stresses around the indentation. It can also be observed in the lower plies due to extensional deformation by bending (56). However, fiber rupture due to tension is not often observed during low velocity impact (65).

Damage coupling :

Depending on the type of loading, one or more modes of failure may be activated (61). Figure 1.16 shows a typical scenario of damage evolution in a laminate :

- Appearance of matrix microcracking and fiber-matrix decohesion (Figure 1.16, step 1).
- Grouping of several microdamages and appearance of transverse cracks. Then appearance of micro-delaminations, when the cracks reach the interface between plies (step 2-3).
- Macroscopic failure, by delamination, fiber rupture and matrix cracking, depending on the type of loading and stacking sequence (step 4).

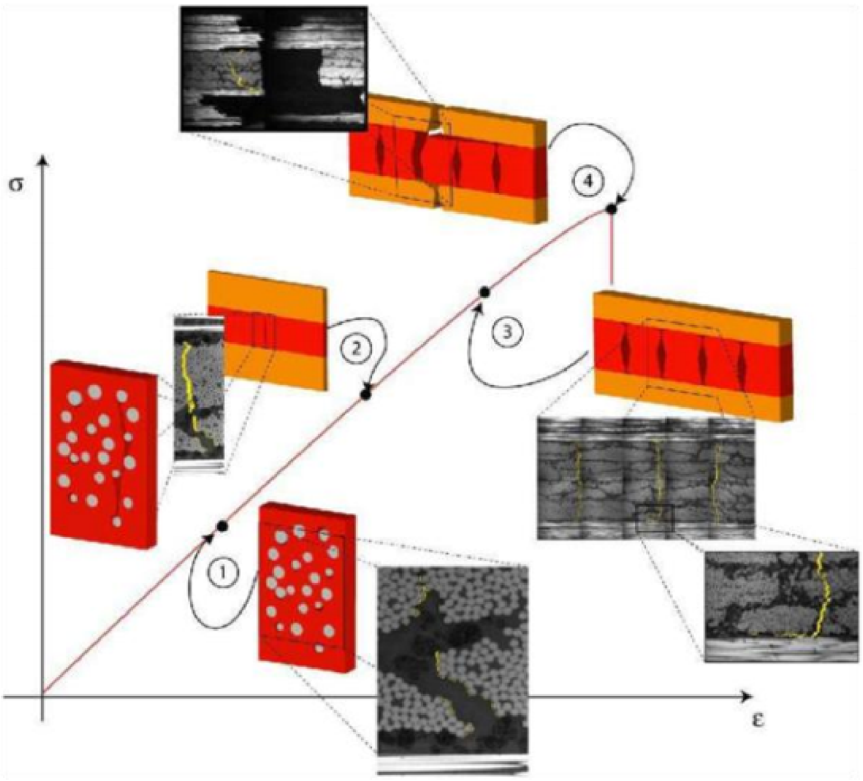

Figure 1.16 – Chronology of composite laminate failure (61).

Permanent indentation :

The final residual indentation after relaxation of the impact load is called permanent indentation. Several studies explain such permanent deformation : Abi Abdallah et al. (66) proposed a theory based on the blocking of debris inside matrix cracks, preventing them from closing, as shown in Figure 1.17. Figure 1.18 shows a typical permanent indentation obtained by low velocity impact on laminated composites (55).

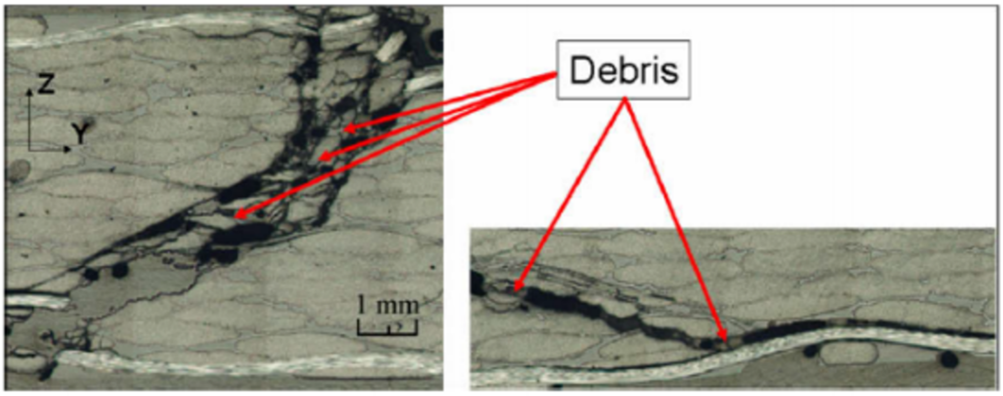

Figure 1.17 – Blocking of debris inside matrix cracks (66).

Shi Seng et al. (67) and Tan et al. (68), took into account the part of the indentation related to plastic deformation caused by shear. Chen et al. (69) presented a study showing that indentation can also be influenced by fiber failure.

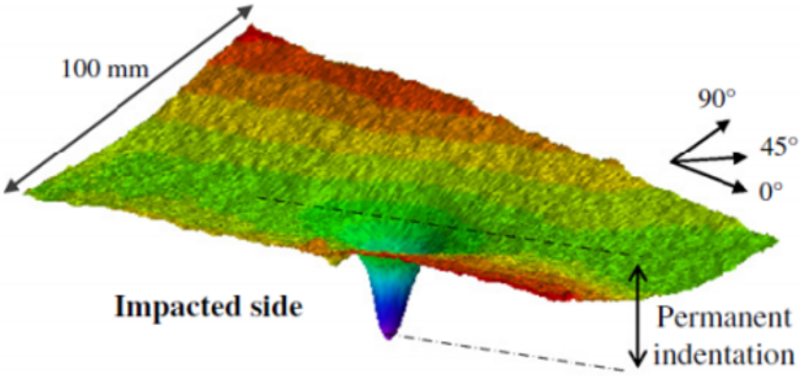

Figure 1.18 – Typical permanent indentation measured by DIC on the impacted face (55).

1.1.4. Loads affecting the impact resistance of composites

- **Effect of temperature :** The effect of temperature variations for both low and high temperature ranges has been experimentally studied in relation to impact damage on Carbon/Epoxy laminates. Increasing the temperature of a CFRP laminate resulted in a decrease in the impact-induced delamination zones.

  Rio et al. (70) examined the impact response of CFRP laminates at low impact velocities under low-temperature conditions. Square specimens of Carbon/Epoxy laminates with different sequences (unidirectional, cross-ply, quasi-isotropic, and woven) were tested using a drop weight test. The test temperature ranged from 20 to -150°C. The damage was measured by C-scan inspection, and damage mechanisms were studied by optical and scanning electron microscopy. Figure

1.19 shows that, cooling the laminate before impact had an effect on the damage similar to that of increasing the impact energy, i.e., a greater extension of matrix cracking and delamination, a deeper indentation on the impacted side, and a more severe fiber detachment. The threshold energy decreased by up to 50% in the quasi-isotropic laminate when the temperature dropped from 20 to -150°C. Low temperatures produced interlaminar residual thermal stresses in the quasi-isotropic composites, high enough to accelerate matrix cracking and delamination during low-velocity impact.

A : Impacted side, at 20°C (left), -60°C (center) and -150°C (right)

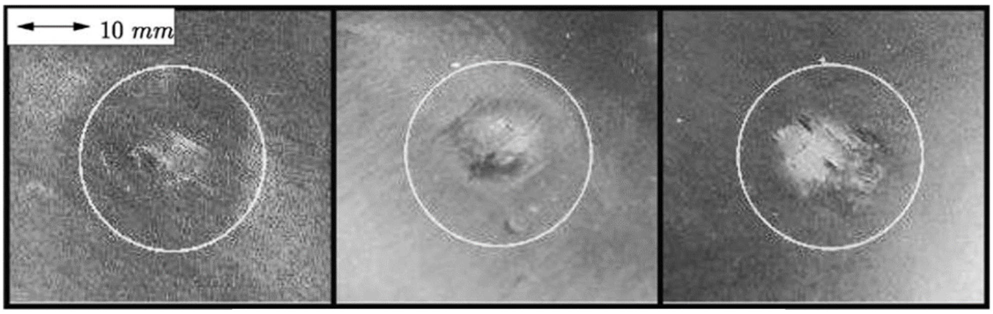

B: Non-impacted side, 20°C (left), -60°C (center) and -150°C (right)

Figure 1.19 – Effect of temperature on the impact behavior of Carbon/Epoxy laminates (70).

- **Fatigue and repeated impacts :** The analysis of impact fatigue phenomena was presented in the study by (72). The fatigue life was found to be a function of fiber orientation relative to the impact loading direction. There is a minimum impact energy for failure to occur.

  Roy et al. (73) found that a well-defined impact-fatigue (S-N) behavior was observed in notched composites with 63.5% glass fiber/vinyl-ester resin. The residual strength measured after impact fatigue showed initial strength retention at high impact energy levels, followed by gradual and then rapid drop. The residual modulus and fracture toughness showed a gradual decrease with increasing number of impacts. The composite failure under impact-fatigue was explained by the concentration of volume micro-cracks.

  Jang et al. (74) show that for a given laminate, there exists a critical incident energy, E_c, beyond which significant damage in the form of delamination will occur under a single repeated impact. In this case, the slope b of the curve $(\frac{LogP_m^N}{LogP_m^0})$ as a function of $logN$ (where N is the number of repeated impacts, P_m^0 is the

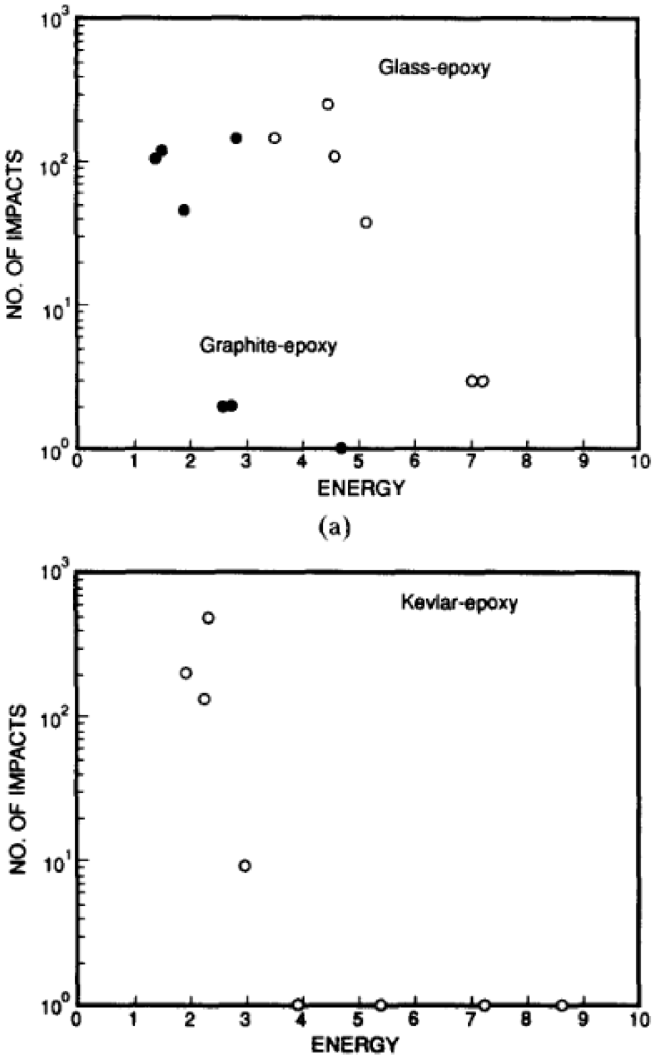

(a)

(b)

Figure 1.20 – Number of impacts to create the first delamination as a function of incident energy for : (a) glass-epoxy and graphite-epoxy, and (b) Kevlar-epoxy composites (74).

maximum load at the first impact and P_m^N is the maximum load at the N^{th} repeated impact), can be used as an index of damage tolerance ; the smaller b is, the more resistant the material is to damage. Figure 1.20(b) demonstrates that, when an incident energy of about 4 J or above was applied to the Kevlar-fabric composites, delamination would occur at the first impact. When an incident energy of approximately 3 J was used, no delamination was detected until the tenth impact. Clearly, the critical incident energy, E_c, to produce delamination damage in this composite is between 3 and 4 J. As shown in figure 1.20(a), the glass-fabric/epoxy material delaminated when impacted twice with an incident energy (E_i), of about 7 J. For all the epoxy composites studied, a cumulative mode of matrix microcracking was found to prevail at the sub-critical stage of impact-fatigue response before the formation of macroscopic delamination. When repeated impacts continue after the onset of delamination, the delamination cracks increase in size and number, resulting in a continuous loss of composite strength and stiffness.

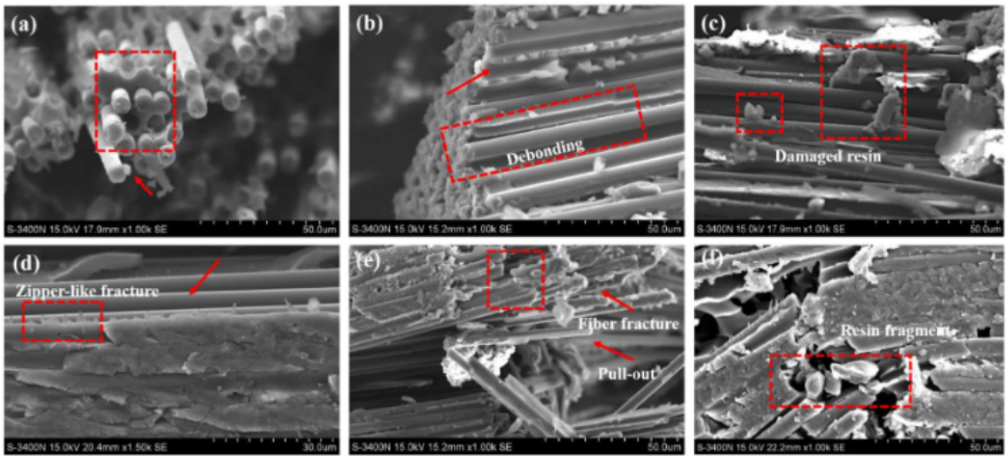

Figure 1.21 – SEM observations : (a) original sample, (b) sample subjected to 8 hours of aging, (c) sample subjected to 24 hours of aging. SEM shear sample : (d) original sample, (e) 8-hour aging sample, (f) 24-hour aging sample (75).

- **Aging :** The aging of composites results from the combined action of temperature, humidity, and environmental pressure, as well as from the conditions of their implementation (type of process, cooking cycle inducing residual stresses) and the structure of the material (76). It corresponds to an often irreversible evolution of the material's properties, and its study requires complex, multi-physical, and multi-scale approaches. By focusing on the effects of aging on mechanical behavior, we exclude aging processes such as chemical aging, photo-chemical aging (which remains a superficial phenomenon a few micrometers away from the specific properties of composites), etc. and we generally focus on wet and thermal aging (50).
  Figure 1.21 shows images from the scanning electron microscope (SEM) of three-point bending and interlaminar shear tests of different specimens, it concludes that the impact resistance of CFRP has been improved : Figure 1.21(a) shows the morphology of the fracture of the virgin specimen, with a few fibers pulled out but still adhering to the surface, indicating good interfacial bonding. Figure 1.21(b) shows the morphology of the fracture of the specimen aged for 8 hours, with some fibers clearly pulled out of the matrix. The surface is smooth without resin, indicating that the bonding strength between fiber and matrix is significantly reduced. Figure 1.21(c) shows the case of 24 hours. The fiber surface is smooth and separates from the resin, and the resin structure is seriously damaged, confirming that the interfacial bonding strength is further reduced, leading to a continuous decrease in mechanical properties. Figure 1.21(d) shows the fiber is well wrapped by the resin without detachment. Figure 1.21(e) shows the brittle fracture of the resin disappears, indicating that compared with the original samples, the samples aged for 8 hours are more resistant, confirming that the impact resistance of CFRP has been improved. Figure 1.21(f) shows that the fiber and resin are

severely damaged, with a large number of fiber and resin fragments, indicating that after hygrothermal aging, shear performance decreases significantly.

1.1.5. Multi-impacts of composite structures

Rezasefat et al. (84) describe an experimental and numerical study that investigates how pre-existing impact damage affects the low-velocity impact response of Carbon Fiber Reinforced Polymer (CFRP). The results indicate that the location of impact plays a crucial role in determining the mechanical response and damage to composite skin panels. When the impact location moves towards the panel boundaries, there is a significant increase in impact bending stiffness. Moreover, the presence of pre-existing impact damage measuring 805 mm^2 from a 40 J impact at the center of the skin panel results in a more complex impact response that is dependent on the impact location with respect to the previous damage area. However, when the impact is far away from the previous damage, the panel shows no significant difference in response compared to a similar impact on an undamaged specimen.

Kueh et al. (85) provide a review of recent research works on the response of sandwich structures to single and repetitive low-velocity impacts. The paper covers impact energies ranging from 0.06-360 J, impact velocities of 0.5-34.2 m/s, and repeated impact numbers up to 400 times. The main performance metrics used to evaluate impact resistance are force-time, displacement-time, velocity-time, acceleration-time, force-deformation, energy-time, and energy absorption. The review recommends an integrated, non-dimensional term to combine all these metrics for overall impact performance assessment. Failure modes of sandwich structures under impact include fiber breakage, matrix cracking, skin perforation, skin-core debonding, skin delamination, core crushing, core shear, core buckling, and skin wrinkling. The paper also covers factors that affect sandwich structure resistance, such as the thickness and stacking sequence of skin, core thickness, core density, core number, impactor mass, impactor velocity, impactor geometry, temperature and moisture, and support condition. Repetitive impacts are dominated by indentation, penetration, and perforation and are more destructive since they compromise further the strength and integrity of the sandwich structures. Even so, repetitive impact behavior though more realistic is comparatively less studied compared to single impact. Variation of the energy absorbed plastically correlates inversely with the impact number, since the elements that will be damaged at low energies are already broken, leaving only elements that require more energy to be damaged. In addition, with the new surfaces created, more energy is dissipated in the form of friction. Lower impact energy causes then a higher impact number to full perforation.

The dimensionless impact resistance efficiency index relating the most critical parameters is introduced by Abo Sabah et al. (90) to ensure a meaningful impact performance assessment on the sandwich beam designs. The impact resistance efficiency index takes into account the mass of the structures as well since lightweight is one of the chief attractive features for advanced structures. For such purpose, an impact resistance efficiency index, I_e, is introduced as the following equation :

$$I_e = \frac{E_{\text{abs}} \cdot F_{\max}}{A_d \cdot g \cdot m_b \cdot t \cdot \sigma_{\max}} \tag{1.2}$$

where E_{abs} is the absorbed energy, $F_{\max}$ is the maximum contact force, A_d is the damage area, g is the gravitational acceleration, m_b is the sandwich beam mass, t is the sandwich beam thickness, and $\sigma_{\max}$ is the maximum stress in the sandwich beam. The chief reason I_e contains various effects is such that it is in a dimensionless form. Such a concept is applied in the theories of Buckingham's Pi and similitude, commonly seen in the fluid mechanics studies. This work demonstrates by means of this newly proposed impact performance index that, with a low penalty of mass and thickness addition due to a dual-core design, the new sandwich beam design improves considerably the overall impact behavior of that employs conventional configuration.

Huo et al. (86) discusses the study of the delamination propagation behavior of multidirectional CFRP composite laminates under two identical indentations with different loading distances. The study found that delamination link-up is a distinguishing damage feature for multiple-indented laminates, and the critical loading distance for delamination link-up can be predicted using the proposed method (based on a concise Hashin-type delamination propagation criterion). The study concludes that, neighbouring damage effects cause a larger projected delamination area than the sum of two identical out-of-plane quasi-static indentation cases, figure 1.22. The study also suggests that the reduction in the effective delamination growth threshold at the critical delamination link-up interfaces was independent of the indentation force. However, the study has the limitation that the first indentation delamination and its effects on the global critical second indentation stress profile were not considered. The study recommends the use of the cohesive zone model (CZM) to model the delamination damage because of the need for modeling techniques that account for delamination-induced ply material degradation. The study acknowledges the need for further research considering additional factors such as stress wave, rate sensitivity of material, plate vibration, laminate configuration, delamination growth in arbitrary directions and ply interfaces, and more complex loading conditions consisting of three or more indentations.

Deka et al. (87) aimed to investigate the effects of high-velocity impact on S2-glass/epoxy laminates under single and multi-site near sequential and simultaneous impact conditions. The results showed that sequential impact led to a higher increase in new surface creation compared to simultaneous impact. Additionally, for two and three projectile impacts, sequential impact resulted in a 23.0% and 14.2% increase in delamination damage (projected surface), respectively, compared to simultaneous impact. The residual velocity of the projectile was influenced by stress wave interactions along the primary yarns and the amount of delamination damage developed. As projectiles impacted the damaged regions, the decrease in contact stiffness reduced the ability of the laminate to absorb energy, resulting in an increase in exit velocity in both sequential and simultaneous impact scenarios. The study found that the delamination

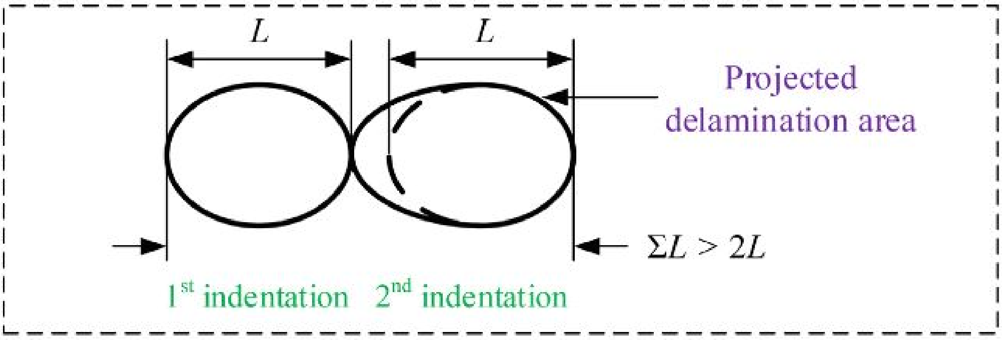

Figure 1.22 – Influence of neighbouring damage on delamination growth in multiple indented composites (86).

parameter S_d (delamination scale factor, introduced to match the predicted results to experimental values, the value of S_d is iterated based upon the laminate architecture and interface condition), and the strain softening parameter m_i (to take account of the phenomenon where the material experiences a decrease in its stiffness or resistance to deformation as the applied strain increases), were the most sensitive in achieving close correlation with the experimental test results in the modeling study.

Vaidya et al. (88) investigates the response of S2-glass/epoxy balsa core sandwich structures to high-velocity impact through experiments and finite element modeling. The study models the progressive damage and delamination of the composite face-sheet using LS-DYNA with material model MAT 162. Impact on the balsa wood core was simulated using MAT 2 and MAT 143. The study shows that simultaneous impacts result in significantly more damage compared to single impacts, and that the balsa wood core is effective in absorbing energy. The study found that FEA captured the main features of the impact phenomenon and predicted different damage modes in close agreement with the experiment.

Garzon-Hernandez et al. (126) investigated the impact mechanical behavior of SFR (thermoplastic polymers reinforced with short fibres) thermoplastics under single and multiple impacts, using SCFR PEEK (short carbon fibre reinforced polyether-ether-ketone) as the baseline material. The results showed that the ballistic limit from single impact cannot be extrapolated to sequential and simultaneous tests. Sequential tests resulted in a reduction in the ballistic limit when a second or subsequent projectile impacts the target, while simultaneous impact tests showed a reduction in the ballistic limit with respect to single impact. The interaction between cracks propagation, stress waves, and complex bending effects were observed to govern the fracture mechanisms and the damage extent.

Boyd et al. (127) evaluated the multi-impact performance of 3WEAVES2/SC-15 composites with and without TPU (thermoplastic polyurethan) film inter-layers of varying thicknesses. The results showed that the use of TPU film inter-layers with 3-D pre-forms significantly increased durability and damage tolerance. However, much work still needs to be done, including examining the unique properties of different TPU films, developing a modeling framework, creating a hybrid composite, and performing higher energy impact testing on thicker sections. The research demonstrated promise for designing more durable composite systems to meet emerging structural composite applications.

1.1.6. Input parameters

In terms of impact events, the figure 1.23 summarizes the range of energy for each type of impact on an airplane (95). The impact energy is on average 22.82 J with a standard deviation of 18.77 J.

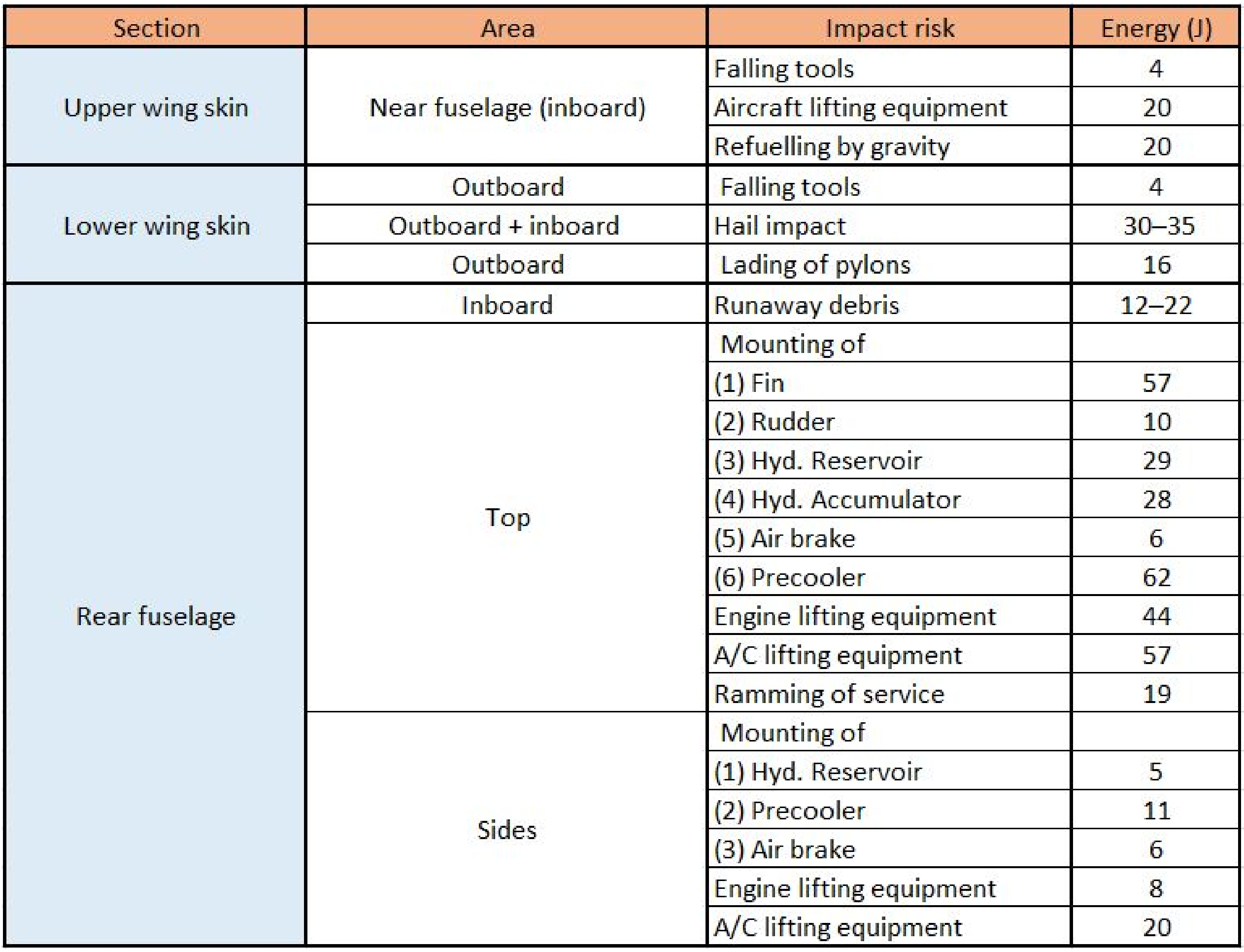

Section	Area	Impact risk	Energy (J)
Upper wing skin	Near fuselage (inboard)	Falling tools	4
		Aircraft lifting equipment	20
		Refuelling by gravity	20
Lower wing skin	Outboard	Falling tools	4
	Outboard + inboard	Hail impact	30–35
	Outboard	Lading of pylons	16
Rear fuselage	Inboard	Runaway debris	12–22
	Top	Mounting of	
		(1) Fin	57
		(2) Rudder	10
		(3) Hyd. Reservoir	29
		(4) Hyd. Accumulator	28
		(5) Air brake	6
		(6) Precooler	62
		Engine lifting equipment	44
		A/C lifting equipment	57
		Ramming of service	19
	Sides	Mounting of	
		(1) Hyd. Reservoir	5
		(2) Precooler	11
		(3) Air brake	6
		Engine lifting equipment	8
		A/C lifting equipment	20

Figure 1.23 – Risks and energies of typical impacts on an airplane.

In the automotive industry, hailstones and gravel impacts remain the most common. The roof, hood, trunk, and front and rear bumper remain the most affected components. In a world where the use of composites is not only developed in aeronautics, taking into account these effects for the new generation cars (with a very important percentage of composites, example in figure 1.24), understanding the impact phenomena will be undoubtedly useful for this field too.

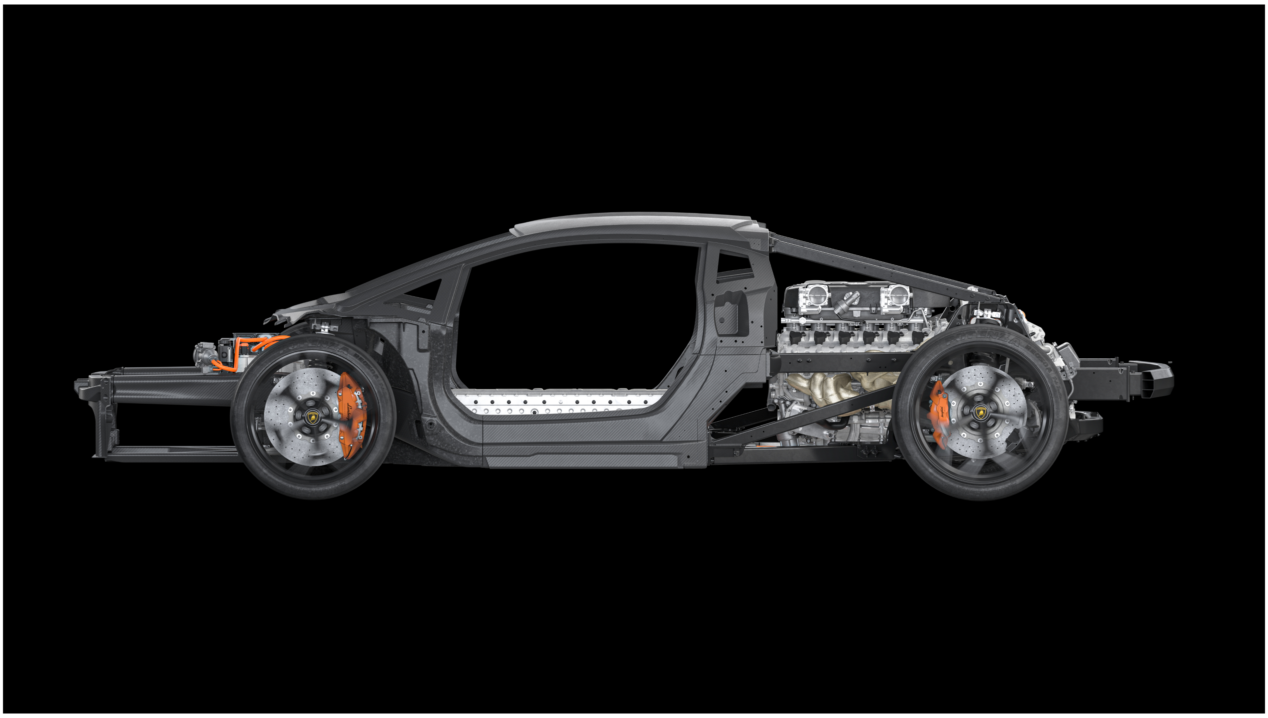

Figure 1.24 – The Lamborghini composite LB744 "monofuselage." The entire front structure is composite with aluminum alloys used for the rear. Photo Credit : Lamborghini (139)

The Pareto chart (figure 1.25), whose data is taken from a report by the French national road safety agency on gravel projections (96), traces the distribution of the number of gravel in decreasing order of frequency, with a cumulative line on a secondary axis in the form of a percentage of the total. It can be observed that 80% of the gravel in our sample weighs between 0.25 and 1.25 g, and the weight of the heaviest gravel is 3.9 g, which corresponds to an energy of a few J for a speed between 0 and 130 km/h (personal cars) and about ten J for a maximum speed of 372.6 km/h (corresponding to the speed record at which Colombian Juan Pablo Montoya was flashed while driving a Formula 1).

The report concluded that the gravel is not projected backwards from the vehicle, but lifted vertically with a tendency to describe a trajectory in the direction of the vehicle's movement. This implies that only the speed of the following vehicle can provide the necessary energy to break its windshield, hood, bumper, or other component hit by a gravel lifted by the preceding vehicle, knowing that the height of the rear and lateral projections exceeds 1 m from 60-70 km/h, and that the projection distance, or more precisely the distance traveled by the car during the lifting of the gravel, is around 20 to 25 m for rear projections and 2 to 3 m for lateral projections.

As for hail, its size varies between 5 mm and 5 cm in diameter, and up to 15 cm in extreme cases. Its density is about 0.85 to 0.90 g/cm^3. It should be noted that as soon as water droplets have a temperature of -13 °C, they transform into an icy core, which is the beginning of the hail (102).

The ANELFA (Association Nationale d'Études et de Lutte contre les Fléaux Atmo-

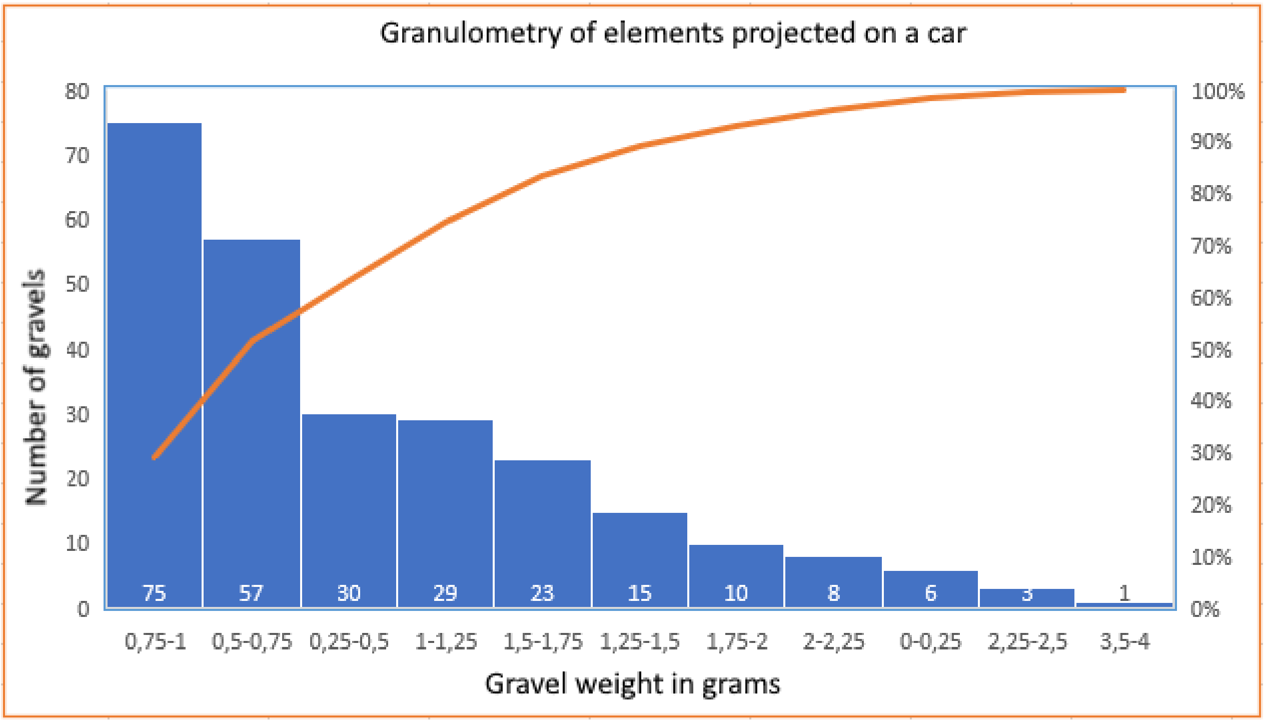

Figure 1.25 – Distribution of the gravel recovered during the the first test campaign of the french national road safety organization.

sphériques) offers a scale constructed using hail meters based on the measurement of nearly 4000 hail falls recorded in France since 1988. Table 1.1 summarizes the impact parameters of the hailstones.

1.1.7. Low and medium velocity impact test benches

Low Velocity Impact (LVI) tests on composites can be conducted using various types of equipment. Typically, impact is induced using an oscillating pendulum (Izod and Charpy), a falling weight, a rotating inertia wheel, or a projectile driven by a gas gun. When the velocity and kinetic energy of a striking mass vary, energy is transferred and work is applied to the specimen (energy is absorbed through elastic and plastic deformation, hysteresis effects, friction between the specimen and test setup, and acquisition of kinetic energy by the specimen).

To achieve a desired average impact velocity, the most commonly used test benches are the drop tower and gas guns or Hopkinson bars. For gas guns, by changing the compressing fluid, the section and length of the gun, the mass of the projectile, and the distance between the gun and the specimen, impact velocity can be varied. Figure 1.26 shows the frequently used configuration of compressed gas guns. The free-edge condition is preferred to maintain a behavior more representative of a large structure (77). Fully clamped boundary conditions are also generally used and representative of small or medium-sized parts (39) tested following various standards such as Airbus AITM 1-0010 (78). Instrumentation for this type of test is limited by sensor performance requirements. It is possible to instrument the projectile with a force sensor or

Diameter (mm)	Mass (g)	Velocity (m/s)	Kinetic energy (J)
5	0.06	9.7	0.003
10	0.48	13.7	0.045
15	1.61	16.8	0.23
20	3.81	19.4	0.72
25	7.44	21.7	1.75
30	12.86	23.8	3.63
40	30.49	27.4	11.5
50	59.56	30.7	28
60	102.9	33.6	58
70	163.4	36.3	108

TABLE 1.1. – Mass, velocity and impact energy of hailstones.

accelerometer, but this method has limitations : impact velocities below 50 m/s and signal losses caused by frequent wire rupture (77). E. Olivier (53) implemented an experimental procedure to follow the propagation of delaminated surfaces by attaching US sensors to the periphery of the largest delaminations and recording A-scans in real-time.

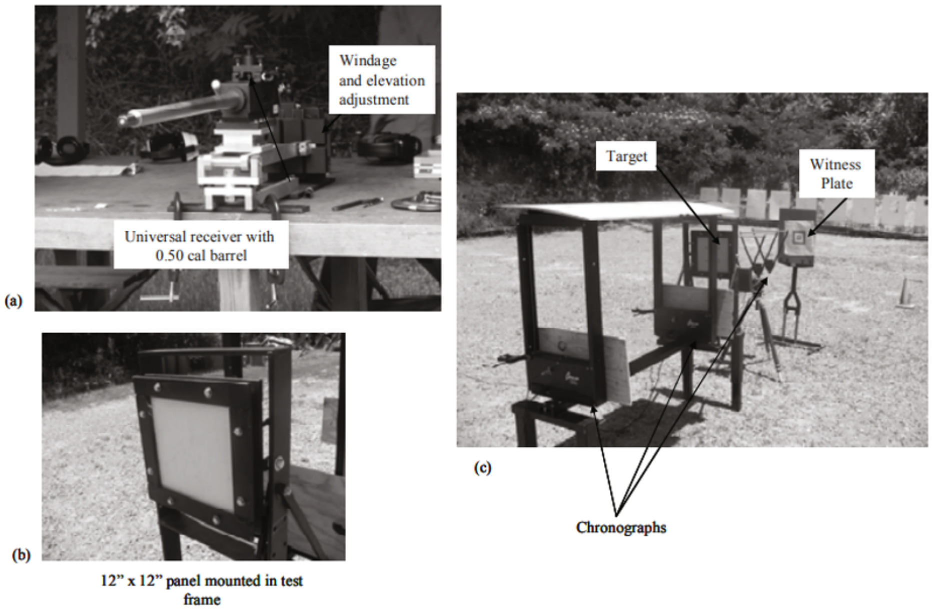

Figure 1.26 – Example of a single-barrel gas gun for ballistic impact testing : (a) gun and adjustment elements, (b) close-up view of the target and setup, (c) assembly showing pairs of chronographs and the target (5).

Referring to the energy absorbed by the sample, by measuring the projectile velocity before and after impact, the simplified expression for absorbed energy is :

$$E_{\text{absorbed}} = \frac{1}{2} \times m_{\text{ball}} \times (V_{\text{initial}}^2 - V_{\text{residual}}^2) \tag{1.3}$$

Hosur et al. (41) observed that the impact of the gas cannon causes more severe damage than the impact of the falling mass. After a certain energy level, the response of the laminate is similar for both types of impact, indicating that the effect is localized at the point of impact and that the extent of damage is almost the same.

To measure the residual velocity of the ball, P. Deconinck (16) sets up a system with multiple laser beams in order to try to grid the area in which the projectile was likely to bounce using a laser whose beam is reflected between two parallel mirrors. The use of high-speed cameras for velocity measurement is possible by respecting the camera's parallelism with the projectile trajectory and the rules of focus, namely, the correct adjustment of the three internal exposure parameters "the exposure triangle" (shutter speed, aperture, and ISO sensitivity).

Precision ballistic chronographs also provide accurate velocity measurements over a wide variety of shooting conditions. The use of these chronographs remains possible provided that the trajectory of the ball is controlled without damaging the chronographs. It should be noted that several types of chronographs are not certified, and it is up to the user to seek to ensure the accuracy of the chronograph.

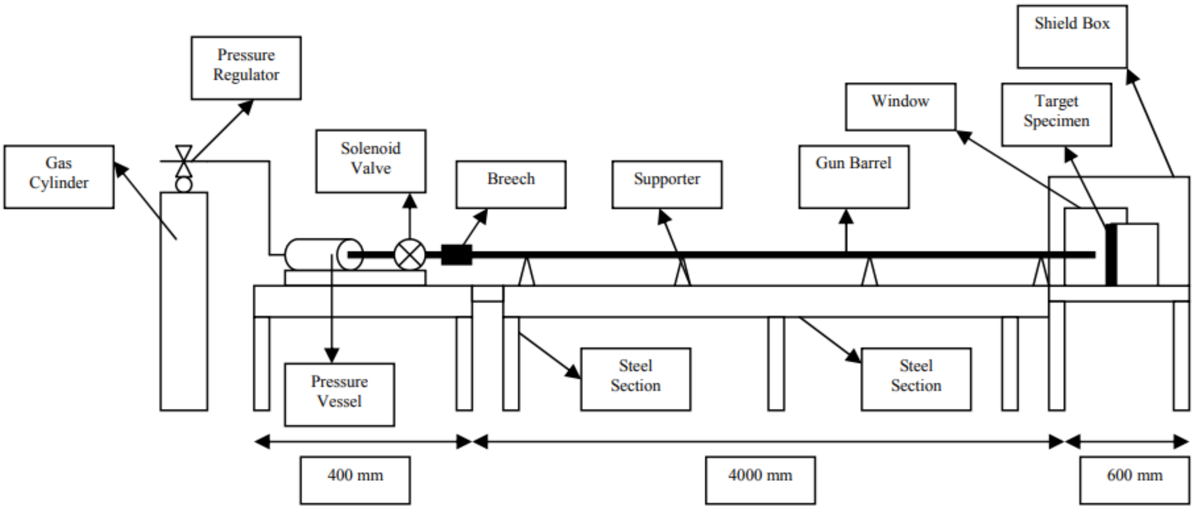

Figure 1.27 – Gas launcher for high-speed impact testing (5).

Trellu et al. (80) created a speckle pattern on the sphere to track its motion using image correlation techniques developed by Passieux et al. (81). This enables the measurement of the impact force curves as a function of ball displacement for different shooting velocities. Regarding boundary conditions, the composite plate is only supported on an impact window that corresponds to the area of interest in the specimen.

Figure 1.27 shows the general configuration of a gas launcher used for high-speed impact tests. The system consists of a pressure vessel, a firing mechanism, a launch unit, a capture chamber, and a velocity measurement unit. This type of cannon is capable of launching a projectile with an initial velocity of less than 700 m/s at a reservoir pressure of 150 bars. A higher velocity is possible if a lighter projectile and higher reservoir pressure are used (82). Further details on the development and instrumentation of cannons are studied in Chapter 2.

The literature lacks precise definitions of the terms used to differentiate between the various cases of impact and multi-impact, so that certain multi-impacts cases are still missing from the literature, such as the comparison between cases of sequential impact at different energies and simultaneous impact, the effect of the number of simultaneous impacts on composite structures, the effect of the distance between impacts, etc. More precise definitions are proposed in Chapter 3.

1.2. Impact modeling methods for composite materials

To limit the cost of experimental tests required for the validation of composite structures, numerical modeling is generally used, which also allows for a finer physical understanding of the phenomenon under study by imagining new tests and validating new observations (79). Numerical simulation also makes it easier to establish similarity rules to account for scale effects between the test model and the real model (32).

It should be noted that, unlike numerical models, analytical models make it possible to directly see the influence of impact parameters on the global response and extent of delamination, allowing for rapid pre-sizing of composite structures, with simple and unique impact geometries and configurations (other models are required to simulate post-impact damage growth) (107), but do not provide precise information on the nature of damage within the laminate. Model types can be mainly divided in three (108) :

— **Energy-based models :** a global model focused on energy transfer and storage within the system during dynamic events. They often involve deriving equations of motion based on the system's potential and kinetic energy, and can provide insights into the overall energy distribution and dissipation during vibrations or impact events (108).

— **Mass-spring models :** The plate is represented by its mass and stiffnesses in membrane, bending, and shearing, and the impactor, which is very rigid compared to the plate, is modeled by a point mass. These models are often limited to a specific impact configuration (109).

— **Multi-degree of freedom models :** This model fully takes into account the dynamic behavior of the structure, and the response of the impacted structure is derived from the combination of the different natural modes of the entire structure.

Looking back to numerical methods, two approaches are distinguished in the literature for in-plane damage ; the discrete approach and the continuous approach :

The first approach proposed ((79), (110), (112)) consists of considering cracking as a local decohesion of the material and thus having a discrete view of damage. The structure is discretized into volume elements linked together by damageable elements, figure 1.28. This approach provides damage patterns that are consistent with experimental tests. However, they are not easily transportable to industrial calculation codes due to their sensitivity to meshing and their reliance on strong assumptions, such as the verticality of matrix cracks (plies must be very thin compared to the total thickness of the laminate) (32). The same approach is not applied to fibers, for meshing complexity reasons (79).

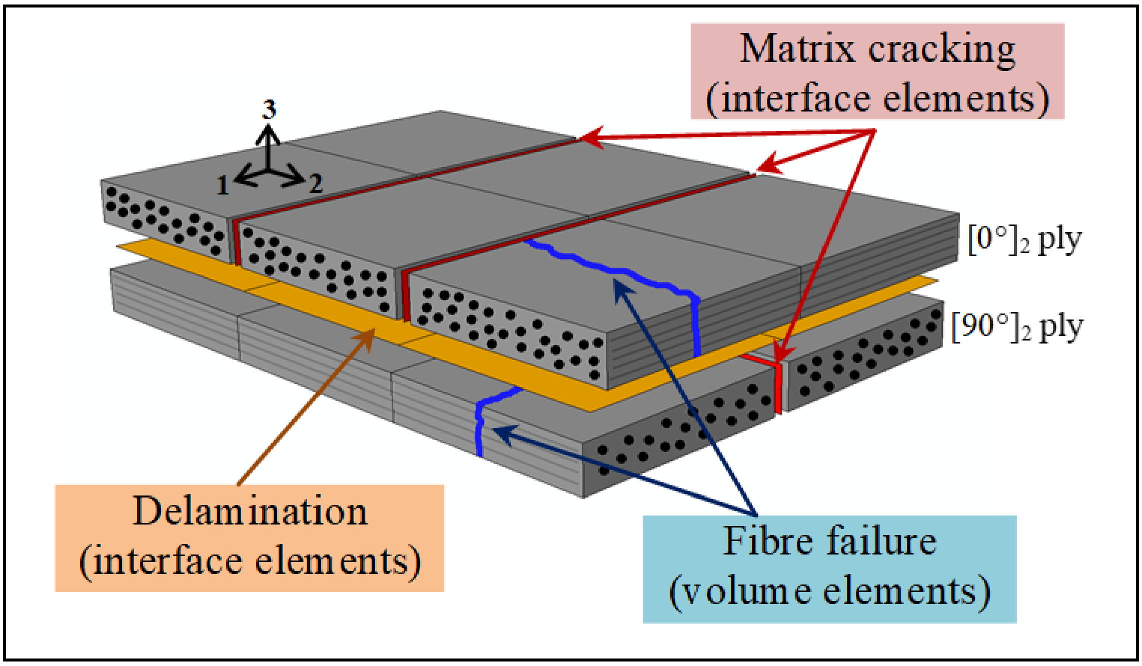

Figure 1.28 – A discrete ply modeling of damage principle (79).

The second approach relies on the continuity of damage within the ply. These models are based on continuous damage mechanics, and the damage to the constituents of the laminate plies is integrated into the behavior law through its effects (32). To model delamination, cohesive zone elements are used to join the plies together while allowing for the degradation of this interface (32). Material models based on continuous damage mechanics also provide damage patterns that are consistent with experimental observations. The advantage of this approach over the first one is that it is less intrusive because it only requires the implementation of a material behavior law and not specific finite elements. Its use is more frequent with explicit industrial calculation codes (LS-DYNA, Abaqus, etc.). Softening behavior models, i.e., models with a progressive transition from the damaged state to complete rupture of the material, require certain precautions, as they can artificially localize damage in a row of elements and are therefore more sensitive to meshing (32).

In order to model the damages caused by impact, the construction of the numerical model (contact and displacement) and the material model (to predict the initiation and propagation of damages) is necessary, see figure 1.29. It should be noted that the failure of composite structures is due to both local and global phenomena of the laminated structure, which represents another source of difficulty in numerical modeling.

Typically, the experimental setup components, such as the impactor and the claming system, are represented using rigid elements since they are assumed to be non-deformable with respect to the composite plate.

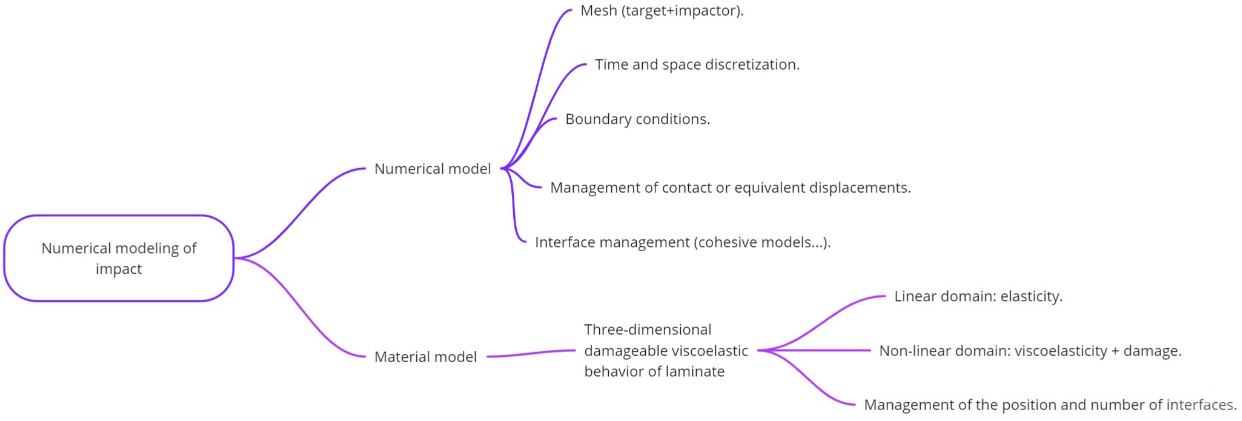

Figure 1.29 – Scheme for constructing a numerical model of impact loading.

To more quickly and easily solve the non-linearities associated with impact loading (geometric, contact, etc.), and avoid divergences associated with these non-linearities, the numerical solution is mainly of an explicit dynamic type, or implicit when low-speed damages are assimilated to a quasi-static out-of-plane indentation, table 1.2, compares the two resolution methods.

To describe delamination, several approaches are possible (113), namely : First, rupture criteria that are not complicated to implement and allow the initiation of delamination to be predicted. Then, crack propagation is considered instantaneous and leads the structure to failure. Second, Griffith criteria, used for delamination propagation. However, initiation of delamination is not described by this approach. Third, cohesive zone models that can handle both the initiation and propagation of delamination.

1.2.1. Damage criteria

Many damage criteria are available in the literature ((114), (115), (116), (117)), differing mainly by the number of parameters to identify. These criteria consist of comparing the applied stresses to experimentally obtained admissible values.

The Hashin criterion (114) is widely used due to its simplicity of implementation. It takes into account fiber ruptures and matrix cracking (rarely used for delamination, which is often modeled by introducing cohesive zones at the interface). Hashin proposed different failure modes associated with the fibre tow and the matrix, considering, in both modes, differences in tension and compression, as shown in figure 1.30. Its formulation can be summarized by the following equations :

	Implicit	**Explicit**
Solving a linear system (expensive)	When the problem is not sufficiently regular or is strongly non-linear, Newton's iterative process requires many iterations or fine time steps, leading to prohibitive costs.	No solving of a linear system is required. Quantities are obtained directly, reducing computational cost per increment.
Convergence to equilibrium	Increment validation requires residue minimization, but it does not guarantee overall convergence regardless of the time step.	The explicit solution requires user expertise to understand and validate the results due to potential errors caused by absence of iterations.
Stability	Implicit schemes are unconditionally stable with a judicious choice of β and γ, enabling larger time steps compared to explicit schemes.	Explicit schemes are conditionally stable. If $\Delta t < \left(\frac{h}{c}\right)$, the computation can become expensive due to a high number of increments.
Non-regular solutions	Non-regularities can hinder Newton's iterative process, causing convergence issues.	Absence of an iterative process allows addressing such problems, but user expertise is crucial for interpreting and validating the obtained results.

TABLE 1.2. – Comparison of resolution methods for a finite element problem (32).

- Fiber rupture in tension ($\sigma_{LL} \geq 0$) :

$$S_{ft} = \left(\frac{\sigma_{LL}}{X^T}\right)^2 + \alpha \cdot \left(\frac{\sigma_{LT}}{S^L}\right)^2 = 1 \tag{1.4}$$

  Here, α accounts for the shear stress for fiber rupture in tension and is equal to 1 (114) or 0 (118).

- Fiber rupture in compression ($\sigma_{LL} \leq 0$) :

$$S_{fc} = \left(\frac{\sigma_{LL}}{X^C}\right)^2 = 1 \tag{1.5}$$

- Matrix cracking in tension ($\sigma_{TT} \geq 0$) :

$$S_{mt} = \left(\frac{\sigma_{TT}}{Y^T}\right)^2 + \left(\frac{\sigma_{LT}}{S^L}\right)^2 = 1 \tag{1.6}$$

- Matrix cracking in compression ($\sigma_{TT} \leq 0$) :

$$S_{mc} = \left(\frac{\sigma_{TT}}{Y^C}\right)^2 + \left(\frac{\sigma_{LT}}{S^L}\right)^2 = 1 \tag{1.7}$$

- Out-of-plane delamination in tension ($\sigma_{T'T'} \geq 0$) :

$$S_{dt} = \left(\frac{\sigma_{T'T'}}{Z^T}\right)^2 + \left(\frac{\sigma_{LT'}}{S^H}\right)^2 + \left(\frac{\sigma_{TT'}}{S^H}\right)^2 = 1 \tag{1.8}$$

— Out-of-plane delamination in compression ($\sigma_{T'T'} \leq 0$) :

$$S_{dc} = \left(\frac{\sigma_{T'T'}}{Z^C}\right)^2 + \left(\frac{\sigma_{LT'}}{S^H}\right)^2 + \left(\frac{\sigma_{TT'}}{S^H}\right)^2 = 1 \tag{1.9}$$

The table 1.3 describes each variable.

Variable	**Description**
σ_{LL}	Longitudinal stress
σ_{TT}	Transverse stress
$\sigma_{T'T'}$	Out-of-plane stress
σ_{LT}, $\sigma_{LT'}$, $\sigma_{TT'}$	In-plane shear stress in the LT, LT', and TT' planes, respectively
X^T, X^C	Longitudinal tensile and compressive strengths, respectively
Y^T, Y^C	Transverse tensile and compressive strengths, respectively
Z^T, Z^C	Out-of-plane tensile and compressive strengths, respectively
S^L	In-plane shear strength
S^H	Out-of-plane shear strength

TABLE 1.3. – Description of the Hashin criterion variables.

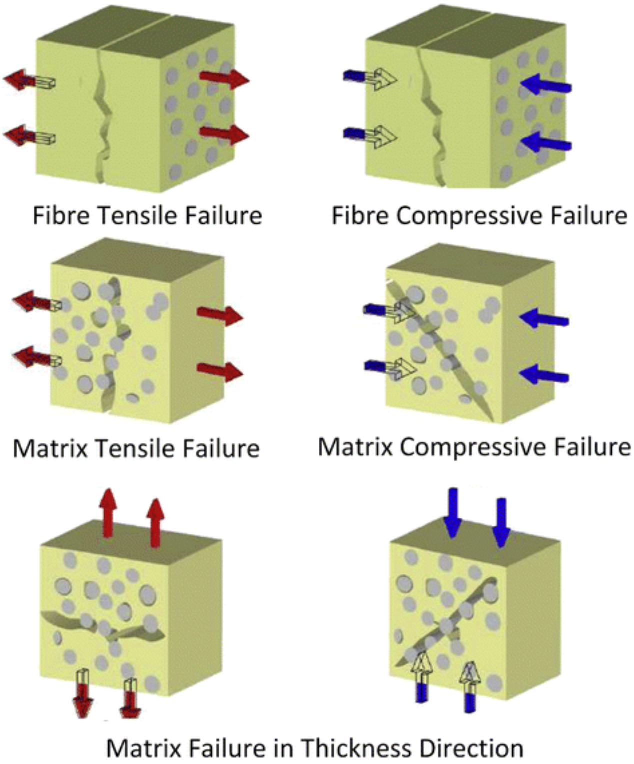

Figure 1.30 – Illustration of failure modes described in Hashin-type failure criteria (51).

1.2.2. Damage evolution

The evolution of damage can be driven by different variables :

- d_f : fiber rupture.
- d_m : matrix cracking.
- d_d : delamination.

Their values evolve from 0 (undamaged state) to 1 (completely damaged state) (practically, for numerical convergence reasons, the maximum value is set to 0.999). Their evolution depends on the value of the criterion S_{xx} $(xx = fc, ft, mt, mc, dc, dt)$ compared to 1, according to the following equation (83) :

$$d_i = \alpha_i . \max(\mathrm{Sup}[S_i] - 1, S_i^0) \tag{1.10}$$

The Sup function allows preserving the maximum value of S_i during the simulation. S_i^0 is the damage threshold, which is set to 1 in the case of the Hashin criterion. α_i is the parameter representing the kinetics of damage. A higher value indicates a faster progression of the corresponding damage, a sensitivity analysis must be conducted for each type of damage. To account for the effect of damage on the ultimate strength values, they are updated by multiplying the initial rupture property and stiffness values by $(1 - d_i)$.

1.2.3. Delamination propagation criteria

Assuming that G_{IC}, G_{IIC}, and G_{IIIC} are the interlaminar fracture toughnesses for the three pure modes (I, II, and III), a propagation law based on these values governs the expansion of the initial crack. Practically, two or three delamination modes can be coupled, then it is necessary to calculate the toughness for the mode mixity seen by the crack front. Several propagation criteria are proposed in the literature :

- Power law : One of the most used criteria in the literature for carbon/epoxy laminates (122), it is expressed as follows :

$$(\frac{G_I}{G_{IC}})^\alpha + (\frac{G_{II}}{G_{IIC}})^\alpha + (\frac{G_{III}}{G_{IIIC}})^\alpha \geq 1 \tag{1.11}$$

  where α is the shape parameter allowing adjustment of the experimental points. When $\alpha = 1$, the linear criterion is used, and when $\alpha = 2$, the quadratic criterion is imposed (120)

- Benzeggagh-Kenane :

  More recent, it can be expressed in 2D as in 3D (assuming that $G_{II} = G_{III}$), with the possibility of differentiating or not the II and III fracture modes :

  In 2D :

$$G = G_{IC} + (G_{IIC} - G_{IC})(\frac{G_{II}}{(G_I + G_{II})})^\alpha \tag{1.12}$$

In 3D :

$$G_C = G_{IC} + (G_{IIC} - G_{IC})(\frac{G_{II} + G_{III}}{G_I + G_{II} + G_{III}})^{\alpha} \tag{1.13}$$

The crack propagation is governed by the degradation at the end of the damage variable d based on bilinear, trapezoidal, polynomial, or linear polynomial laws. The curve 1.31 presents the main parameters of the damage variable in a typical linear traction-separation curve used for fracture modes I, II, and III. (125)

Geubelle and Baylor (135) used a bi-linear traction-separation relationship applied to matrix cracking and delamination problems in laminated composite plates. To simulate delamination problems in composite materials, Hamitouche et al. (121) used an irreversible bi-linear damageable behavior model. Camacho and Ortiz (136) used a linear model for impact problems with damage in brittle materials. Simulation of delamination using the Finite Element Method (FEM) can be performed, among others, using the Virtual Crack Closure Technique (VCCT) or using cohesive zone models. There are other numerical analysis methods such as the XFEM or extended Finite Element Method and the multi-scale approach (120).

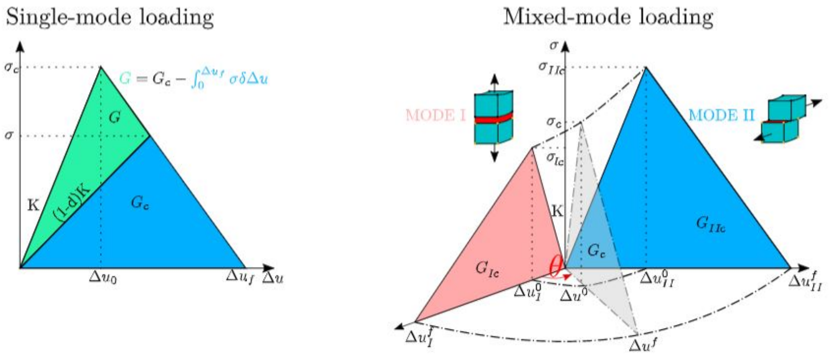

Figure 1.31 – Typical linear traction-separation curve used for fracture modes I, II, and III.

The damage variable d has a linear impact on the numerical stiffness. When $d = 0$, the interface remains intact, while $d = 1$ indicates complete damage of the interface, resulting in the dissipation of a surface energy equal to G_c. This variable can be expressed as in equation 1.14 :

$$d = \frac{\delta_m^f(\delta_m - \delta_m^0)}{\delta_m(\delta_m^f - \delta_m^0)} \tag{1.14}$$

where δ_m^f, δ_m^0 are, respectively, the initial and final effective displacement. δ_m is the equivalent displacement value taking into account fracture modes I, II, and III. It is obtained as follows :

$$\delta_m = \sqrt{\delta_n^2 + \delta_s^2 + \delta_t^2} \tag{1.15}$$

where σ_i $(i = n, s, t)$ denotes, respectively, the stress vector in the normal (n), shear (s), and tangential (t) directions.

$$\begin{cases} \sigma_n = K(1-d)\delta_n \\ \sigma_s = K(1-d)\delta_s \\ \sigma_t = K(1-d)\delta_t \end{cases} \tag{1.16}$$

According to the Benzeggagh-Kenane law, δ_m^f is expressed as follows :

$$\delta_m^f = \begin{cases} \frac{2}{K\delta_m^0}[G_{IC} + (G_{IIC} - G_{IC})\xi^n] & \delta_n > 0 \\ \sqrt{(\delta_s^f)^2 + (\delta_t^f)^2} & \delta_n < 0 \end{cases} \tag{1.17}$$

where $\beta = \frac{\delta_s}{\delta_n}$ and μ is experimentally determined, and $\xi = \frac{\beta^2}{1+\beta^2}$. When the fracture is more dominated by mode I, $\xi = 0$, and when the fracture is rather dominated by mode II ($\xi = 1$ and $\mu = 0$).

The value of K in the Benzeggagh-Kenane law is a material-dependent parameter. It represents the ratio of the mixed-mode fracture toughness, G_{IIIC}, to the mode I fracture toughness, G_{IC}. In other words, K can be defined as :

$$K = \frac{G_{\mathrm{IIIC}}}{G_{\mathrm{IC}}} \tag{1.18}$$

In addition, The VCCT method is based on the fact that the energy released during delamination propagation is equal to the work required to close the crack in its initial position. The rate of energy release is related to nodal forces and relative nodal displacements. However, the calculation of fracture parameters requires nodal variables and topological information of the nodes upstream and downstream of the crack tip, which generates difficulties generally overcome by the use of cohesive zone models (Cohesive Zone Model : CZM) (120).

Cohesive finite elements (COH3D8 in the Abaqus library) can predict both delamination initiation and propagation. However, they have their own definition of the stiffness of the cohesive layer, or interfacial stiffness, with a dependence on the element size in the crack propagation zone (138)

The modeling of delamination is usually done by introducing cohesive zones at the interface, the major advantage of this model is to take into account the existing coupling between the different modes of linear fracture mechanics ensuring the ability to predict delamination initiation and propagation(121).

The cohesive model relates stresses to displacement jumps across an interface where the crack can form. The initiation of damage is related to the maximum values of the different stresses at the interfaces. However, when the energy dissipated in the cohesive element is equal to the critical SERR of the material, the tension becomes zero. Thus, a new crack front is formed (121). A CZM element is characterized by the crack initiation conditions, and the crack growth function.

In LS-DYNA, solid elements ELFORM 19 and ELFORM 20 are intended to be used with cohesive material models. The formulation of element 19 defines traction on the mid-surface as midpoints between the nodes, and the element has four integration points. The element accepts an initial volume of zero, meaning it can be used for bonding between solid elements. ELFORM 20 is identical but has offsets for shells (123).

1.2.4. Simulation of multi-impact using FEA

Very few studies have treated numerically multi-impact configurations on composite structures. In particular, Deka et al. (87) used Hypermesh and Finite Element Model Builder (FEMB) for pre-processing, while LS-DYNA was used to analyze the damage caused by high-velocity projectile impact on a three-layer S2-glass-epoxy composite plate. The material model MAT 162, which is based on Hashin's failure criteria and incorporates the Continuum Damage Mechanics (CDM) approach, was used to simulate the damage caused by impact on the composite laminate. The strain softening parameters for the composite laminate were calibrated using quasi-static punch shear tests, and a combination of four different sections were used to describe the load versus displacement curve. The simulation maintained the same specimen dimensions and boundary conditions as the experiment. The study demonstrated the feasibility of using FEA to simulate multi-impact on composites and provided insights into the damage mechanisms involved. The impact velocity was held constant at 223.1 m/s (standard deviation = 19.1 m/s), which is above the ballistic limit. The average energy absorption was 43.9 J, figure 1.32. Plate elements were used, delaminations were not modeled, the main objective was to reproduce the perforation.

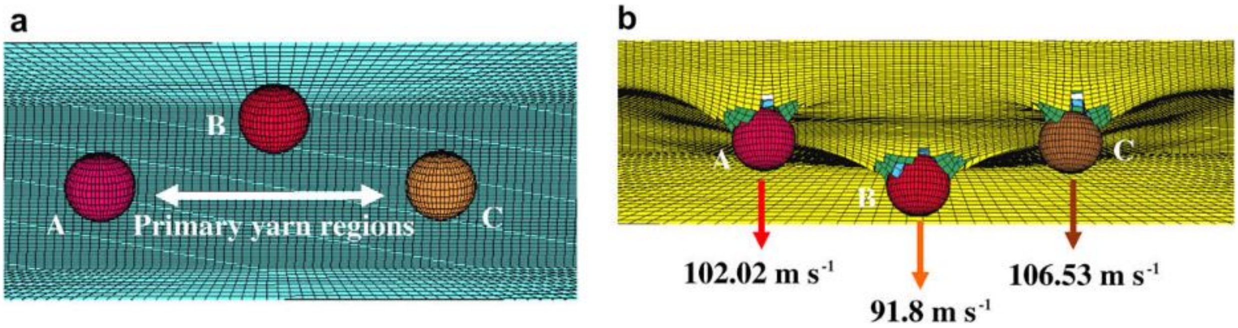

Figure 1.32 – (a) Simultaneous impact positions of the three projectiles and (b) residual velocity after penetration (87)

.

In Rezasefat et al. (84) study, the finite element models were developed at four levels of complexity to simulate the damage behavior of carbon fiber reinforced polymer (CFRP) composites subjected to low-velocity impacts. The simplest simulations were performed on single elements under cyclic loads to verify the accuracy of the progressive damage model. The simulations were performed using C3D8R elements (8 nodes volume element with reduced integration) with enhanced hourglass control and a cohesive element interface between plies. The simulation of multiple impacts was done in a single-step explicit FE model, where the material state at the end of each loading step becomes the initial material state for the next step. The approach of hitting the panel by impactors at the same simulation step was considered valid, figure 1.33. The mechanical properties of the CFRP composites used in the simulation were obtained from experiments or literature.

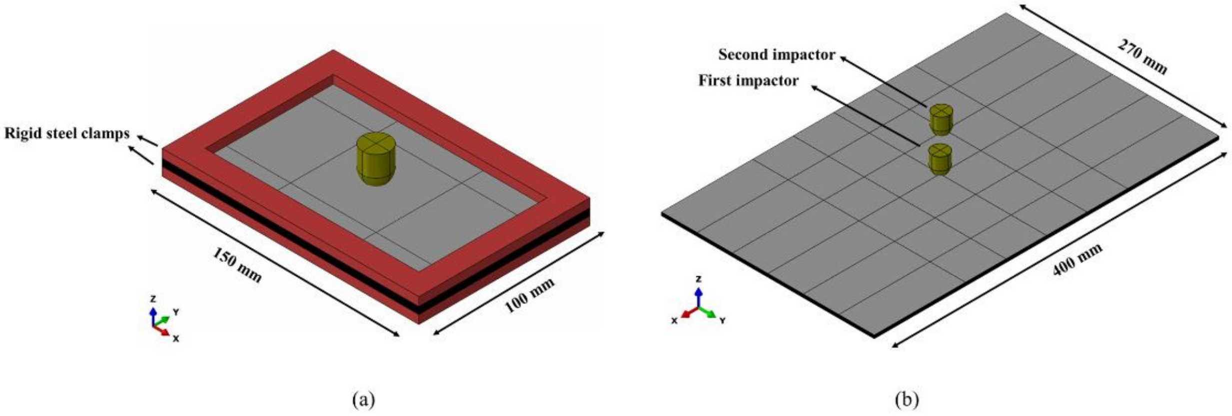

Figure 1.33 – The FE models : (a) Impact on coupon specimen, (b) Multiple impacts on skin panel (84).

In the literature, case studies in FEA for sequential impacts are missing, due to the time required to return to equilibrium of the impacted plates and the complexity of the plate stabilization after impact (especially in explicit), we therefore propose to modify the DPM to optimize computation time in sequential configurations. Moreover, in practice, it is difficult to have simultaneous cases with a time lag of 0 ms. We then propose to perform simultaneous cases with a small time lag and compare them with perfectly simultaneous cases. Several other multi-impact configurations are tested experimentally and numerically, and certain modifications to the DPM are introduced to take account of the phenomena observed experimentally. Throughout this thesis, a test-simulation dialogue is maintained, comparing experimental results to numerical results at each step, and feeding the data analysis with observations noted during post-processing to achieve comprehensive analysis results.

Conclusion

This literature review chapter has provided a comprehensive overview of the behavior of composite structures under impact conditions. Through an extensive analysis of existing research, several key findings and insights have emerged. However, the study of multi-impact behavior is still lacking. Few articles cover this topic, and even then we generally mix up several impacts arriving at the same time and those arriving repeatedly. The numerical study of multi-impact is also very limited, with the absence of certain cases such as sequential impacts, which are extremely resource-intensive given the time required to allow the plate to stabilize.

The main conclusions from this chapter are :

- Firstly, it is evident that impact loading can induce various damage mechanisms in composite materials, including delamination, fiber breakage, matrix cracking, and interfacial debonding. The severity and extent of damage depend on factors such as impact energy, projectiles' shape and nature, material properties, stacking sequence and boundary conditions.
- Secondly, the structural performance of composite materials tends to degrade over multiple impact events, as cumulative damage accumulates and weakens the material's integrity. Understanding the progressive damage evolution and its effects on structural response is crucial for ensuring the long-term durability and reliability of composite structures. However, a detailed description of the phenomena involved is lacking to explain these different increases in damage following several impacts, and whether or not this is always the case.
- Thirdly, research efforts have been directed towards developing experimental techniques and numerical models to capture the complex behavior of composite structures under impact loading. Advanced testing methods, such as high-speed imaging, digital image correlation and US control, have enabled the characterization of damage initiation, propagation, and post-impact residual strength.
- Fourthly, numerical simulations, including finite element analysis and multiscale modeling, have provided valuable insights into the stress distribution, energy absorption, and failure mechanisms of composite structures under impact conditions. These modeling approaches facilitate the optimization of composite structures for enhanced impact resistance and damage tolerance. In the case of multiple impacts, this is not the case, given the limited number of studies that focus on these more complex cases, which are more costly in terms of calculation time but, on the other hand, more general than a single impact case.
- Furthermore, impact test benches are various, from classic machines that guide displacement and force contact between the impactor and the plate using a falling mass, to those in the form of bars or cannons. However, there is a scarcity of test benches that control both the spatial and temporal lag between impacts and the number of impacts, which are very important input parameters for multi-impact studies.

Overall, this chapter highlights the importance of understanding the impact behavior of composite structures and its implications for real-world applications. By synthesizing the existing knowledge and identifying research gaps, it serves as a foundation for the subsequent experimental and numerical investigations presented in the following chapters. The advancements in testing methods, damage monitoring, and data analysis showcased in this study contribute to the ongoing efforts in designing robust and reliable composite structures capable of withstanding impacts and multi-impacts.

This thesis plan is therefore to develop a reliable experimental bench for the study of multi-impact behavior of composite structures, and then to pilot a test-calculation dialogue to introduce the missing cases of multi-impact in the literature, both experimentally and numerically.

CHAPTER 2 :

DEVELOPMENT OF A COMPRESSED AIR CANNON FOR MULTI-IMPACTS TESTING

2. Compressed air cannon for multi-impacts testing

Introduction

Understanding the response and damage evolution of composites subjected to multiple impact events is crucial for designing robust and reliable structures capable of withstanding complex loading scenarios. To facilitate this research, the development of specialized test rigs that can generate controlled and repeatable multi-impact conditions is essential.

In this chapter, we present the development and characterization of a novel test rig, namely the "Compressed Air Cannon", designed specifically for studying the multi-impact behavior of composite materials. The Compressed Air Cannon offers several advantages over traditional impact testing methods, such as drop weight towers or pendulum impactors. It allows for controlled and adjustable impact energy, impact angle, spatial and temporal lag as well as the number of impacts, enabling a wide range of multi-impact scenarios to be investigated (see appendix A).

The primary objective of this chapter is to provide a detailed description of the design and construction of the Compressed Air Cannon test rig. We will discuss the key components, including the pressurized air system, projectile launch mechanism, target mounting arrangement, and data acquisition system. Additionally, the calibration procedures and validation experiments conducted to ensure the accuracy and reliability of the test rig will be outlined.

Furthermore, we will present the experimental methodologies employed to assess the multi-impact response of composite specimens using the Compressed Air Cannon. This includes the selection of appropriate impact parameters, specimen preparation and mounting techniques, and the instrumentation for capturing impact-induced responses such as displacement and damage progression. The data obtained from these experiments will provide valuable insights into the damage mechanisms and the energy absorption characteristics presented in chapters 3 to 5.

2.1. Purpose and input parameters

The purpose of this chapter is to present the development of an air cannon for multi-impact testing on composite structures. The control of the main factors of the impact study, i.e. impact energy, impact velocity, impactor size and boundary conditions, is a main objective. In addition, other parameters such as the number of impacts, simultaneity and repeatability of impacts must be precisely controlled to ensure reliable results. It is also important to control the falling height of the projectiles and the number of cannons to be launched sequentially or simultaneously. To monitor damage in-situ, the system must be equipped with sensors to measure the deformation of the composite structures and track the various damage mechanisms. These data can be correlated with numerical models to better understand and then predict the behavior of materials subjected to multiple impacts under other conditions.

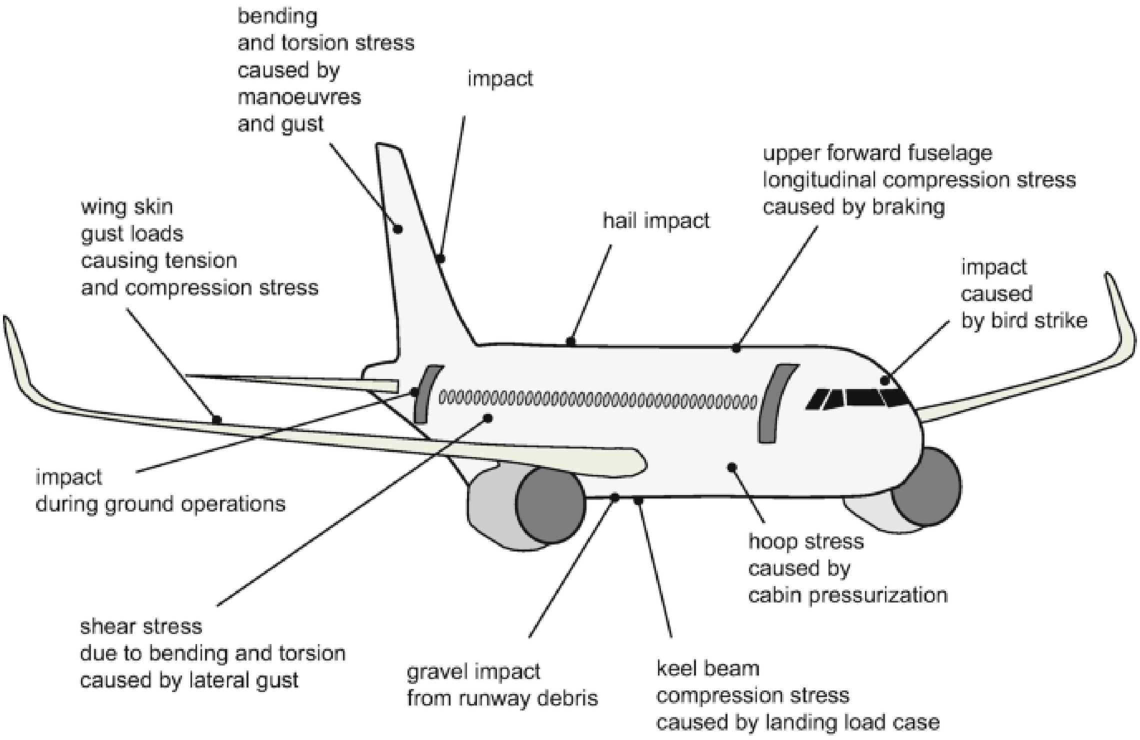

Figure 2.1 – Multi-impacts examples and resulting stresses (94).

Multi-impact testing of composite structures is an innovative way to evaluate the resistance to repeated, sequential or simultaneous impacts of these materials, unlike single impact tests, which measure the resistance to a single impact at a given velocity and energy. Multi-impact tests provide more realistic conditions by exposing the structure to multiple impacts of varying shapes and sizes at varying energies over varying areas. This provides a better understanding of the behavior of composites under real-life cycle conditions, where the structure may be randomly subjected to several impacts during its life cycle. For example, in cases of projection of external objects such as debris and gravel, hailstones, bird strikes, tire debris, tool drops during manufacturing or maintenance operations, figure 2.1. The originality of the multi-impact tests comes from taking into account the synergistic effects of the interaction of stress waves induced by the different projectiles and which modify the global response of the structure. These tests enable the acquisition of more accurate and detailed data on composites' performance in real-life cycle situations. The results of these tests can help to improve the design of composite structures by allowing researchers to determine the variation in the amount of energy absorbed during multiple impacts and understand the interaction between the damage due to these impacts, and thus optimize the impact resistance.

The development of this new test bench involved several key steps. First, it was essential to determine the application requirements and functional specifications of the cannon, namely to make sequential or simultaneous multi-impacts in different areas of the target plate for a given velocity and energy range and given projectile shapes and sizes. Then, we identified and improved technical solutions that meet these requirements which are also effective and efficient. Once the design was finalized, we proceeded to the manufacturing and assembly of the cannon components. Testing and verification was performed throughout the manufacturing process to ensure the quality and accuracy of the system. Finally, once the cannon is completed, calibration tests are performed to verify that all functionality and performance are within the original specifications and to test the reliability of the cannon. Throughout this process, careful planning, thoughtful design, and rigorous testing have resulted in a reliable and accurate test system that can be used to validate the performance of impact loaded structures in a variety of application areas.

Input parameters :

Understanding the interaction between several impacts is the ultimate goal of this work. However, this behavior will always depend on some general parameters like the material, the number of plies, the stacking sequence, etc. Although, these parameters do not directly affect the development of the air cannon, it is then important to focus on the key parameters for the study of the "multi-impact" aspect and for the choice of technical solutions to develop the dedicated test bench, such as : impact energy, impact velocity, impactor size, impactor stiffness and boundary conditions. Therefore, we have set the following objectives :

- **Required velocity interval**

Impact velocities are generally classified into 3 categories :

- Low velocity : this category is generally defined as less than about 10 m/s. This may include situations such as low speed automobile impacts or falling objects (tools drop during maintenance or manufacturing operations, luggage, etc.) from a relatively low height.
- Intermediate velocity : this category is generally defined as being between approximately 10 m/s and 100 m/s. This can include ground impact situations such as hailstones, road gravels, birdstrikes or drones impacts, etc.
- High velocity : this category is generally defined as greater than approximately 150 m/s. This can include high impact situations such as high-altitude bird strikes and space debris impacts. For example, impacts on propeller blades, such as those caused by engine explosions.

Over the short and medium term, we are seeking to identify and understand the interaction between low and medium velocity impacts and then reproduce hail or gravel impact situations. Therefore, we are designing the length and volume of the reservoirs to go up to 100 m/s. For the pressure, we are taking the maximum pressure allowed by the laboratory's air compressor (9 bars). It should be noted that it will always be possible to realize higher speed impacts by adding a compressed air booster at the entrance of the air reservoirs or by changing the used gas, etc.

▪ Required energy interval

The impact energies can vary depending on the mass and speed of the projectile. They are generally classified into 3 categories :

— Low impact energy (less than 10 J) : these impacts generally result in minor damage. For example, hail impacts (up to 40 mm diameter hailstones) or small gravels.

— Medium impact energy (between 10 and 50 J) : these impacts can cause more significant damage, such as cracks in the material. For example, hail impacts, which are one of the most common types of ground impacts, can vary in size and energy, but in general, typical hail impacts have an energy of 5 to 20 J, according to data from ANELFA (Association Nationale d'Études et de Lutte contre les Fléaux Atmosphériques).

— High impact energy (between 50 and 5000 J) : these impacts are often associated with more severe accidents, such as vehicle collisions or aircraft accidents.

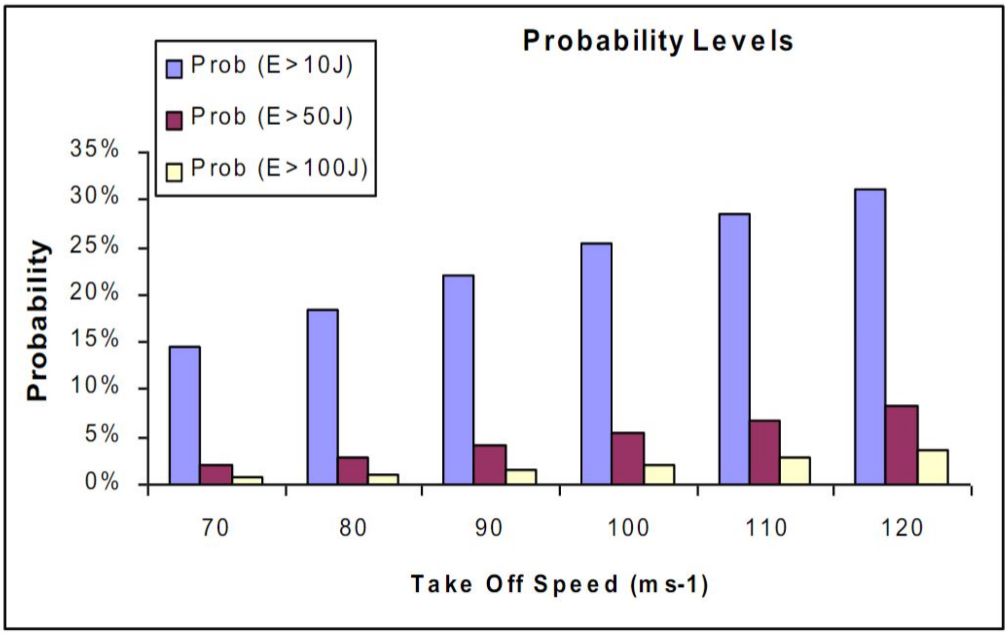

Figure 2.2 – Impact energy probability as a function of take-off speed (based on runway debris collected from 4 British military air bases (84)).

The purpose of this work is mainly to understand the interaction between several impacts, and not necessarily to reach the structure that best resists the impacts, so it is not important to go to high impact energies and to save the material of the specimens as well.

We have chosen to perform impacts up to 50 J in order to cover a range of energies from low to medium. It is also the energy where there is the highest probability of impact near the ground for an aircraft, figure 2.2. However, it is important to underline that is also possible to easily increase the impact energy by modifying the mass of the projectile.

- **Impactor material, shape and dimensions**

To ensure reproducibility of the multi-impact tests and to facilitate numerical modeling, we opted for an impactor that can be assumed to be infinitely rigid (made of steel, which can absorb and dissipate a large amount of energy without deforming or breaking). Secondly, a smooth and uniform surface is chosen, which facilitates the measurement of the impact force and the energy absorbed during the collision. The impactor must also be available in large quantities and of the same dimensions. For this purpose, we used surface-treated steel balls to perform the multi-impact tests. To study the effect of impactor size, 10 and 20 mm diameter balls are used.
In order to be able to make impacts with hail and gravel, we provided a sabot to ensure the tightness and the repeatability of the impact parameters (friction, simultaneity, etc.).

- **Clamping system dimensions**

The distance between the impacts is one of the key parameters, so it was decided to perform tests on the largest plate dimensions we can manufacture using the laboratory thermopress taking into account the edges section cutting. Then, the impacts would be on a 350x350 mm^2 plates.

- **Why not a conventional impact machine or cannon ?**

The standard impact test machines only allow single or repeated impacts with limited velocities and energies, but they do not allow precise management of the time and space lag between impacts, nor of the number of impacts per desired multi-impact configuration. The Hokpinson bars and other cannons allow to reach higher energies, but do not allow a large number of simultaneous/out-of-phase impacts while varying the impact areas, angles of impacts, etc. For that, we have chosen the development of a new cannon for the specific objectives of this study.

The following procedure is proposed for developing the compressed-air cannon and validating its performance, a detailed presentation of each step is given next :

Set input parameters (basic projectile characteristics and desired range of energy and velocity)

↓

Theoretical calculation of velocity (and energy) at cannon exit

↓

Calculate theoretically the velocity, energy and trajectory of the ball at impact

↓

Set key design parameters (impact energy and the cannons' lengths)

↓

Set maximum distance between cannon exit and plate to be impacted

↓

Verify cannon repeatability

↓

Design other cannon components (reservoirs, mounting systems, control programs, etc.)

↓

Define procedures and operating modes

2.2. Mathematical formulation of key cannon design parameters

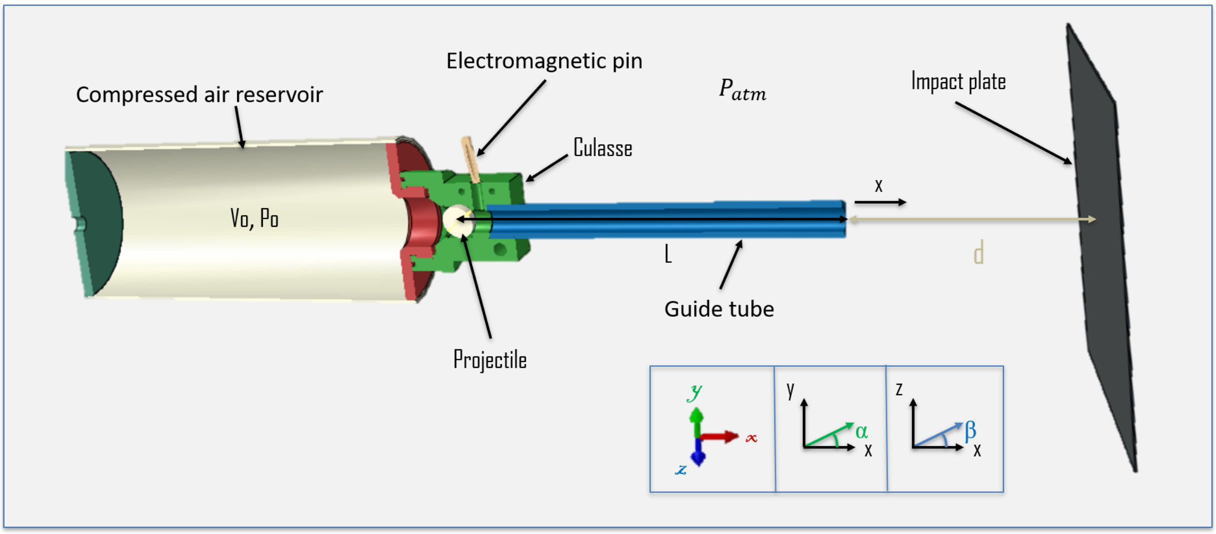

Figure 2.3 – Cross-section of an air cannon.

We are interested in the kinetic energy at the instant of impact E_{c_i} of a projectile (steel ball) of mass m_p, launched from a cannon with an initial air pressure P_0, towards a plate at a distance d from the cannon exit. We model the cannon as a reservoir of volume V_o connected to a long guiding tube of length L and cross-section S, the shot is released by an electromagnetic pin (see figure 2.3). Once the projectile is launched along x, the cannon reservoir volume $V(x)$ increases as function of x, the pressurized air contained in the reservoir $P(x)$ expands according to Boyle-Mariotte's law :

$$P(x) = \frac{P_0 V_0}{V(x)} = \frac{P_0 V_0}{V_0 + S \cdot x} \tag{2.1}$$

Assuming the projectile is a rigid body, according to Newton's second law :

$$\sum \vec{\mathrm{F}}_i = m_p \cdot \vec{a} \tag{2.2}$$

Where $\vec{\mathrm{F}}_i$ represents the external forces exerted on the projectile, and $\vec{a}$ is the acceleration of its center of mass G.

The external forces are the compressed air force $SP_p(x)$, minus the air force SP_{atm}, and minus the frictional force (F_f) between the projectile and the guiding tubes, where $P_p(x)$ is the compressed air pressure, P_{atm} is atmospheric pressure. If the cannon is not inclined, the equation of motion at the exit of the tubes is then written (where v_e is the velocity at the exit of the cannon) :

$$S.P_p(x) - S.P_{atm} - F_f = m_p \cdot \frac{dv}{dt} = m_p \cdot v \cdot \frac{dv}{dx_p} \quad (v = \frac{dx}{dt} \Longrightarrow dt = \frac{dx}{v}) \tag{2.3}$$

$$\Longrightarrow \int m_p \cdot v.dv = \int (S.P_p(x) - S.P_{atm} - F_f).dx_p$$

$$\Longrightarrow \frac{1}{2} m_p.v_e^2 = P_0.V_0.\ln(1 + \frac{S.L}{V_0}) - S.L.P_{atm} - L.F_f$$

$$\Longrightarrow v_e = \sqrt{\frac{2}{m_p}\left(P_0 \cdot V_0 \cdot \ln\left(1 + \frac{S \cdot L}{V_0}\right) - S \cdot L \cdot P_{\text{atm}} - L \cdot F_f\right)} \tag{2.4}$$

The equation 2.4 is used to check the cannon's repeatability, see figure 2.6. Subsequently, the kinetic energy at the exit of the cannon E_{c_e} can then be expressed as :

$$E_{c_e} = \frac{1}{2} m_p.v_e^2 = P_0.V_0.\ln(1 + \frac{S.L}{V_0}) - S.L.P_{atm} - L.F_f \tag{2.5}$$

Among these parameters, P_{atm} and F_f are known (in this case, neglecting the coefficient of friction distorts the calculation in relation to the experimental results, which may be due to the tight adjustment of the inner diameter of the guiding tubes. F_f is not neglected but measured precisely using the inclined plane, figure 2.4), P_0 is defined by the maximum capacity of the laboratory compressor (9 bars), m_p and S are defined by the scientific application of these tests (see the section 2.1 Purpose and input parameters), $m_p = 32.7$ g for steel balls of 20 mm diameter and 4 g for balls of 10 mm diameter.

Before looking for the expression of E_{c_i}, it is necessary to complete the calculation of the velocity at the exit of the cannon v_e, in which case the coefficient of friction is required. The maximum value of the friction coefficient f was measured using the experimental device shown with the notations used in figure 2.4, its expression is given by equation 2.6.

$$f = \frac{P_M - P_p \sin(\alpha)}{P_p \cos(\alpha)} = 0.19 \pm 0.02 \tag{2.6}$$

where, P_M is the weight at which the steel ball of weight P_p starts moving. α represents the angle of inclination of the cannon relative to the ground (x-axis in figure 2.3).

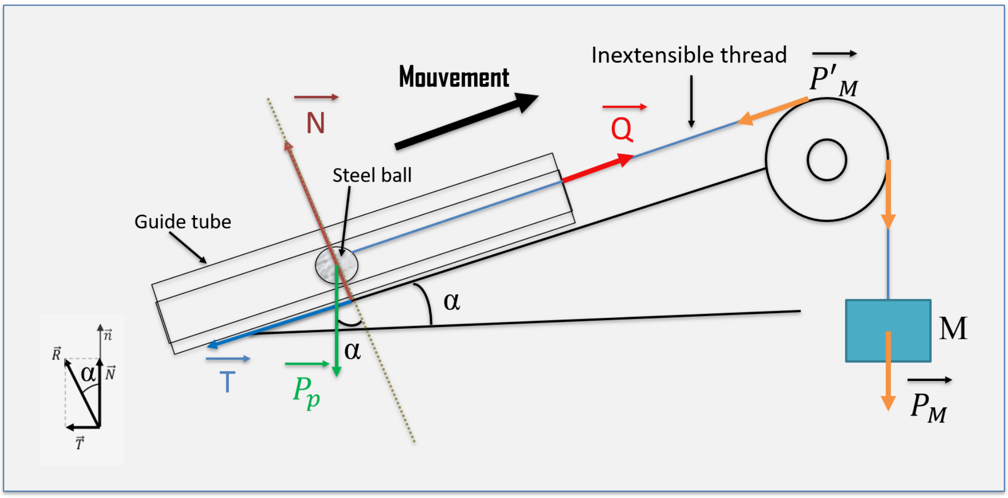

Figure 2.4 – Experimental setup for static friction factor measurement

As shown in figure 2.5, from 0.0055 m^3, the term V_0 has little influence on the impact energy value. For example, for the final design and at 4 bars, the velocity at the exit of the cannon is equal to 51.55 m/s for a V_o of 0.0055 m^3, it is equal to 49.23 m/s for 0.001 m^3 and to 52.03 m/s for 0.05 m^3.

L remains the most important parameter for the sizing of the cannon's guiding tubes. In addition, the volume of the guide tubes for the balls of 20 mm of diameter is 9.42×10^{-5} m^3, it is 5.1025×10^{-5} m^3 for the balls of 10 mm of diameter, it is thus important to ensure a necessary volume for the balls of 20 mm which will be sufficient for the balls of 10 mm (the opposite is not true), 0.0055 m^3 is the chosen volume of the reservoirs.

To size the cannons, we need to find the right length of the guiding tubes according to the desired energy and the dimensions of the projectiles (which are already fixed). We then need to find a formula that links the energy at the moment of impact E_{c_i}

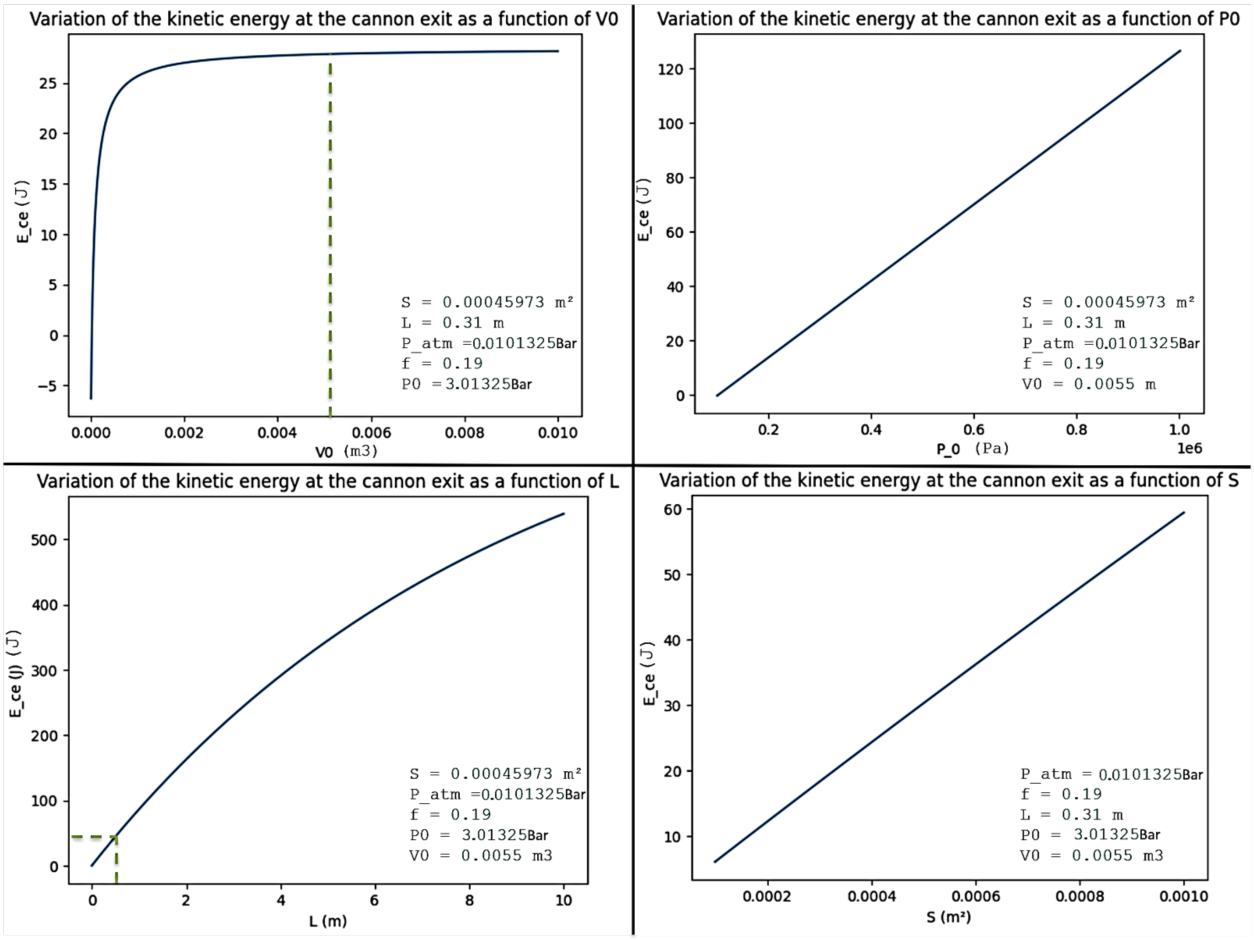

Figure 2.5 – Kinetic energy values at the cannon's exit as a function of the other design parameters (chosen design values in dotted line).

(and not E_{c_e}, since the energy of the projectile decreases with the distance from the cannon exit to the plate to be impacted) and the length of the cannons. We note that equation 2.7 is also used to size the cannon lengths, where $\overline{P}$ is the average pressure all along the cannon :

$$L = \frac{v_e^2 \cdot m_p}{2 \cdot S \cdot \overline{P}} \tag{2.7}$$

Many cannons are positioned horizontally. In our case, to change the distance between impacts, we change the inclination of the cannons (we can also change the inclination just to study the effect of the impact angle). Looking at each cannon, the most important inclination is α, since we can consider x to be the axis of each cannon separately. The kinetic energy at the moment of impact E_{c_i} given by an accelerated ball from its velocity at the exit of the cannon (v_e), as a function of the angle of its trajectory to the horizontal (α), is given by equation 2.8, where d is the distance it has travelled from the cannon exit and α is the angle between the horizontal and the vertical (figure 2.3), and g is the gravitational acceleration.

$$\boxed{E_{c_i} = \frac{m_p}{2}\left[v_e^2 - 2g.d.\tan\alpha + \left(\frac{g.d}{v_e \cdot \cos\alpha}\right)^2\right]} \tag{2.8}$$

We have taken a cannon length of 650 mm for the 10 mm diameter balls to reach up to 100 m/s, and a cannon length of 300 mm allowing to reach up to 100 J with the 20 mm diameter balls.

During experimental campaigns, it is generally necessary to change the impact energy on a given impact zone. In our case, if the plate is far from the cannon exit, we cannot impact the same point with two different energies. Therefore, depending on the desired range of energy, we need to set a maximum distance d_{max} to reduce the drop of the ball, with a precision of $\pm\frac{a}{2}$ (a is the precision parameter to be set). This time, both angles of inclination (figure 2.4) must be taken into account to track the exact trajectory of the ball, d_{max} can be determined with the equations of the trajectory :

$$\begin{cases} y(x) = -\frac{1}{2} \cdot \frac{g \cdot x^2}{\cos^2(\alpha) \cdot v_e^2} + \tan(\alpha) \cdot x + h \\ z(x) = x \cdot \frac{\cos(\beta)}{\cos(\alpha)} \end{cases} \tag{2.9}$$

where h is the height from which the projectile is launched, β is the angle between the depth and the horizontal (figure 2.3).

To impact the same point with two different impact energies, and thus two different velocities at the cannon exit (v_1 and v_2), where v_1 is the minimum velocity corresponding to the smallest energy value of the range covered by the experimental campaign and v_2 is the maximum velocity, the maximum distance between the cannon exit and the plate, which must not be exceeded, is given by :

$$\boxed{d_{max} = \sqrt{\frac{(v_1 \cdot v_2)^2}{v_2^2 - v_1^2} \cdot \frac{2 \cdot a \cdot \cos^2(\alpha)}{g}}} \tag{2.10}$$

This distance allows also the accessibility to the area between the cannon exit and the plate to be impacted, in order to put measuring instruments or other devices. We set a distance of 0.96 m allowing to realize impacts at 15 J and 30 J with an accuracy over the impact zone of $\pm\frac{1}{2}$ mm.

The two most important relationships are those shown in the boxes. In addition, several other parameters can be calculated, for example, the ball takes 31 ms to impact the plate at a velocity of 30 m/s. Indeed, the time of flight, t, to cross a distance d is given by the equation 2.11.

$$t = \frac{d}{v_e \cdot \cos\alpha} = \frac{v_e \cdot \sin\alpha + \sqrt{(v_e \cdot \sin\alpha)^2 + 2 \cdot g \cdot h}}{g} \tag{2.11}$$

To measure the ability of the cannon to reproduce the impact parameters, while varying the velocity, the angle of impact, the distance d, the guiding tubes, etc., an experimental campaign was conducted to verify the repeatability. The maximum error measured between shots of 0.5 to 4 bars, in 0.5-bar increments, is 0.9%, see 2.6 and 2.7 (based on 3 tests per pressure and 5 different pressures per cannon). The exit velocity results correlate very well with the analytical model presented above, the repeatability across all five cannons is quite accurate, the experimental curves are superposed, figure 2.6. The velocity reaches 50 m/s at 4 bars, as expected, so the experimental campaign can be launched and the results can be reliable, given the reduced error, figure 2.7.

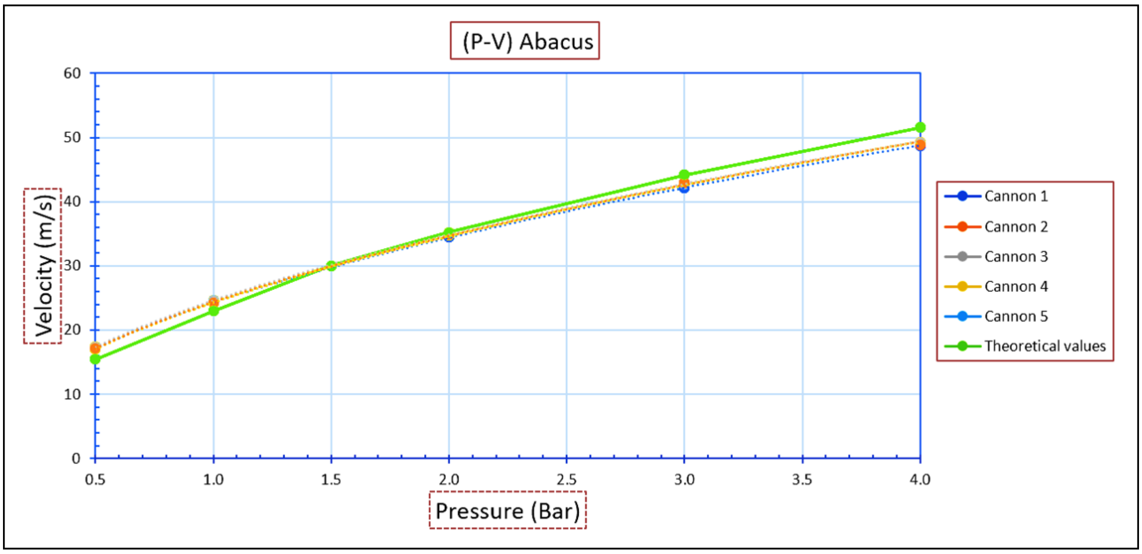

Figure 2.6 – (P-V) Abacus : experimental tests of impact velocity as a function of reservoir pressure and comparison with theoretical calculations.

In order to use the high-speed camera to measure the velocities just before and after impact, a reliable and cheap way to measure the velocities at the exit of the cannons was sought. These measurements were carried out using a chronograph, it measures the speed by calculating the duration of passage of the ball between the two infrared rays, see figure 2.8. As this chronograph is not certified, the comparison of the velocity measurements with the chronograph and with the high speed camera was carried on. The idea is to measure the time of crossing of the ball between the two gaps (t) with the high speed camera, and to compare this value with the one displayed on the chronograph, the maximum difference between the measurements is 0.68 m/s for tests between 20 m/s and 55 m/s.

Experimentally, the kinetic energy stocked in the structure (see more details about this energy in figure 3.18), is measured with the velocities just before impact and just after impact, using the following formula :

$$\boxed{\Delta E_c = \frac{1}{2} \cdot m_p \cdot (v_i^2 - v_f^2)} \tag{2.12}$$

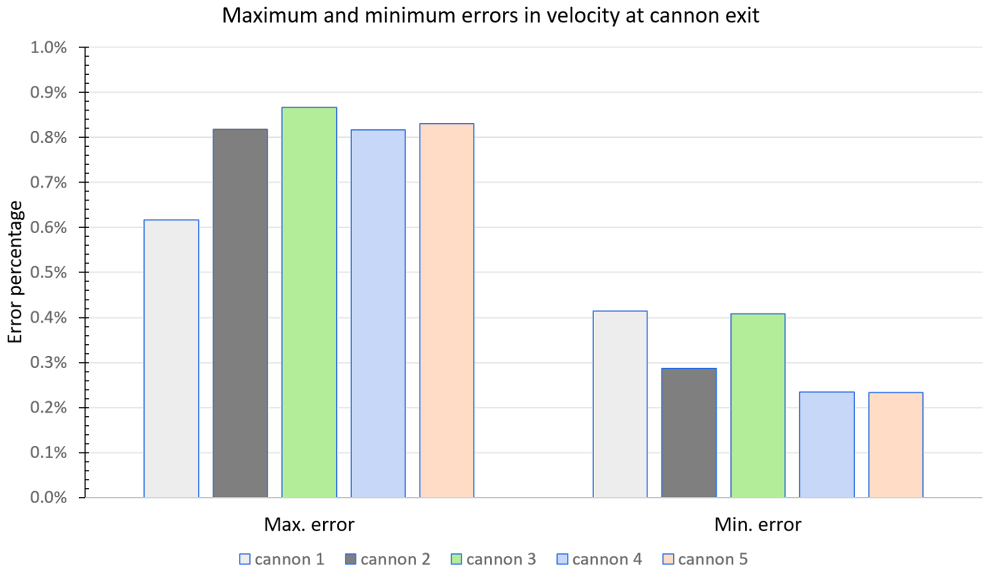

Figure 2.7 – Max. and min. errors in velocity at cannon exit.

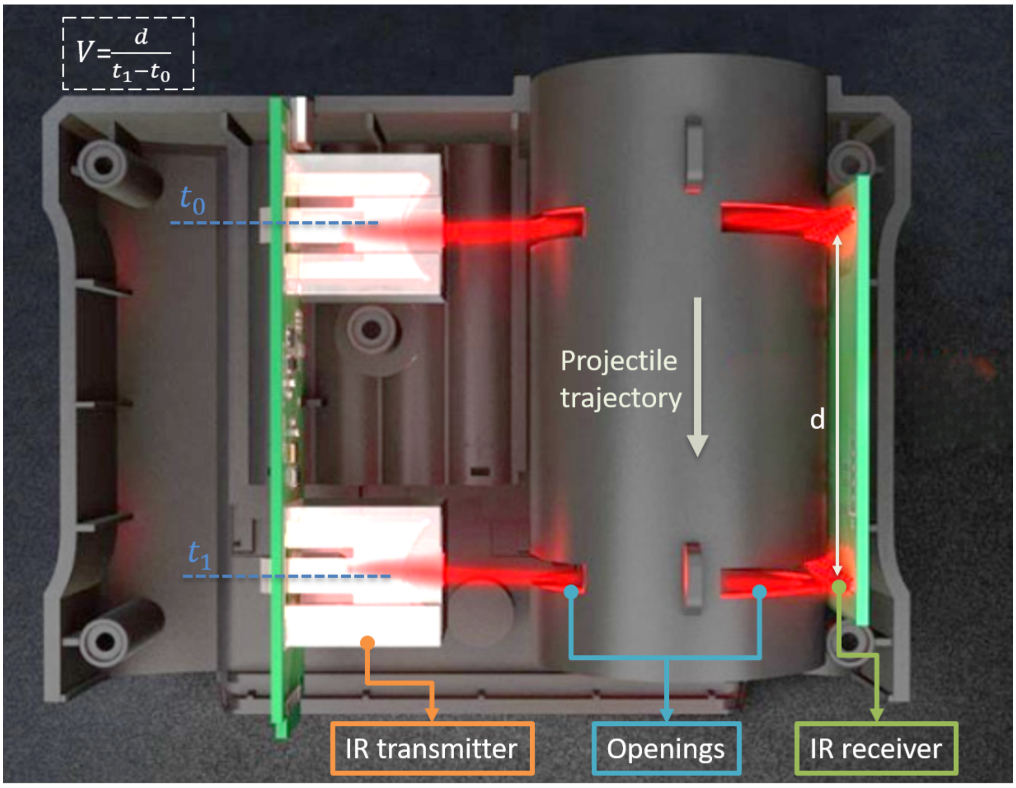

Figure 2.8 – Working principle and verification of chronograph measurements.

where v_i is the velocity before impact, and v_f is the velocity after impact.

To check the consistency between experimental and numerical results, we need to be able to compare the energies and forces involved during the impacts. Given that the balls cannot be fitted with force sensors (which risk breaking), we need to find an alternative method for plotting the load-displacement curves. This was made possible by processing the films from the high-speed camera (HSC). Using the HSC, the ball's displacement is tracked to deduce the time-displacement curve (figure 2.9), we then plot the polynomial function (of 6th order) that fits best through the experimentally recorded points, figure 2.10(a). Using the formula of this curve, time-acceleration curves are then plotted (by calculating the second derivative of the function). This value is multiplied by the ball's mass, and finally the distance-force curve, figure 2.10(b).

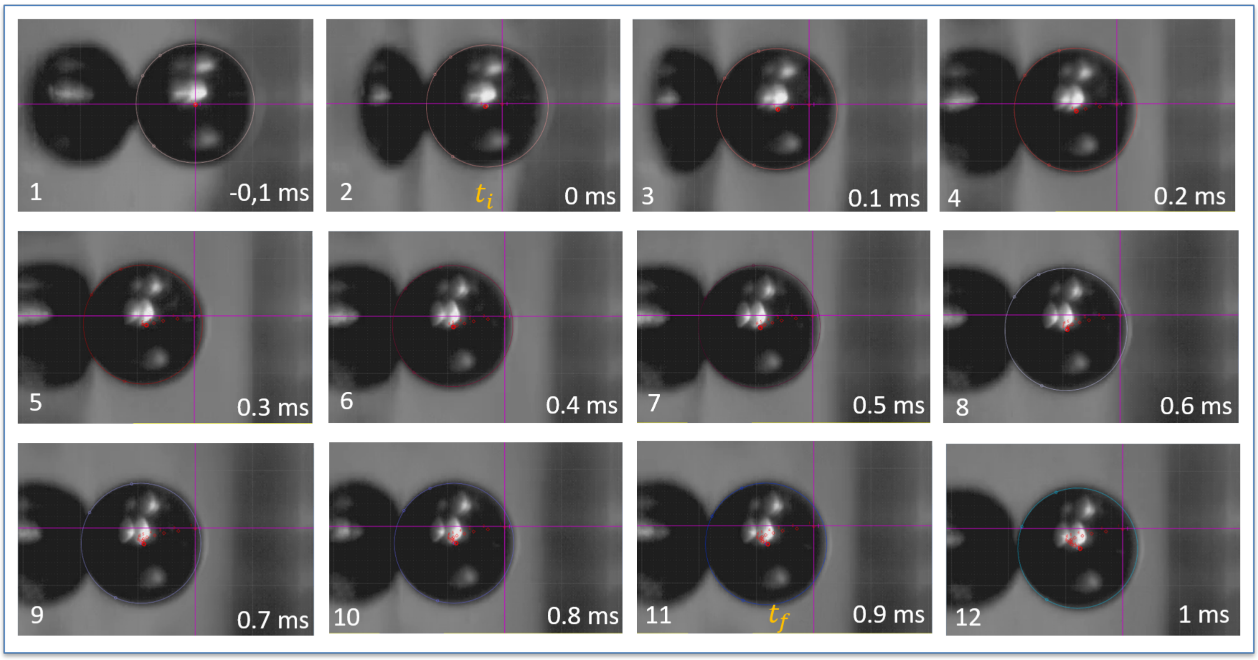

Figure 2.9 – Tracking the ball's trajectory with the high speed camera. $t_i = 0$ ms : initial contact time, $t_f = 0.9$ ms : end of contact time.

It is important to mention that we draw a circle as the contour of the ball, to accurately differentiate the ball's center of gravity, and then to reduce the error due to the angle between the trajectory of the ball and the high-speed camera, see figure 2.9. This method is much better in terms of results than tracking a ball point (which usually changes over time due to the light emitted by the projectors and the reflective properties of the ball's surface, and above all it changes with the rotation of the ball). It is worth mentioning that the accuracy and reliability of the force curve depend on various factors, such as the quality of the camera images, the precision of the marker tracking procedures, etc. However, with careful data analysis, high-speed camera footage can be a valuable tool for capturing and plotting load-displacement curves in dynamic experiments, figure 2.10. Since the curve must start at point (0,0), we link point (0,0) to the value in 0 of the interpolation function.

Once the impact energy and length of the cannon have been set, the next step is to look at the sizing methods for the other cannon components (reservoirs, firing system), followed by the control program and operating modes.

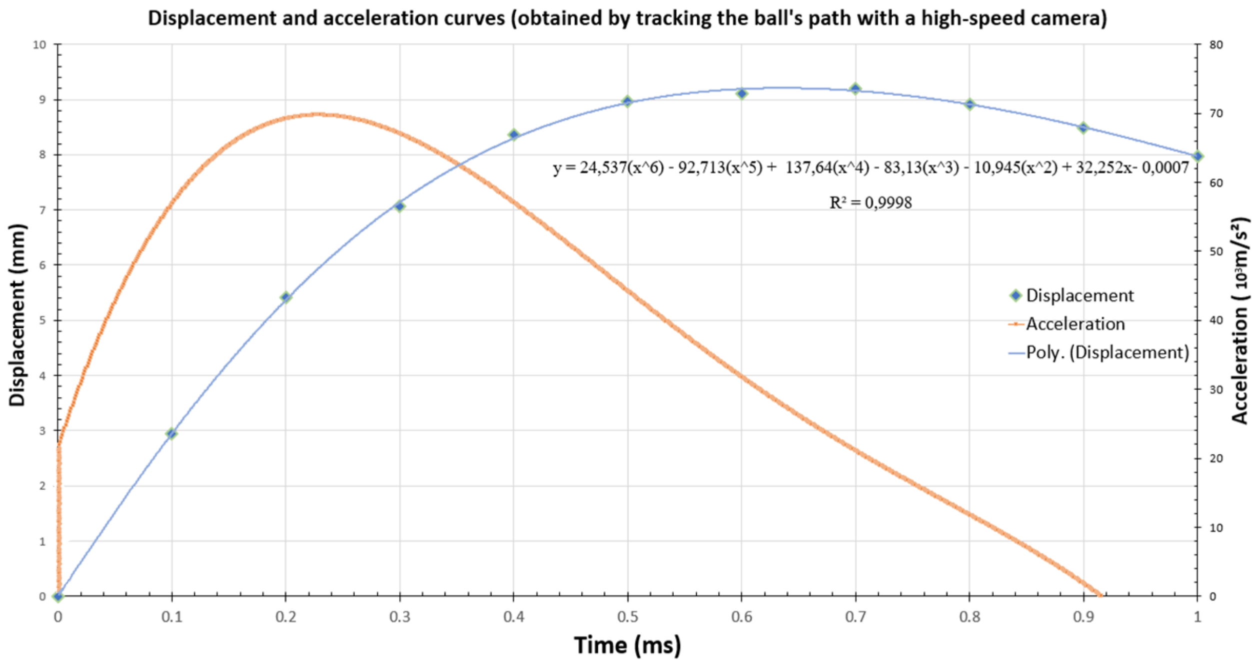

(a) Displacement and acceleration curves

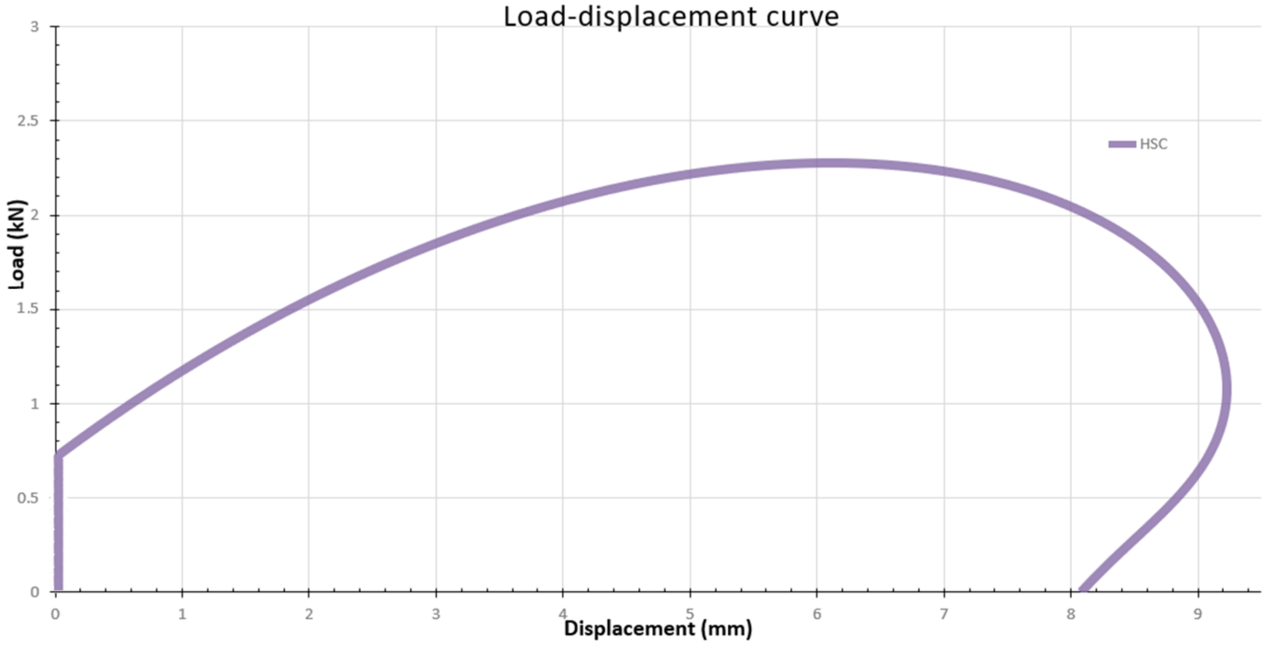

(b) Load-displacement curve

Figure 2.10 – Construction of distance-force curve.

2.3. Design of compressed air reservoirs

The ASME (American Society of Mechanical Engineers) code, section VIII, division 1, 2017 edition, offers formulas for calculating shells subjected to internal pressure. For cylindrical shells (circumferential stress), Figure 2.11 (a) shows the used formula. As is usual with the ASME code, corrosion (and tolerances) must be considered in the

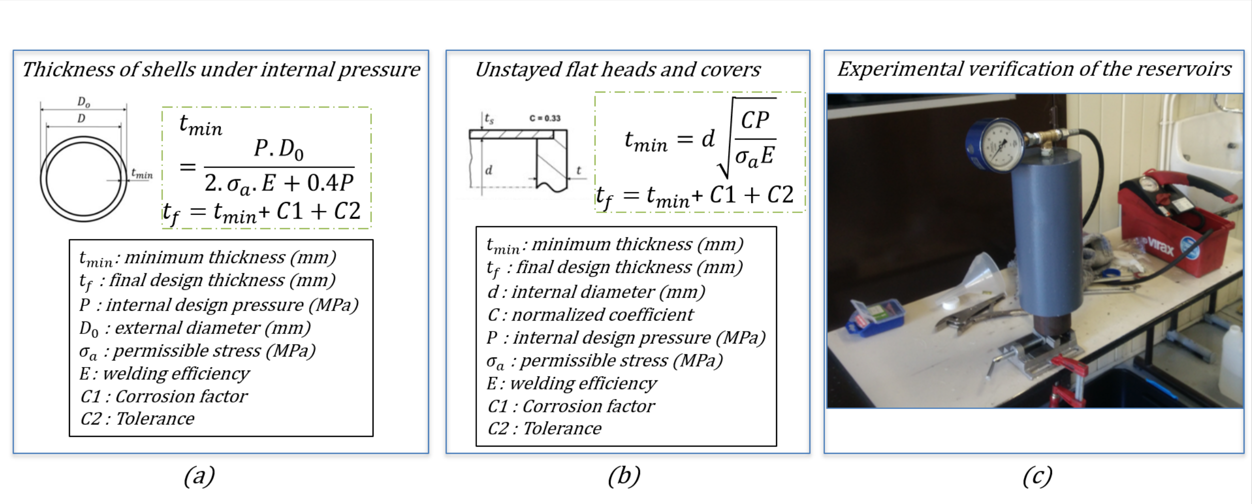

Figure 2.11 – Compressed air reservoir design : (a) cylindrical part (b) flat circular part (c) : hydraulic verification test.

application of all design formulas (see UG-25 Corrosion). Corrosion allowances must be added to the results later. Allowable stresses are listed in ASME code section II, part D. In our case, we also coated the reservoirs with an anti-corrosion protection paint, $C1$ and $C2$ are successively considered equal to 0.7 mm and 0.85 mm respectively.

Efficiency Factor E (weld factor in our case) for longitudinal joints (Category A) shall be determined in accordance with paragraph UW-12. Basically E is between 0.7 to 0.85. For these calculations, a security ratio in regard to the maximum operating pressure of 1.5 has been considered (P_{max} is then equal to 13.5 bars).
For overcrowding reasons, the external diameter of the reservoirs has been fixed to facilitate the assembly/disassembly and the inclination of the cannon ($D_0 = 150$ mm), D is then equal to 145 mm. Finally, the thickness of shells under internal pressure is $t_f = 2.5$ mm ($t_{min} = 0.96$ mm).

For the unstayed flat heads and covers (Figure 2.11 (b)), C is a factor depending upon the method of attachment of head, shell dimensions and other items listed in (ASME Code Section VIII-Division 1- UG-34 (d)), it equals 0.33 in this case. t_f is equal to 10 mm ($t_{min} = 8.43$ mm).

Experimentally, a hydraulic test was performed to verify the performance of the reservoirs (Figure 2.11 (c)), even according to the diagram on page 216 of European directive 2014/68/EU (On the harmonization of the laws concerning the placing of pressure equipment on the market), this case is not concerned by the requirements mentioned in article 4 of the this directive. Indeed, the chosen volume of the reservoir : 5.5 L, pressure : 9 bars. so $P.S.V = 49.5 bar.L$, the limit is 50 bar.L with air (group II gas).

2.4. Sealing and triggering system

To ensure the axial sealing of the triggering system, a bonded seal is used to prevent compressed air from leaking along the axis of a cannon (external sealing) (Figure 2.12), this seal is composed of an outer metal part, and an inner rubber part which ensures sealing by contact with the ball which is pressed into the rubber part. On the other hand, to prevent leaks between the metal spacers and the interior of the cannon, an O-ring seal is used to ensure the radial sealing of the system and prevents compressed air from leaking around the perimeter of the O-ring seal (interior sealing). By using both a bounded seal and an O-ring seal, the system achieves a satisfying sealing protection against both axial and radial leaks. The spacers are blocked by a shoulder on the front and by an inner circlip (housed in the inside of the cannon) on the rear.
To guarantee the quality of this sealing system, the reservoirs are filled with compressed air at different pressures. At each pressure, the bleed valves are closed for several minutes, to ensure that the pressure does not drop over time.

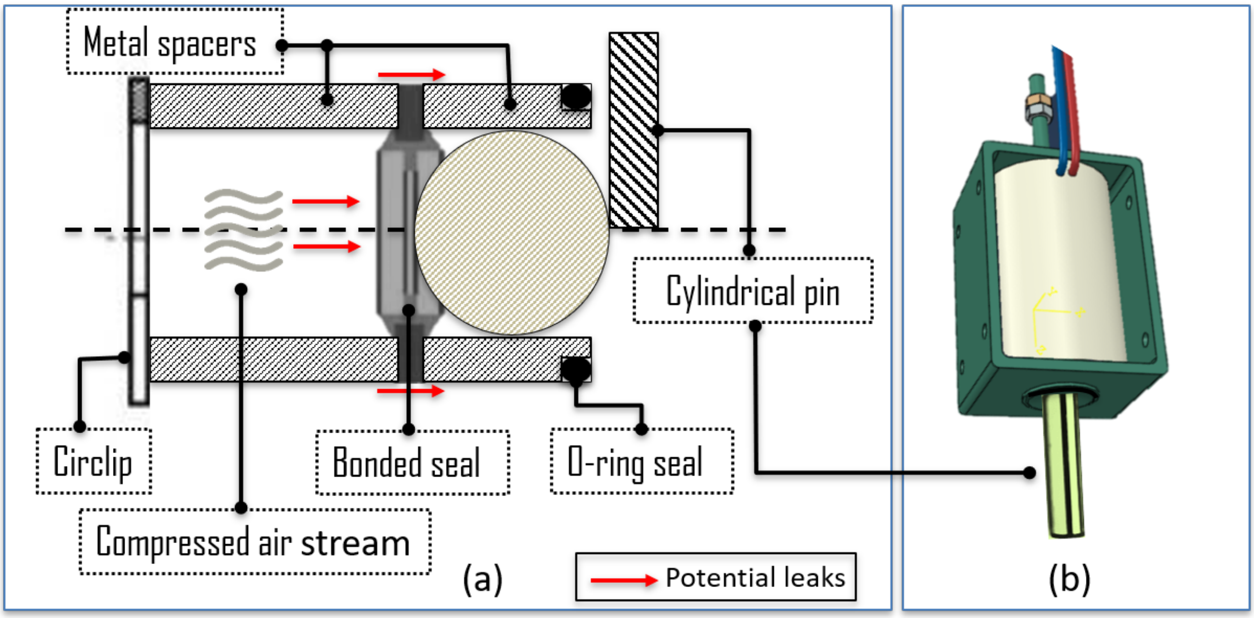

Figure 2.12 – (a) Sealing and triggering system, (b) 3D view of the solenoid.

The triggering of a shot is provided by a cylindrical pin controlled by a solenoid electromagnets (NAFSA ERC60-20/C ED = 5%, with a maximum force of 54.8 N), where ED is the ratio of the total duration of power-ups to the total duration of the cycle sequence. The core of the solenoids is attracted by the magnetic field of the coil during power up and remains maintained by the magnetic field delivered by the permanent magnet. Then a simple inversion of the polarity of the power supply makes it possible to neutralize the magnetic field of the magnet which has the effect of releasing the core.
The electromagnets of the ERC series are linear electromagnets of simple effect, in which the movement of stroke from the initial position to the final one is carried out by

the action of electromagnetic forces, the return to the initial position is carried to effect by external forces or by a spring integrated to the electromagnet. Their life in number of operations is much greater then some other series since its guide is manufactured with friction bearings with teflon film. ED is usually expressed as a percentage. The lower ED is, the greater the force, but the time of use is less, it is therefore necessary to apply a numerical control in order not to use these electromagnets more than once every 10 seconds.

2.5. Vibration and clamping system of the plate

We have verified the fixation of the plates by making several tests to determine the resonance frequencies and the modal shapes of a simple structure from the Frequency Response Function (FRF), and finally verify that these two parameters do not change after each new installation of the plate on the cannon frame.
The frequency response function (the ratio between the response of the structure and the excitation force) is obtained by using a two-channel analyzer equipped with an accelerometer and a hammer with a force sensor, see figure 2.13(a).

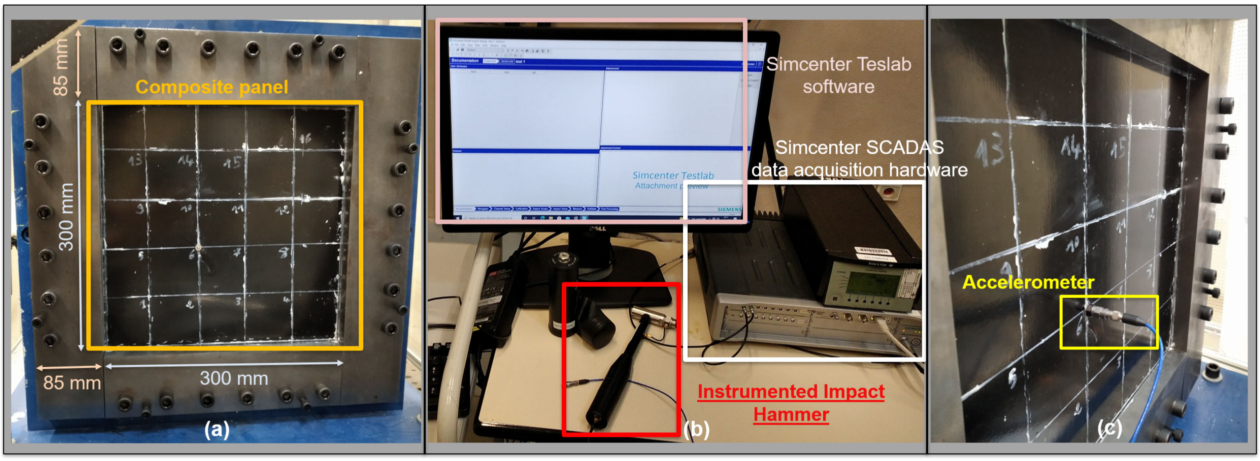

Figure 2.13 – Clamping system of the plates on the cannon : (a) support 2 and measuring points, (b) acquisition system, (c) accelerometer location.

The modal frequency and modal damping can be determined from all frequency response measurements (except when the excitation or response is in a zero displacement point). However, to have sufficient accuracy, it is necessary to make several measurements at different points of the structure.
Practically, these frequency response measurements are made using a two-way analyzer. The excitation forces (obtained with an impact hammer or a white noise generator) are measured by a force transducer and the resulting signal is applied to channel A of the analyzer. The response of the structure under study is measured with an accelerometer and the resulting signal is applied to channel B of the analyzer. The frequency response function of the structure is the complex quotient of the acceleration by the

force in the frequency domain. With an impact hammer excitation, the response is measured at a fixed point used as a reference point, and the hammer excitation point sweeps the different points of the structure used for the model, figure 2.13.

The natural frequencies are the easiest to determine. A resonance is marked by a peak in the modulus curve of the frequency response function. The accuracy of the measurement can be increased by measurement by reducing the frequency range or by using a zoom around the frequency concerned, see figure 2.14(a).

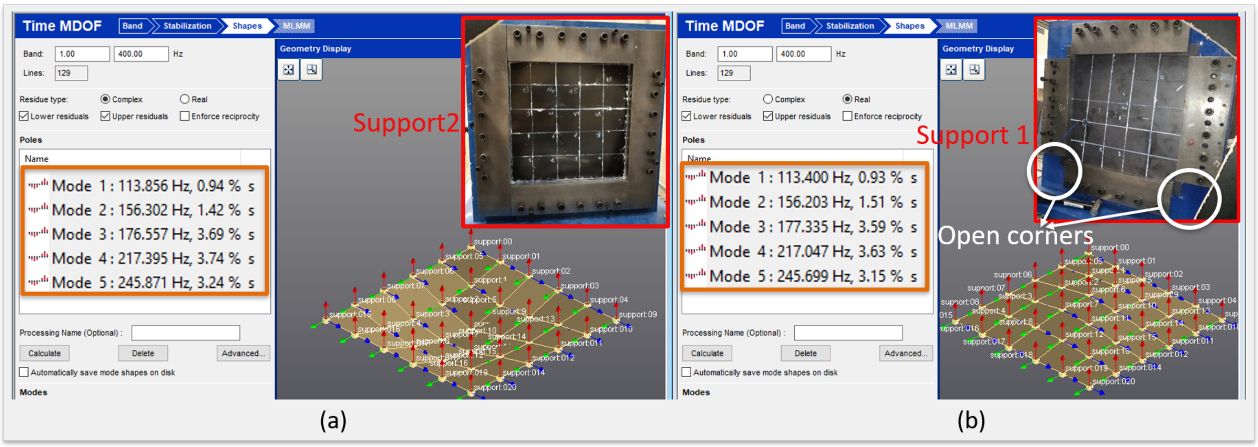

(a)

Band: 1.00 400.00 Hz
Lines: 129
Residue type: ● Complex ○ Real
☑ Lower residuals ☑ Upper residuals ☐ Enforce reciprocity
Poles
Name
Mode 1 : 113.856 Hz, 0.94 % s
Mode 2 : 156.302 Hz, 1.42 % s
Mode 3 : 176.557 Hz, 3.69 % s
Mode 4 : 217.395 Hz, 3.74 % s
Mode 5 : 245.871 Hz, 3.24 % s
Processing Name (Optional) :
☐ Automatically save mode shapes on disk

(b)

Band: 1.00 400.00 Hz
Lines: 129
Residue type: ○ Complex ● Real
☑ Lower residuals ☑ Upper residuals ☐ Enforce reciprocity
Poles
Name
Mode 1 : 113.400 Hz, 0.93 % s
Mode 2 : 156.203 Hz, 1.51 % s
Mode 3 : 177.335 Hz, 3.59 % s
Mode 4 : 217.047 Hz, 3.63 % s
Mode 5 : 245.699 Hz, 3.15 % s
Processing Name (Optional) :
☐ Automatically save mode shapes on disk

Figure 2.14 – Checking whether the frequencies and eigenmodes of the plates with the two types of support are the same : (a) results with support 2, (b) results with support 1.

To determine the modal shapes, it is assumed that the modes are decoupled. In practice, mechanical structures are often weakly damped (<1%). This implies that the modes are weakly coupled. For each frequency, the amplitude of the frequency response function is the sum of the contributions of all modes. When the modes of the structure are weakly coupled, the response of the structure in the proximity of a resonance frequency f_r, is mainly due to the contribution of this mode. For a structure modeled by a 1 degree of freedom system, the FRF is purely imaginary at resonance. The value of the imaginary part of the FRF, at resonance, for a structure with weakly coupled coupled structure is proportional to the modal displacement. Therefore, by examining the amplitude of the imaginary part of the FRF, for different points of the structure, we can determine the modal displacement for each point. Thus, the modal shape can be traced from the modal displacements. The procedure is then repeated to determine all the modal shapes in the chosen frequency range, see figure 2.14(a).

After checking that the plate fixing conditions are still the same after assembly and disassembly, the second aim of this section will be to show the two types of support used. Doubts were expressed about the open corners of support 1, so we made a second support with closed corners, and then checked the mounting of the plates with the two types of support. The result shows that there is no great difference between the two.

A support open on the corners (1) was used at first (figure 2.15 (a)), it was replaced by a support (2) closed, see figure 2.15 (b). A new experimental analysis was launched, the results show that the frequencies and eigen modes are the same (with a small error due to the experimental manipulation itself), see figure 2.14.

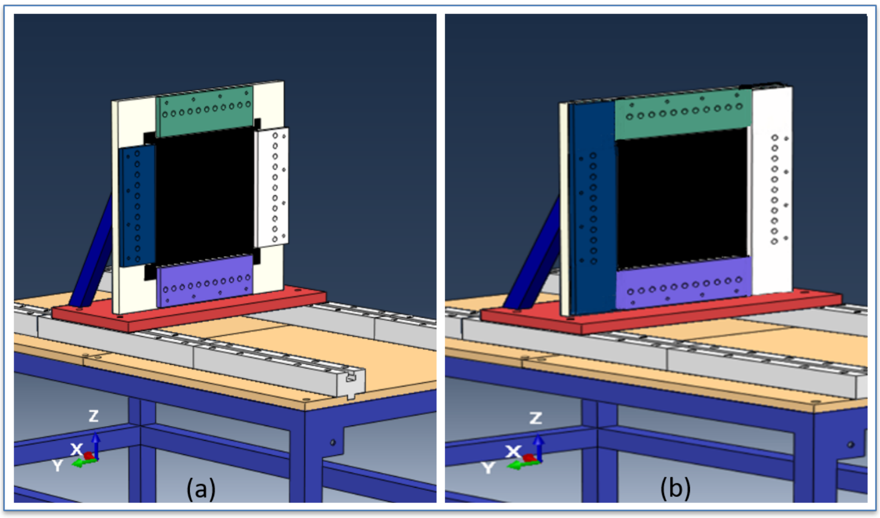

Figure 2.15 – (a) previous support(1), (b) new support(2).

Finally, we used the new support, which posed less problems.

All the mechanical parts of the air cannon have been set up, the process of automating the firing system and securing it will be shown next.

2.6. Automated impacts and data acquisition

We used NI (National Instruments) cards for real-time signal generation and acquisition. These cards are designed to interface with a variety of sensors, instruments, and other equipment to measure and control signals with high accuracy and precision. To collect data from displacement sensors (operating at 392 kHz), a NI 9222 was employed , which is a data acquisition module designed for measuring high-speed voltage signals. With its ability to acquire data at rates of up to 50 kS/s, the NI 9222 can capture high-frequency signals and deliver them to a host computer for analysis. Its differential inputs provide excellent noise rejection, ensuring accurate measurements even in noisy environments as an air cannon.
Similarly, a NI 9205 was used for pressure sensors data acquisition. It can provide up to 16 channels of simultaneous sampling with 16-bit resolution and a maximum sampling rate of 250 kS/s.
The NI 9485 output module was used to control electromagnets. It features 8 channels, each channel provides access to a solid state relay (SSR) for switching voltages up to 60 VDC (direct current) or 30 Vrms (root mean square voltage), with switching current up to 750 mA per channel. This same card was used to externally trig the IR high speed camera rear chassis with a 3.3 V TTL (Transistor-Transistor Logic) pulse (5 V max).
A NI cDAQ-9189 CompactDAQ Chassis (8-Slot Ethernet) was used to be able to send the retrieved data directly to the network via ethernet. This allows to launch impacts

remotely.

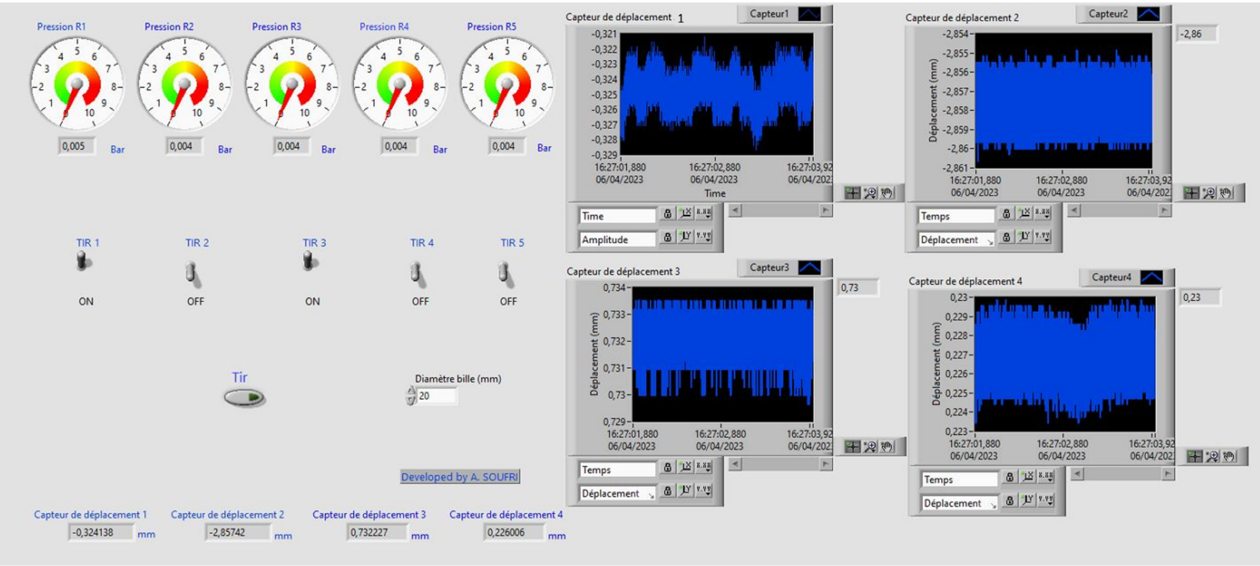

Pression R1 0,005 Bar
Pression R2 0,004 Bar
Pression R3 0,004 Bar
Pression R4 0,004 Bar
Pression R5 0,004 Bar
Diamètre bille (mm) 20
Capteur de déplacement 1 -0,324138 mm
Capteur de déplacement 2 -2,85742 mm
Capteur de déplacement 3 0,732227 mm
Capteur de déplacement 4 0,226006 mm

Figure 2.16 – LabVIEW cannon program : front panel.

To develop measurement, test, and control systems using all these NI cards, the graphical programming environment LabVIEW was used, figure 2.16. LabVIEW provides a graphical programming interface that allows us to create custom applications for controlling the compressed air cannon. This interface includes a wide range of tools for data acquisition, signal processing, control, and communication, which can be easily adapted to suit the specific requirements of our system.

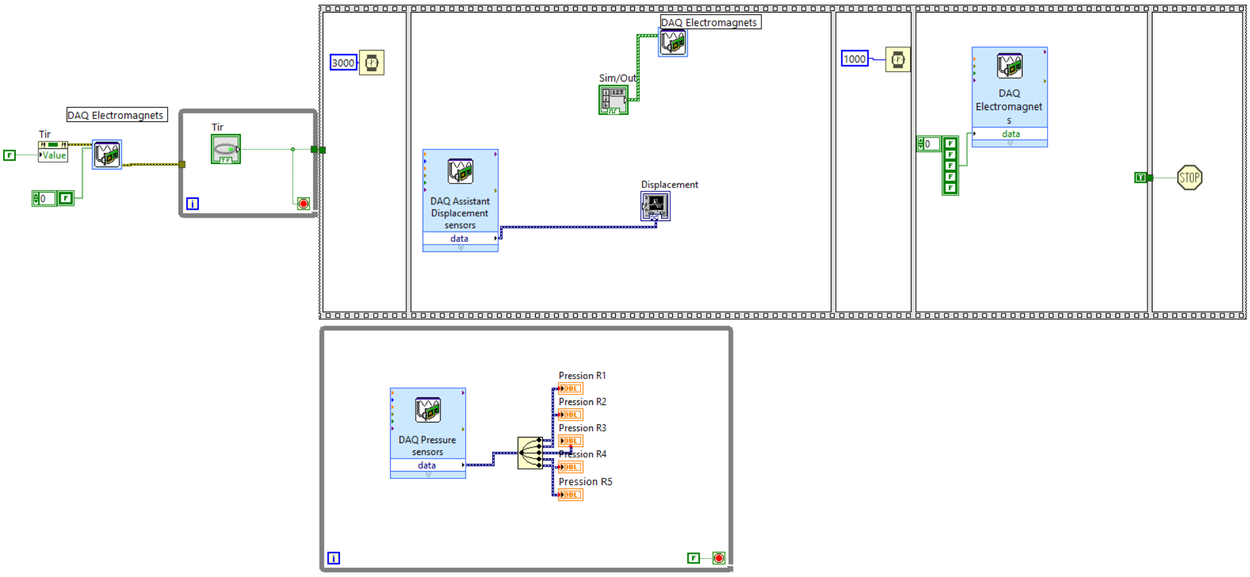

Figure 2.17 – LabVIEW cannon program : example of a block diagram.

To perform sequential impacts, a first program is used, starting by setting the desired pressure per reservoir and then choosing the number(s) of the cannon(s) to be used (unused reservoirs are not charged with compressed air by manually closing the valve positions, see figure 2.21). Additionally, the value of the displacements is reset to zero (for displacement sensors), and the front panel is presented in Figure 2.16.

To create, edit, and run tasks using NI-DAQmx, a different DAQ assistant can be used for each cannon. However, this solution cannot ensure a good precision of signal generation (<1 ms) due to the arbitrary order of execution of commands in the same window of the same structure. Similarly, the execution order of parallel structures is not always the same. To ensure a good precision of simultaneity, the same DAQ assistant is used, which receives a single signal from data containing a 1D array of waveforms to write to the task (see Figure 2.17). Each element in the array corresponds to a channel in the task.

To check the values displayed by the different measuring instruments, a custom scale is created for each component. The equation $y = mx + b$ is used, where x represents a pre-scaled value in volts, and y represents a scaled value (unit depending on the measured physical quantity). The values of "m" and "b" are determined experimentally or according to manufacturers' data-sheets.

For the displacement sensors, gauge blocks are used to verify the displayed and recorded signals/values. The experimental approach is explained in Figure 2.18.

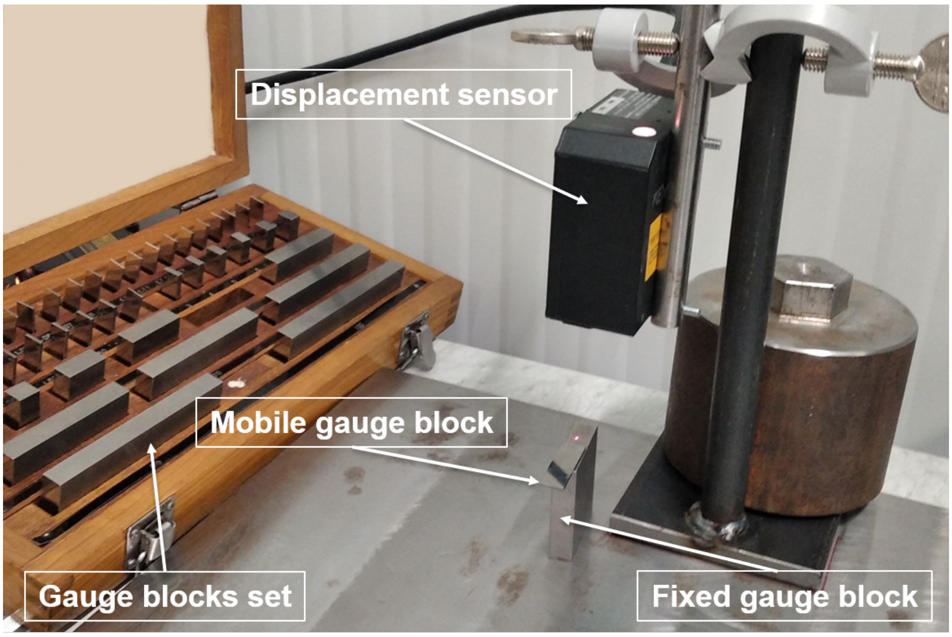

Figure 2.18 – Calibration of displayed values

2.7. Ice and gravel impacts

A sabot a device was used to enable impact tests with different types of projectiles from a single cannon. The ice projectile is placed in a low density open cell foam sabot which can be caught at the end of the barrel, leaving the ice to impact the target unrestrained. The sabot, a cylinder with an external diameter equal to the internal diameter of the cannon, and an internal diameter which varies according to the shape of the gravel or ice to be used as an impactor, is made of a lightweight material (hard foam), cut to the desired shape with a laser cutter, and is designed to break apart upon the exit of guiding tubes, allowing the projectile to separate and continue downrange at high speed. See figure 2.19, for an illustration of these applications.

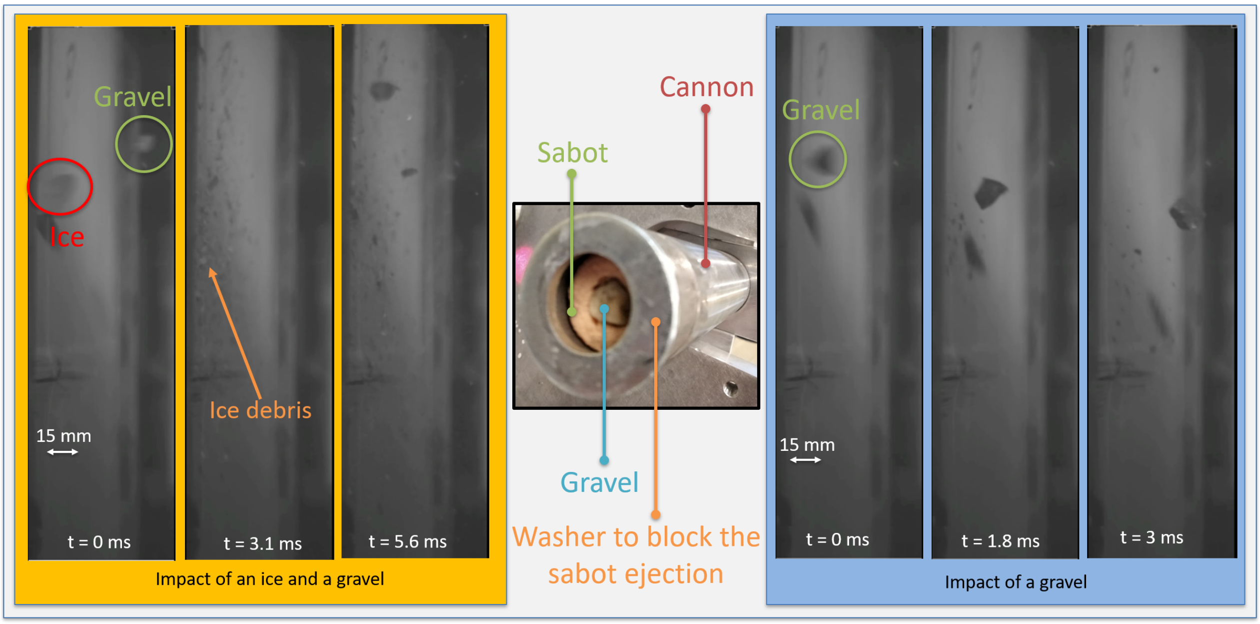

Figure 2.19 – Example of ice and gravel impacts with the compressed air cannon.

Since the mechanical properties of the ice are highly dependent upon temperature, the ice must be launched at a consistent temperature e.g. -17°C, with only minor variations of plus or minus 1 degree allowed. This can be achieved by firing the gun within a few minutes of removing the ice from the freezer (128).

2.8. Description of the air cannon components

Height and floor dimensions	1600 x 1000 x 3000 mm^3
Weight of the frame	250 kg
Maximum power	6 kW
Maximum voltage	3*420 V+N - 50Hz
Maximum air pressure	9 bars
Noise level (impact)	>80 $dB(A)$
Draining time of the reservoirs	10 s

Table 2.1. – Device features.

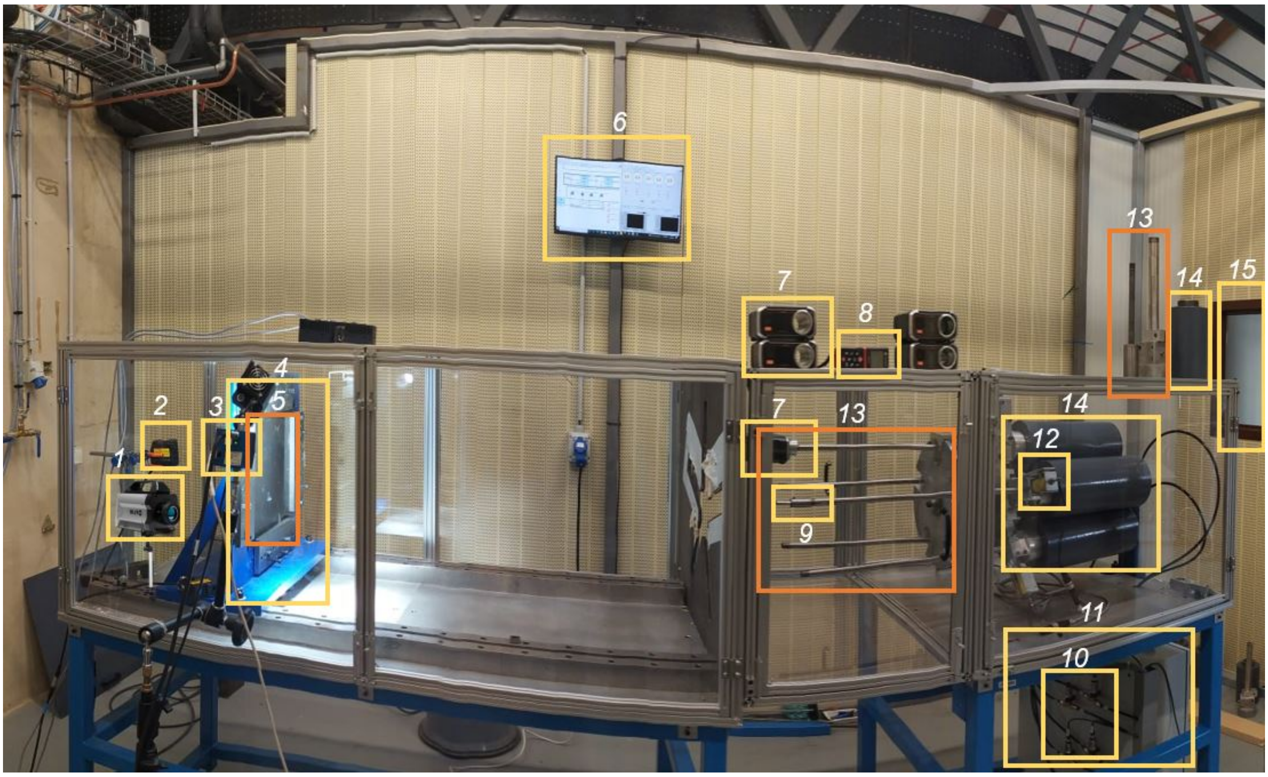

Figure 2.20 – Compressed air cannon test bench : (1) Infrared camera (2) Displacement sensors, (3) High-speed camera, (4) Clamping system, (5) Composite panel, (6) Setting up TV, (7) Chronographs, (8) Laser rangefinder, (9) Laser sight, (10) Pressure sensors, (11) Electrical enclosure, (12) Triggering system, (13) Guiding tubes, (14) Compressed air reservoirs, (15) Control room.

The air cannon system, installed in a test room, is composed of (see figure 2.20, and also appendix A) :

- A welded structure supporting 5 cannons arranged in the default position horizontally, independently tiltable, and can be rotated to suit the desired angle of impact or to change the distance between impacts. The cannons are made of :
  - An air reservoir : capacity 5.5 L ; external dimensions (diameter 150 mm ; length 350 mm) ; skin thickness 2.5 mm ; flat heads thickness 10 mm ; steel S235 ; operating pressure 9 bars.
  - A guide tube adapted to the diameter of the steel balls (10 or 20 mm).
  - Breech whose shutter actuated by an electromagnet, the design of these shutters makes it possible to operate them manually before loading the balls and automatically for the shots.
  - An electrical box in which the power supplies for the electromagnets related to the shutters are located.
- A welded structure supporting the target (vertically arranged plate).
- Measurement elements :

  - Thermal high-speed camera (FLIR X6800sc) to monitor and track the damage of composite plates in real-time
  - The chronographs (Acetech Airsoft Gun AC6000 BT) to measure the projectiles speed at the exit of the tubes
  - The high-speed camera (MotionBLITZ EoSens®mini2) working allows the measurement of the projectiles velocity before $v_i[m/s]$, during and after $v_f[m/s]$ impact.
  - Four laser position sensors (Keyence LK-H082) working at a maximum of 392 KHz placed at the back of the plate to measure its displacement during the impacts.
  - Pressure sensors (Schneider electric XMLP010BC71F), to control pressure in the reservoirs.
    After each impact, the plates are checked by an ultrasonic control (C-scan) in immersion, with a 25 MHz immersion transducer with spherically focused lens used to transmit and receive the signal.

The cannons are controlled from a control room including (see figure 2.21) :

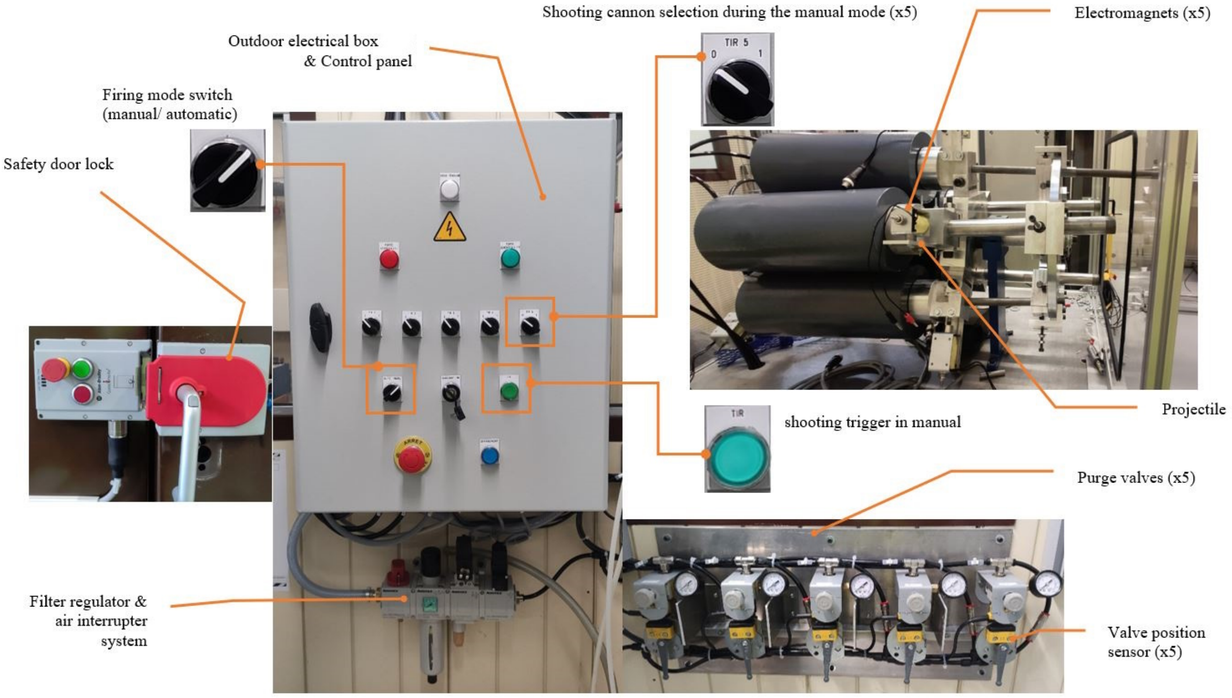

Figure 2.21 – Control room essentials, and the electromagnets and projectiles location in the cannon.

- An electrical enclosure for power and control.
- A pneumatic supply panel located under the electrical enclosure including :
  - A manual decompression valve.

  - A filter and regulator.
  - A pressure gauge.
  - A pressurization solenoid valve.
  - A pressure switch.
- Components for the supply of each compressed air reservoir including :
  - A manual valve with an RFID (Radio Frequency IDentification) safety sensor to ensure that the valve is open.
  - A pressure regulator with a pressure gauge.
  - A one-way valve mounted in parallel to the above components and passing in the direction of the reservoir to the pneumatic system.

2.9. Operating Procedures

Figure 2.22 displays the operating protocol for the compressed air cannon.

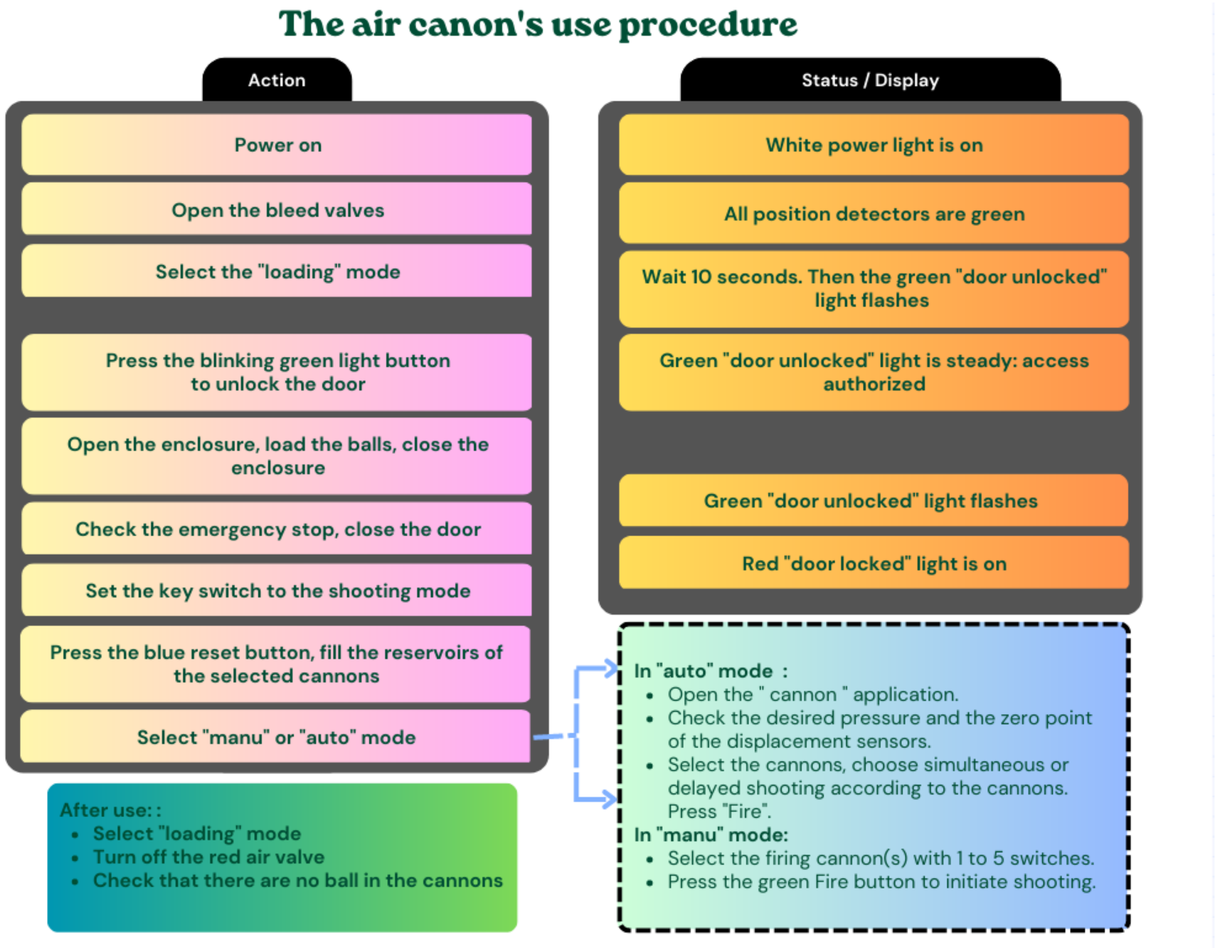

After use: :
- Select "loading" mode
- Turn off the red air valve
- Check that there are no ball in the cannons

In "auto" mode :
- Open the " cannon " application.
- Check the desired pressure and the zero point of the displacement sensors.
- Select the cannons, choose simultaneous or delayed shooting according to the cannons. Press "Fire".

In "manu" mode:
- Select the firing cannon(s) with 1 to 5 switches.
- Press the green Fire button to initiate shooting.

Figure 2.22 – Operating protocol for the air cannon.

Running modes :
The start of the air cannon is conditioned by :

- Electricity and compressed air supply servitudes.
- The release of the 2 emergency stop devices.
- The access door to the testing room locking.
- The reset of the safety chain from the "reset" button located on the electrical enclosure.

The air cannon has two operating modes :

- Automatic : The triggering of the impacts is triggered from a PC.
- Manual : The triggering of the impacts is carried out from the operating devices located on the control panel.

In automatic mode, the key switch "Loading/Firing" must be in the "Firing" position, the electromagnets are controlled by the PC, subject to the safety conditions (door of the test room closed). In manual mode, the key switch "Loading/Firing" must be in the "Firing" position, the electromagnets are controlled by the green luminous push button "SHOOT (TIR)" located on the control panel subject to the safety conditions (door of the test room closed).

The automation of this unit is controlled by a configurable safety relay SICK Flexisoft.

Stop modes :
The system has two shutdown modes :

- Stopping by releasing the service organs.
- The emergency stop is controlled by 2 push buttons.
  - One is placed on the electrical cabinet of the control room.
  - The second one at the level of the entrance door of the test room.

They are wired as dual channels to the I1 and I2 inputs of the configurable SICK FlexiSoft safety relay (folio 3, module 2SICK2).
All actuators are controlled directly by the Flexi-Soft safety relay. In case of emergency stop, the outputs are set to 0 :

- The 1KMG contactor powering the 5 electromagnets driving the cannon shutters (output Q3 module 2SICK2).
- The general compressed air solenoid valve of the pneumatic panel 4EV1 (output Q4 module 2SICK2).
- The 24 V secured (mark 10.3) supplying the output interface controlled by the PC for firing in automatic mode (Q4 module 2SICK5). This output cuts the selection relays KAUT1 and KAUT2. The contacts of these 2 relays ensure the cut-off of the electromagnets.

Air cannons should be operated by authorized and qualified operators. Adjustment and maintenance operations must be carried out by specialized operators.

Main security features :

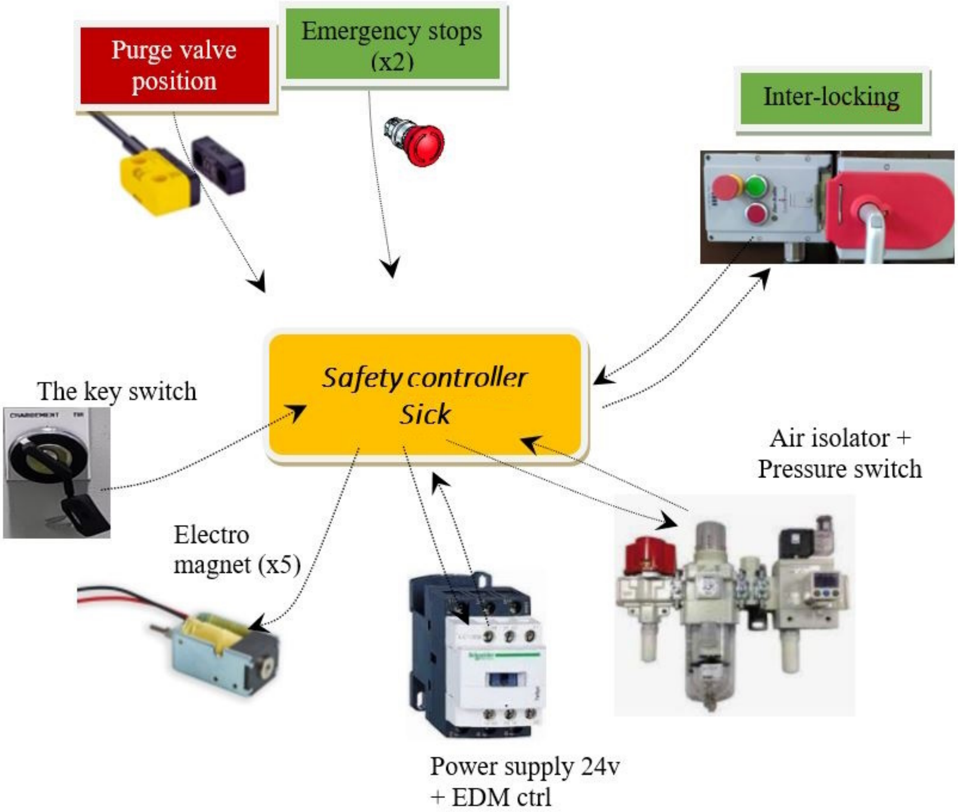

Figure 2.23 – Safety system overview.

- The air cannon equipment is totally encased by Lexan protectors, 5 mm thick on the lateral sides and 6 mm on the upper part. The lateral protectors are mobile, they are mounted on hinges and they are set up to limit the projections in the test room.
- The equipment is located in a test room, which can only be accessed via a set of 2 hinged doors equipped with an Allen Bradley type 442G guard locking device. The contacts of this safety switch are connected in dual channels to the I3 and I4 inputs of the configurable safety relay SICK FlexiSoft (folio 3, module 2SICK2). Opening the door provides an emergency stop function (see figure 2.23).
- The door release is controlled via output Q1 of the configurable safety relay module 2SICK2. This undervoltage release can be activated if the following conditions are met :
  - Pressure switch 7P6 detects zero pressure in the pneumatic network, input I1 of the configurable safety relay SICK FlexiSoft (folio 7, module 2SICK4).

  - The 5 manual valves feeding the air cannon reservoirs are through-valves ; the through-valves are controlled by RFID sensors SICK STR1 wired in dual channels to the inputs I3 to I8 of the configurable safety relay SICK FlexiSoft module 2SICK4 and I1 to I4 of module 2SICK5.
  - A time delay of 10 seconds has elapsed after opening the general solenoid valve 4EV1 to allow sufficient time to purge the reservoirs and the pneumatic system.
- Safety instructions are in place on the access door to the test room.

  The electrical enclosure has a main switch with a handle that can be padlocked in the isolation position.

  The pneumatic panel has a manual pressure relief valve that can be padlocked in the position of isolation of the pneumatic network.

Apave Group for risks Management was able to ensure that the equipment examined complied with the regulatory provisions applicable to it.

2.10. Insights on outcomes

Using this particular cannon, a detailed study of several new impact configurations is made possible, for example :

- Analyze the difference between sequential and simultaneous impacts in cases involving interference or absence thereof in damage zones.
- Investigate the interaction of simultaneous impacts at varying distances between impacts.
- Explore the effect of the number of impacts on tested configurations, considering a fixed energy per ball and subsequently a fixed total energy, encompassing 1, 2, 3, 4, or 5 impacts.
- Examine the influence of the size of the impactor in 10 and 20 mm ball impacts.
- Investigate the effects of both repeated and simultaneous impacts at different energy levels.
- Explore the multi-impact cases involving gravels and hailstones.
- Assess the interaction of waves by incorporating piezoelectric sensors on the plates subjected to impacts.
- Study repeated simultaneous impacts.

According to the FAA (Federal Aviation Administration), an airline reports 8 composite structure damages per aircraft (on average), of which 87% are due to impact, which corresponds to a cost of $200,000/aircraft (122).
Using this cannon, the scientific community will be able to gain a better understanding of multi-impact effects and to reduce companies' losses by producing more optimized and reliable composite parts.

Conclusion

In this chapter, we have presented the development and characterization of the Compressed Air Cannon, a specialized test rig designed for studying the multi-impact behavior of composite structures. Through careful design and construction, we have created a versatile and reliable tool that offers controlled and adjustable impact parameters, allowing for a wide range of impact scenarios to be investigated.

We have described the key components of the Compressed Air Cannon, including the pressurized air system, projectile launch mechanism, target mounting arrangement, and data acquisition system. The calibration procedures and validation experiments have ensured the accuracy and reliability of the test rig, providing confidence in the experimental results obtained. We have also detailed specifications for the cannon to be developed, and provided the essential equations for the development of such a cannon.

Through the experimental investigations conducted using the Compressed Air Cannon, we have gained valuable insights into the multi-impact behavior of composite specimens. The data obtained from these experiments must allowed us to analyze the damage mechanisms, energy absorption characteristics, and other mechanical properties of composites subjected to multi-impact loading. This knowledge is essential for designing composite structures that can withstand real-world multi-impact scenarios with enhanced durability and performance, and more essential for us to ensure the dialogue between experiments and numerical calculations in chapters 3-5.

In conclusion, the development of the Compressed Air Cannon test rig represents a significant advancement in the study of multi-impact behavior in composite structures. Its capabilities for controlled and adjustable impact scenarios, coupled with the insights gained through experimental investigations, contribute to the broader understanding of composite materials and must facilitate over the long term the development of more reliable and durable structures in various engineering applications.

Chapter 2

CHAPTER 3 :
MONO-IMPACT BEHAVIOR OF COMPOSITE STRUCTURES

3. Mono-impact behavior of composite structures

Introduction

The mono-impact behavior of composite structures has been a subject of extensive research due to its significant implications for the design and performance of various engineering applications. Understanding the response of composite materials to a single impact event is essential for ensuring their structural integrity and reliability under dynamic loading conditions. This chapter presents an investigation into the mono-impact behavior of composite structures, combining experimental and numerical approaches to gain insights into the underlying mechanisms and enhance the predictive capabilities.

This chapter presents in detail all the means and methods used during the course of this thesis, listing in particular the material and manufacturing methods, as well as in-situ and post-mortem impact monitoring. It also presents the DPM and some of the modifications made to it. The primary aim of this chapter is to verify the consistency of the measurement tools and methods used by the various means, by cross-referencing the results obtained by each means with the others, and then to validate the performance and reliability (and limitations) of the DPM by comparing it with the experimental results.

Various impact parameters, such as impact energy, impact velocity, projectiles' diameter, impact angle and spatial location of impacts, are carefully controlled to simulate real-world impact scenarios. Through high-speed imaging, load measurement technique, IR imaging and non-destructive evaluation methods, the response of composite materials under mono-impact loading is analyzed. Complementing the experimental investigations, the numerical simulations enable the exploration of different impact scenarios, parametric studies, and virtual testing of composite structures under mono-impact conditions. By integrating the strengths of the experimental and numerical approach, a more holistic understanding of the underlying physics governing the mono-impact behavior of composites and their failure mechanisms is performed.

3.1. Nomenclature

We will use the following nomenclature to distinguish the different configurations tested in this thesis : "configuration A/B/C/D/E/F*". Where A is either Sq to indicate sequential cases, Si to indicate simultaneous impacts or M to indicate a mono-impact case. B is either ⌀10 to denote the use of 10 mm diameter balls or ⌀20 to denote the use of 20 mm diameter balls. C specifies the projectile energy in J. If this energy is provided by each ball, then D is equal to Ba (per ball), and the energy value is specified in C. If D is T (in total), then the value of C represents the total energy with all the balls. Next, E denotes the impact position, generally explained in a schematic at the beginning of the following chapters to distinguish the different possible impact positions, a summary of the impact positions can also be found in the appendix D. F denotes the number of impacts in question, and finally, if "*" is added, it means that it is a configuration of repeated impacts. For example, the designation configuration Si/⌀20/15J/Ba/O/2 means that it is a configuration of 2 simultaneous impacts with an energy of 15 J per ball using 20mm diameter balls positioned at O-position, as shown in Figure 5.1. We note that tests at 15J with 20 mm diameter balls are carried out at a velocity of 30 m/s (at 87 m/s for 10 mm diameter balls), the other velocities at different energies can be calculated knowing that 20 mm diameter balls weigh 32.7 g whereas 10 mm diameter balls weigh 4 g).

A	B	C	D	E	F
Sequential (Sq) Simultaneous (Si) Mono-impact (M)	Diameter 10 or 20mm	Energy (J)	Per ball (Ba) In total (T)	Impact position I,J,K,L,M,N,O,P	Number of impacts

To simplify the reading of this document, we have added this same nomenclature in appendix B. For a more general overview of the tests carried out during this thesis, please refer to the appendix C.

3.2. Materials & Methods

3.2.1. The used material

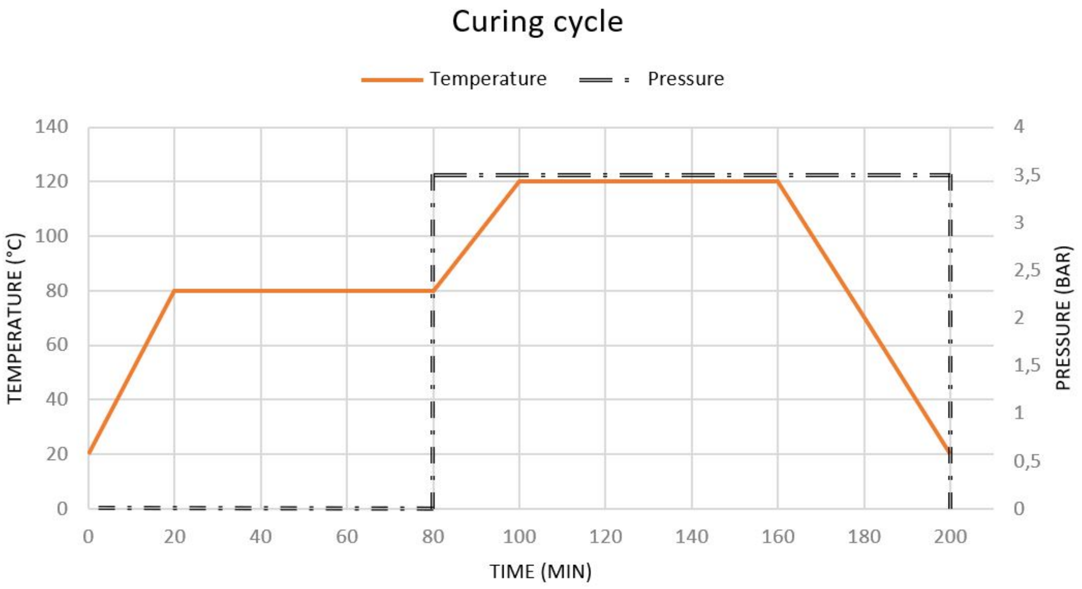

Figure 3.1 – Curing cycle of carbon/epoxy plates.

Composite laminates were processed using the draping method and press molding of a 380×380 mm^2 unidirectional carbon fiber/epoxy prepreg, widely used in the transportation field due to their high specific mechanical properties, fabricated by Gurit, with a resin content of 37%. The resin used is an epoxy SE 84LV (Low temperature cure epoxy prepreg), which was cured with a ramp rate of 2°C per minute. The minimum viscosity temperature for curing is 99°C, and the dry glass transition temperature is 115°C. The cure dwell time was 1 hour. To ensure cure homogeneity and remove defects related to pre-cure steps, an 80°C temperature plateau was inserted before polymerization. A pressure of 3.5 bar was applied to increase the mechanical properties of the plates. The curing cycle is shown in Figure 3.1. This curing cycle is based on the supplier's data, but the pressure has been set after a number of preliminary tests to reduce defects after manufacture and ensure uniform thickness for the different panels manufactured.

Fibers are High Elongation Carbon (HEC) with a reinforcement weight of 150 g/m² per ply. The stacking sequence is $[0°/-45°/90°/45°]_s$, which leads to a planar isotropic laminate that behaves the same in all orientations, see figure 3.2. This classic "industrial" material/sequence is fixed throughout this work to reduce the parameters involved in the multi-impact study, it also economizes the material by using only 8 plies.

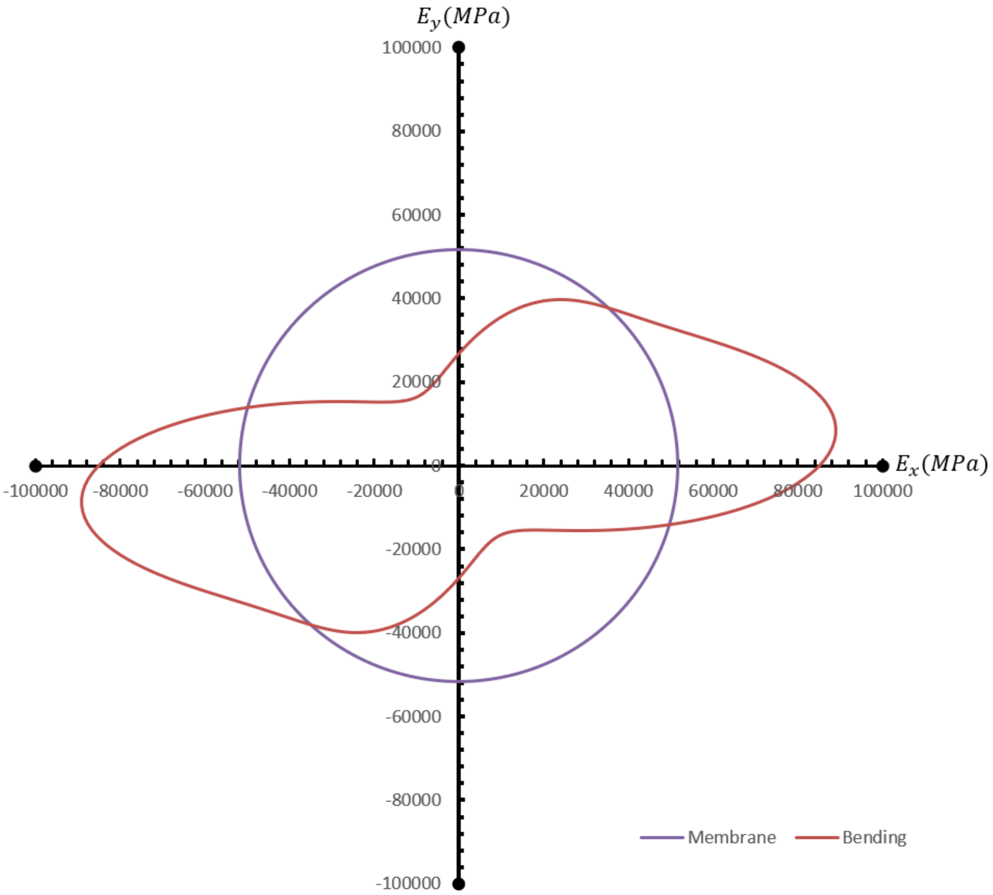

Figure 3.2 – Polar diagram for the used laminate sequence of carbon-epoxy composite.

For the numerical part, the average material properties used are given by Gurit (the material manufacturer), the missing material properties were supplemented with standard values or values taken from the literature ((131), (132),(133)). We summarize below these properties. The aim of the numerical part is primarily to be able to understand phenomena that are difficult to monitor experimentally (wave propagation and interactions, changing impact parameters without repeating time-consuming and expensive experimental campaigns, etc). At first, this part of the project was just a supplementary plus, which explains why no full characterization of the material was carried out, but then the numerical work became more important, given the significant results obtained. Another current project aims to take this numerical modelling a step further, with full material characterization underway.

TABLE 3.1. – Material properties.

$$\rho_V = 1600 \times 10^{-12} \quad \text{tonne/mm}^3 \qquad \text{(Volumetric mass density of volumes)}$$

$$\rho_I = 10 \times 10^{-12} \quad \text{tonne/mm}^3 \qquad \text{(Volumetric mass density of interfaces)}$$

$$E_{lt} = 134000 \quad \text{MPa} \qquad \text{(Longitudinal Young's modulus in traction)}$$

$$E_{lc} = 121000 \quad \text{MPa} \qquad \text{(Longitudinal Young's modulus in compression)}$$

$$E_t = 8300 \quad \text{MPa} \qquad \text{(Transverse Young's modulus)}$$

$$\nu = 0.3 \qquad \text{(Poisson's ratio)}$$

$$G_{lt} = 5200 \quad \text{MPa} \qquad \text{(Shear modulus in the plane)}$$

$$G_{tz} = \frac{E_t}{2(1+\nu)} \qquad \text{(Shear modulus through thickness)}$$

$$\sigma_t^f = 40 \quad \text{MPa} \qquad \text{(Transverse failure stress in traction)}$$

$$\tau_{lt}^f = 90 \quad \text{MPa} \qquad \text{(Shear failure stress)}$$

$$\sigma_0 = 200 \quad \text{MPa} \qquad \text{(Crushing stress)}$$

$$\epsilon_{0t} = 0.0185 \qquad \text{(Tensile fiber failure strain)}$$

$$\epsilon_{0c} = -0.0112 \qquad \text{(Compressive fiber failure strain)}$$

$$G_{Ic} = 0.25 \quad \text{N/mm} \qquad \text{(Delamination mode I fracture toughness)}$$

$$G_{IIc} = 1 \quad \text{N/mm} \qquad \text{(Delamination mode II fracture toughness)}$$

$$\lambda_{comp} = 0.05 \qquad \text{(Compression reinforcement coefficient)}$$

$$G_{ft} = 60 \quad \text{N/mm} \qquad \text{(Tensile fiber fracture toughness)}$$

$$G_{fc} = 10 \quad \text{N/mm} \qquad \text{(Compressive fiber fracture toughness)}$$

$$RD = 500000 \quad \text{MPa/mm} \qquad \text{(Delamination interface stiffness)}$$

$$RF = 1000000 \quad \text{MPa/mm} \qquad \text{(Matrix cracking interface stiffness)}$$

$$RB = 10000 \quad \text{MPa/mm} \qquad \text{(Non-return matrix cracking interface stiffness)}$$

$$E_{moy} = \frac{E_{lt} + E_{lc}}{2} \qquad \text{(Average longitudinal Young's modulus)}$$

After curing, each specimen of dimensions $350 \times 350 \times 1.4$ mm^3 is cut from the 380×380 mm^2 plate with a diamond bore and then measured to verify their thickness.

The plates are checked by an ultrasonic control (C-scan) in immersion after manufacturing to avoid possible manufacturing defects. The principle is to transmit a sound signal into the composite panel and to examine its reflections, transmissions and diffractions. We used the Pulse-Echo method, where the translator acts as transmitter and receiver, coupled using water. Ultrasonic waves are generated by the transducer that converts an electrical signal into mechanical vibrations. These vibrations are then transmitted through the material being inspected. When ultrasonic waves encounter an interface between two materials with different acoustic impedances (the product of the material's density by the velocity of the wave considered in the material), a portion of the energy is reflected and another portion is transmitted through the interface. This reflection is detected by the transducer, which converts the mechanical vibrations back into an electrical signal. By analyzing this signal, we can determine the position, size, and other characteristics of defects or interfaces.

At the interface between two materials, the composite material (1) (with acoustic impedance Z_1) and water/air (2) (with acoustic impedance Z_2), a portion of the incident acoustic energy (E_i) will be transmitted to material 2 (E_t), while a portion will be reflected and remain in material 1 (E_r), according to the following equations :

$$E_\mathrm{t} + E_\mathrm{r} = E_\mathrm{i}$$

$$\begin{cases} E_t = E_i \cdot \dfrac{4Z_1Z_2}{(Z_1+Z_2)^2} \\ E_r = E_i \cdot \dfrac{(Z_2-Z_1)^2}{(Z_1+Z_2)^2} \end{cases}$$

In order to enhance the visibility of echoes, the signals are amplified. The adjustable attenuator also allows us to adjust the signal amplitude. In most cases, we have used a gain of 26 to improve the visibility of the signal return (although this requires larger thresholds to avoid seeing signal disturbances). The device incorporates filters to enhance the signals. Composite materials, being highly attenuating, act as low-pass filters on ultrasonic waves. Therefore, it is necessary to use relatively wideband filters, especially for lower frequencies. Since the plate is quite large, we have used a support to prevent plate buckling under the effect of water, thus obtaining better B/B'/b and b'-scan results.

We used a 25 MHz transducer (NDT Automation IU25X1-1.5) and the UltraPAC Immersion Systems device, see figure 3.3 modified from Mistras Group. Knowing that the smallest detectable defect is equal to $\frac{\lambda}{2}$. Detecting small defects will therefore require a reduction of wavelength, and therefore an increase in frequency, to achieve this

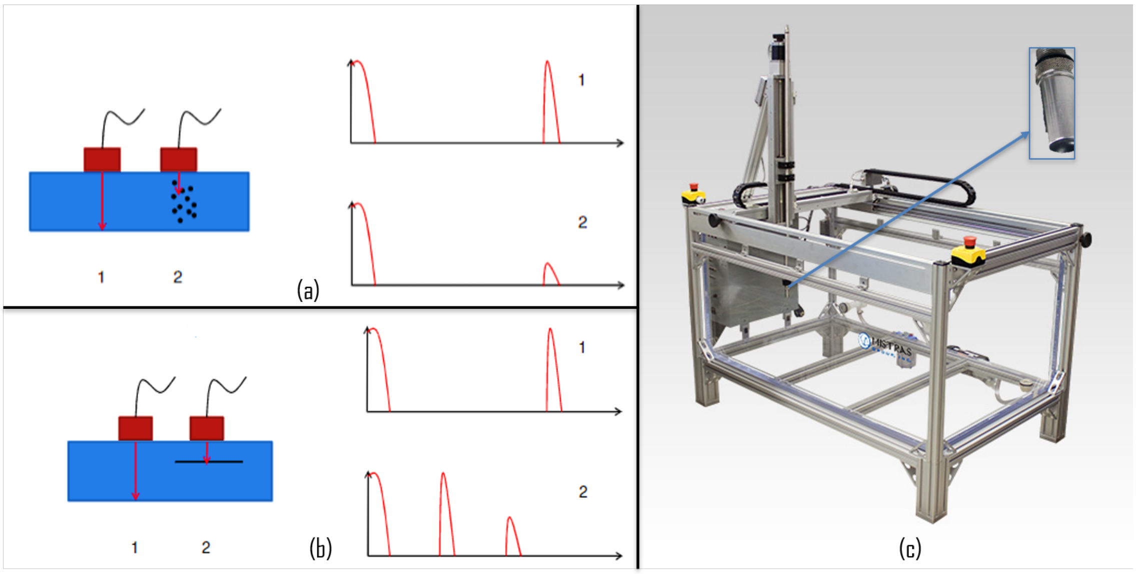

Figure 3.3 – Principle of porosity (a) and delamination (b) detection, immersion system (c).

we used a 25 MHz transducer, which can then detect defects down to 0.055 mm, i.e. a defect of barely 31% the width of the composite ply. The used transducer is concave (focused) for a greater sensitivity.

The delamination is characterized by the appearance of a clear echo and total or almost total loss of the bottom echo. On the other hand, porosities are characterized by a drop in bottom echo and a possible increase in bottom noise (but not systematic). If placed in the same plane, they can give an intermediate echo, see figure 3.3.

For data analysis, we essentially compare experimentally obtained C-scans with numerically obtained C-scans. Of the two types of measurement (amplitude and time-of-flight), we rely more on time-of-flight measurements to determine the position of delaminations and compare them with the numerical model.

3.2.2. Compressed air cannon

A detailed presentation of the compressed-air cannon is given in Chapter 2. In this section, we only provide brief details of the instrumentation and methods used.

The experimental test bench (appendix A) consists of five compressed air cannons. Each cannon is equipped with an automatically controlled triggering system based on the selected shooting configuration, using a Labview program. The setup is instrumented with four displacement sensors (Keyence LK-H082), working at 100 kHz each, positioned at the rear of the plate to measure displacement during impacts. It is also equipped with a high-speed thermal camera (FLIR X6800sc) to capture and analyze thermal signatures recorded during impacts, enabling the reconstruction of damage scenarios and their correlation with the structural response of the plate and numerical simulations.We can then observe in-situ and post-mortem impact damage of the studied material.

The velocity of the projectiles exiting the cannons is measured using chronographs (Acetech Airsoft Gun AC6000 BT), while the velocities before and after impact are measured using a high-speed camera (MotionBLITZ EoSens-mini2). This allows the determination of velocity vectors and the energy absorbed during impact. Following the impacts, the plates are analyzed using immersion ultrasonic testing (C-scan). The impacts are performed using 20 mm or 10 mm diameter steel balls with a mass respectively of 32.7 g and 4.0 g.

3.3. Mono-impact test configurations

In this chapter, we present a study of a single impact on composite structures. Our method includes several unconventional approaches compared with those existing one in the literature. Accordingly, we will present various new investigations and data analyses to demonstrate the applicability of our test bench and damage monitoring method, as well as the extension of the study to more complex cases of multiple impacts. All these single-impact configurations are part of a multiple-impact parent configuration, which will be examined in Chapters 4 and 5.

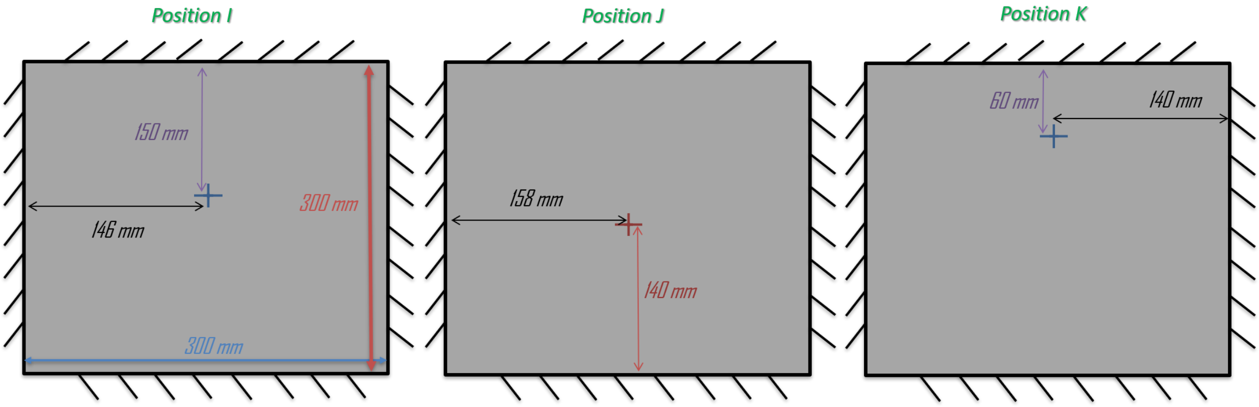

Figure 3.4 – Mono-impact positions : I, J and K.

The figure 3.4 illustrates the different mono-impact positions. To link these configurations, we can start studying the effect of the distance from the edges of the panel and study the effect of the impact angle, and then start building an experimental database to homogenize the delaminated surfaces as a function of the local bending stiffness.

First, we will study each of these configurations. All the results were based on three specimens by configuration to confirm the repeatability level. For data analysis, reasoning and results that are similar in various configurations are not repeated.

At the analysis step of results from more complicated configurations (with 3 or more impacts, with perforation, etc.), we realized how difficult it was to extract the multi-impact character and the interaction between several impacts from the experimental data, given that we had results including the interferences between impacts, without detailing each impact on its own. We therefore turned to the DPM numerical model to better understand the phenomena related to such complicated cases. To do so, we began by confirming and validating the model in a simple mono-impact case.

3.3.1. Configuration M/⌀20/15J/Ba/K/1

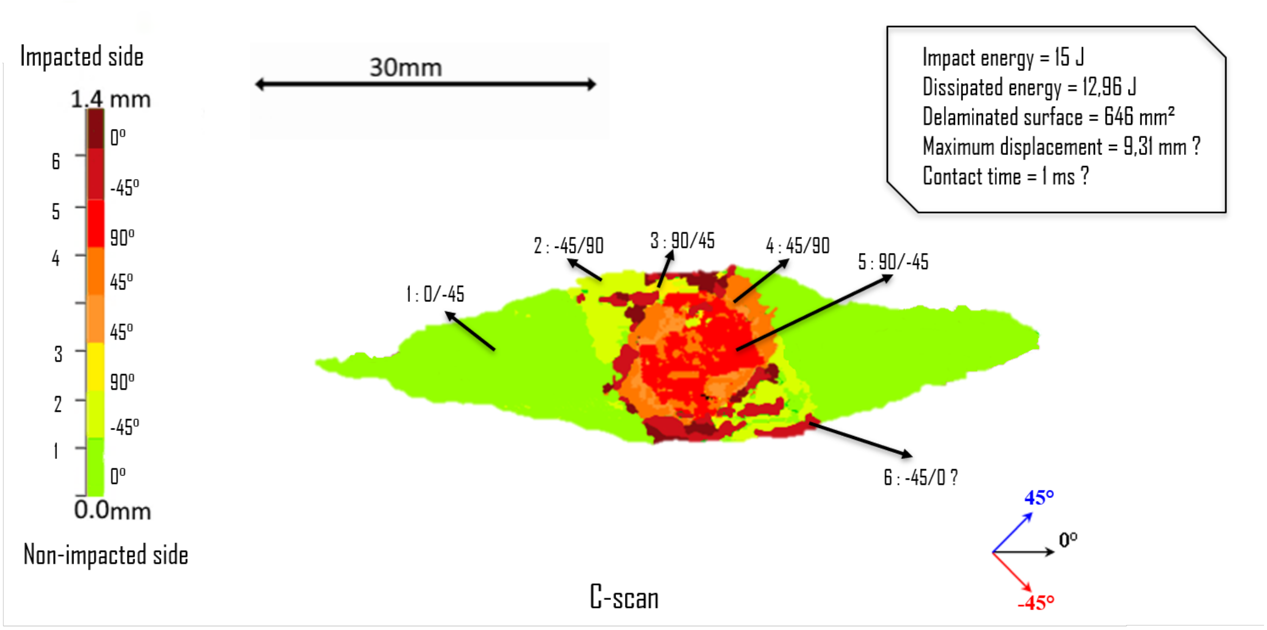

Figure 3.5 – C-scan of a mono-impact (configuration M/⌀20/15J/Ba/K/1).

In this configuration, the impact is made by a 20 mm diameter ball at an energy of 15 J (velocity of 30 m/s). The average dissipated energy per ball is 12.92 J with a standard deviation of 0.06 J, resulting in an average maximum displacement of the impactor of 8.79 mm (with a standard deviation of 0.84 mm), figure 3.5. The average impact time in the three trials is approximately one millisecond (the value of the contact time is highly dependent on the acquisition frequency of the high-speed camera, and a question mark is placed on the figure to remind that this value is not exact. A similar situation applies to the displacement measured with the HSC). These values are measured by tracking the ball trajectory with a high-speed camera. In this first case, using the C-scan method, we measure an average delaminated surface area of 653 mm^2 with a standard deviation of 32 mm^2. We can distinguish the different interfaces and orientations of the delamination through the thickness.

Clearly, the area under the impactor is in compression, and the delaminated surface is due to the separation of the "inferior" ply in the direction of impact. The delamination direction is then given by the direction of the "inferior" ply. This same principle is repeated for the different interfaces. The figure shows the first interface between the 0° and -45° plies, followed by the second interface between the -45° and 90° plies, and so on. Between the two 45° plies, there is no delaminated surface, and we can even consider these two plies as a single one (as is the case with the numerical model). Finally, we have 6 well-identified interfaces. On the other hand, the closer we get to the impacted side, the more the elements are damaged and the more it is difficult for the sound wave to penetrate the plate, so it is harder to distinguish the delaminated surfaces under the impactor. In the figure, we doubt about interface 6, as it is possible that what we are visualizing on this C-scan is just a signal noise from the impacted surface, as it is difficult to find a larger delaminated surface under the impactor then interface 1 (as this surface is under compression, it will not tend to delaminate, but we may instead have matrix cracking and fiber breaks that further impede delamination propagation). Find more details on the shape and projected surface of a delamination in the configuration M/⌀20/15J/Ba/J/1.

Next, we present the DPM model (figure 3.6), the model adjustments (figure 3.8) and a comparison of numerical and experimental results (figure 3.12). Initially developed for simulating impacts on composite structures, this model enables the observation of various types of damage, including delamination, matrix cracks, and fiber breaks.

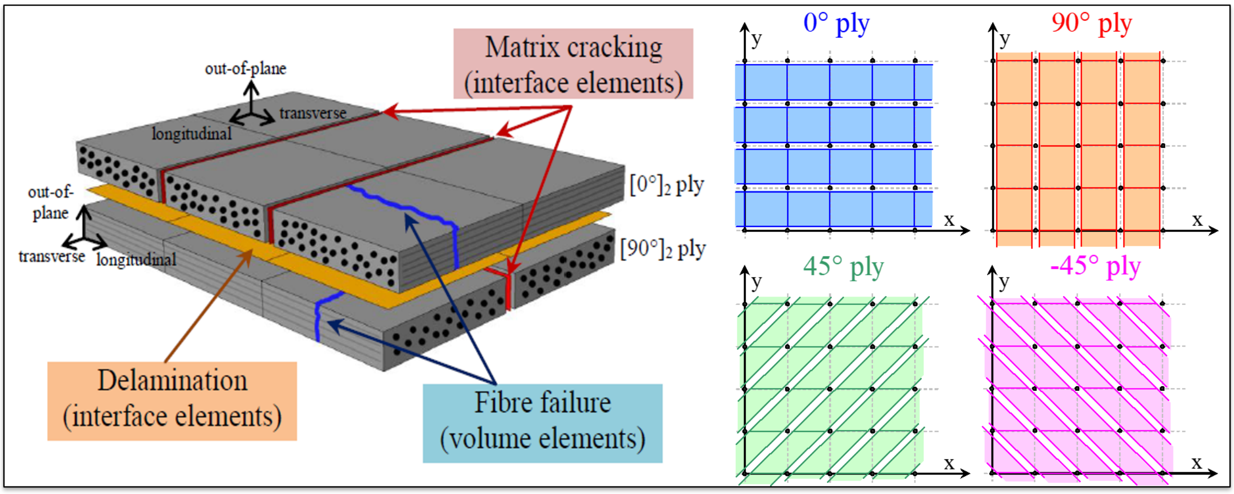

Figure 3.6 – DPM priciple and the 4 mesh types of 0°, 90°, 45° and -45° plies (79).

The Discrete Ply Model (DPM) is developed by Bouvet et al. (79). The DPM is a model designed at the mesoscale level (scale of the ply), see figure 3.6. The plies are divided into strips of volume elements. Cohesive interface elements with zero thickness are placed between the plies to account for delamination. Additional interface elements are used between the strips, along the length of the ply, to represent matrix cracking. The coupling of inter/intra-laminar damage is automatically accounted for by the model. In addition, coupling is ensured between the intra and inter-ply damages and information exchange between delamination and volume elements for fiber breakage, and between matrix cracking and volume elements for matrix cracks. The DPM considers also the discontinuity caused by shear matrix cracks primarily induced by three stress components (the mesh of each layer represent the material's orthotropic properties to facilitate the formation of these cracks), see figure 3.7(a). To ensure proper representation of crack directions (even if inclined directions are not accurately represented to maintain simplicity), the ply is divided into small strips along the longitudinal direction, with one volume element in width and thickness, figure 3.7(d). In our case, the ply thickness (0.175 mm) is small compared to the total laminate thickness (1.4 mm), this approximation seems to be reasonable, it also justifies the use of a single finite element in the ply thickness. These strips are then connected using interface elements of zero thickness. In 3.7(b) and 3.7(c), a schematic representation of delamination scenario is provided. However, this scenario initiates with the development of matrix cracks within the impact zone located below the impactor. These cracks, oriented transversely (in the (l, t) plane, where l represents the longitudinal or fiber direction and t represents the transverse direction), progressively propagate along the fiber direction during the loading process. Consequently, within each ply, a strip comprising fibers and resin becomes detached and slides in the normal direction of that ply (z). This detached strip generates a region of tensile stress between two successive plies, making it susceptible to inducing delamination within this region.

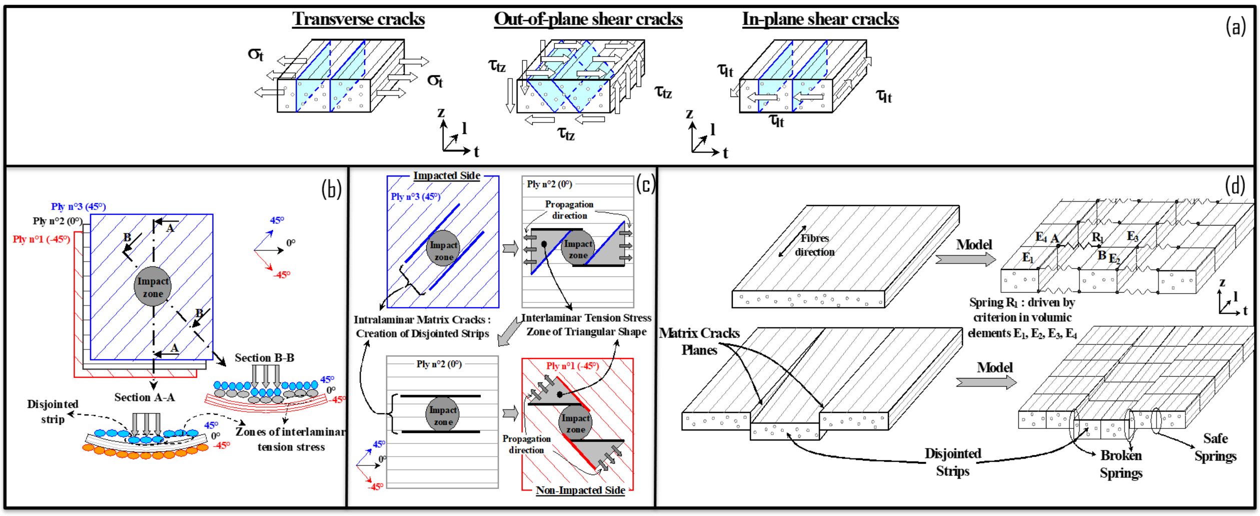

Figure 3.7 – Functional principle of the elements : (a) The three types of matrix cracks inner the ply, (b) formation mechanism of delaminations, (c) interface tension stress zones, (d) model of the ply (79).

The aim of the DPM is to simulate different failure modes of composites as schematized in figure 3.6 by a complex 3D mesh following the orientation of each ply. The damage is modelled as follows :

- Fiber failure is taken into consideration as a continuum damage inside the volume and is calculated via the sum on the 8 integration points of the element with a bilinear material law (equation 3.1) which considers the crack surface energy.

$$\int_V \left(\int_0^{\epsilon_1} \sigma_l d\epsilon_l\right) \cdot dV = S \cdot G_{ft/c} \tag{3.1}$$

With V and S being the element volume and section, G_{ft} represents the critical strain energy release rate in the opening mode into the fiber direction for the tensile case, and G_{fc} for the compressive case. Moreover, σ_l and ϵ_l denote the longitudinal stress and strain, respectively, while ϵ_1 represents the strain at the total degradation of fiber stiffness.

When the strain threshold is achieved on one of the 8 integration points (and taking into account the longitudinal strain extrapolation according to the out-of-plane direction) in tensile or compressive fiber failure, respectively ϵ_{0t} and ϵ_{0c}, a damage variable is used to apply a linear decrease in the calculation of the stress. Stresses are determined from the damaged orthotropic elastic stiffness matrix. Moreover, in compression, we take into consideration a plastic behavior and a crushing stress σ_0 (129).

— Delamination is taken into account by using interface elements between consecutive plies (figure 3.6). Damage in delamination interface elements is managed by energy dissipation of fracture mechanisms. The delamination criterion is a linear coupling of three modes : the opening mode I and the transversal shear modes II and III. Mode II and III are not distinguished here. The criterion uses a linear law of mixed-mode delamination propagation with energy release in each mode (equation 3.2). λ_{comp} is the compression reinforcement coefficient which enables to take into account the positive effect of the out-of-plane compressive stress on the shear fracture toughness. σ_{z^-} is the negative value of the stress according to z-direction.

$$\frac{G_{\mathrm{I}}}{G_{\mathrm{Ic}}} + \frac{G_{\mathrm{II}} + G_{\mathrm{III}}}{G_{\mathrm{IIc}}\left(1 - \lambda_{\mathrm{comp}}\sigma_{\mathrm{z}}^-\right)} \tag{3.2}$$

— Matrix cracking is considered with interface elements between two juxtaposed volume elements, as illustrated in figure 3.6. The damage in matrix cracking interface elements is managed by Hashin's failure criterion, calculated in neighboring volume elements (equation 3.3).

$$\left(\frac{\sigma_t^+}{\sigma_t^f}\right)^2 + \frac{\tau_{lt}^2 + \tau_{tz}^2}{(\tau_{lt}^f \cdot \left(1 - \lambda_{\mathrm{comp}}\sigma_{\mathrm{t}}^-\right))^2} \leq 1 \tag{3.3}$$

Where (l, t, z) are respectively for the longitudinal, transverse, and out-of-plane directions, and σ_t^f and τ_{lt}^f represent the transverse and the shear failure stresses, respectively. σ_t^+ is σ_t if positive and 0 otherwise and σ_{t}^- is the negative value of σ_{t}. λ_{comp} enables to take into account the positive effect of the transverse compressive stress on the shear failure.

The execution of explicit calculation code of Abaqus involves a mesh generator coded in Fortran used to create the set of nodes and elements for the simulation. Then, the mesh is inserted into an input file for Abaqus (input file), which contains material data, boundary conditions, and the definition of different calculation steps. Finally, a user-defined material law in Abaqus (VUMAT) is coded in Fortran to incorporate behavior laws for each damage phenomenon. The calculation is then launched from the CALMIP platform (www.calmip.univ-toulouse.fr), which provides excellent computing resources, 180 cores on 5 nodes were used to perform these calculations. For example, a case with a duration of 2 ms (configuration Si/⌀20/30J/T/N/4) is calculated over 30 h on 5 nodes and comprises around 5 million elements and 20 million degrees of freedom.

To ensure that information is exchanged between neighboring elements, these elements must be in the same CPU. By using 5 nodes in our case, we have certainly saved computing time, but elements that do not belong to the same CPU do not communicate. On the other hand, the 8 Gauss points of the same element are necessarily in the same CPU, as Abaqus doesn't split an element into two.

One of the main adjustments made to the DPM during this work was the removal of the delamination and matrix cracking elements (when damaged) to better simulate plate perforation; these elements are removed and the model managed the general contact (option all exterior of Abaqus (130)). However, this causes problems in the z-direction, as the elements are small, when delamination is removed, the model has to manage contact on very small parts, and this abrupt removal poses a problem when there are too many distorted elements (at 30 J, for example), For this reason, we do not remove elements in these configurations, as otherwise excessive distortions may occur. For these same configurations, where the elements are too distorted, we reduce the direct user control from 10^{-8} s to 0.5×10^{-8} s or even less, if necessary. The critical time step Δt_c is calculated using formula 3.5. It is shown that the time step must satisfy the condition 3.4 (32).

$$\Delta t < \Delta t_c \quad \text{where} \quad \Delta t_c = \frac{2}{\omega^{L_c}} \tag{3.4}$$

This implies that the time step is limited by a critical time step, which is related to the highest natural frequency of the discretized structure, ω^{L_c}. It is shown that this frequency is bounded by the natural frequency of the most critical element in the mesh, which depends on the characteristic size of that element denoted as L_c, and the wave velocity in that element denoted as c (approximately equal to $\sqrt{\frac{E}{\rho}}$, where E is the elastic modulus and ρ is the density).

Thus, we have :

$$\Delta t \lesssim \eta \cdot \frac{L_c}{c} \tag{3.5}$$

where η is a safety coefficient for stability.

When two elements are stacked one on top of the other, they are normally held together by a delamination element (which is completely damaged in the central zone, under the impactor). If these elements are not removed, the contact between two consecutive plies will be managed by the compression in the delamination element. However, if the delamination element is removed, the contact will no longer be governed by delamination but by the general contact. Therefore, the choice between the two options leads to a shift from one phenomenon to another, which is expected to be nearly similar (although friction is not taken into account by delamination but by general contact) in simple cases like this configuration (figure 3.9) but will significantly alter the behavior in more complex configurations (such as perforation at 30 J or with a 10 mm ball at 15 J but at a velocity of 87 m/s, involving multiple simultaneous impacts, etc.).

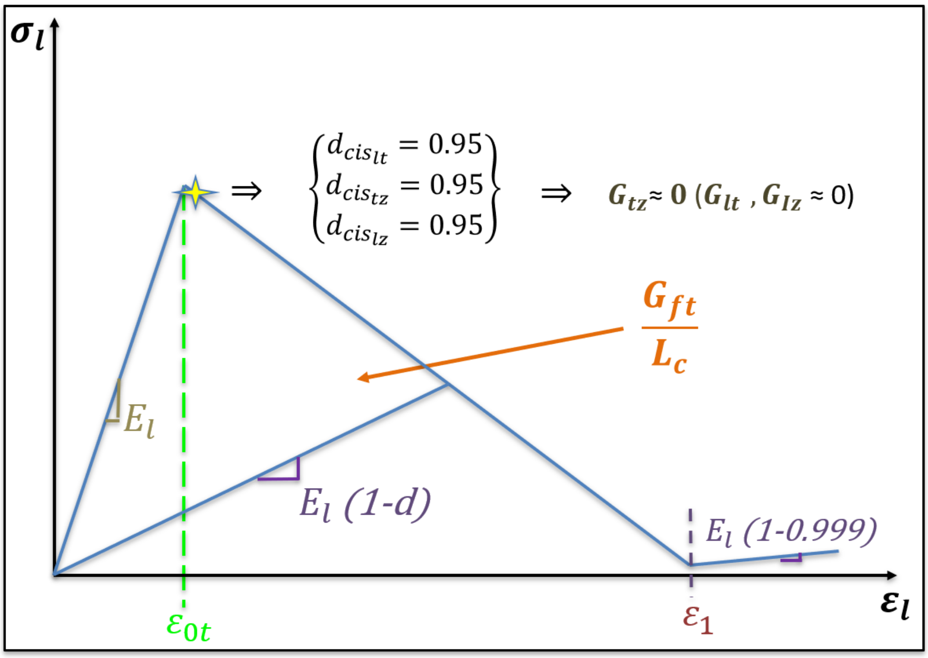

Figure 3.8 – Traction-separation law defined for single loading.

The significant difference between these two solutions is that the contact forces are no longer localized in the same location and that friction is not taken into account by delamination but by general contact. In the case of a delamination element, it only transmits forces where there are nodes, but it is not the case for general contact; delamination transmits one force between two nodes, whereas general contact transmits one force between a node and a surface (more precisely, on all four nodes of the surface).

It is obvious that after deleting these elements we have to manage the contact between the plate and the various elements, which is expensive in terms of computation. We note that the error between the total delaminated area predicted numerically and that obtained experimentally is reduced from 19% to almost 6% when removing elements, figure 3.9.

Dealing with the fiber failure, as soon as damage initiation takes place, we immediately set the shear damage variables ($d_{cis_{lt}}$, $d_{cis_{tz}}$, and $d_{cis_{lz}}$) to 0.95 (no further damage is applied to avoid excessive distortion), see figure 3.8. We consider this approach to be more physically accurate, since an element loses its shear stiffness as soon as it starts to break. In contrast, the current laws gradually reduce stress in the l-direction by multiplying it by $(1-d)$ to dissipate energy. Fiber damage is controlled on average over the 8 Gauss points, our solution localizes the damage and provides a much more realistic representation of real-life scenarios.

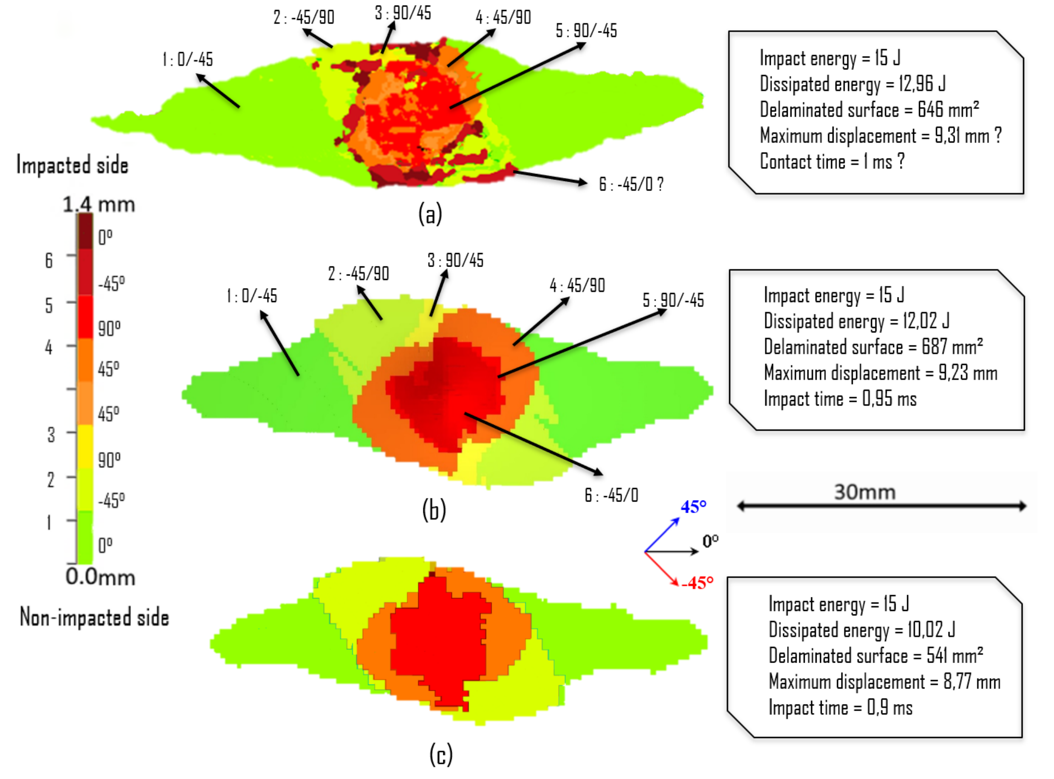

Impact energy = 15 J
Dissipated energy = 12,96 J
Delaminated surface = 646 mm²
Maximum displacement = 9,31 mm ?
Contact time = 1 ms ?

Impact energy = 15 J
Dissipated energy = 12,02 J
Delaminated surface = 687 mm²
Maximum displacement = 9,23 mm
Impact time = 0,95 ms

Impact energy = 15 J
Dissipated energy = 10,02 J
Delaminated surface = 541 mm²
Maximum displacement = 8,77 mm
Impact time = 0,9 ms

Figure 3.9 – Comparison of experimental (a) and numerical result (b,c) : (a) C-scan, (b) with interface suppression and (c) without interface suppression (configuration M/⌀20/15J/Ba/K/1).

From a numerical perspective, the energy dissipated by the ball is 12.02 J, with a maximum displacement of the impactor of 9.23 mm and an impact time of 0.95 ms. The projected delaminated surface area is 687 mm^2. The average error in the delaminated surface area is almost 6% (figure 3.9 and figure 3.5). We also observe a compression zone between the last ply and the penultimate ply beneath the impactor, as well as a tension zone between these plies away from the impactor (figure 3.10). This explains why the most delaminated surface area is between the last and penultimate ply. We find the same interfaces and orientations of delamination within the thickness as those obtained experimentally (figure 3.9). It is logical that the delaminated surface in figure 3.9(b) is smaller than 3.9(a), because as friction is added, it limits shearing forces and thus reduces damage.

Subsequently, this numerical model helped us to refine our method of determining impact times (reprocessing the videos from the high-speed camera for greater accuracy). The model also showed us that we should have placed the displacement sensors

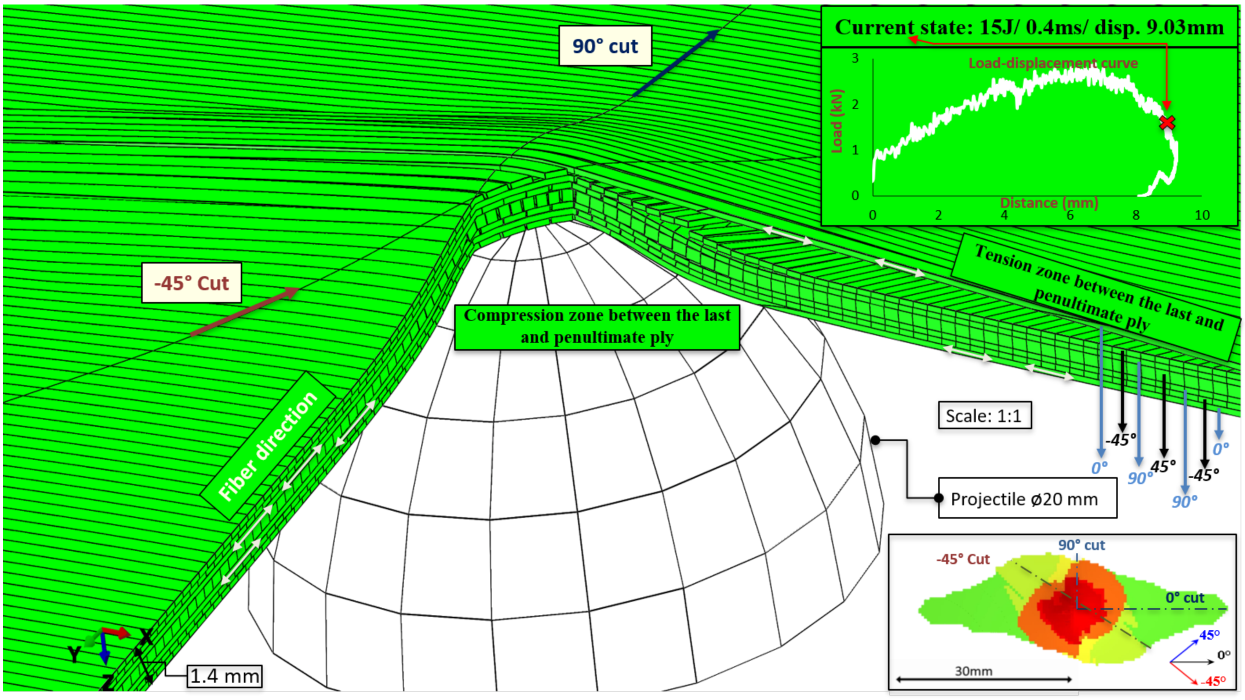

Figure 3.10 – Multi-cut view, creation of delamination (DPM).

exactly behind the point of impact, to track the displacement of each impactor (as this is the only way to know the impact of the plate displacement in the impact zone, in the case of multiple impacts, see configuration Si/⌀20/15J/Ba/N/5 for more details), especially as the interaction between several impacts far from the point of impact is increasingly complicated. Measurements far from the points of impact are difficult to interpret, since they result from several impactors and not one in particular. Then, measurements of impact times and maximum plate displacement or applied forces will certainly be wrong far from the point of impact, as the wave is delayed in arriving at a distant point. The model also helps to accurately track damage formation ; figure 3.11 shows the formation of delamination as a function of time, we explain this mechanism in more detail in the configuration M/⌀20/15J/Ba/J/1.

To gain a comprehensive experimental understanding of damage formation mechanisms, it is crucial to employ an in-situ monitoring method. Traditional approaches, such as post-mortem analysis using C-scans, only provide a retrospective perspective on the damage. In order to overcome this limitation, the implementation of an in-situ monitoring technique becomes imperative. By utilizing real-time observation and data acquisition during the damage process, we can capture the dynamic evolution and intricate details of the damage mechanisms as they unfold. This enables us to gather valuable insights that would otherwise be missed with post-mortem analysis alone. In-situ monitoring offers a more holistic and accurate assessment of the damage formation, facilitating a deeper understanding of the underlying mechanisms and leading to more effective mitigation strategies.

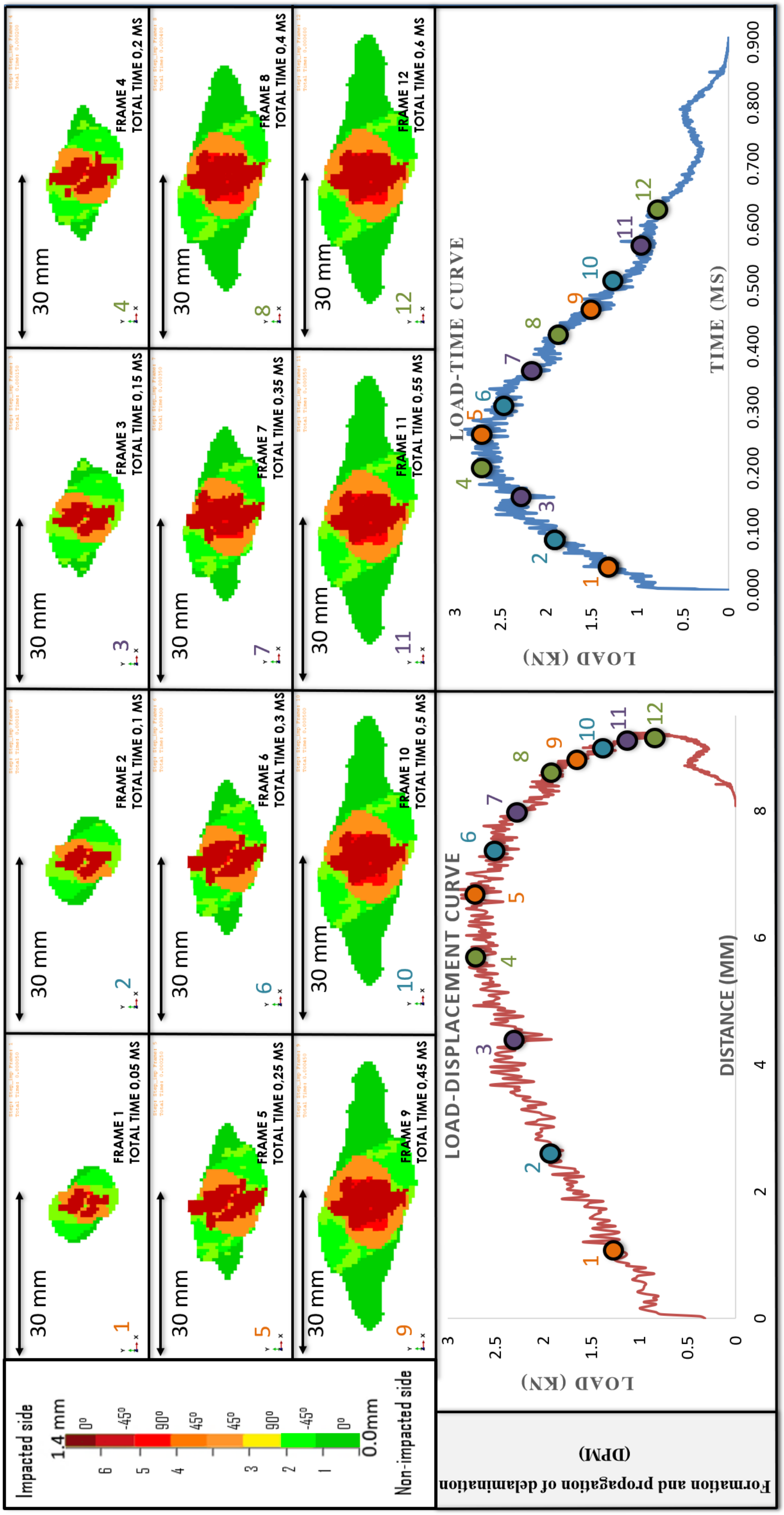

Figure 3.11 – Formation and propagation of delamination (DPM), M/⌀20/15J/Ba/K/1.

The in-situ damage mechanisms of impacts were not being monitored, and the experimental perspective was limited to post-mortem analysis only. To overcome this problem, high-speed infrared camera monitoring was introduced, and used the SVD (Singular Value Decomposition) method to process these results. SVD is a powerful mathematical technique used for matrix factorization. It decomposes a given matrix into three separate matrices : U, Σ, and V. The matrix U represents the left singular vectors, Σ is a diagonal matrix containing the singular values, and V represents the right singular vectors. It is particularly useful in dimensionality reduction, as it allows to identify the most significant patterns and features within a dataset. Defects can be detected by analyzing the singular values, which represent the relative importance of each mode of variation (a specific direction in which data may vary, represented by the eigenvectors (singular vectors) of the data matrix). Large singular values indicate significant variations, while small singular values correspond to regions of low variation. By thresholding the singular values, we can identify and locate areas in the film that deviate from the expected patterns, thus enabling effective defect detection and characterization.

In order to process the infrared thermography film, which consists of a sequence of n images of real temperature values of size $l \times L = m$ pixels, we transform each image into a vector by concatenating its columns. By doing the same for each of the n images, we construct the matrix A of dimensions $m \times n$, where the i^{th} column contains the information of the i^{th} image of the film.

We used a MatLab program to perform the following key steps :

- Load the first image and its corresponding time from the thermal film.
- Allow the user to choose a region of interest on the image.
- Create a database containing the selected images and their corresponding times.
- Perform Principal Component Analysis (PCA) on the images.
- Normalize the images and perform Singular Value Decomposition (SVD).
- Rearrange the columns of the principal components to obtain images.
- Calculate the weights of the principal components.
- Perform Independent Component Analysis (ICA) on the images.
- Display the resulting images obtained from ICA.

Then we need to analyze the images obtained to be able to highlight the physical character in a few ones. The figure 3.12 shows the result of this analysis on the film, we directly recognize the projected delaminated surface. Later, we also recognize vertical fiber breakage at 90° and matrix cracking at -45° (it is important to constantly point out that the camera is positioned behind the plate, non impacted face, and then a symmetry of the image versus the 0° direction is obtained, as in figure 3.12). Figure 3.12 shows a perfect correlation between the C-scan and the SVD method, the main advantage of the SVD lies in the fact that the result is instantaneous and does not require the plate to be dismantled and placed in water to perform the C-scan. In the

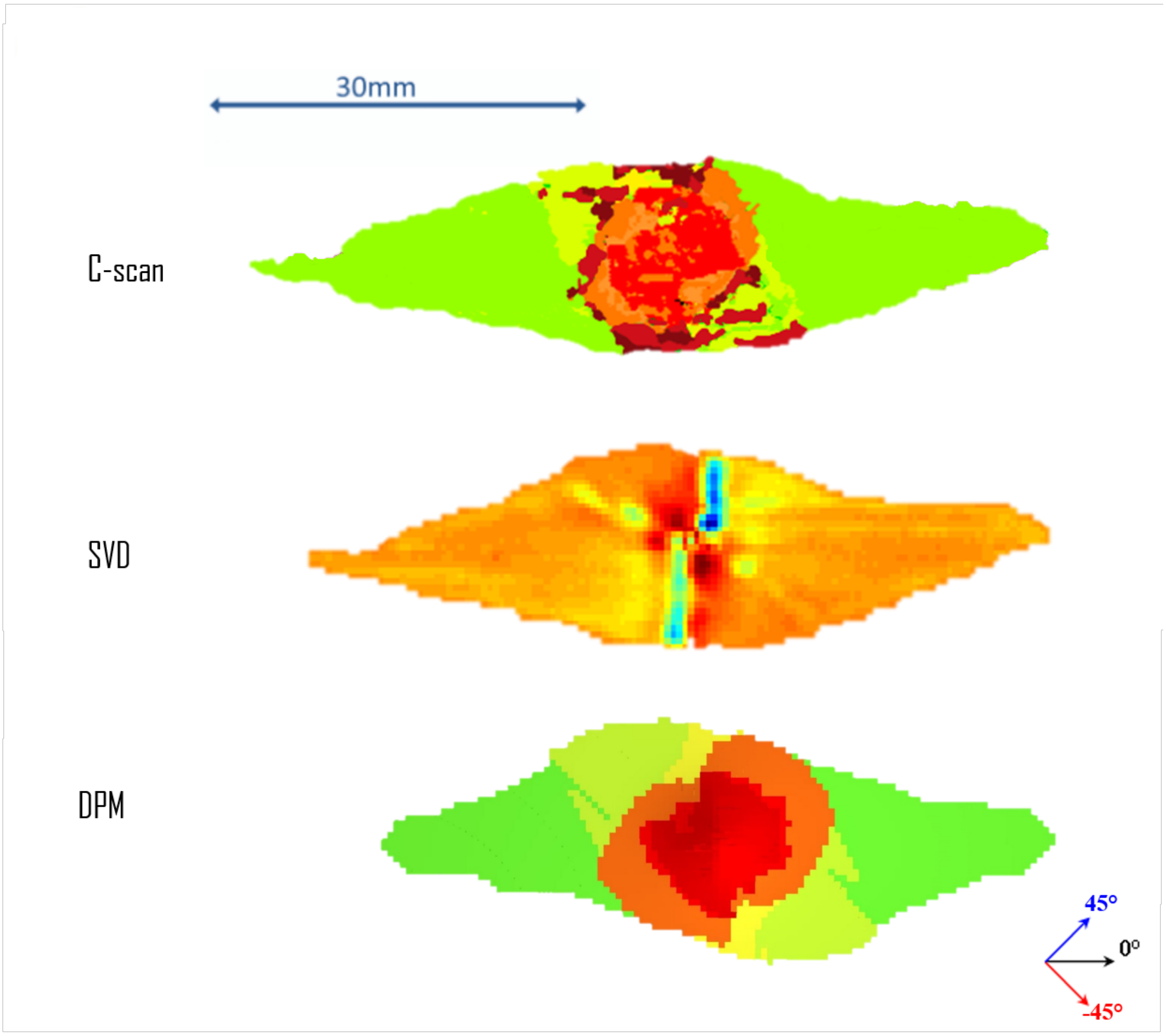

Figure 3.12 – Comparison of delaminated surface after impact obtained experimentally, by SVD analysis and numerically, M/⌀20/15J/Ba/K/1.

future, we will be looking at the benefits of using thermal monitoring in general to track impact damage in-situ. We can then, in equivalent configurations in terms of the energy involved, show only the images from the thermal films to illustrate the size of the delaminated surfaces.

By analyzing the images taken directly from the thermal film, the damage within the material can be identified. Matrix cracking and delamination occur first, followed by fiber breakage at the center of the impact and at 90°. To make sure we are dealing with fiber fracture and not just matrix cracking, we have carried out microscopic observation, see figure 3.14. In this way, we were able to recognize the breakage of fibers at -45° (in the 90° ply) and 0° (in the -45° ply), which were emerging at the surface. Looking back to the figure 3.13, the thermo-signature is used to confirm that

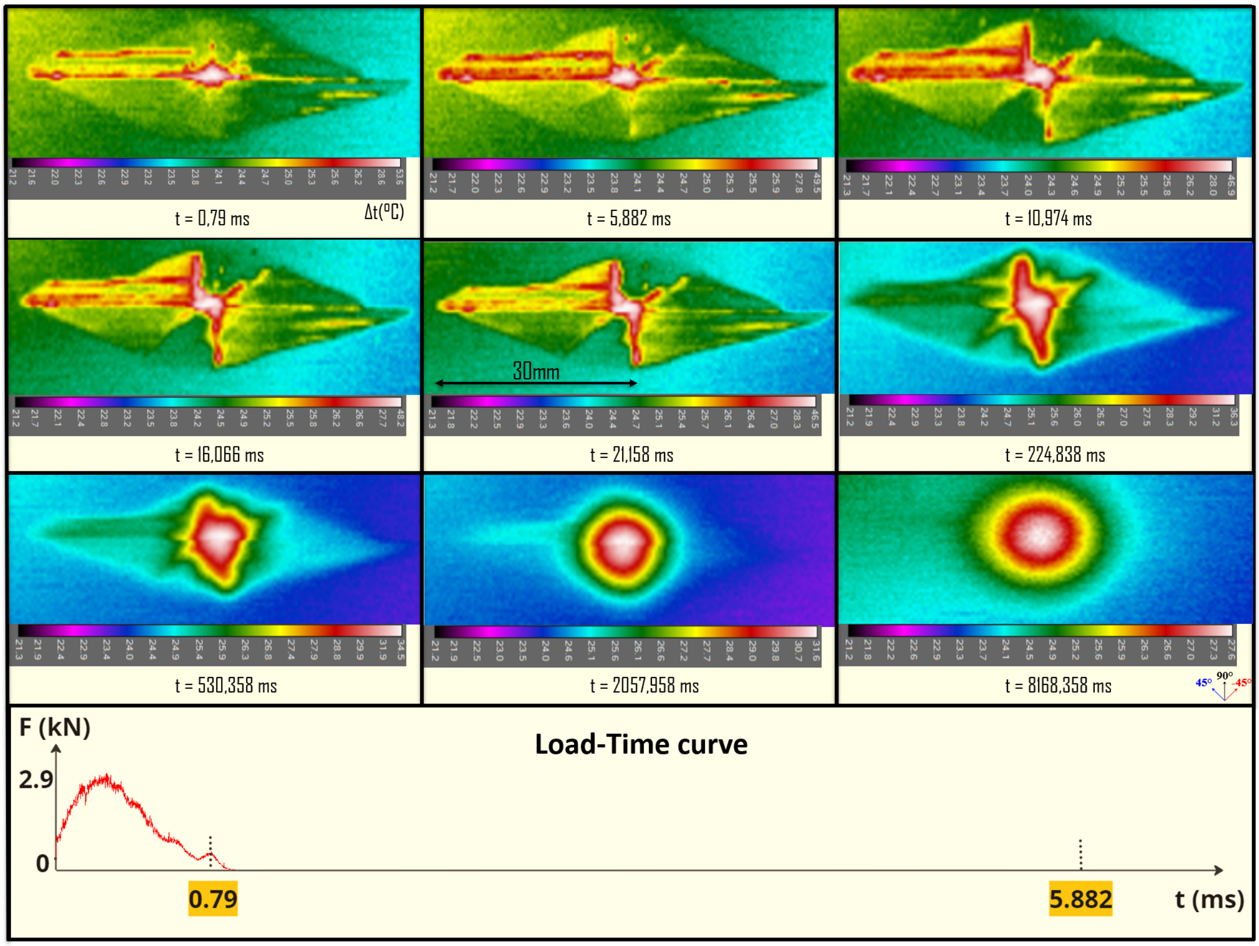

Figure 3.13 – Thermographic monitoring of impact damage.

the break at 90° is indeed a fiber break in the volume of the material. From this same figure, we have a first estimate of the diffusion time through one ply, since the fiber breakage crosses three plies in about 16 ms, the diffusion time per ply would then be of the order of a value strictly less than 5.3 ms (since fiber breakage has obviously not occurred at t = 0ms). It should be noted that this fiber break is not on the outer surface (the surface observed by the thermal camera), but rather in the volume of the plate, which explains the reduction of the thermal signature of the fiber breakage. Finally, on the figure 3.14, we have a 0° fiber breakage in the -45° ply, then a -45° fiber breakage in the 90° ply and finally a 90° fiber breakage in the 45° ply ; following the same reasoning, we expect a fiber break at -45° in the 0° ply, which we can't see with the thermal camera as the heat dissipation doesn't go through the whole thickness of the material, nevertheless this result is confirmed with the help of the microscopic observation shown in figure 3.16 (see the times corresponding to this observation in figure 3.13).

Matrix cracking in the last ply is also easily recognized between thermal images and microscopic observation. It should be noted that, during the measurements, an emmisivity of 0.92 was considered in line with the values of literature ((140), (141), (142)). Note that the camera is slightly non-perpendicular to the composite panel.

We were able to record experiments with up to 2000 Hz, depending on the recording window needed. Finally, we can also deduce the temperature evolution corresponding to each damage type. These measurements are specific to the tests in this work, and the thermal signatures obviously depend on the breaking energies involved and their position in relation to thickness, etc. In particular, because heat conduction is greater in the l-direction (the direction of the fibers, which are more conductive than other elements). :

- ΔT° Fiber breakage [8°C - 31.6°C]
- ΔT° Matrix cracking (≈ 5°C)
- ΔT° Delamination (≈ 3°C)

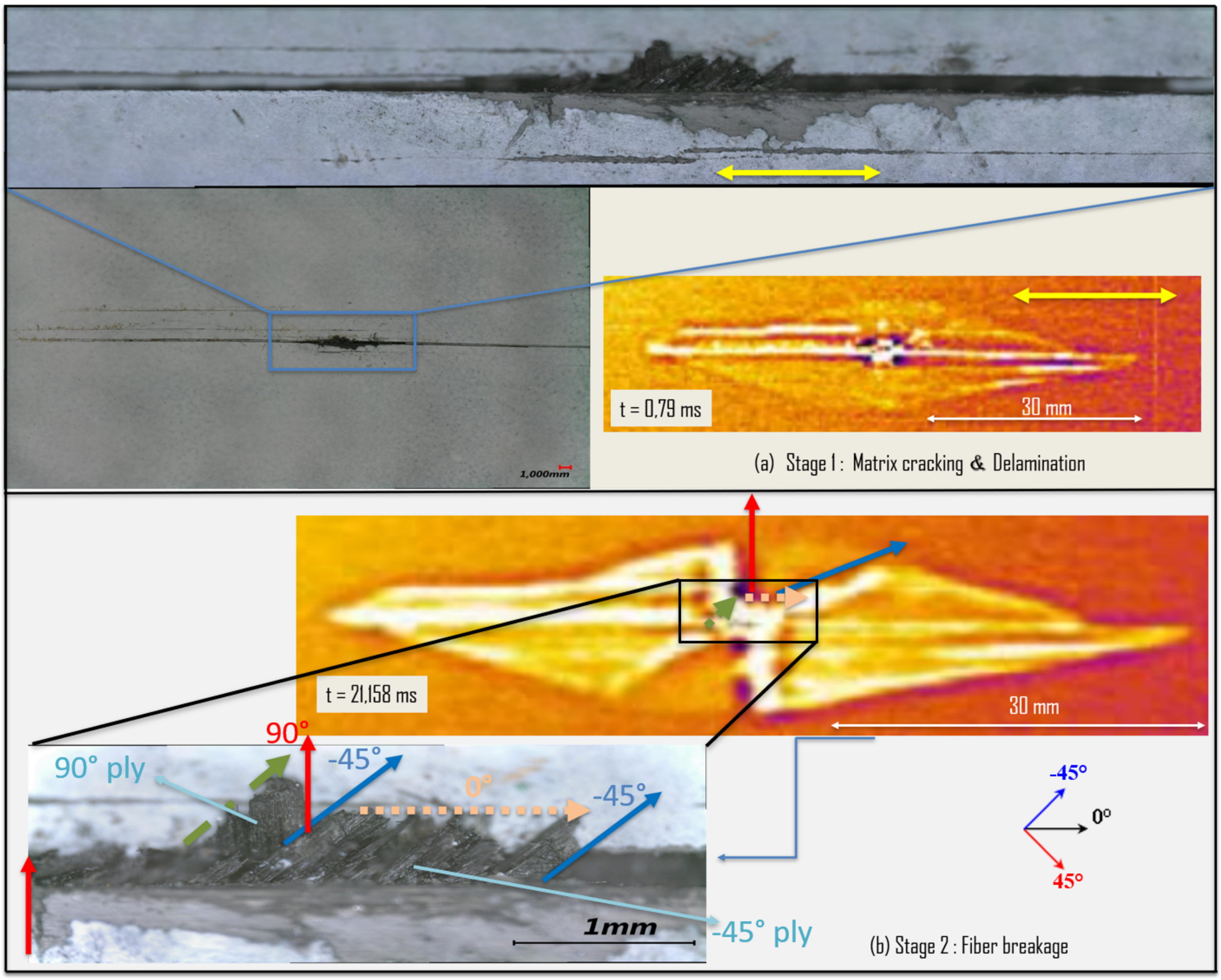

Figure 3.14 – Cross-analysis between thermography and microscopic observation.

Another way of processing the data from the high speed camera was to calculate the temperature field gradient using a Sobel filter via a Python program, see figure 3.15. It is important to note that, a Laplacian filter can also be used. From this figure, we can see that matrix cracking comes first (event 1), followed by delamination and finally fiber breakage (subsequent events). We confirm this conclusion more clearly using the numerical model in the configuration M/⌀20/15J/Ba/J/1. Indeed, the numerical model shows that cracking and delamination occur before the fibers break.

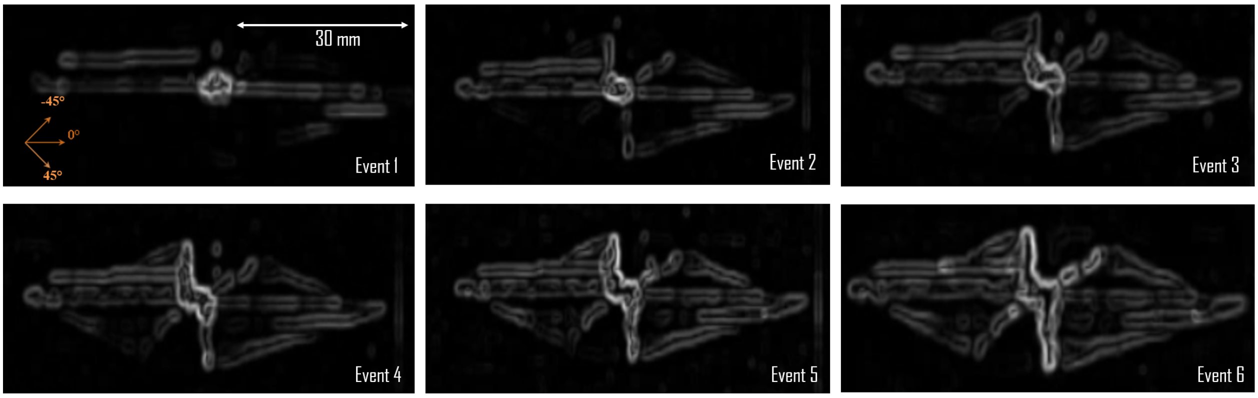

Figure 3.15 – Filtred thermal film images.

It should be noted that we do not record all the events in all the volume of the material. The figure shows fiber breaks on the impacted side, which we cannot record if the camera is on the non-impacted side, see figure 3.16. There must be a part of the thermal energy arriving on the non-impacted side, but it is small because fibre conduction is greater than the other elements, so conduction dissipation is greater in the l-direction.

We also took advantage of these thermographic films to evaluate (a preliminary evaluation only to validate the orders of magnitude) the critical strain energy release rate corresponding to matrix cracking ; figure 3.17 shows the choice of the characteristic length (L_c) used to perform the calculation. Also, we avoid the central matrix cracking, which opens up too much and can distort the calculation, as we do not just see the crack on the last ply, but also the ply above it. We also avoid making these same considerations for fiber fracture for two reasons :

1. If we consider fractures at the center of the impact, there are multiple cracks occurring at the same location, and the calculated rate will not correspond to a single fracture.
2. If we consider fractures at a 90° angle, we are not directly measuring the actual temperatures because this crack occurred within the volume of the material. The observed crack is not on the ply of surface.

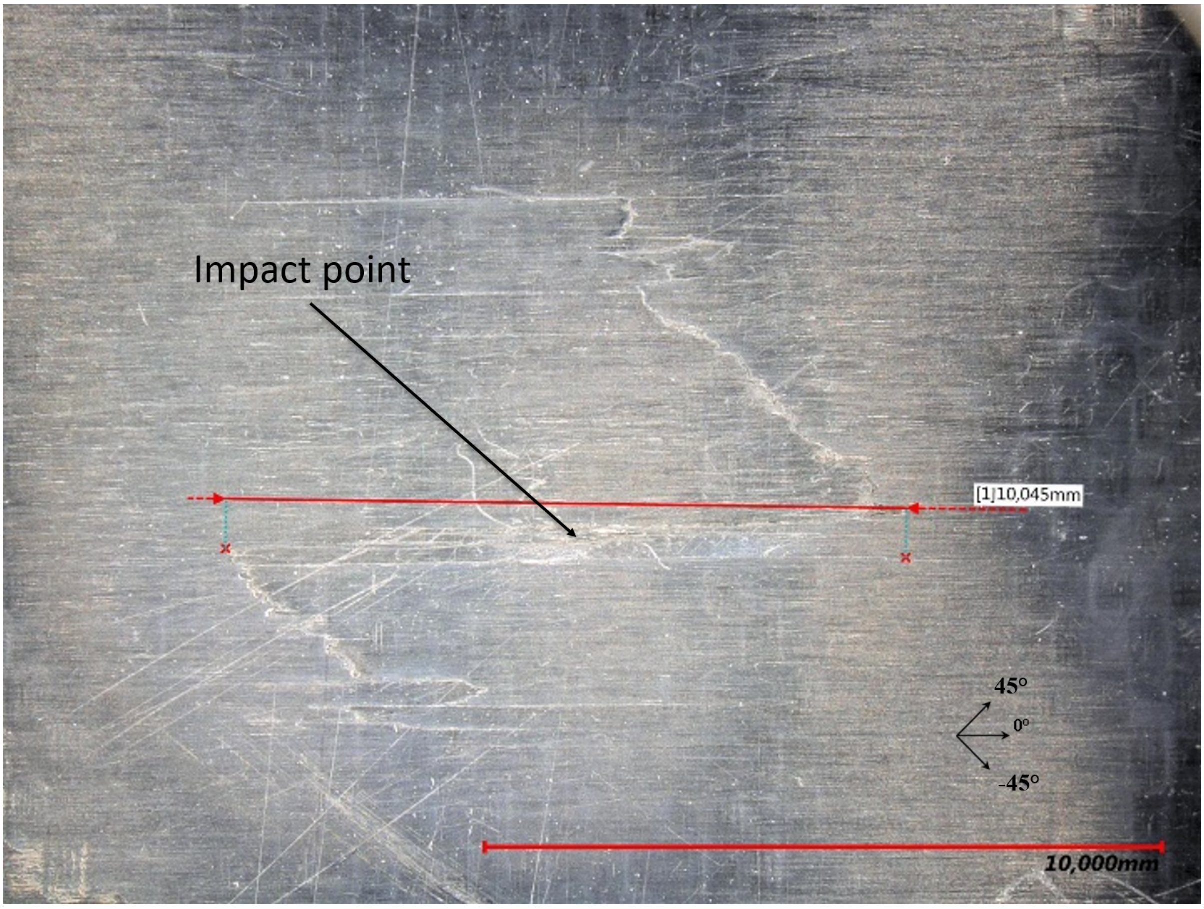

Figure 3.16 – Impact damage of the impacted side.

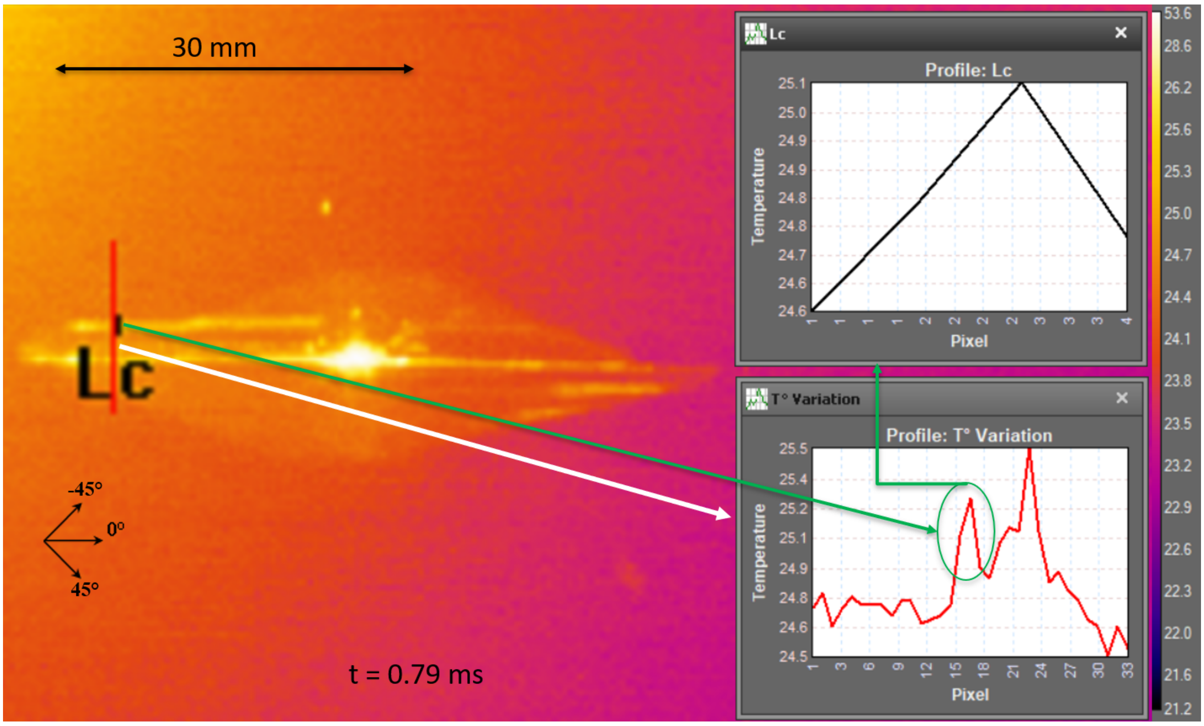

Figure 3.17 – Calculation of critical strain energy release rate.

Here is the calculation method for matrix cracking, where the area under the curve is evaluated, and 1D ply is assumed, then the energy dissipated in heat per unit area, G_c (with Taylor-Quinney coefficient β_{int}, which expresses the efficiency of the thermo-mechanical conversion, defined by Rittel (143) as the ratio of the thermal dissipation to mechanical work involved in the deformation process, generally assumed to be equal to 0.9), is directly calculated. This is a first approximation, that does not depend on time, despite a diffusion effect with thermal conduction, but the area under the curve remains the same (137) :

$$\beta_{int} \cdot G_c = \int_{L_c} \rho \cdot C_p \cdot \Delta T \cdot dL \tag{3.6}$$

$$\Longrightarrow G_c = \frac{\rho \cdot C_p \cdot \int_{L_c} \Delta T \, dL}{\beta_{\text{int}}} = 0.37 \quad kJ/m^2 \tag{3.7}$$

where ΔT is the temperature variation, L_c is the characteristic length, ρ is the density of the material, and C_p is the specific heat capacity value taken from Emeryet et al. (134). The values taken into account are summarized in the table 3.2.

Variable	Value
Density (ρ)	$1600\,\mathrm{kg\,m^{-3}}$
Specific heat capacity (C_p)	$882\,\mathrm{J\,kg^{-1}\,K^{-1}}$

Table 3.2. – Variable values for G_c estimation.

This value corresponds to known orders of magnitude, the aim here is just to have an order of magnitude to validate that this is indeed matrix cracking. For the studied material, the fracture toughness of delamination was estimated to about 0.25 and 1 kJ/m^2 in mode I and II respectively, see table 3.1. But this is just an estimate and cannot be generalized so easily.

Looking back to the numerical model, we note that the load-displacement curve obtained numerically and experimentally are very similar, see figure 3.18 and figure 3.19. It should be remembered that the experimental curve is obtained by deriving twice the ball displacement curve obtained with the high-speed camera, so all brutal events (especially dynamic phenomena due to the back-and-forth movement of elastic waves, particularly those at very high frequencies, along the thickness of the plate) are not captured. The numerical model then gives more detail about the ball-plate contact, with the various force-drop events corresponding to different damages. We can then explore the other curves obtained numerically to understand energy dissipation. The area hatched in yellow in figure 3.18 is the initial kinetic energy of impact. When the ball starts to rebound, its velocity passed through zero at the point of maximum displacement. From that moment on, the ball rebounds (one part of the energy returned to the ball), this one is hatched in green on the figure. The difference between the two (i.e. the area of the load-displacement curve) is mainly the energy dissipated by

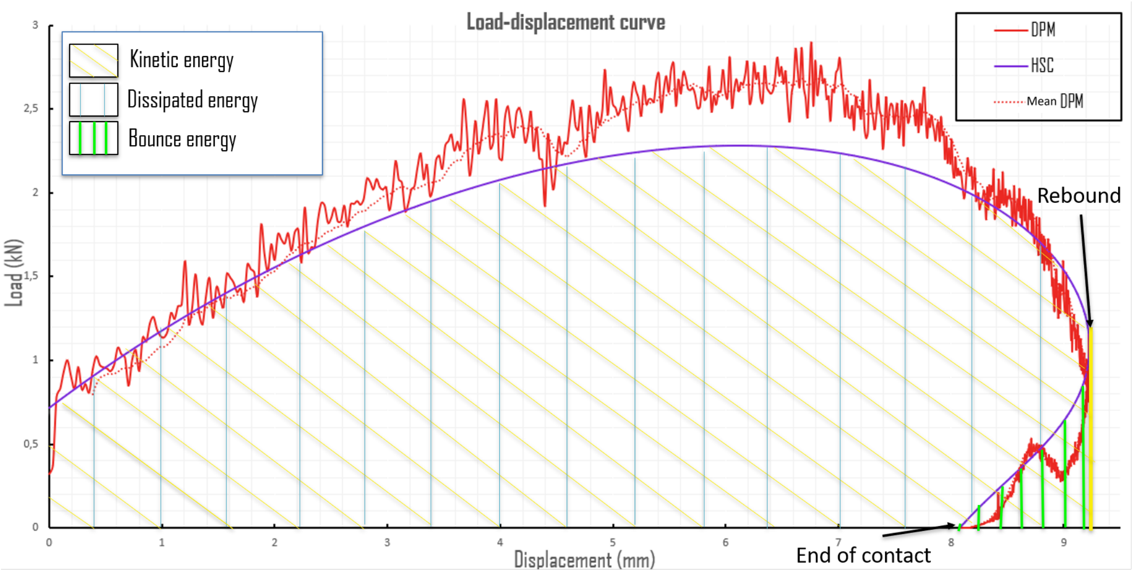

Figure 3.18 – Experimental vs. Numerical Load-Displacement curve.

plate damage, friction and viscous phenomena, plus kinetic and strain energy present in the plate at the end of the contact (blue hatching on the figure), as also shown in figure 3.31, and not only the energy dissipated in the plate. We verify that the sum of bounce energy and "dissipated energy" (between double quotes because strain and kinetic energy also exists and are not technically dissipated) is equal to the ball's kinetic energy. At the end of the impact, we observe that in this configuration less than a tenth of the kinetic energy is recovered in the ball's return.

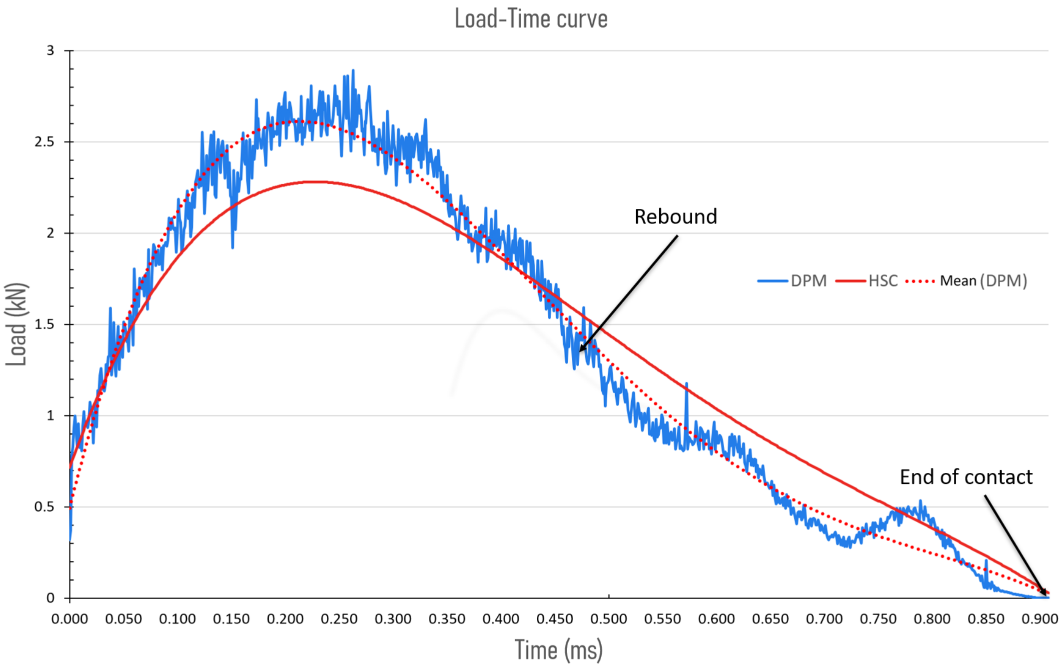

Figure 3.19 – Experimental vs. Numerical Load-Time curve.

From figure 3.20, we observe that most of the energy transferred to the plate is strain and kinetic energy (between 60 and 90% in this case, 80% on average) and the other small part consists of damage and frictional energy. The kinetic energy of the ball rebound corresponds to about 20% of the initial impact energy, which seems a little bit higher than the experiment. Finally we check that the energy balance is correct by ensuring that the sum of energies remains constant.

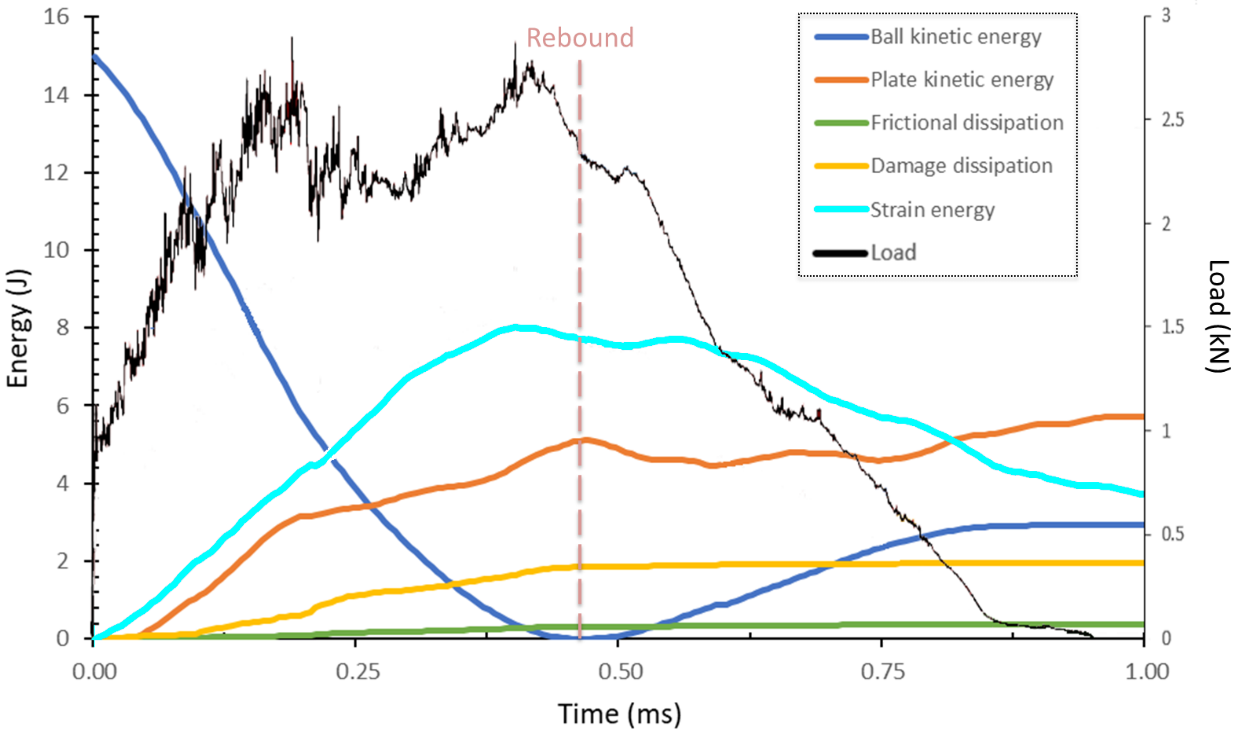

Figure 3.20 – Variation of different forms of energy during impact (DPM).

Finally, for this configuration, in order to measure the velocity of wave propagation in the plate, a series of tests was conducted before and after impact, using Piezoelectric Ceramic Copper Buzzer, protected with polyimide film tape (Kapton), to mesure the maximum velocity in different directions of the wave in the structure, see figure 4.3. During these tests, we noticed that the wave transferring in the plate before and after the impact showed a delay of the time of flight for the response signals (after impact signal is delayed), and there is an attenuation on the amplitude of the signals. For the FFT analyses, before the impact, the peak of amplitude appears at 8172 Hz with amplitude of 0.049 mV. After the impact, the peak of amplitude appears at 8372 Hz with amplitude of 0.047 mV, figure 3.21. From the limited results of few simple tests, it proves that the lamb wave is quite sensitive to the impact.This direction is an interesting perspective for this work, for the smart composite structures, if there is a transducers network inside, it will be possible to detect the location of the impact damage.

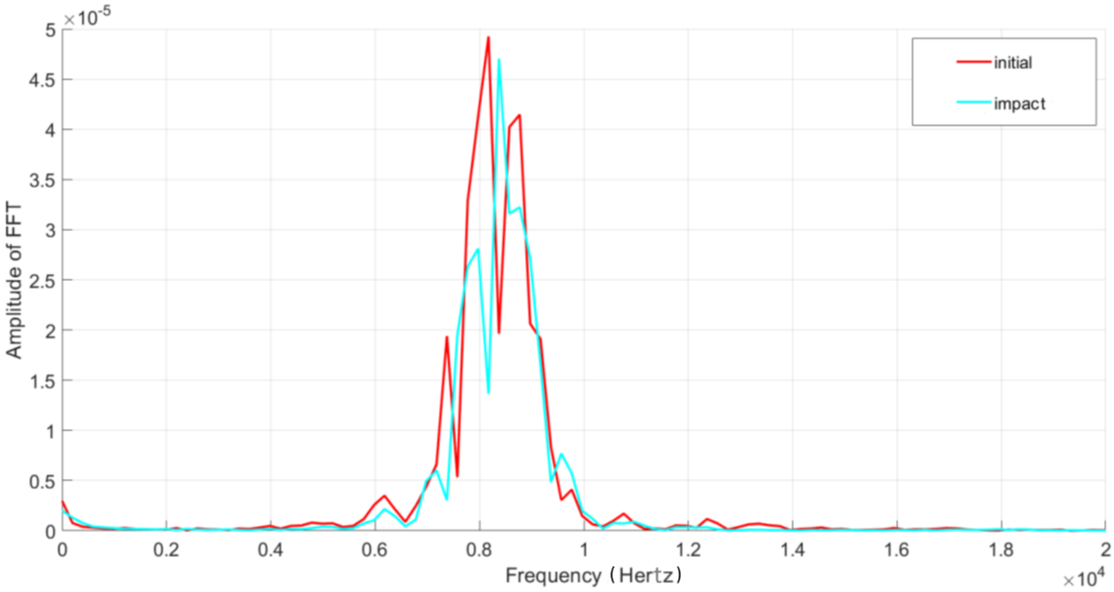

Figure 3.21 – FFT analysis of piezoelectric sensor signals before and after impact.

The aim of what has been shown in this configuration is to demonstrate the coherence between the different methods used and the robustness of the numerical model. In the following, we will not show the complete list of results obtained by the different methods in all configurations, but rather we will show the most important data per configuration that will contribute to the study of our main topic.

3.3.2. Configuration M/⌀20/15J/Ba/J/1

In the configuration M/⌀20/15J/Ba/J/1, the average dissipated energy per ball is 12.66 J with a standard deviation of 0.95 J, resulting in an average maximum displacement of the impactor of 7.52 mm (with a standard deviation of 0.73 mm). We measure an average delaminated surface area of 731 mm^2 with a standard deviation of 45 mm^2 (figure 3.22). We can distinguish the different interfaces and orientations of the delamination within the thickness. Interface 6 is not reached because of the large amount of damage under the impactor, the sound wave struggles to penetrate these areas, signal return is negligible.

From a numerical perspective, the energy dissipated by the ball is 10.56 J, with a maximum displacement of the impactor of 7.54 mm and an impact time of 0.9 ms. The projected delaminated surface area is 385 mm^2, figure 3.23, the fibers break too prematurely, slowing the propagation of delamination. We suspect that this is due to the non-inclusion of dynamic effects (strain rate for example) and the thickness extrapolation of the fiber strain failure criterion. In our one case, we take classical extrapolation coefficients of 1.366 and 0.366 (corresponding to Gauss points set at a distance of $\frac{1}{\sqrt{3}}$), which means that for opposite values of strain (i.e. for a pure bending deformation),

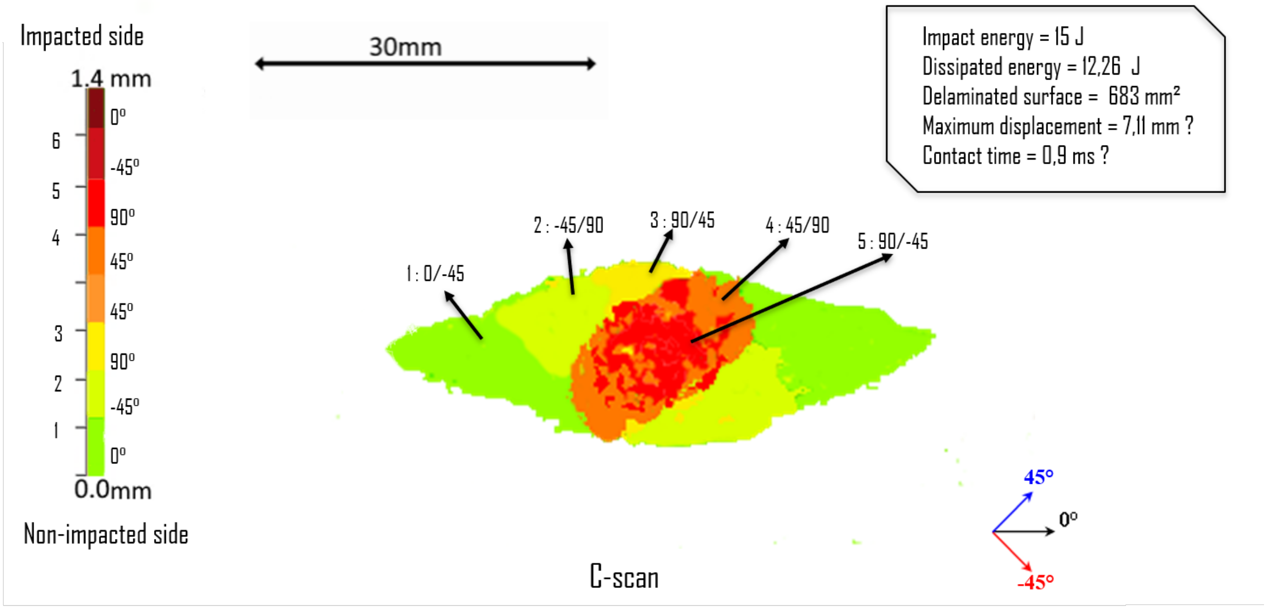

Impact energy = 15 J
Dissipated energy = 12,26 J
Delaminated surface = 683 mm²
Maximum displacement = 7,11 mm ?
Contact time = 0,9 ms ?

Figure 3.22 – C-scan of configuration M/⌀20/15J/Ba/J/1 mono-impact.

the extrapolated value would be 1.732 times greater. For example, we would expect fiber failure in a case of pure bending 1.73 times earlier in the extrapolated case than in the case without extrapolation. A more detailed study of how to extrapolate needs to be carried out.

Using the numerical model, we attempt to explain the shape of the delaminations per interface (the orientation is explained in configuration M/⌀20/15J/Ba/K/1) :

Delamination occurs as a result of matrix cracking in a ply closer to the impact (ply 2 from the non-impacted side, figure 3.24). The ply on the non-impacted side (1 in figure 3.24) then continues to propagate the delamination as it is under tension. Naturally, the direction of delamination propagation is given by the lower ply, since it is this ply that propagates delamination. At this level, we can expect delamination to take the form of a parallelogram (shown here in red 3.25a). In fact, it is the creation of matrix cracking in one ply that leads to delamination in the lower ply (relative to the direction of impact). This order (matrix cracking followed by delamination, is perfectly in line with the thermal camera results presented in configuration M/⌀20/15J/Ba/K/1).
In the direction perpendicular to the fibers of ply 1 at 0°, it is not this same ply that controls the direction of delamination, as matrix cracking in this same ply will stop it. On the other hand, it is the ply closest to the impacted face (ply 2 at -45° in this case, figure 3.24) which controls delamination as a result of the tensile stress applied to it in its fiber direction, and which will also control the direction of delamination in respect of the other interface closest to the impacted face, and so on. It is an iterative process between plies. Although it will not always be the last ply, in the case of a very high ply number for example, it is rather the first matrix crack farthest from the

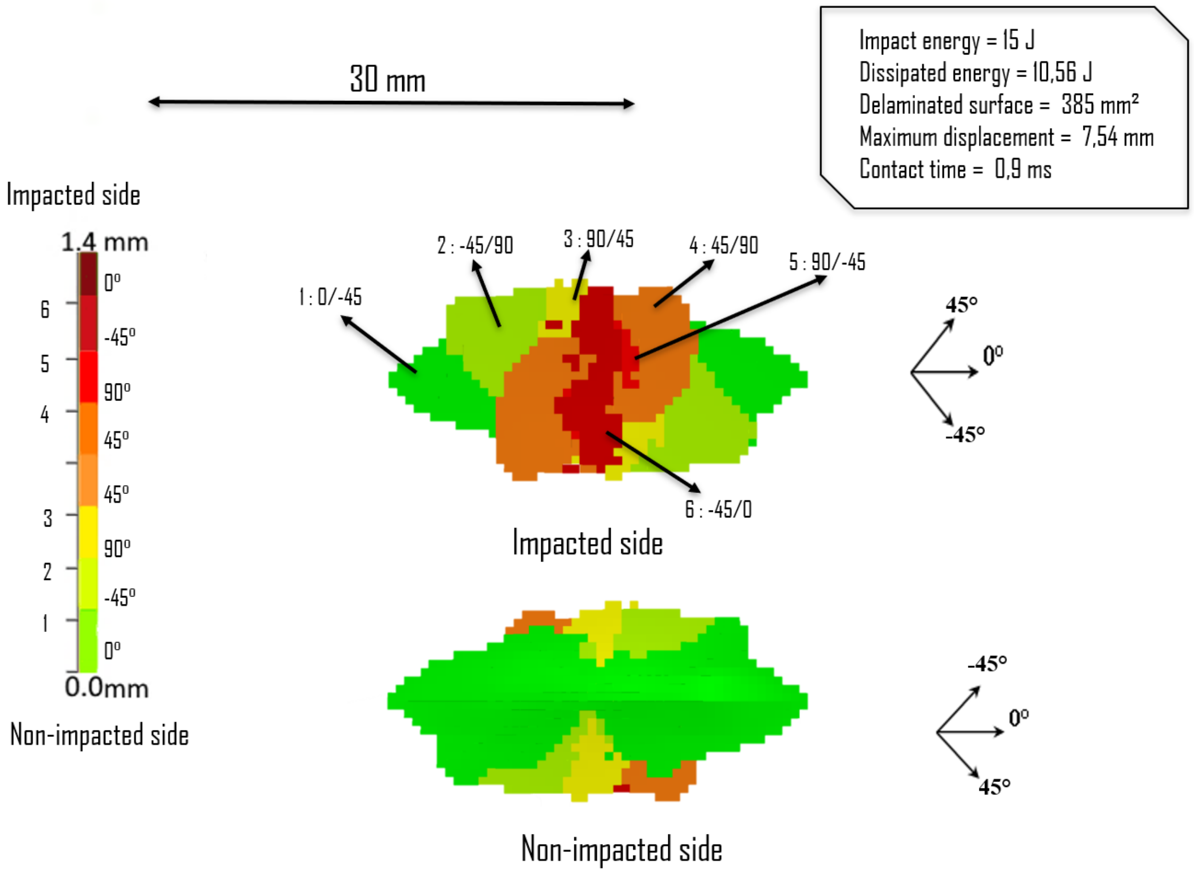

Figure 3.23 – DPM C-scan of configuration M/⌀20/15J/Ba/J/1 mono-impact.

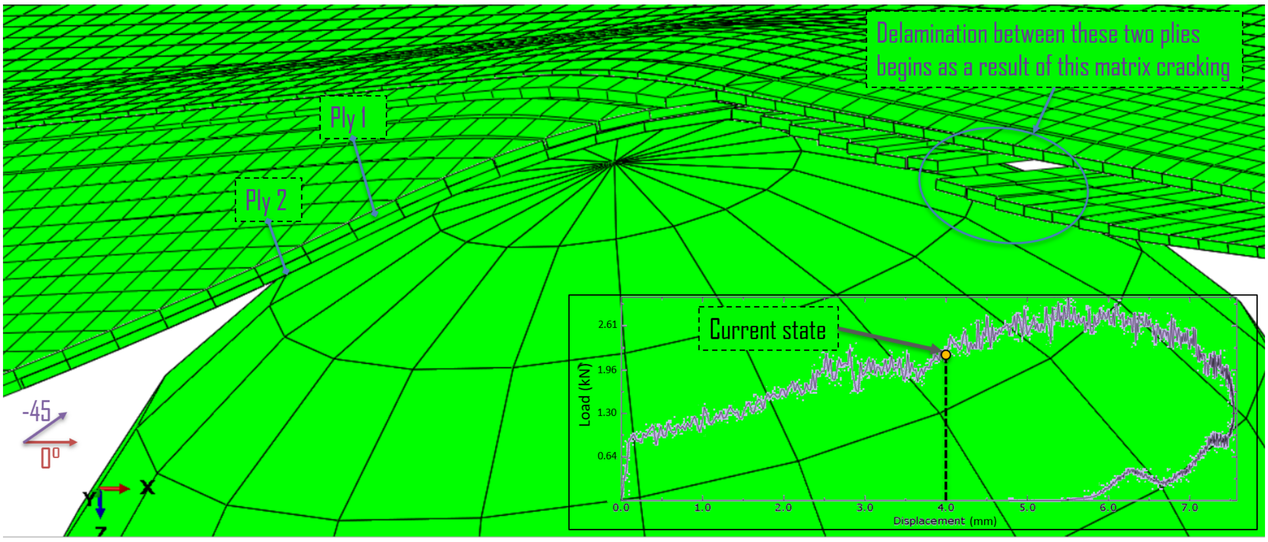

Figure 3.24 – Role of matrix cracking in delamination initiation.

impactor that will take place and trigger the process (or maximum out-of-plane shear at mid-thickness). We have already explained why the interface between the last and penultimate ply is the longest. Consequently, since the 0° ply is going to delaminate, the direction of the overall delamination shape is given by the direction of the fibers in the ply below the most delaminated interface. Figure 3.7b&c show that matrix cracks, occurring in the (l, t) plane, propagate along the fiber direction during loading. As a result, within each layer, a strip consisting of fibers and resin becomes disjointed and slides in the z-direction (normal direction of the layer). This disjointed strip creates an interlaminar zone of tension stress between two consecutive plies, making it susceptible to delamination in that area. Figure 3.7(c) presents a schematic representation of this scenario using a stacking sequence of [-45°, 0°, 45°], where -45° denotes the lower layer and 45° represents the upper layer, the disjointed strips of the first two layers are depicted, illustrating the interlaminar zone of tension stress. This zone, bounded by the disjointed strips of the adjacent layers, exhibits a triangular shape with increasing size from the impacted side to the non-impacted side. Figure 3.7(b) shows the interlaminar zones of tensile stress between the -45°/0° and 0°/45° layers.

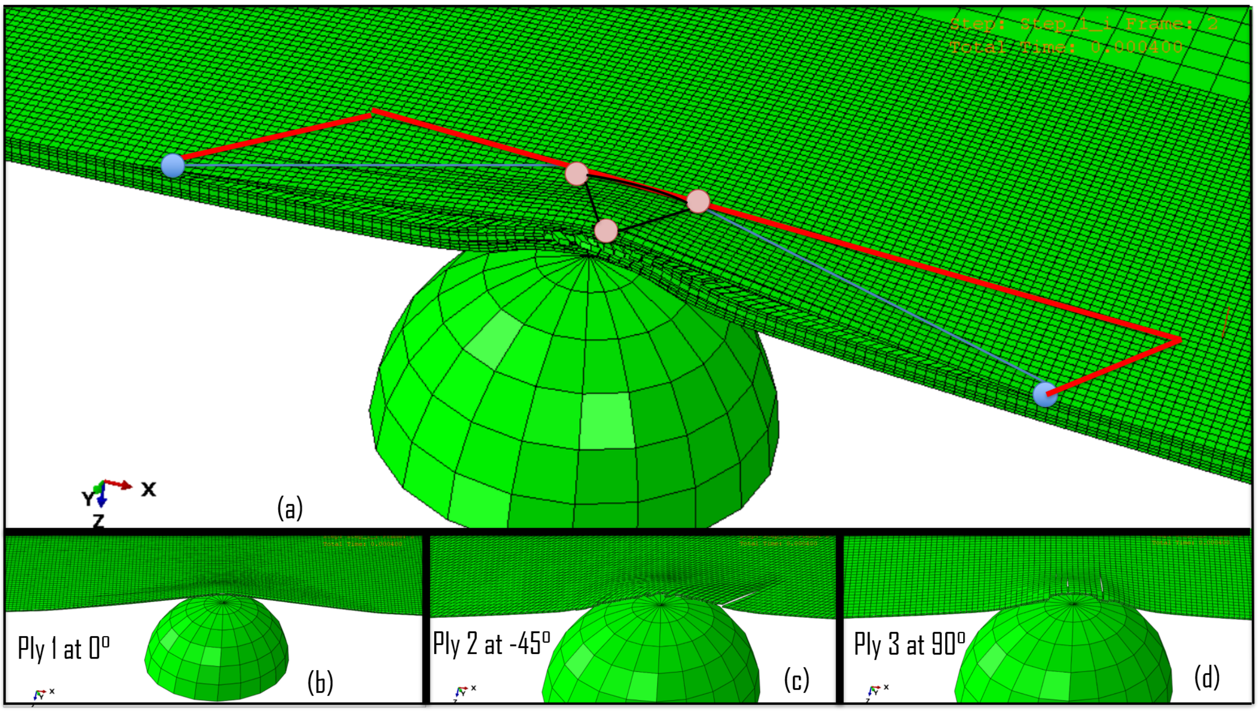

Figure 3.25 – Interface delamination shape formation mechanism.

3.3.3. Configuration M/⌀20/15J/Ba/I/1

In this configuration, the average dissipated energy per ball is 12.58 J with a standard deviation of 0.54 J, resulting in an average maximum displacement of the impactor of 9.76 mm (with a standard deviation of 0.14 mm). We measure an average delaminated surface area of 724 mm^2 with a standard deviation of 9 mm^2 (figure 3.26). We can distinguish the different interfaces and orientations of the delamination within the thickness. Interface 6 is not reached because of the large amount of damage under the impactor, the sound wave struggles to penetrate these areas, signal return is negligible. From these first three configurations, we can see that the closer the impact is to the

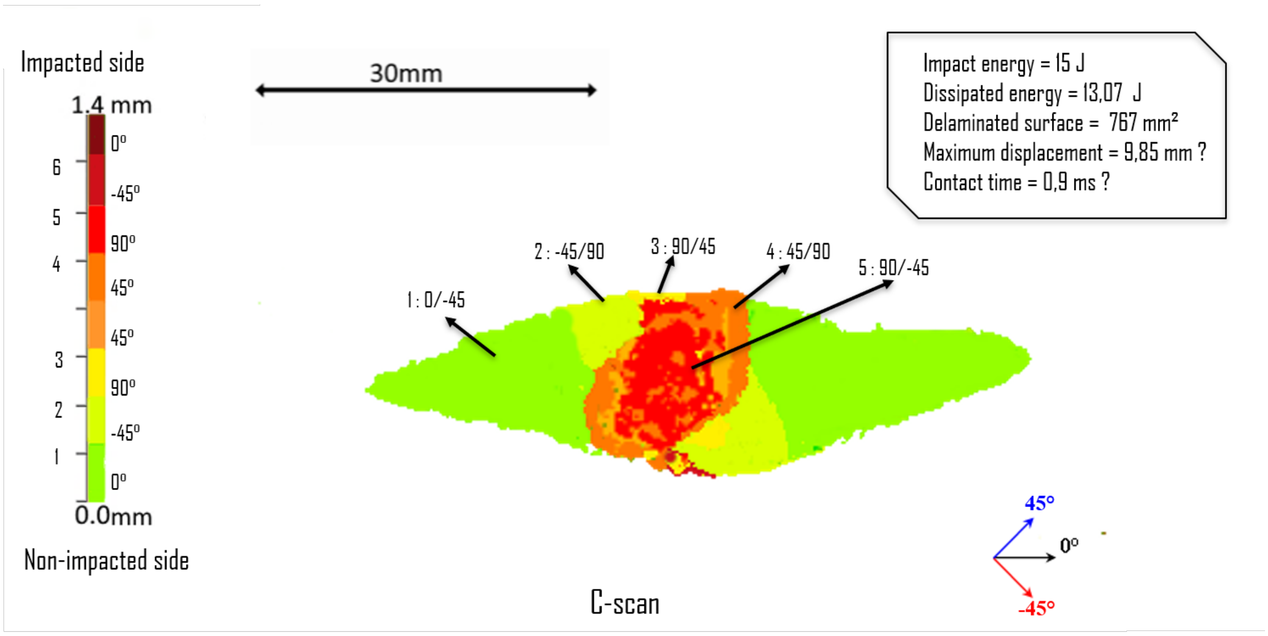

Figure 3.26 – C-scan of configuration M/⌀20/15J/Ba/I/1 mono-impact.

center of the plate, the smaller is the delaminated area. This is due to the fact that the plate is large and flexible enough to store energy in elastic form, which is not the case when the impact is close to the edges, where more energy is dissipated in the plate.

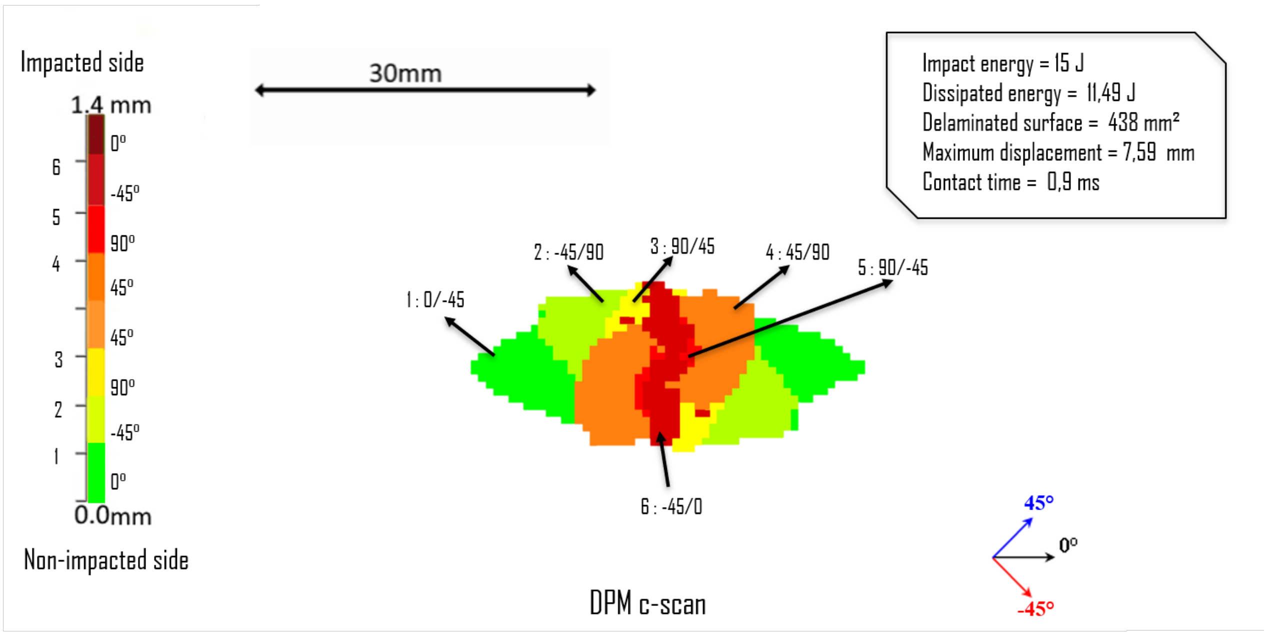

Figure 3.27 – DPM C-scan of configuration M/⌀20/15J/Ba/I/1 mono-impact.

From a numerical perspective, figure 3.27, the energy dissipated by the ball is 11.49 J, with a maximum displacement of the impactor of 7.59 mm and an impact time of 0.9 ms. The projected delaminated surface area is 438 mm^2. As for configuration

M/⌀20/15J/Ba/J/1 (the impact point is slightly displaced), the plate is therefore more flexible than reality, and the fibers break too prematurely, slowing the propagation of delamination.

In figure 3.28 we observe all the fiber breakages under the impactor. Fiber breaks in the penultimate ply prevent delamination propagation, as explained above. A fiber break in the last ply could have considerably reduced the delaminated area.

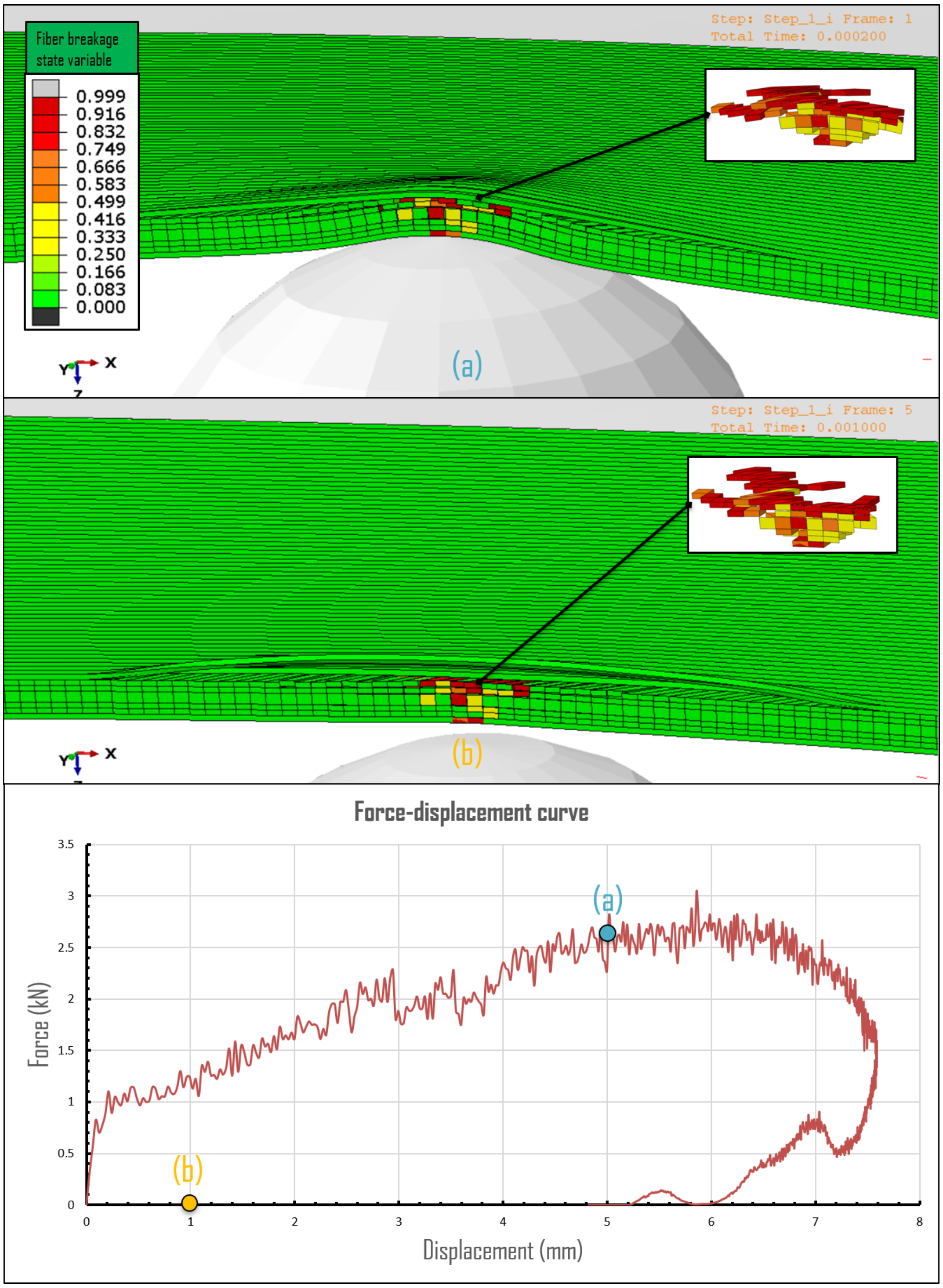

Figure 3.28 – Fiber breakage (DPM) : (a) at 0.2 ms, (b) at 1 ms, configuration M/⌀20/15J/Ba/I/1.

In figure 3.29 we can see all the matrix cracking around the impact. We note that this matrix cracking is perpendicular to the fiber direction of the last ply, and is probably what stops the delamination propagating in this direction. We also note that these matrix cracks is discontinuous, due to the abrupt criterion of matrix cracking, which releases stresses in the neighboring element as it breaks the interface (it is not a physical phenomenon) ; as a sudden break occurs, there are areas where the Hashin criterion is close to 1 in volume elements far from the delaminated zone, it is so close to 1 that when an element breaks suddenly, the criterion is relaxed a little in the neighbouring element, which then does not break. However, towards the center of the impact, where the CZMs are all damaged, no issues are observed.

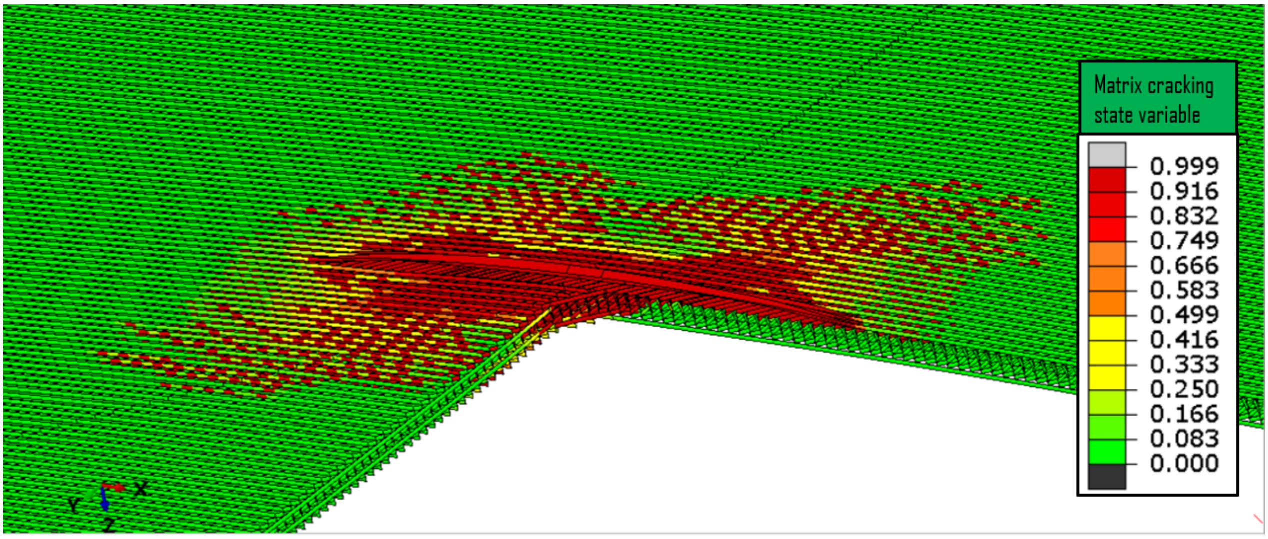

Figure 3.29 – Matrix cracking (DPM) of configuration M/⌀20/15J/Ba/I/1 mono-impact.

For a further explanation of delamination formation, figure 3.30 shows the shape of delaminations per interface. The first 2 interfaces to the impacted side (interfaces 5 and 6) show little delamination as they are in compression. These little delaminations are mainly a consequence of the fiber breakage under the impactor.

The figure 3.31 shows the breakdown of energies and in particular the distribution of dissipated energies between the various phenomena. On the other hand, the energy dissipated through damages is just as important in fiber rupture as in delamination. Even if matrix cracking does not dissipate much energy, it is important to recall that it initiates and drives many of the phenomena explained above.

Finally, we varied the impact angle on the numerical model between 0 and 7°, as was done experimentally. The results show that the difference is small and may be neglected.

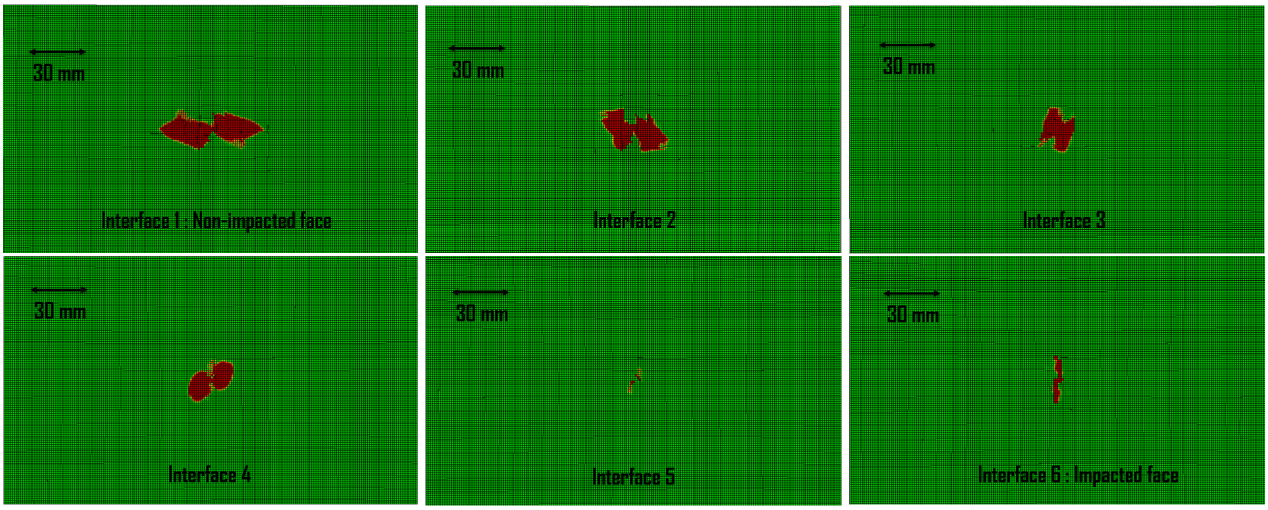

Figure 3.30 – Delamination shape by ply (DPM).

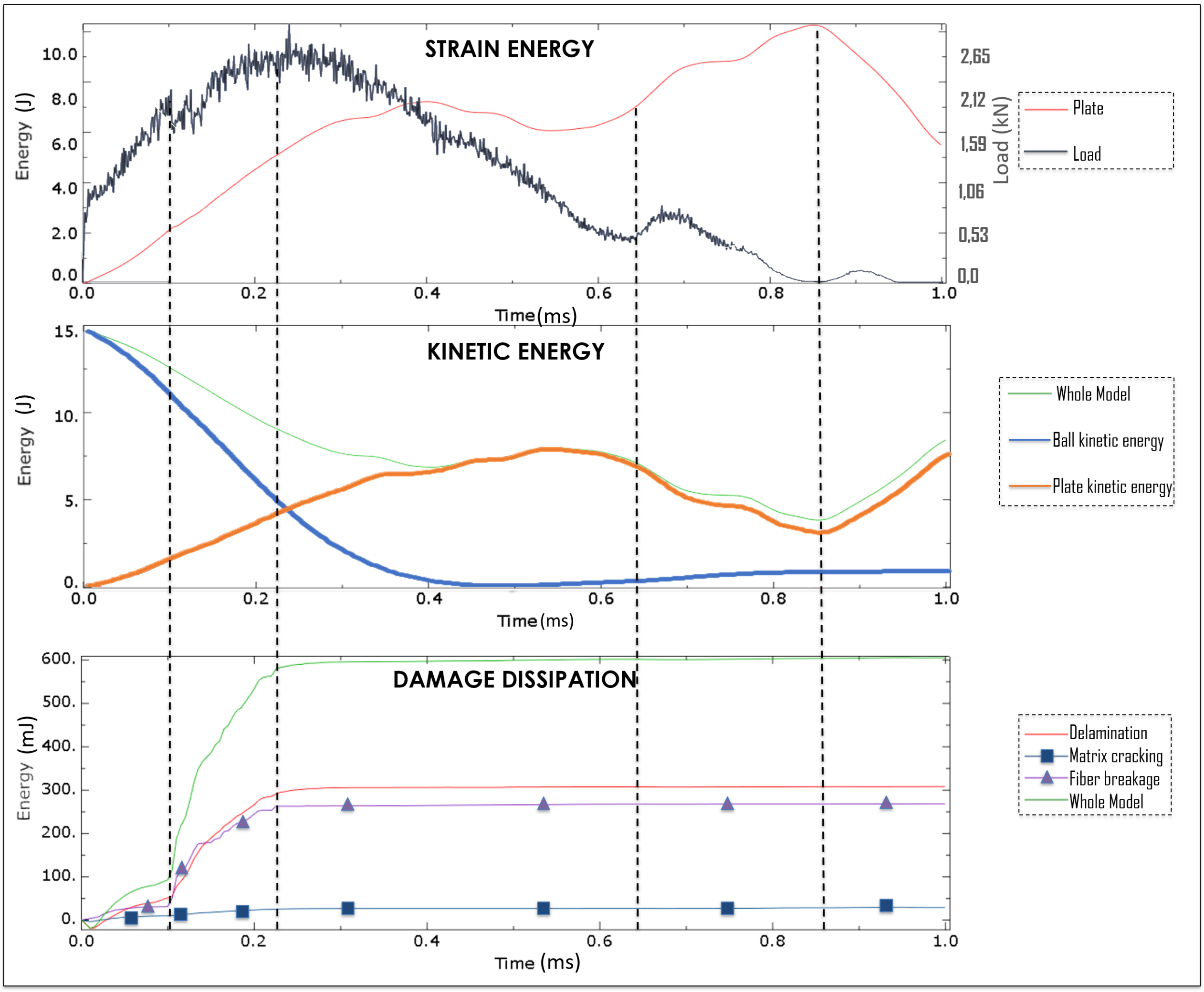

Figure 3.31 – Energy distribution within the composite material (DPM).

3.3.4. Configuration M/⌀20/30J/Ba/K/1

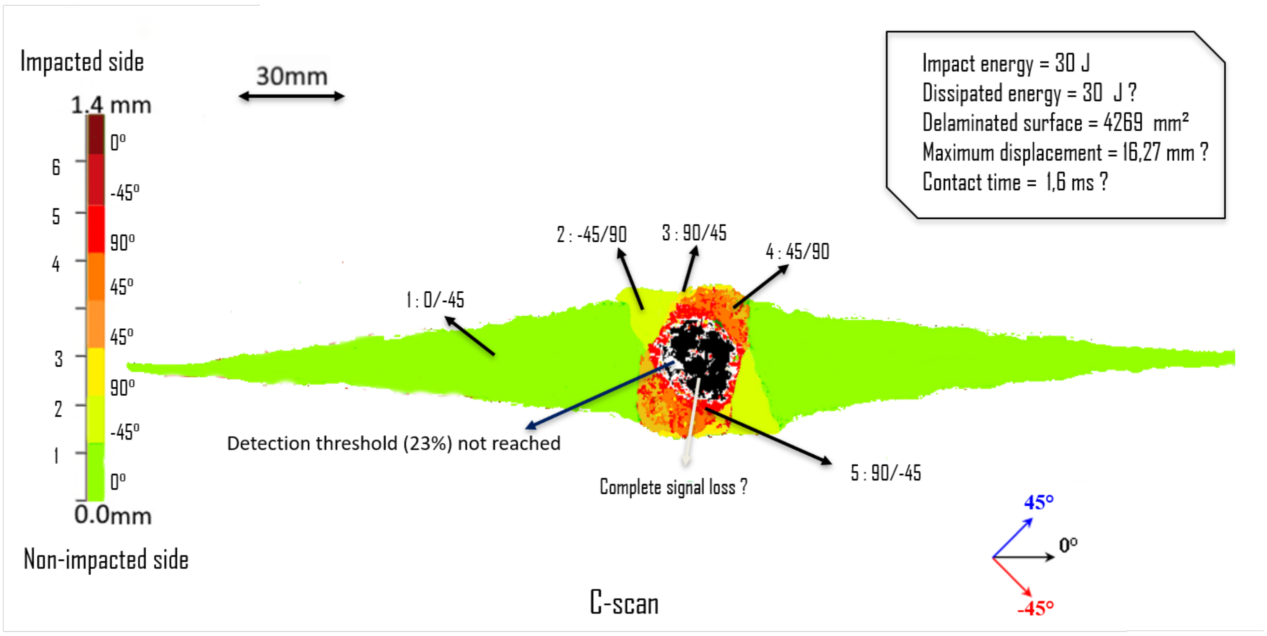

Figure 3.32 – C-scan of configuration M/⌀20/30J/Ba/K/1 mono-impact.

The 20 mm diameter projectiles are launched with a kinetic energy of impact of 30 J (velocity of 43 m/s). The plates have been perforated, so it is difficult to judge the amount dissipated in the plate experimentally. The impact time is 1.6 ms (compared with 1 ms for the 15 J configurations). However, the plate is not completely perforated : the hole created by the projectile during impact is closed once the ball has pierced the plate, as shown in figure 3.35. We measure an average delaminated surface area of 4222 mm^2 with a standard deviation of 48.54 mm^2 (figure 3.32). We can distinguish the different interfaces and orientations of the delamination within the thickness. All delaminated surfaces are larger compared to the 15 J configurations, but especially interface 1, which reaches the edges of the plate. It is important to note that the loss of signal return is related to the chosen synchronization threshold (12%). But for the same C-scan parameters used in the 15 J configurations, here we notice a total loss of signal due to the breakage of these surfaces, which become too inclined, and the signal return is subsequently very weak. It should be borne in mind that the plate is perforated rapidly during impact and then resealed afterwards, thanks to the plies that do not come detached because of matrix cracking which occurs earlier than fiber breakages. We explain this point of view in more detail later in this configuration.

From a numerical perspective, figure 3.33, the energy dissipated by the ball is 30 J, which means that the ball is completely stopped by the plate, so the model only predicts a quasi-perforation of the plate, unlike the experiments. The maximum displacement of the impactor is 18.7 mm and an impact time of 1.9 ms. The projected delaminated surface area is 1384 mm^2, figure 3.35. Compared to the experiments, the main difference is that interface 1 does not delaminate as in real-life conditions.

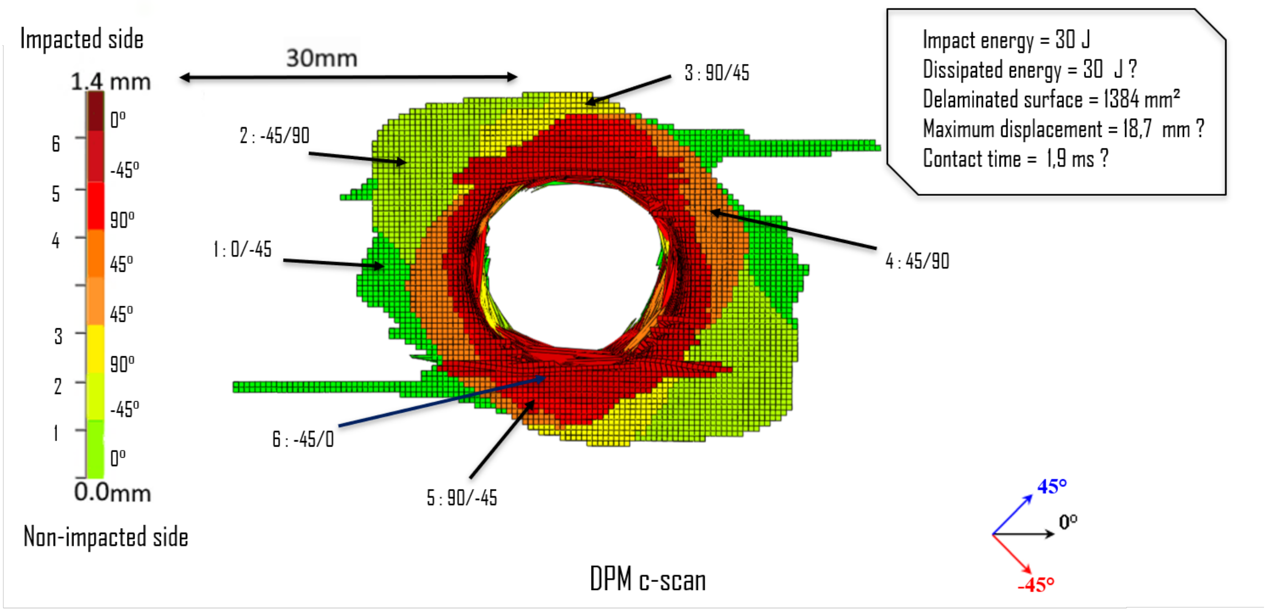

Figure 3.33 – DPM C-scan of configuration M/⌀20/30J/Ba/K/1 mono-impact.

It appears that the fibers are broken precociously and thus stop the delamination propagation. Once again, precise mechanical characterization is required to examine this problem in detail. We also remind you that to make this numerical calculation converges, the broken delamination elements are removed from the model as explained in figure 3.8, this abrupt removal of the elements concentrates the stress applied to the fibers and also contributes to their premature destruction. Figure 3.34 shows the difference between the driving damage : in numerical modelling (a&c), it is mainly fibre breakage, whereas in (b), it is mainly matrix cracking of the last ply that directly generates the important delaminated surface of interface 1.

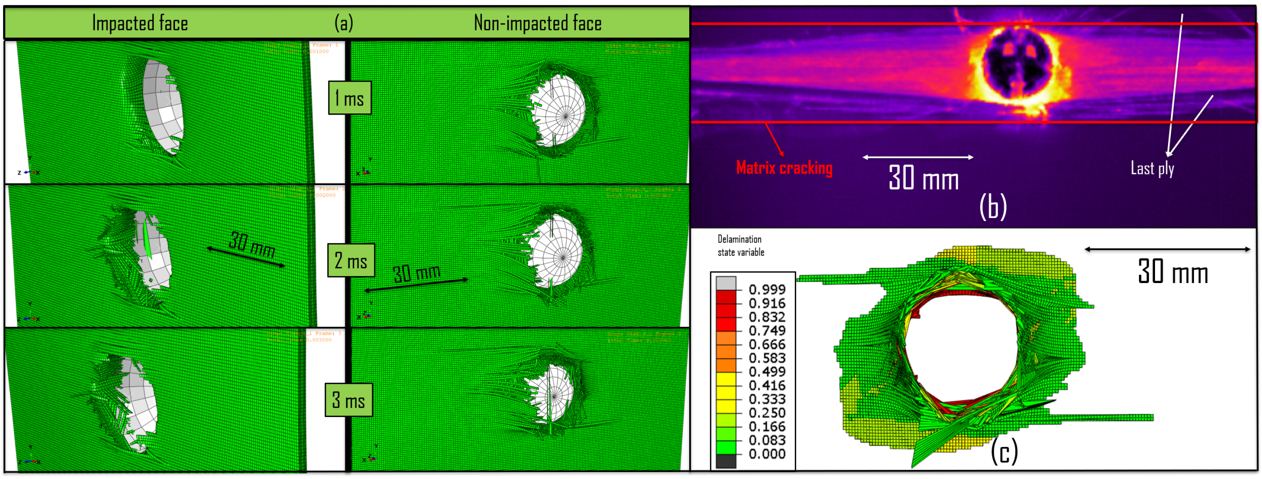

Figure 3.34 – (a,c) Driving damage mechanisms : DPM, (b) experiments.

By analyzing the thermal film images (figure 3.35), we once again confirm that matrix cracking comes first. But more importantly, this figure shows the important role of cracking in driving impact damage scenarios in composite materials. Indeed, the matrix cracking we see at t = 1.905 ms directly causes the delamination of interface 1, and it is this same matrix cracking that seals the plate after perforation by the ball, making it dangerous from an industrial point of view. In fact, if we only check the plate with a post-mortem inspection process (visually, with a C-scan or other), we will not realize that the plate is completely perforated in its center. On the other hand, with in-situ thermal analysis, we can clearly see that, in terms of mechanical characteristics, the plate is completely perforated at its center, see figure 3.35 at (t = 1.905 ms). Interestingly, the delamination process at interface 1 is different from the conventional one (with matrix cracking in the lower ply) : here, it comes directly from contact with the ball that detaches the last ply. The matrix crack at 0° to the center of the impact splits the latter ply in two, allowing the ball to close the surface again.

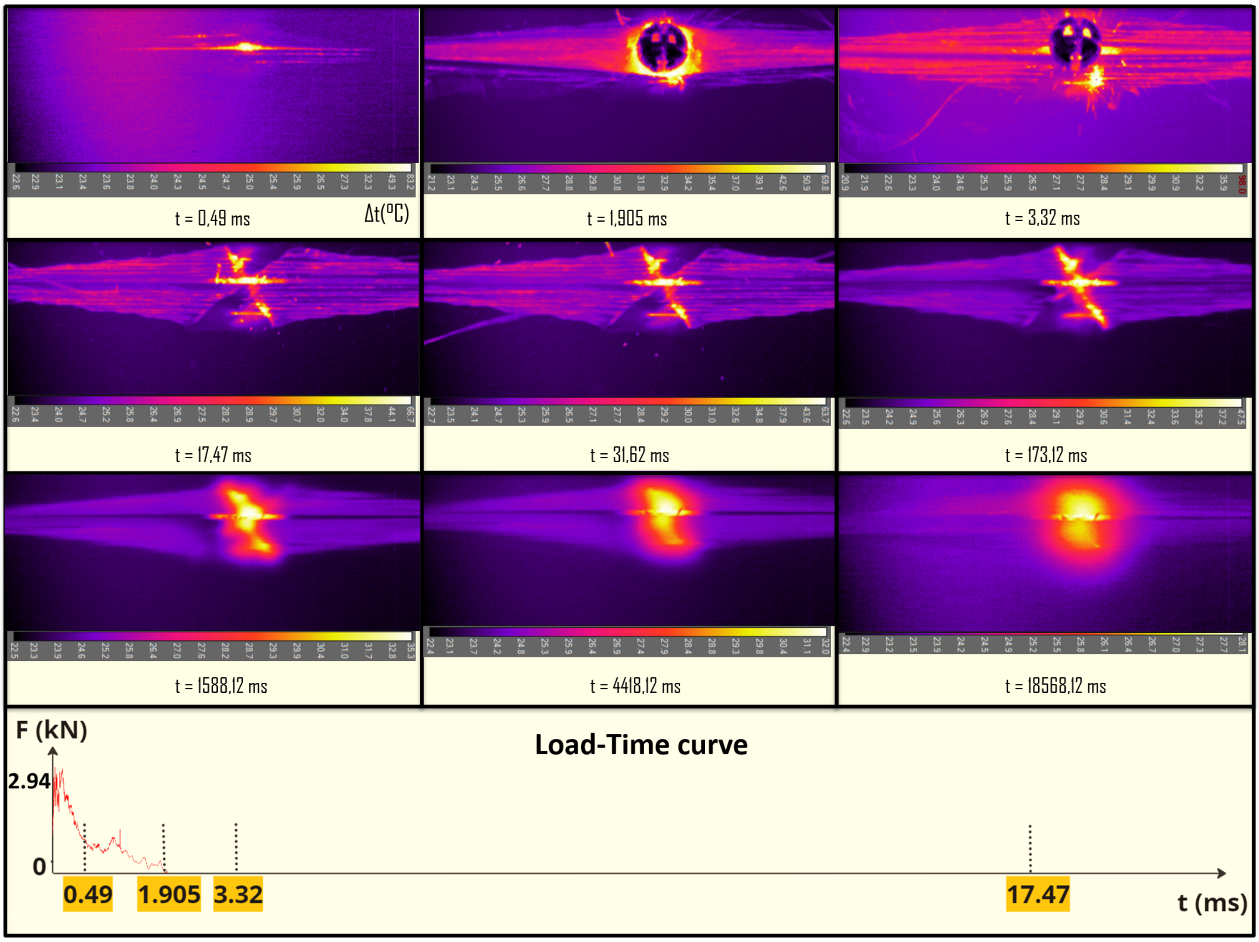

Figure 3.35 – Thermal film images from behind the plate and a schematic of the load-time curve.

3.3.5. Configuration M/⌀10/15J/Ba/K/1

The 10 mm diameter projectiles are launched with a kinetic energy at the moment of impact of 15 J at a velocity of 87 m/s. The plates have been perforated. The impact time is 0.6 ms (compared with 1 ms for the 15 J-Ø20 mm configurations). The plate is rapidly perforated, the energy supplied is concentrated locally, given the small size of the ball, and leads to rapid fiber breakage, given the ball's velocity, so the impact contact is also reduced to 0.6 ms. We measure an average delaminated surface area of 1424 mm^2 with a standard deviation of 26.48 mm^2 (figure 3.36).

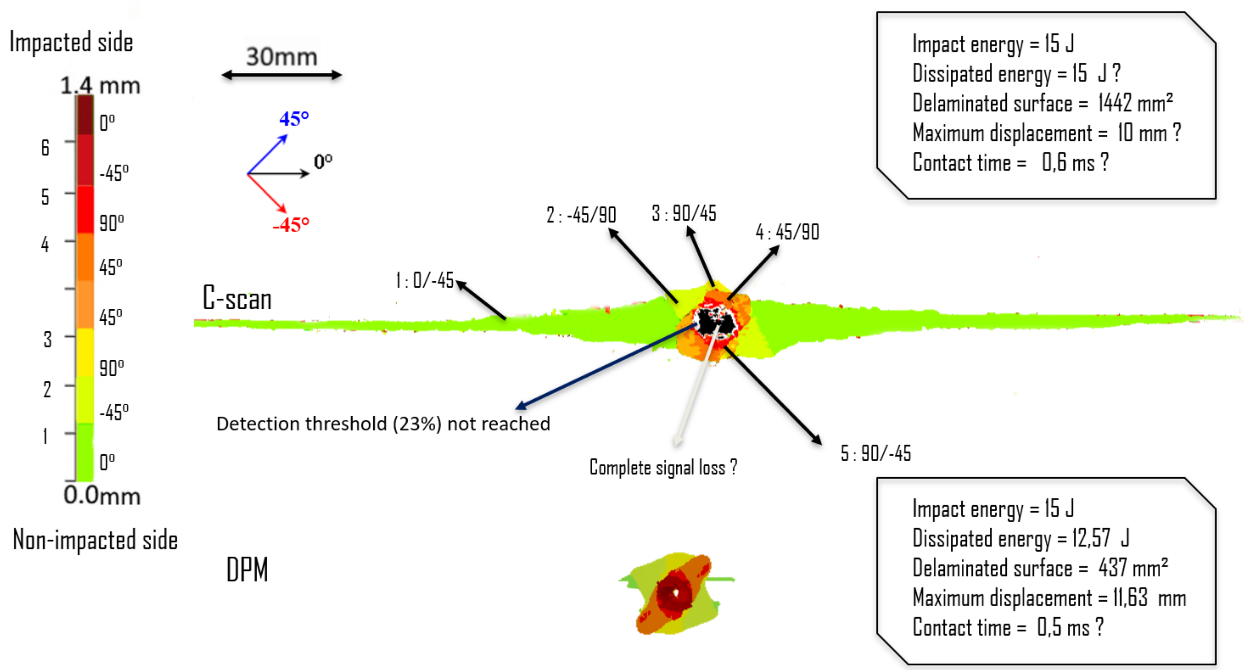

Figure 3.36 – C-scan of delaminated surface : DPM vs. Experiments (configuration M/⌀10/15J/Ba/K/1).

Compared with configuration M/⌀20/30J/Ba/K/1, we find most of the phenomena observed in the configuration M/⌀10/15J/Ba/N/1, in these two configurations, there was no complete perforation in the model, whereas there was in the experimental tests. To improve the model, further work is needed on the energy dissipated by fiber breakage, which is obviously becoming an important factor in simulating perforation. However, we notice a brutal drop in force, which must correspond to a large fiber break, figure 3.37(a). After that, the phenomena are similar, but occur rapidly and without large displacement for the 20 mm ball, figure 3.37. This sudden fiber break also prevents delamination propagation in the numerical model. Meanwhile, experimentally, it is always matrix cracking in the last ply that drives the damage.

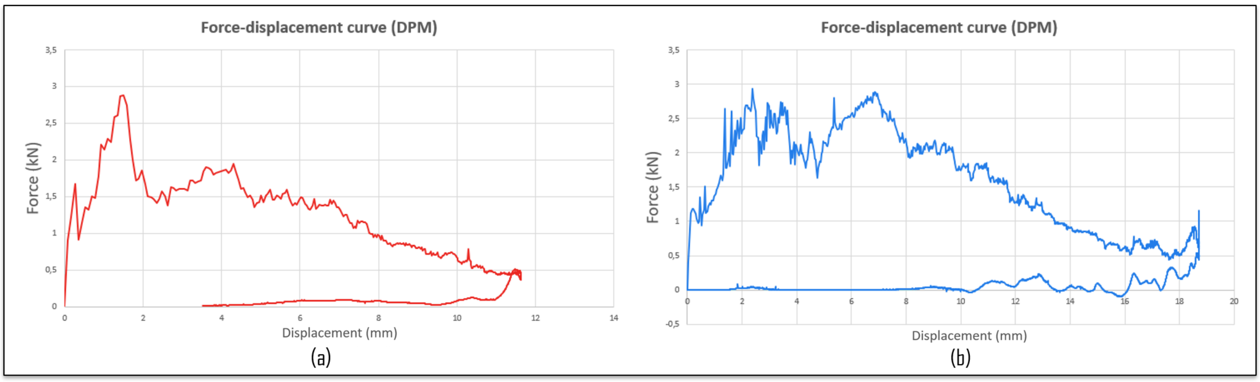

Figure 3.37 – Load-Displacement curves : (a) configuration M/⌀10/15J/Ba/K/1, (b) configuration M/⌀20/30J/Ba/K/1.

Conclusion

To conclude this chapter, we demonstrated that the different techniques used to study the impact on composite structures are coherent. C-scans and the SVD method provide a post-mortem perspective on delamination. Infrared thermal camera analysis and numerical modelling, enable us to understand the phenomena during the impact time. Overall, the different methods are complementary and reliable for in-situ and post-mortem monitoring of impacts on composite structures. We can then consider using these different methods to study the multi-impacts behavior of laminated composite structures.

By combining the experimental and numerical findings, we have gained a comprehensive understanding of the mono-impact behavior of composite structures. The results highlight the influence of various factors, including the impact location, projectiles' diameter, impact energy and velocity, on the response of composites under mono-impact conditions. This knowledge is enriched by an understanding of the phenomena of initiation and propagation of different types of damage on composite material structures. The next step is to check whether these phenomena are the same in the case of multiple impacts, and whether the impact parameters play the same role in this case.

Chapter 3

CHAPTER 4 :
MULTI-IMPACTS : SEQUENTIAL VS. SIMULTANEOUS

4. Multi-impacts : Sequential vs. Simultaneous

Introduction

As real-world scenarios often involve situations where structures experience multi-impact loading, this study will provide crucial insights into the response and performance of laminated composite materials, aiding in the design of resilient and damage-tolerant structures. This chapter begins by presenting the different terminologies used to distinguish the different impact and single-impact configurations. These different configurations are then studied and cross-referenced to identify the most critical and interesting configurations to be examined in greater detail afterwards. We then carried out a number of simultaneous and sequential impact tests, in order to highlight the difference between the two cases and the phenomena at play in each of them, in order to be able to distinguish the more critical and richer configuration to be examined in detail. On the numerical level, a new method of modeling sequential impact cases without incurring high computational costs is proposed. Finally, this chapter illustrates the importance of the notion of time in multiple impact configurations and how this can affect the impact behavior of composite structures.

4.1. Definitions

There are several types of impact depending on the time between impacts and their repetition, see figure 4.1 :

- Mono impact : a single impact during the life of a part in an impact zone (damage zone due to a given impact) without interactions with others. In practice, the load curves are used to find the beginning and end of the projectile/plate contact, but we will rather use the displacement curves to differentiate between different impact configurations to keep in mind that after an impact the plate still vibrates, which changes the behavior of the plate to the next impact.
- Multi-impact : Several impacts on a composite structure. In this category we distinguish other sub-categories :
  - Sequential impacts : If displacement equilibrium is achieved after an impact, we refer to this as a sequential impact (if the point of impact or the impactors are not the same) and repeated impact (if the point of impact and the impactor are the same).
  - Simultaneous impacts : two impacts at points A and B are considered perfectly simultaneous, if the impact at point B occurs before the stress waves due to the impact at point A reaches the impact area B, see figure 4.2. The

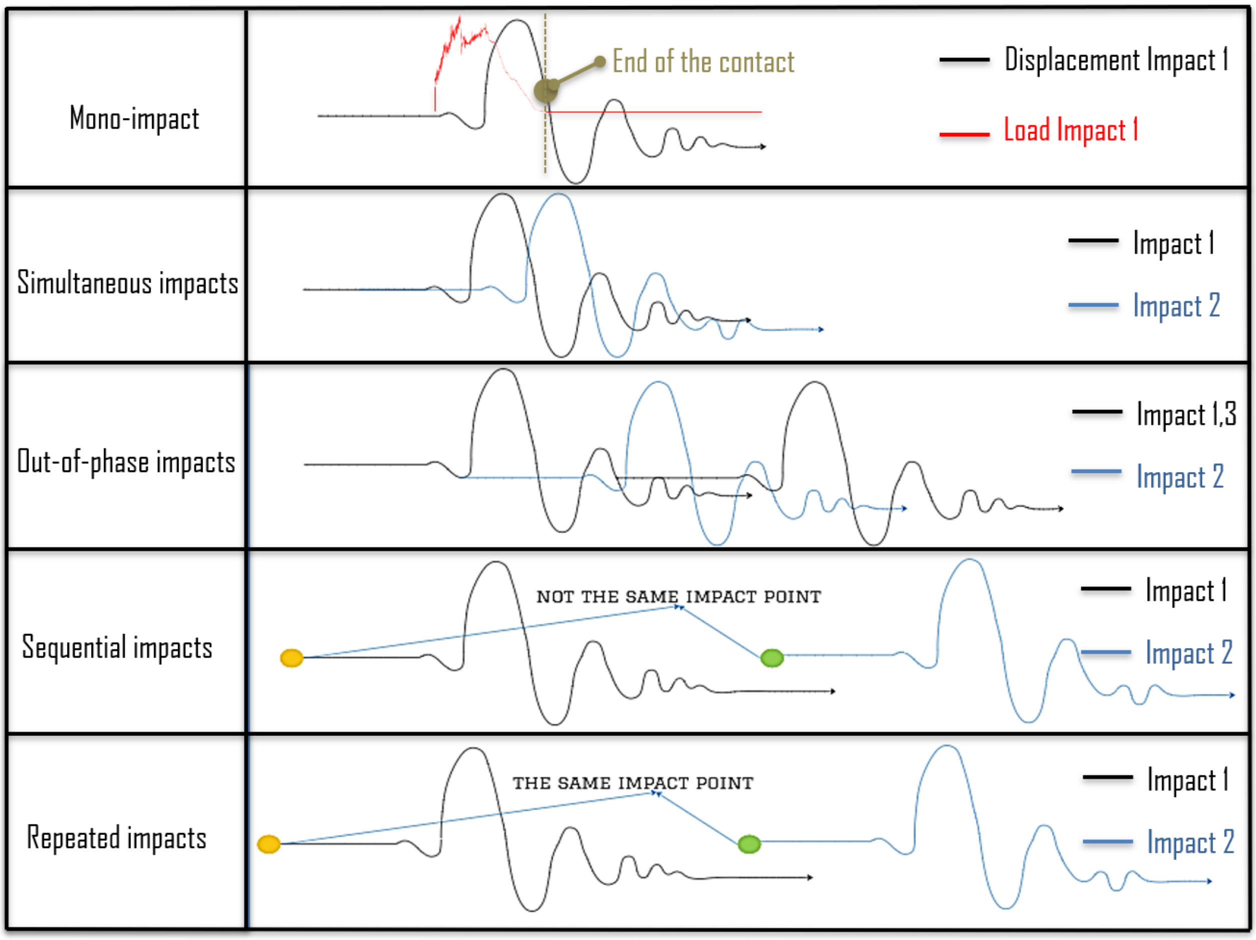

Figure 4.1 – Multi-impacts types definitions based on impact-induced displacement.

impact time and the local displacement at B are not disturbed by the impact at A. In practical terms, multiple impacts are called simultaneous if the last arriving one happens between the start and the end of the contact of the first arriving ball, see figure 4.1.

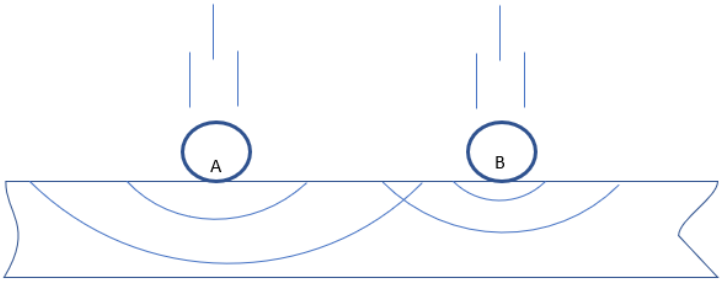

Figure 4.2 – Illustration of simultaneous multi-impacts.

Finally, if simultaneous impacts are repeated, we refer to them as repeated simultaneous impacts.

- Out-of-phase multi-impacts : Impacts are said to be out-of-phase when they have a fixed period between one another, before the plate returns to equilibrium after the previous impact.

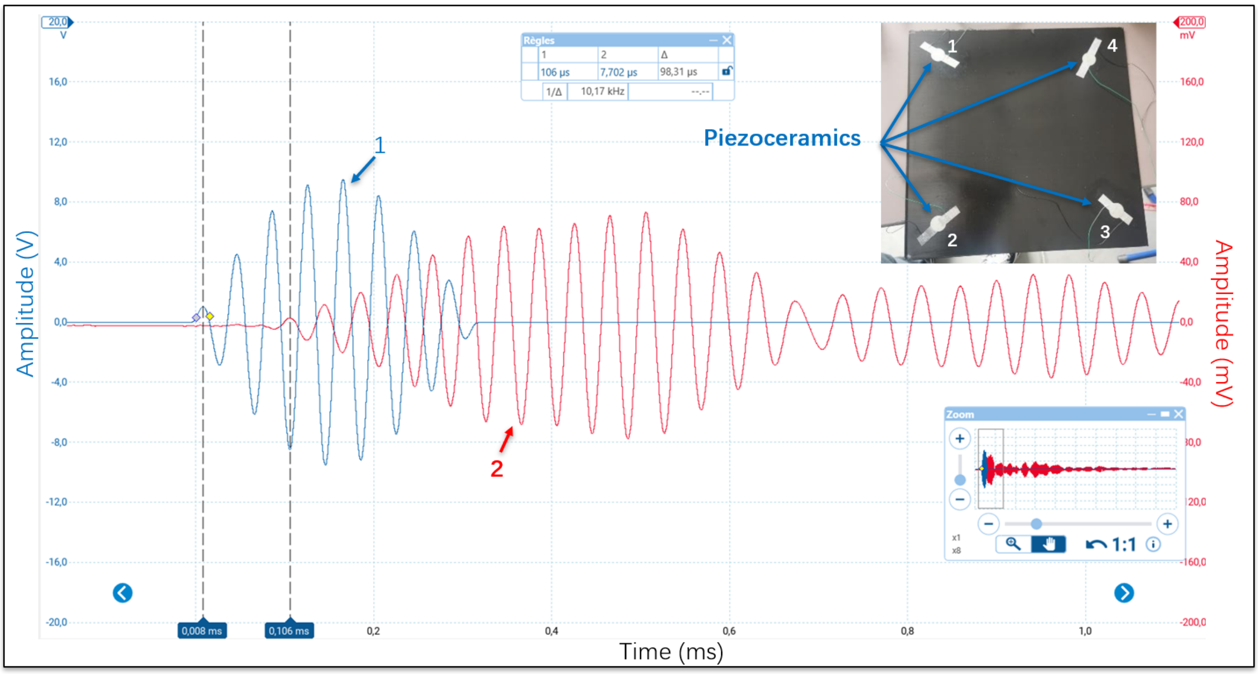

Règles

	1	2	Δ
	106 µs	7,702 µs	98,31 µs
1/Δ	10,17 kHz	--,--	

Figure 4.3 – Wave propagation velocity in the composite plate in different directions.

Apart the mono impact, the other configurations are considered as multi-impacts. it is important to distinguish between these different situations, as we will notice throughout this work, the behavior of the composite structure changes from one configuration to another, as the phenomena involved are not the same.

The aim of this section is to study the difference between an impact, simultaneous impacts and sequential impacts.

4.2. Sequential impacts

4.2.1. Configuration Sq/⌀20/15J/Ba/L/2

In this configuration, the position of the first impacts are shown in figure 4.4. The first impact of this configuration is the same as that of M/⌀20/15J/Ba/I/1. The delaminated surface of this first impact changes as a result of the second sequential impacts, so we note the delaminated surface of impact 1 before the second impact (previous delaminated surface, figure 4.5) and the delaminated surface of impact 1 after the second impact (new delaminated surface, figure 4.5), the first mono-impact

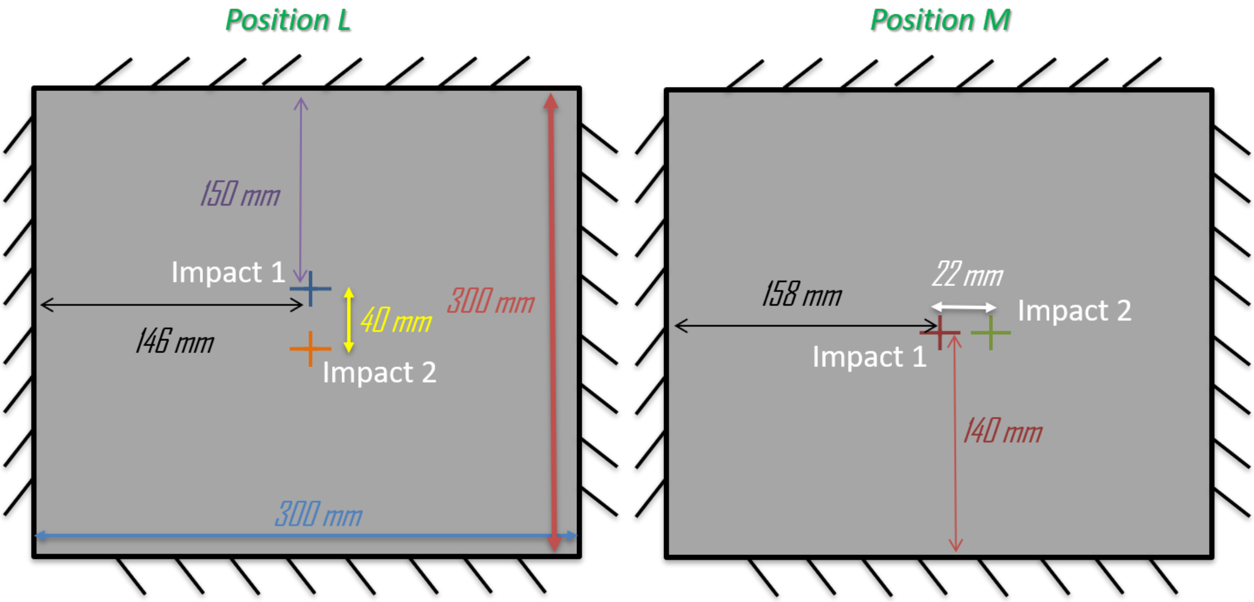

Figure 4.4 – Impact positions L and M.

is shown in figure 3.26. After this first impact, the plate is taken apart to perform the C-scans and then put back on the cannon to perform the second impact, called impact 2 or second sequential impact.

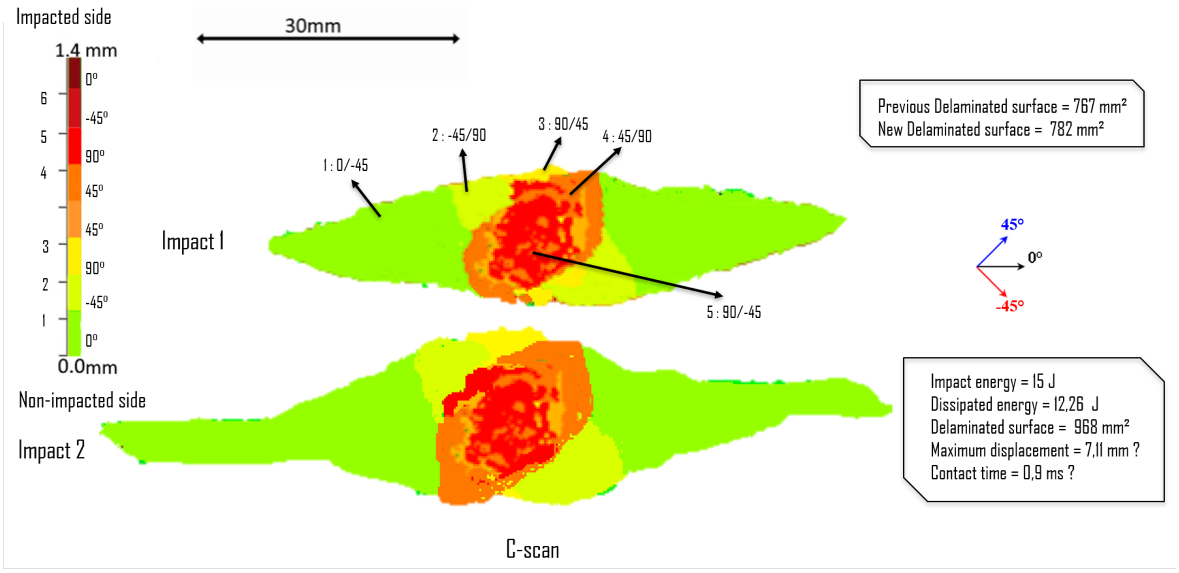

Previous Delaminated surface = 767 mm²
New Delaminated surface = 782 mm²

Impact energy = 15 J
Dissipated energy = 12,26 J
Delaminated surface = 968 mm²
Maximum displacement = 7,11 mm ?
Contact time = 0,9 ms ?

Figure 4.5 – C-scan of delaminated surface (configuration Sq/⌀20/15J/Ba/L/2) : the first impact (Impact 1), and the second sequential impact (Impact 2).

The average dissipated energy for the second projectile is 12.43 J with a standard deviation of 0.26 J, resulting in an average maximum displacement of the impactor of 7.91 mm (with a standard deviation of 0.97 mm). We measure an average delaminated surface area of the second (sequential) impact of 944 mm^2 with a standard deviation of 20 mm² (figure 4.5). We can distinguish the different interfaces and orientations of the delamination within the thickness. We noticed an increase in delaminated area of impact 1 of 3% on average despite the fact that there was no damage in this area due to the second sequential impact, which shows that an impact in a given point can have an impact on a distant point. We will study the relationship between the distance of impact centers and the delaminated area in detail in chapter 5. We note that the delaminated area due to the second impactor is 23% greater than that in the single-impact case, which shows that a previous impact degrades impact resistance even if there is no interference between the delaminated areas. We can assume that the cause is the loss of local rigidity in impact zone 1. To understand the details, we have performed an explicit calculation with stabilization of the plate between the two impacts to reduce the cost and time of the calculation ; the main reason was to decouple the two sequential impacts, doing the stabilization by stops and relaxations technique aims to reduce the cost of calculation. We also noted that when two impacts are close enough, they tend to move closer together in terms of projected damaged area (due to plate deformation and balls sliding), as also shown in the figure 4.17.

On the numerical front, it is complicated to stabilize this plate because of its large dimensions, its flexibility, high inertia and large impacts damages. We will see later that we were obliged to add 21 stabilization steps between the first step corresponding to the first impact and step 23 corresponding to the second impact. A mass scaling process (to decrease calculation time steps by increasing the plate mass, particularly during relaxation steps) could have been a solution, but in our case it poses a particular problem ; we are unable to return to zero mass scaling when we make the second impact on Abaqus, this type of procedure also requires us to redo the verification of inertia and other parameters that change with increasing plate mass. We finally introduced stabilization steps in two successive forms :

- The step where the plate is left free : a time during which the plate moves freely (T_{free} equals to 1.5×10^{-4} s).
- The stop step : velocities and displacements are set at 0. This step consumes no more than 5 seconds of calculation time, it is best to keep the time devoted to these steps as short as possible, we have taken 1×10^{-7} s in our case). During this stop step, no outputs field are requested to reduce the size of the calculation output file (.odb). On the other hand, for the T-free, we asked for these outputs at every step, and we finally realized that we could also optimize by asking for the outputs in just a few steps (once every two steps for example).

At the end of the impact, the plate displacement does not return to zero. We have experimentally noticed that the plate is blocked after impacts, and that its displacement does not return to zero (as we can see on the displacement sensors, figure 4.6, these curves were obtained during tests on configuration M/⌀20/15J/Ba/K/1). This may be due to the fact that we have a pseudo-plastic deformation, due to the permanent indentation that remains and blocks the plate at the impact zone. In the numerical model, see details in subsection 3.3.1 Configuration M/⌀20/15J/Ba/K/1, the version in which delamination and matrix cracking interface are not suppressed, this permanent indentation is managed in the plasticity components of matrix cracking. In this case, we intended not to go directly to the general contact (all exterior) but only to the impactor-top plate contact. This choice enabled us to divide the calculation time by about 3 (thanks to the fact that we didn't have to handle all the calculations for the all exterior contact). However, depending on the type of sequential configuration, in the second impact, the damage caused by the previous impact is so great that volume elements have to be removed, necessitating the use of all-exterior contact to avoid any interpenetration of the elements. In this first version of the model we will also have a plasticity character that we will not have completely in the second version with element deletion (it will have this character but in a less visible way and linked rather to the friction coefficient), this plasticity character is fully observable experimentally where the plate remains locked in a position different from zero after the impact.

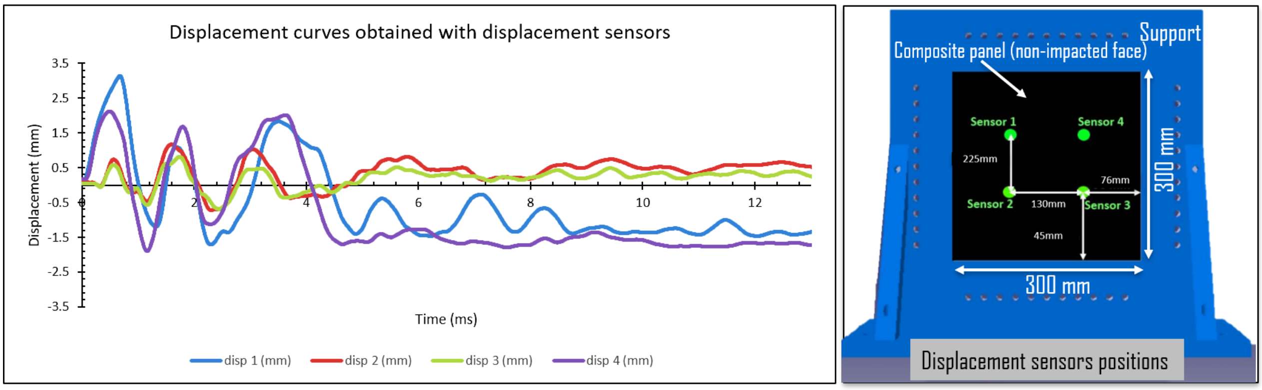

(a) (b)

Figure 4.6 – Displacement curves obtained with displacement sensors and their positions.

The most important thing during the stabilization process is to know whether or not the plate is going to reach the asymptote of its displacement, then the plate will have small oscillations around the value of this asymptote, see figure 4.7. This is particularly important to check around the point of impact, where we will have the second impact. The most revealing nodes for the degree of plate stabilization are the nodes above and below the point of impact. In addition, 23 steps in total is already sufficient, given that 33 steps is always on the same asymptote in terms of displacement, see figure 4.7(b) between 2.6 ms and the start of the second impactor.

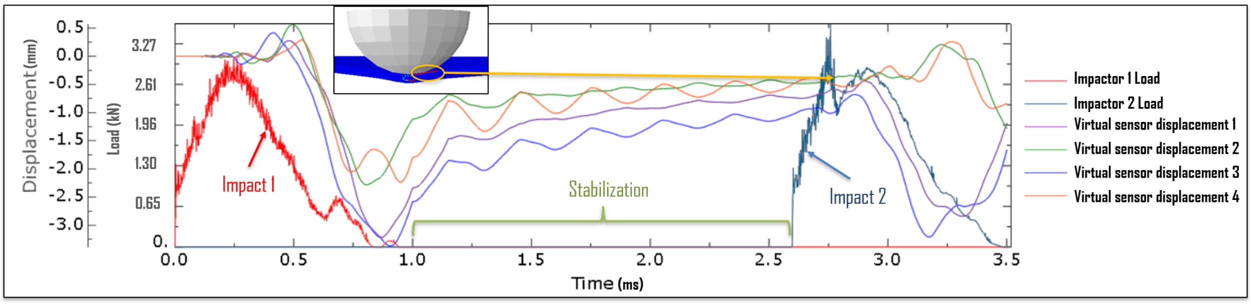

(a) 23 steps : 21 stabilization steps and 2 steps of impact.

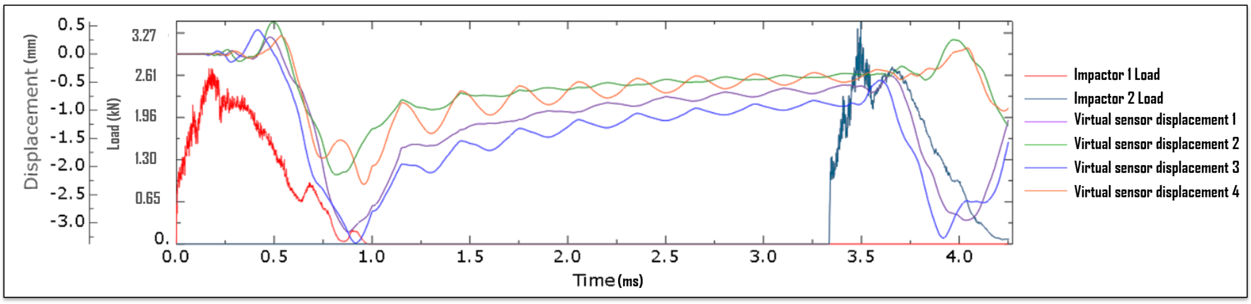

(b) 33 steps : 31 stabilization steps and 2 steps of impact.

Figure 4.7 – Plate stabilization for sequential impact configurations (results for configuration Sq/⌀20/15J/Ba/L/2).

To manage the sequential order of impacts, we use the following formula :

$$z_2 = e_{tot} + R_{ind2} - V_{imp2} \cdot (T_{imp} + N \cdot T_{free} + M \cdot T_{stop}) \tag{4.1}$$

where z_2 represents the z-axis position of the second impactor, e_{tot} is the thickness of the plate, R_{ind2} is the radius of the second impactor, and V_{imp2} is its velocity. T_{imp} is the impact time of first impactor, T_{free} is the relaxation time, and T_{stop} is the stop time. N and M $(= N + 1)$ respectively denote the number of relaxation and stop steps. To stabilize the plate, during the steps, we apply displacement/velocity boundary conditions, each time deleting all the previous conditions (BOUNDARY , op = NEW, type = velocity) and then resetting our boundary conditions one by one. This avoids the risk of data overlap and loss.

Figure 4.8 shows this stabilization process through the difference between plate displacement at the start and end of certain stabilization steps, we see that we are converging on a z-displacement value of 4 mm.

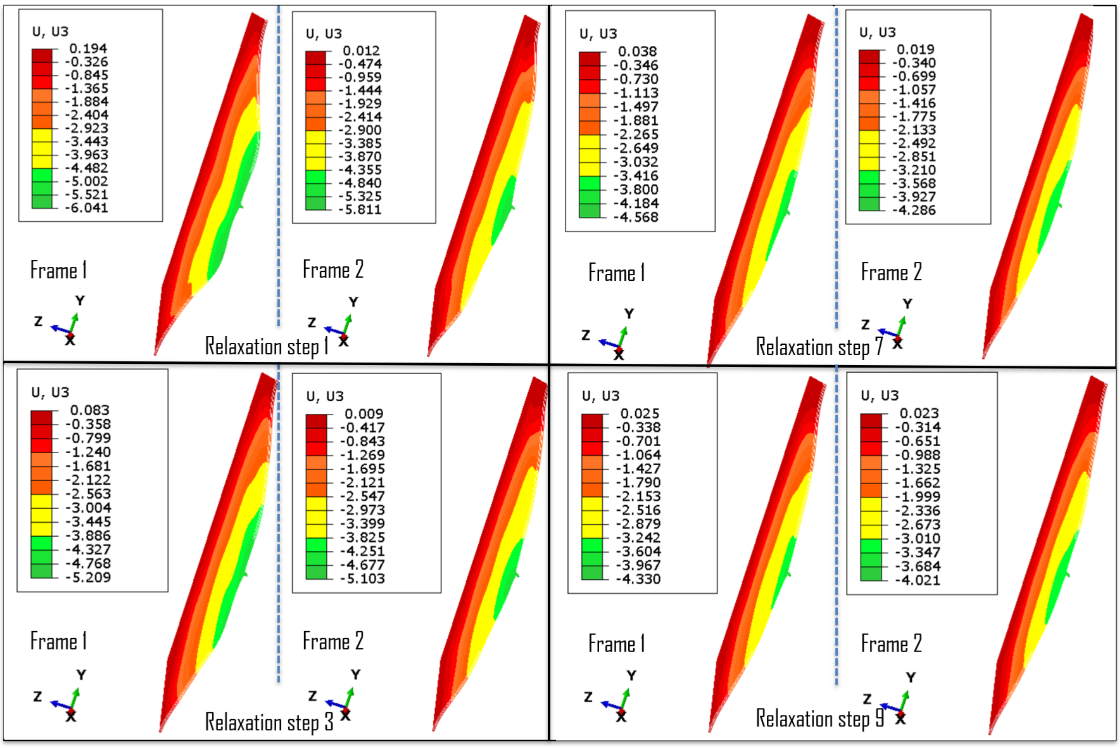

Figure 4.8 – Variation in displacement between start and end frame for each step (deformation scale factor : 5).

From the numerical perspective, the results of the first impact are shown in configuration M/⌀20/15J/Ba/I/1, the energy dissipated for the second projectile is 12.25 J, with a maximum displacement of the impactor of 7.43 mm and an impact time of 0.8 ms. The projected delaminated surface area is 1263 mm², figure 4.9.

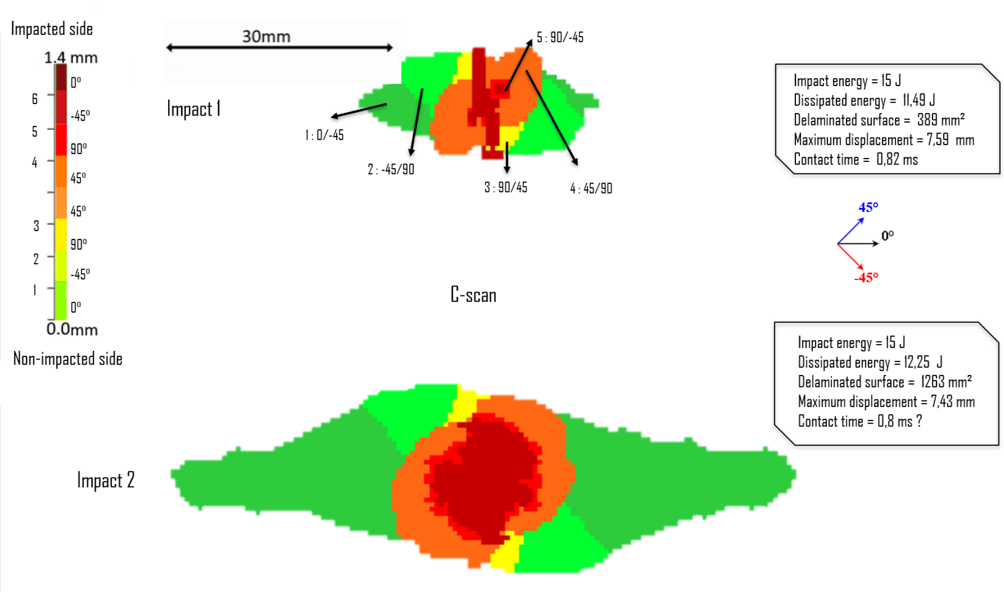

Figure 4.9 – C-scan of delaminated surface (DPM) (configuration Sq/⌀20/15J/Ba/L/2) : the first impact (Impact 1), and the second sequential impact (Impact 2).

We confirm with numerical simulation that there is no interference in damage (matrix cracking, delamination and fiber breakage) between the two impacts zones. On the other hand, we note that the stress wave propagation following the second sequential impacts is altered due to the damage created by the first impactor, see figure 4.10. This changes the vibrational behavior of the plate and reduces the maximum permissible displacement, leading to a greater concentration of stress and damage at the last impact zone, figure 4.7. We can assume that the further spaced the impacts are, the lower the influence of a first impact compared to a second. We will verify the validity of this hypothesis in the fifth chapter.

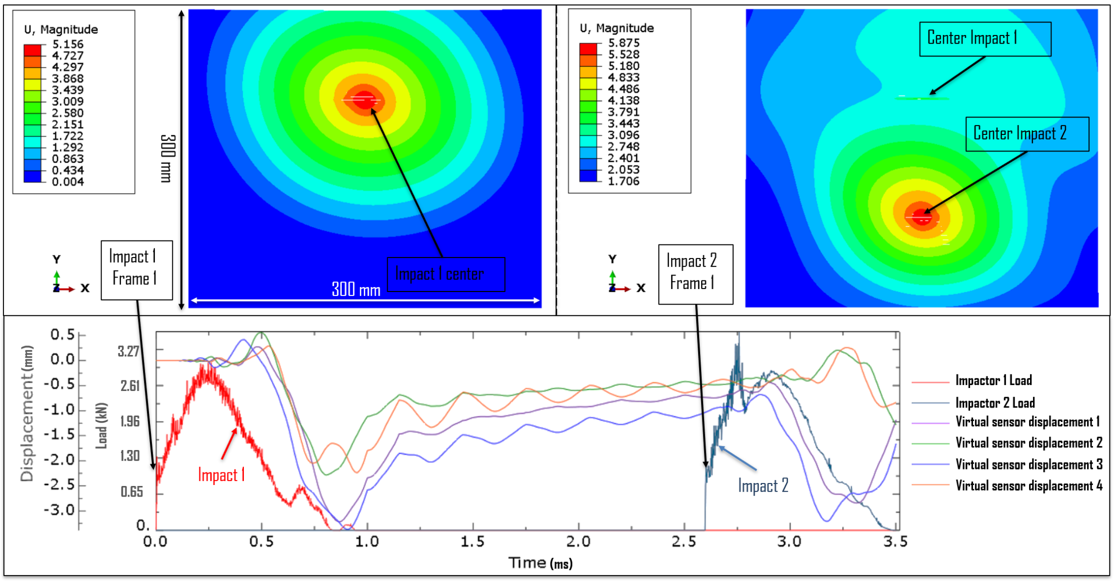

Figure 4.10 – Displacement magnitude in frame 1 of impact 1 and 2.

4.2.2. Configuration Sq/⌀20/15J/Ba/M/2

In this configuration, the position of the first impact is the same as in Configuration M/⌀20/15J/Ba/J/1, the distance between the two impactors centers is 22 mm in the x-direction. After this first impact, the plate is taken apart to perform the C-scans and then put back on the cannon to perform the second sequential impact. The average dissipated energy for the second projectile is 14.16 J with a standard deviation of 1.03 J, resulting in an average maximum displacement of the impactor of 9.95 mm (with a standard deviation of 0.68 mm). We measure an average total delaminated surface area of 1301 mm^2 with a standard deviation of 114 mm^2 (figure 4.11). Compared to configuration Sq/⌀20/15J/Ba/L/2, we obtain a smaller total delaminated area in the case of interfering damaged zones, this is due to the fact that the delaminated area of interface 1 of the impact (which is the largest among the delaminated interfaces of the same impact) is masked by the delaminated area of impact 2, in other words the delaminated area between the centers of the two impacts is shared. If we move the two impact centers further apart in the 0° direction, we would expect the delaminated surface to be larger, since the shared surface would be smaller, as clearly shown on the

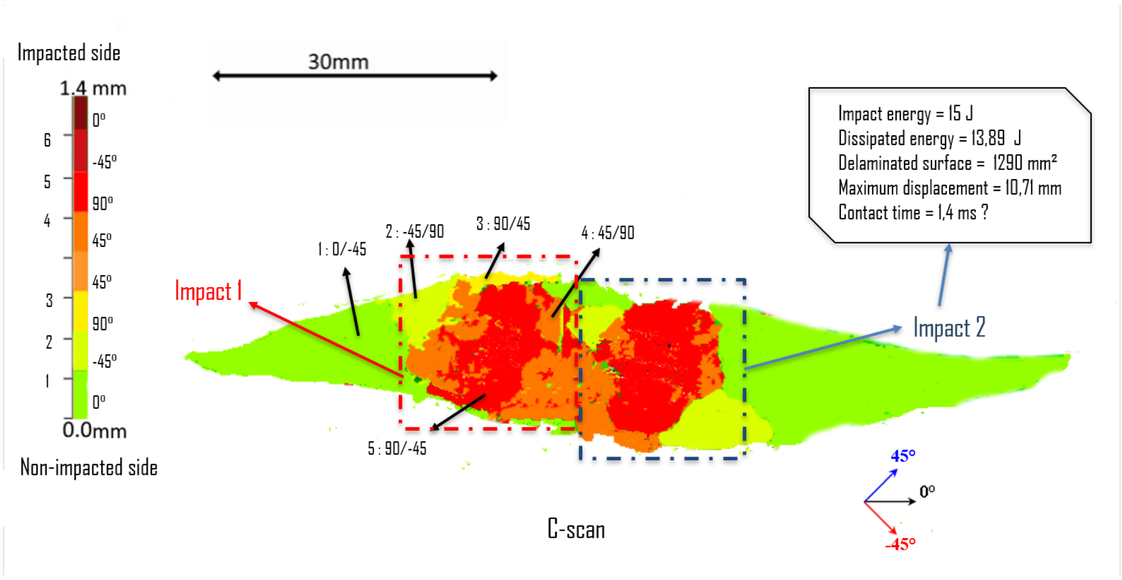

Figure 4.11 – C-scan of delaminated surface : (1) first impact, (2) second sequential impact (configuration Sq/⌀20/15J/Ba/M/2).

numerical model in figure 4.12 (Step 23, Frame 5) where we see a shared delaminated surface between the two impacts. A slight shift in the y-direction is noticeable, this may be due to experimental errors, or to ball sliding, as previously observed in close-impact configurations (figure 4.17 and figure 4.5).

From the numerical perspective, the energy dissipated for the second projectile is 11.36 J, with a maximum displacement of the impactor of 7.81 mm and an impact time of 1 ms. The projected delaminated surface area is 1368 mm^2, figure 4.13. We note here a slight increase in impact time (from 0.9 ms to 1 ms, see previous DPM C-scans figures), allowing for greater energy dissipation. We also note that the surface shared between the two impacts was the interface between the last and penultimate plies. We conclude that if the delaminations due to each impact intersect in a given interface, it will tend to be the last one where the damage will be accumulated.

For the plate stabilization procedure, figure 4.14, we observe in the figure that the plate after the stabilization steps is oscillating around the asymptotic value of its equilibrium displacement. Here, the virtual displacement sensors are placed in the same position as in the experimental model, validating that the plate has been well stabilized before the second impact, and that this procedure can be used to reduce calculation time and ensure reliable explicit calculation.

Finally, We note a sudden drop in the acceleration of the second impact, figure 4.14, corresponding to a large fiber break initiated on the side of the first impactor. This shows once again the influence that a first impact can have on the mechanical behavior of the plate in a different and distant impact zone.

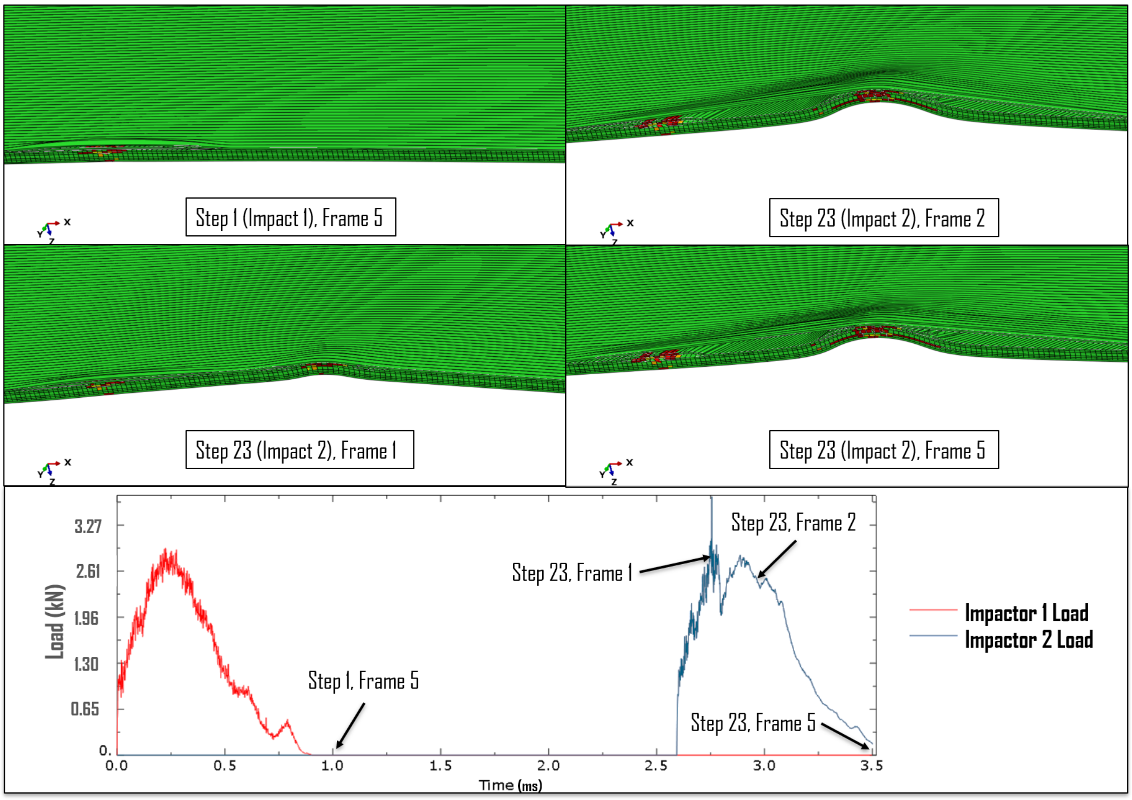

Figure 4.12 – Formation of split delaminated surface between two impacts aligned along the fiber direction in the ply below the most delaminated interface.

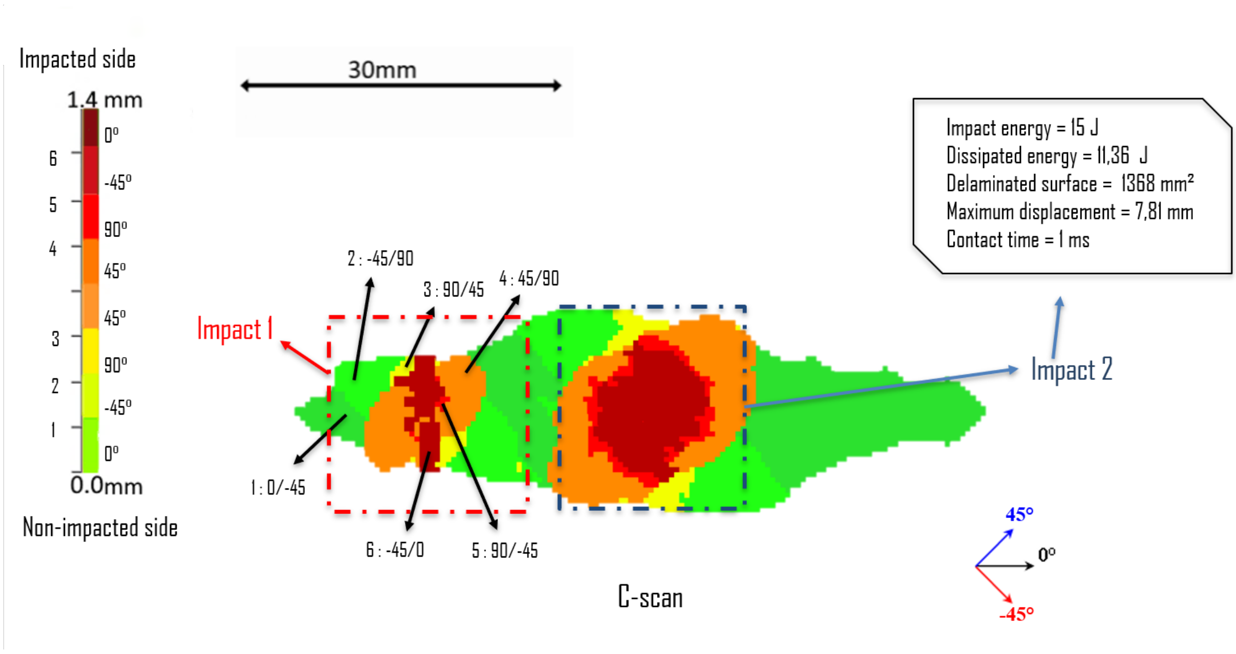

Impact energy = 15 J
Dissipated energy = 11,36 J
Delaminated surface = 1368 mm²
Maximum displacement = 7,81 mm
Contact time = 1 ms

Figure 4.13 – C-scan of delaminated surface (DPM) : (1) first impact, (2) second sequential impact (configuration Sq/⌀20/15J/Ba/M/2).

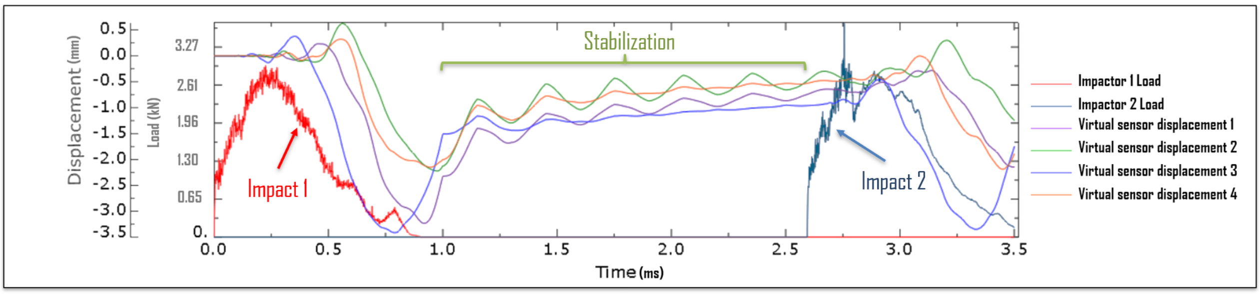

Figure 4.14 – Plate stabilization for sequential impact configurations (results for configuration Sq/⌀20/15J/Ba/M/2).

4.3. Simultaneous impacts

In this section, we propose to repeat the same configurations as in the sequential case in simultaneous mode (the same impact parameters except for the time lag, which is reduced to a value less than 0.5 ms in most cases).

4.3.1. Configuration Si/⌀20/15J/Ba/L/2

In this configuration, we repeat the configuration Sq/⌀20/15J/Ba/L/2 with two simultaneous impacts. The average dissipated energy for the projectile 1 is 13.23 J with a standard deviation of 0.27 J, resulting in an average maximum displacement of the impactor of 8.39 mm (with a standard deviation of 0.2 mm). We measure an average delaminated surface area 1 of 1348 mm^2 with a standard deviation of 67 mm^2 (figure 4.15). The average dissipated energy for the projectile 2 is 12.59 J with a standard deviation of 0.34 J, resulting in an average maximum displacement of the impactor of 11.05 mm (with a standard deviation of 1.17 mm). We measure an average delaminated surface area 2 of 813 mm^2 with a standard deviation of 36 mm^2 (figure 4.15). Compared to the same configuration with sequential impacts, we note here an increase in the total delaminated surface of 23%. Knowing that the delaminated area due to the second impactor in a sequential configuration is 23% greater than that in the single-impact case. This is an expected result, given that the total energy applied to the area surrounding the two impactors is 30 J (15 J + 15 J). The plate will be even closer to its maximum tolerable deformation and the energy dissipated will therefore be greater, resulting in a larger delaminated surface.

Experimentally, we note that, depending on the delay between the balls, the first ball in contact may lose and recover contact with the plate, or it may be the plate's vibration that repels the ball. We will look at these phenomena in more detail in Chapter 5.

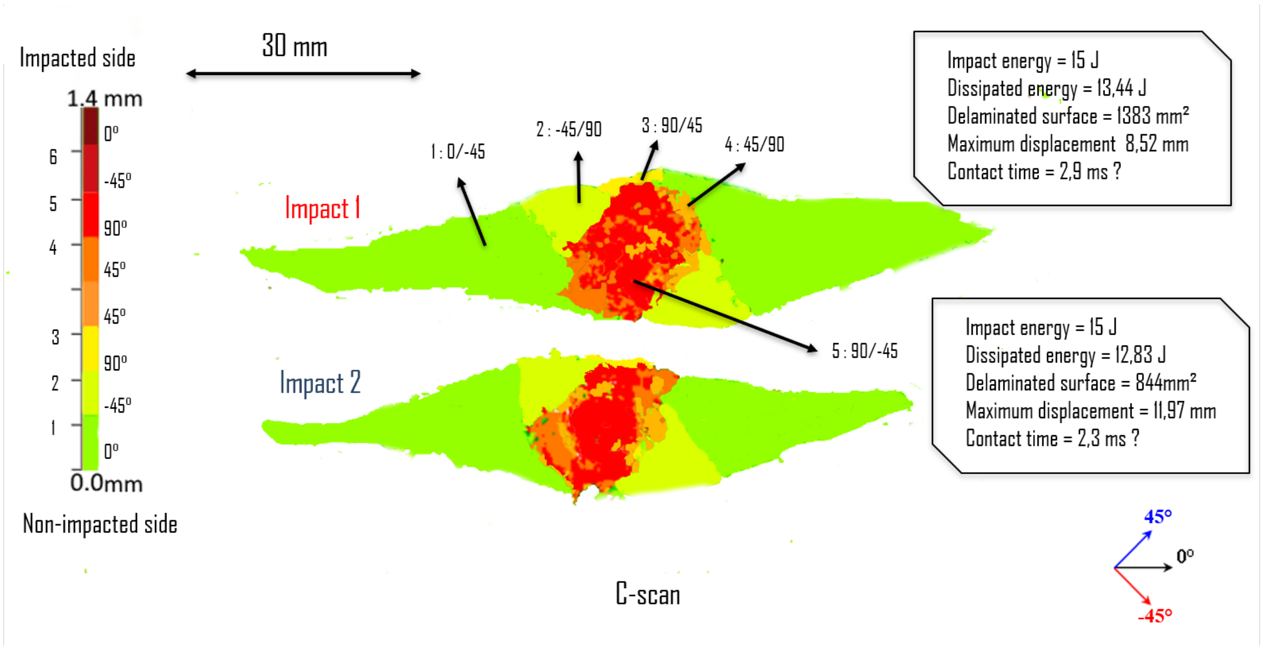

Impact energy = 15 J
Dissipated energy = 13,44 J
Delaminated surface = 1383 mm²
Maximum displacement 8,52 mm
Contact time = 2,9 ms ?

Impact energy = 15 J
Dissipated energy = 12,83 J
Delaminated surface = 844mm²
Maximum displacement = 11,97 mm
Contact time = 2,3 ms ?

Figure 4.15 – C-scan of delaminated surface : 2 simultaneous impacts without damaged surface interference (configuration Si/⌀20/15J/Ba/L/2).

4.3.2. Configuration Si/⌀20/15J/Ba/M/2

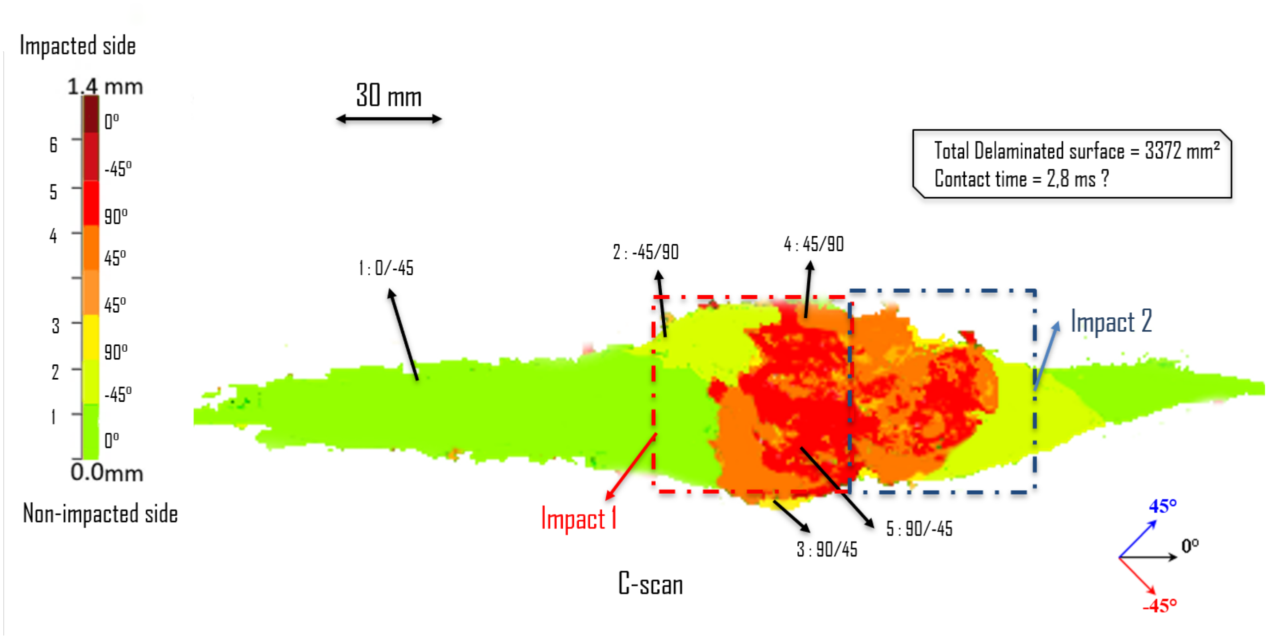

Total Delaminated surface = 3372 mm²
Contact time = 2,8 ms ?

Figure 4.16 – C-scan of delaminated surface : 2 simultaneous impacts with damaged surface interference (configuration Si/⌀20/15J/Ba/M/2).

In this configuration, we repeat the configuration Sq/⌀20/15J/Ba/M/2 with two simultaneous impacts. The total average delaminated surface is 3295 mm² with a standard deviation of 315 mm², figure 4.16. Compared to the same configuration with sequential impacts, we note here an increase in the total delaminated surface of 155%. In terms of the phenomena involved, we are approaching the configuration M/⌀10/15J/Ba/N/1 here. The fact that the total energy of 30 J has been divided over two impactors gives rise to more fiber breakage under the two impactors, which slows down the propagation of delamination in both directions. Note that the delay, even at less than 0.5 ms, is still greater than the perfect case of 0 ms difference, which is indeed the configuration M/⌀10/15J/Ba/N/1. So far, we note that this configuration is the most dangerous of those studied in this chapter in terms of delaminated surface, but the single-impact configuration with equivalent total energy remains more critical. Note that in this configuration, velocity and dissipated energy calculations are based on projectile of cannon 1, as cannons' 2 projectile is hidden by the first one from the high-speed camera, given that the two projectiles are close to each other and aligned along the y-axis and the z-axis (to which the camera is parallel).

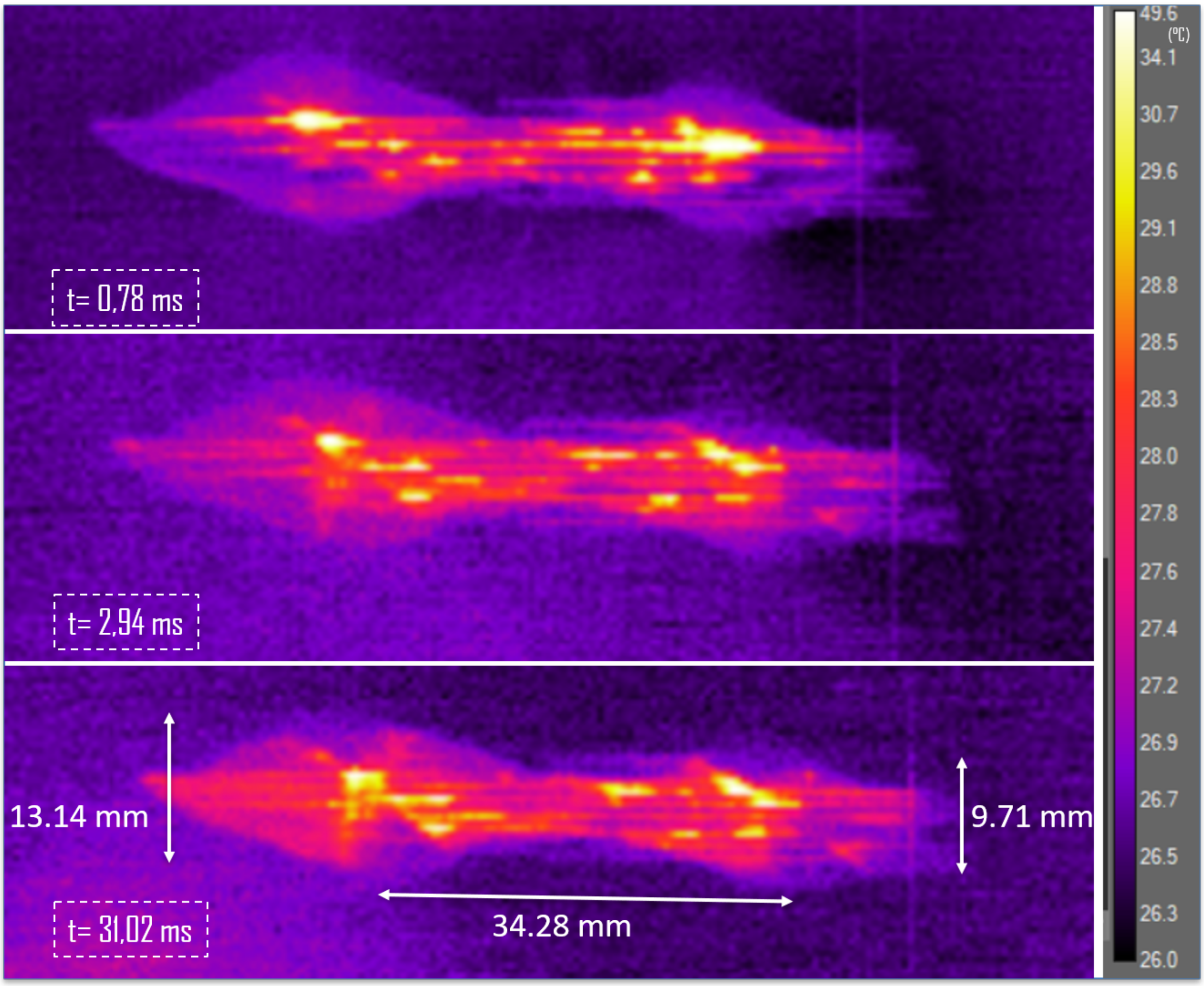

Figure 4.17 – Thermal film images : interference of matrix cracking zones.

In addition to the intersection of the delamination at the last interface noted above with the C-scans and the numerical model, using the thermal film, we obtain a new datum ; we notice interference at the level of matrix cracking produced by the two impactors, see figure 4.17. As in the case of delamination, we note the continuity created by the cracks resulting from each impact. In addition, using the thermal camera, we can see that although the distance between the centers of the impacts on the impacted face is not more than 25 mm, on the non-impacted face this distance is 34.28 mm, which can be explained by the buckling of the plate, given that these two impacts are almost at the centers of the plate, which is also very large and very flexible. There must also be a movement of the ball in the plane during impact. For fiber breakage, it is difficult in this configuration to obtain interference, since fiber breakage is generally localized under the impactor.

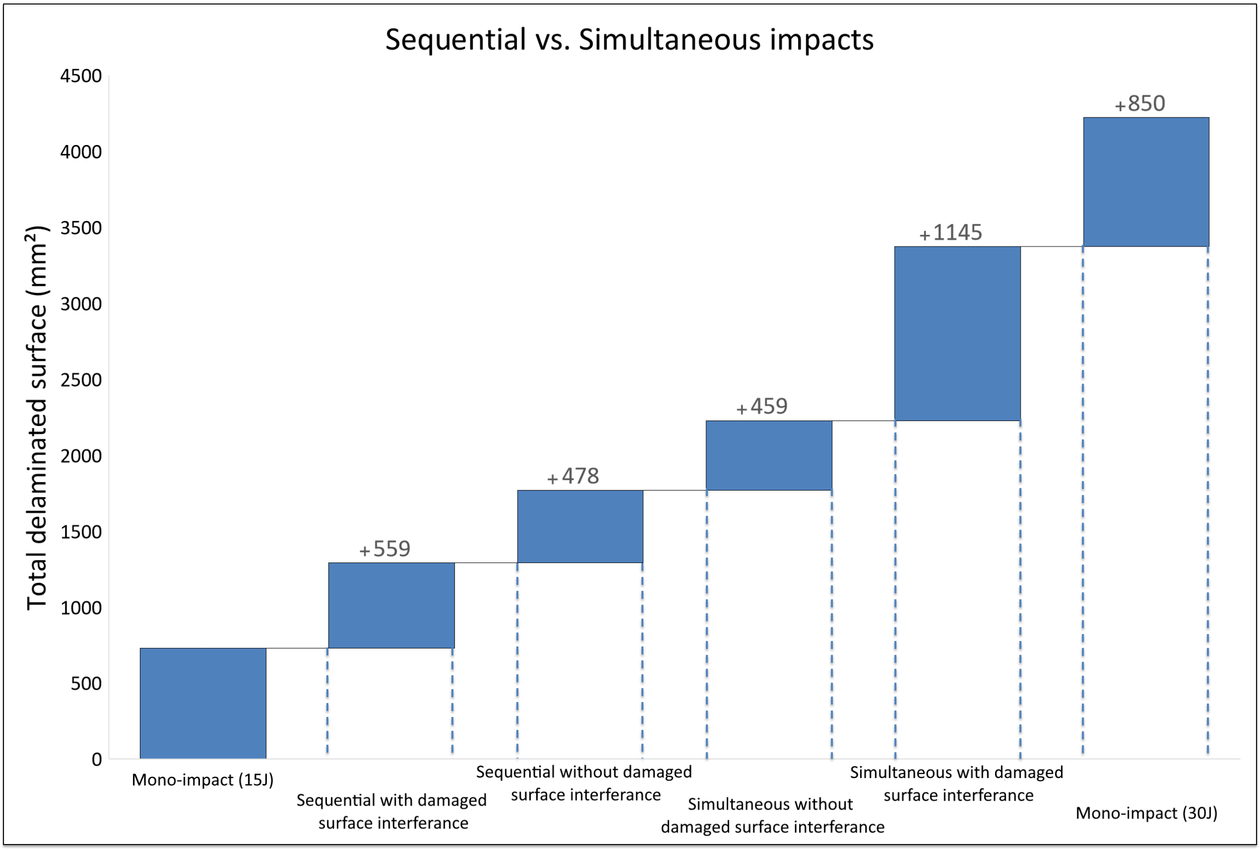

Figure 4.18 – Comparison of sequential and simultaneous impacts in terms of total delaminated area.

Finally, as shown in figure 4.18, the sequential impact configuration on a previously damaged area results in the least delaminated surface, since a large proportion of this surface is shared between the two delaminated surfaces, so the total delaminated surface is consequently smaller. Secondly, the sequential configuration, without damage interferences, delaminates more surface area but less than the simultaneous configurations (it is important to remember that these are only projected delaminated surfaces, and there may be other delaminated surfaces which may change). This is a logical result, given that when analysed by total energy applied, in a simultaneous configuration more energy is always supplied instantaneously than in a sequential configuration, the energy dissipated in a simultaneous configuration is greater and therefore creates more damage in the composite structures. Secondly, as explained in Chapter 3, delamination propagates in the direction of the fibers of the last ply, so it is expected that two impacts aligned in the same x-direction (0°) will cause more delamination than two impacts aligned in y-direction (90°), since delamination in this direction does not exceed a small area around the impactor, damage interfering is unlikely, hence the configuration of simultaneous impacts aligned at 0° generates more damage than the second configuration where impacts are aligned at 90°. The criticality of the damage (especially in terms of delaminated surfaces) is then directly linked to the multi-impact configuration studied and can vary from one case to another. It is very important to distinguish between the different configurations and the critical risks of each one.

Conclusion

In this chapter, we have explored and compared the sequential and simultaneous multi-impacts cases on composite structures, both experimentally and numerically. To conclude, the delay between impacts plays a major role in the initiation and propagation of damage in a composite structure. Moreover, simultaneous damage appears to be more critical than sequential damage. On the numerical level, we have succeeded in modeling sequential impact cases without incurring high computational costs, using the plate stabilization method after the first impact.

The findings from this chapter contribute to the broader understanding of multi-impact behavior in composite structures and provide guidance for future research focus. We then propose, for the next chapter, to examine the simultaneous character of the impacts, in order to understand the influence of impact parameters as a function of projectile delays, and finally to deduce the most critical configuration among all those studied.

Chapter 4

CHAPTER 5 :

MULTI-IMPACTS : SIMULTANEOUS IMPACTS VS. REPEATED SIMULTANEOUS IMPACTS

5. Multi-impacts : Simultaneous impacts vs. Repeated simultaneous impacts

Introduction

Following on from Chapter 4, this fifth chapter looks in more detail at the simultaneous nature of multi-impacts, assessing in-depth the role of time lag in changing the criticality of impact damage, and evaluating the influence of other parameters such as the number of impacts. The aim of this chapter is to find the most influential parameters in multi-impact cases, and to understand why we can have extremely different damage criticalities in multi-impact cases with the same classic single-impact parameters.

This chapter highlights the complexity of the phenomena at play in the case of multiple impacts, and the crucial role of DPM in providing a detailed understanding of the various parameters involved. In some cases, we carry out virtual tests that are difficult to obtain experimentally, given the precision required.

Through this chapter, we aim to provide a comprehensive overview understanding of the similarities and differences between all possible impact cases, enhancing simultaneous impacts and repeated simultaneous impacts on composite structures. This knowledge will contribute to the development of robust design strategies, testing protocols, and mitigation techniques for composite structures subjected to multi-impact loading scenarios.

5.1. Simultaneous impacts : effect of distance between impacts

To study the effect of distance between impact centers, mainly in the 90° direction where there is no interference in delaminated areas, in other directions, more tests are needed to distinguish between cases with or without interfering damage zones. In this section, we compare the delaminated surfaces in configurations with 2 simultaneous impacts at 15 J by a 20 mm diameter ball : configuration M/⌀20/30J/Ba/K/1 (where the distance between impacts is theoretically 0 mm), configuration Si/⌀20/15J/Ba/L/2 (where the distance between impacts is 40 mm), configuration Si/⌀20/15J/Ba/O/2 (where the distance between impacts is 100 mm) and configuration Si/⌀20/15J/Ba/P/2 (160). The first two configurations were presented in chapters 3 and 4, we detail below the two other configurations, the impactors position is shown in figure 5.1.

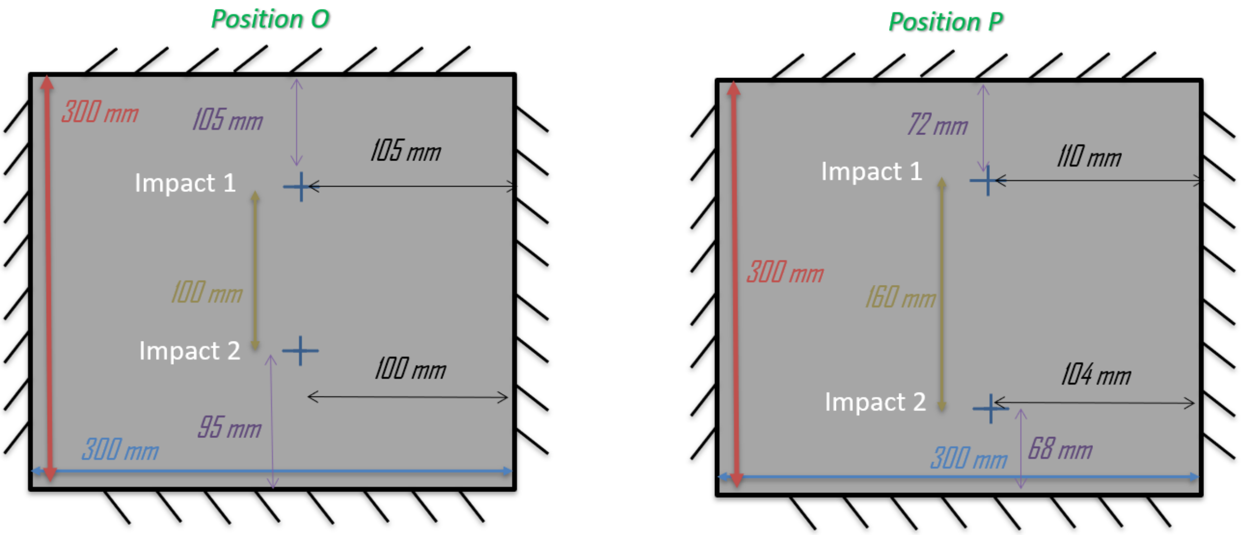

Figure 5.1 – Impact positions for configurations O and P.

Configuration Si/⌀20/15J/Ba/O/2

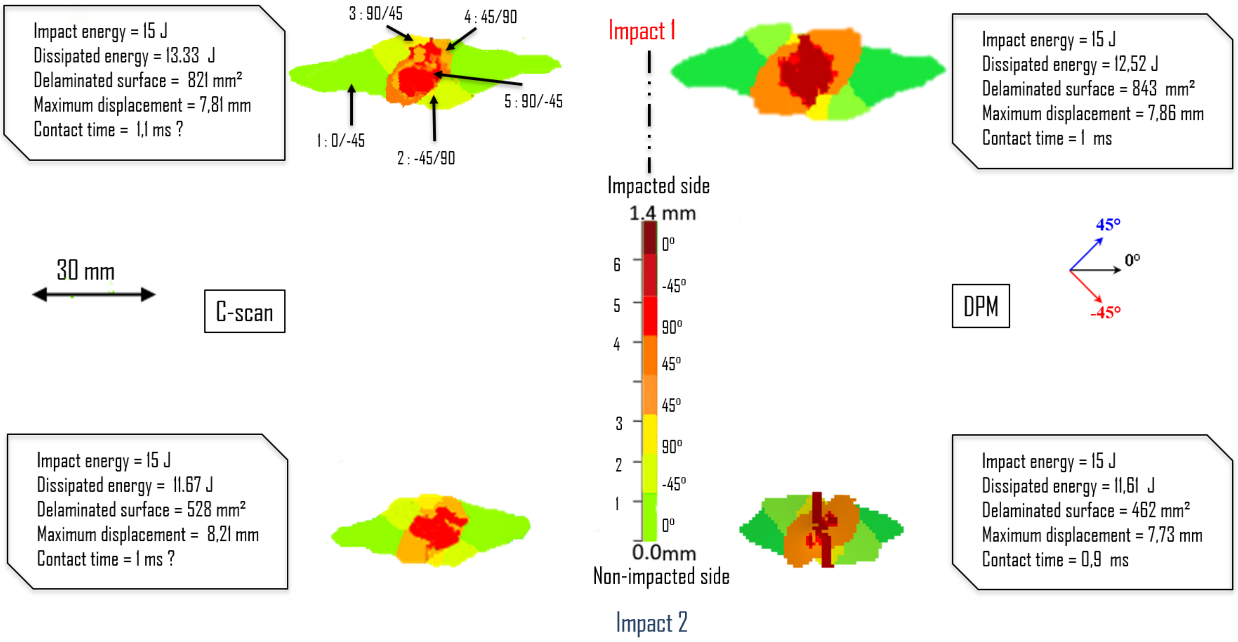
Impact energy = 15 J
Dissipated energy = 13.33 J
Delaminated surface = 821 mm²
Maximum displacement = 7,81 mm
Contact time = 1,1 ms ?

Impact energy = 15 J
Dissipated energy = 12,52 J
Delaminated surface = 843 mm²
Maximum displacement = 7,86 mm
Contact time = 1 ms

Impact energy = 15 J
Dissipated energy = 11.67 J
Delaminated surface = 528 mm²
Maximum displacement = 8,21 mm
Contact time = 1 ms ?

Impact energy = 15 J
Dissipated energy = 11,61 J
Delaminated surface = 462 mm²
Maximum displacement = 7,73 mm
Contact time = 0,9 ms

Figure 5.2 – C-scan vs. DPM of the 100 mm distance between impact centers configuration (configuration Si/⌀20/15J/Ba/O/2).

In this configuration, the distance between the impactors in the 90° direction is 100 mm. The average dissipated energy for the first projectile is 12.97 J with a standard deviation of 0.80 J, resulting in an average maximum displacement of the impactor of 7.95 mm (with a standard deviation of 0.17 mm). We measure an average total delaminated surface area of 813 mm^2 with a standard deviation of 39 mm^2 (figure 5.2). The average dissipated energy for the second projectile is 11.63 J with a standard deviation of 0.11 J, resulting in an average maximum displacement of the impactor of 8.08 mm (with a standard deviation of 0.2 mm). We measure an average total delaminated surface area of 531 mm² with a standard deviation of 19 mm² (figure 5.2). Compared to configuration Si/⌀20/15J/Ba/M/2 (where the distance between impacts is 22 mm along x-direction), we obtain a 150% smaller total delaminated area in this configuration, this is obvious, since the interaction at the delamination level of interface 1 does not occur (as the two impacts are not aligned in the 0° direction), the total delaminated surface is then the sum of the delaminated surfaces due to the two impacts and not the union of the delaminated surface as in configuration Si/⌀20/15J/Ba/M/2. Compared to configuration Si/⌀20/15J/Ba/L/2 (where the distance between impacts is 40 mm along y-direction), we obtain a 47% smaller total delaminated area in this configuration. This shows that the greater the distance between impacts, the less important the multi-impact character, since the total delaminated surface is lower. These experimental results correlate well with the numerical model, see figure 5.2.

Configuration Si/⌀20/15J/Ba/P/2

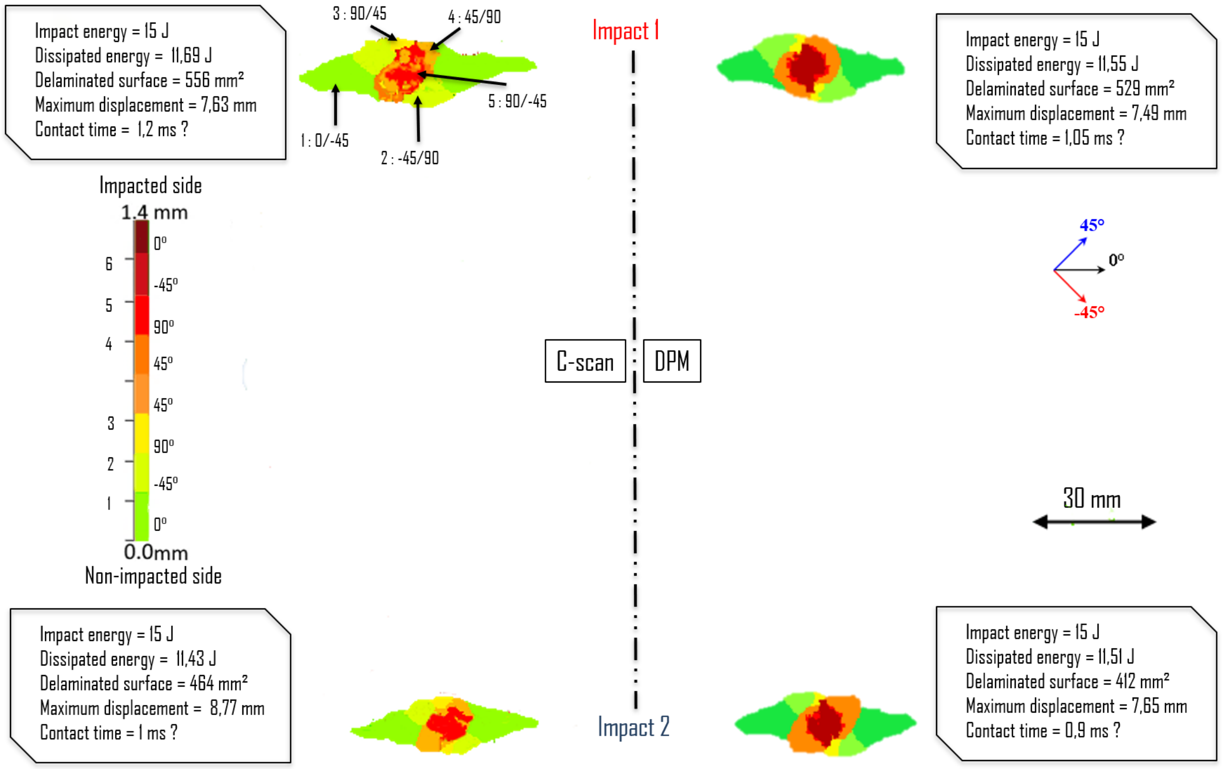

Figure 5.3 – C-scan vs. DPM of the 160 mm distance between impact centers configuration (configuration Si/⌀20/15J/Ba/P/2).

In this configuration, the distance between the impactors in the 90° direction is 160 mm. The average dissipated energy for the first projectile is 12.97 J with a standard deviation of 0.80 J, resulting in an average maximum displacement of the impactor of 7.95

mm (with a standard deviation of 0.17 mm). We measure an average total delaminated surface area of 813 mm^2 with a standard deviation of 39 mm^2 (figure 5.3). The average dissipated energy for the second projectile is 11.63 J with a standard deviation of 0.11 J, resulting in an average maximum displacement of the impactor of 8.08 mm (with a standard deviation of 0.2 mm). We measure an average total delaminated surface area of 531 mm^2 with a standard deviation of 19 mm^2 (figure 5.3). Compared to configuration Si/⌀20/15J/Ba/O/2, we notice 30% less delaminated surface, which confirms that the greater the distance between impacts, the less important the multi-impact character. To explain this, we can observe with the numerical model the difference between the displacement along z of the plate in configuration Si/⌀20/15J/Ba/L/2 and in this configuration, figure 5.4, where displacement is much greater in configuration Si/⌀20/15J/Ba/L/2, we can clearly identify this difference at t = 0.6 ms. Importantly, here we only show the difference between plate vibration in the two different configurations. We do not directly associate the greater displacement in configuration Si/⌀20/15J/Ba/L/2 with the larger delaminated area. Indeed, in the configuration Si/⌀20/15J/Ba/O/2, we are closer to the fixtures, so the tolerated displacement is smaller. But it is clear that we haven't yet reached the displacement limits in either configuration. Finally, in configuration Si/⌀20/15J/Ba/L/2, we apply an equivalent of 30 J over a smaller area than in the other configuration, so local damage is inevitably greater.

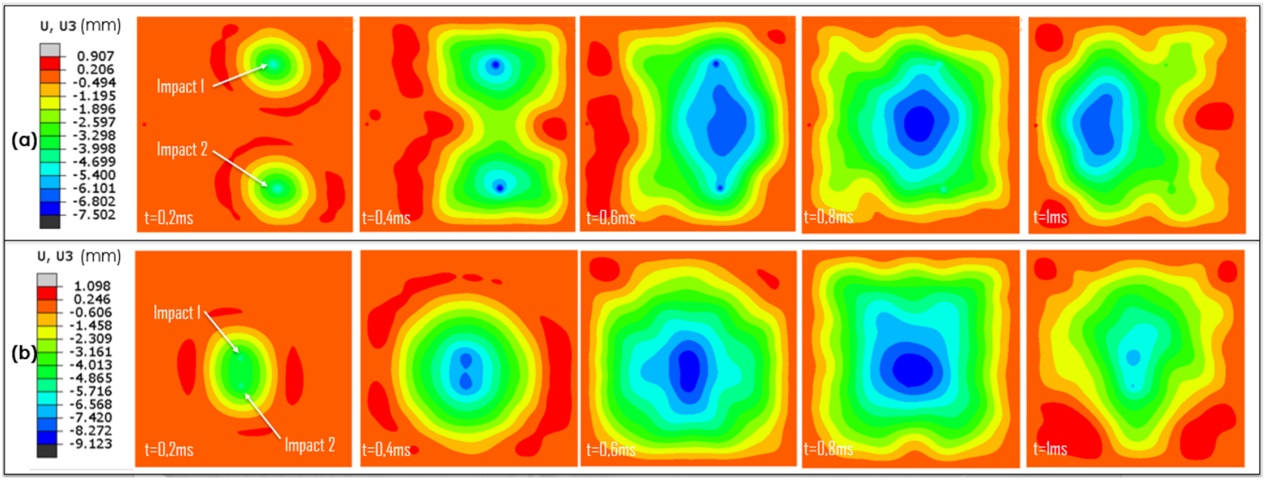

Figure 5.4 – z-displacement : (a) configuration Si/⌀20/15J/Ba/P/2, (b) configuration Si/⌀20/15J/Ba/L/2.

In conclusion, we confirm that the greater the distance between impacts, the more we tend towards a single-impact configuration ; 2 simultaneous impacts are equivalent to twice a single impact, see figure 5.5. The smaller the distance between impacts, the more energy is dissipated locally and the greater the resulting damage. Except in the case of an interspace offset following the 0° direction, where it becomes more important to differentiate between interfered and non-interfered damage zones, if there is interference we then expect a union of the delaminated interface 1, which will then reduce the size of the delaminated zone compared to another configuration without interference of the closest possible delaminated zones.

In our case, we note that from 160 mm between impact centers, the multi-impact character does not play an additional role compared to a single impact (even if it is slightly less than (2 × mono-impact), but the difference is not significant in view of the uncertainties). It should be noted that this result obviously depends on impact energy, projectile mass and velocity, material, stacking sequence, plate thickness and shape, etc. The configuration Si/⌀20/15J/Ba/N/2 (distance between impacts of 102 mm, 70 mm along x and 75 mm along y) confirms that these conclusions are valid for directions other than 90° by introducing the case of 22 mm between the impacts centers along x (Si/⌀20/15J/Ba/M/2). We plot the results of Si/⌀20/15J/Ba/N/2 configuration in figure 5.5 as a function of the greatest distance between x-direction and y-direction to study the effect in one of the two directions, however, it seems that whatever the choice for this configuration we will almost always follow the same power law (see figure 5.5) as the other configurations where the offset is only in the 90° direction. Additionally, the delaminated surface in the 100 mm case (Si/⌀20/15J/Ba/O/2) is comparable to the other configuration with 100 mm distance between impacts (Si/⌀20/15J/Ba/N/2), which may be consistent with the assumption that distance plays the same role in all directions in configurations without interfering damaged zones.

As a perspective, it would be necessary to look at other damage forms, and in particular fiber breakage, and eventually residual strength.

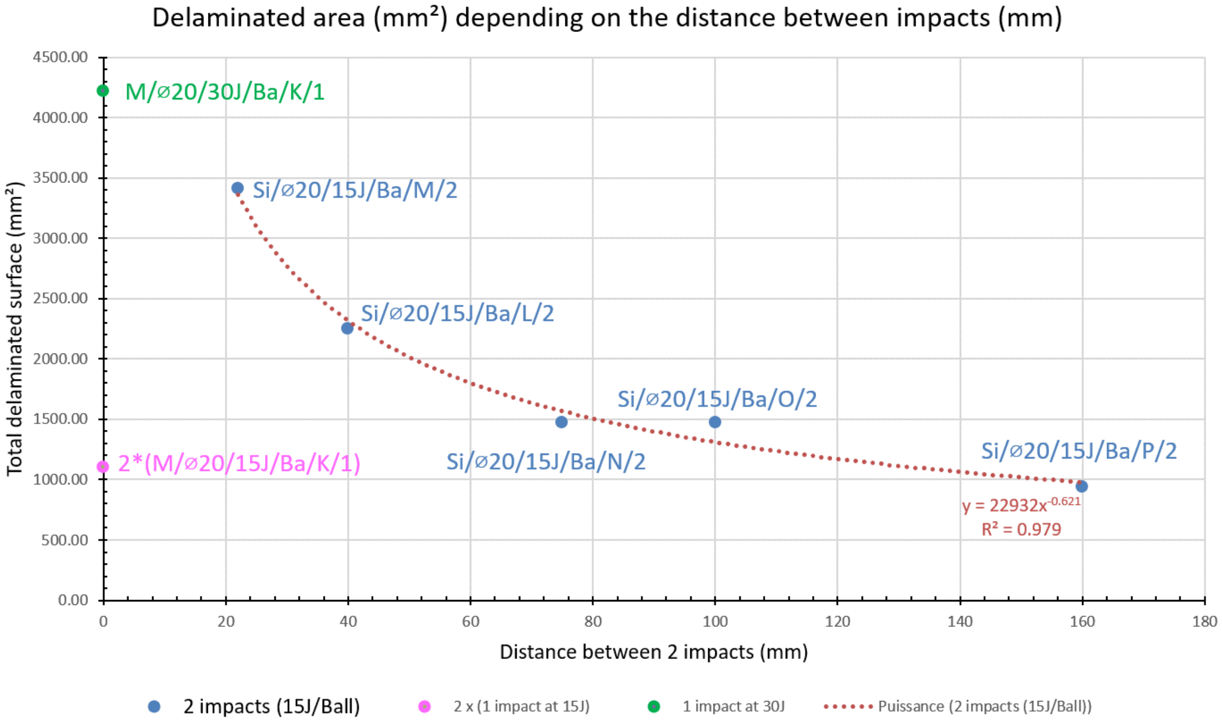

Figure 5.5 – Delaminated area vs. the distance between impacts centers.

5.2. Simultaneous impacts : effect of time lag

During our research, we noticed that with the same impact parameters, the delaminated surfaces differ according to the time lag between impacts, even in a simultaneous impacts configuration. As shown in figure 5.6, in configuration Si/⌀20/15J/Ba/N/2, for the same energy/velocity/projectile size and distance between impacts, the delaminated surface changes as a function of the time difference between impacts.

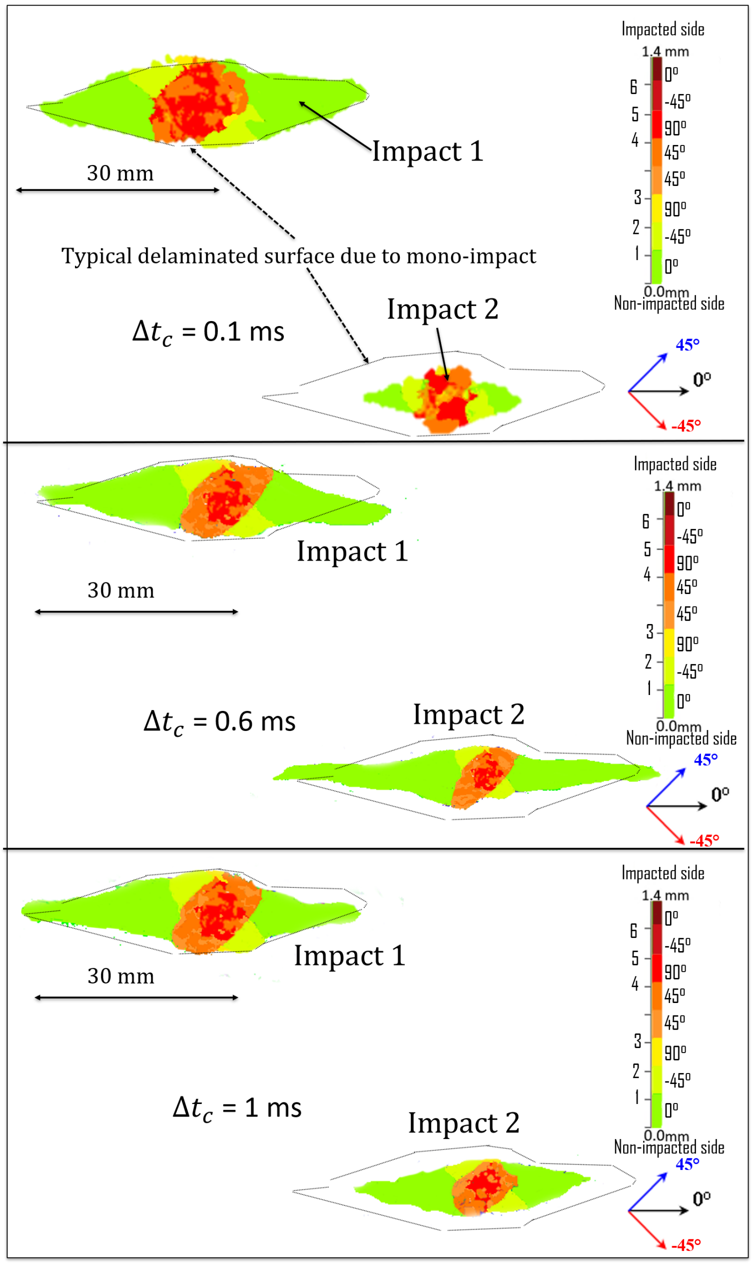

Figure 5.6 – Effect of time lag on delaminated area (C-scan), Si/⌀20/15J/Ba/N/2.

To better understand the reason, we used the numerical model to precisely follow the phenomena involved. Initially, the two projectiles are placed at the same distance from the plate. We call Δt_c the time difference at the beginning of contact between the projectile and the plate, see figure 5.7. We note that at 0.21 ms time lag (which is close to the maximum deformation state in the case of a single impact), the second impactor generates a very large delaminated surface. This is called constructive damage, where the displacement of the second impactor is added (in the same direction [-z]) to that created by the first impactor. In contrast, at 1.45 ms, when the plate is no longer in contact with the first impactor and close to its maximum displacement in the opposite direction to the direction of impact, the second impactor generates less delamination, i.e. a state of destructive damage in which a surplus of energy from the second impactor is transformed into elastic energy to drive the plate back to its 0 displacement and then in the direction of impact. Between these two configurations, at a time lag of 0 ms, the two impactors have a uniform displacement and generate no particular damage state (the difference between the two delaminated surfaces in this case is directly linked to the distance of the impact centers from the edges of the plate, as we observed in chapter 3 : impacts towards the center of the plate are smaller). We can link constructive and destructive damage states to the displacement of the second point of impact. Indeed, we note that if the displacements are additive in the same direction, this will result in a constructive damage state. In the opposite case, where the displacements are in opposite directions, sustaining the displacements will lead to a destructive damage state for the second impact. All this highlights the crucial role played by time lag, which in most configurations results in a larger total delaminated area than a single impact.

Following the delaminated surface caused by the second impactor, we observe that constructive displacement leads to a larger delaminated surface, whereas destructive displacement results in a smaller delaminated surface. This phenomenon can be attributed to the conversion of the ball's kinetic energy into elastic energy. However, as the displacement approaches its maximum value, less energy can be stocked as elastic and a higher proportion of energy is dissipated, leading to increased damage. We do not notice much difference in the delamination created by the first impactor, as the ball generally reaches its maximum load at around 0.21 ms. To check whether there will be a change in the delaminated surface of the first impactor if the time lag between the two impactors is less than 0.21 ms, we ran a new calculation with a time lag of 0.21 ms. We effectively notice a change in the delaminated surface due to the first impactor, see figure 5.8.

This configuration is potentially the most dangerous, since the loading from the second impact comes in addition to the maximum displacement generated by the first impactor. We are convinced that the delamination of the second impact is actually much greater, it is just that in the numerical model there was an early fiber break (which greatly reduces the delaminated surface, as explained in configuration M/⌀20/30J/Ba/K/1). To account for this error, we calculate the ratio of the delaminated surface at the splinter level to the total delaminated surface in all the C-scans conducted thus far. On average, we find that over 50% of the delaminated surface originates solely from the splinter. This implies that for the current configuration (Δt_c

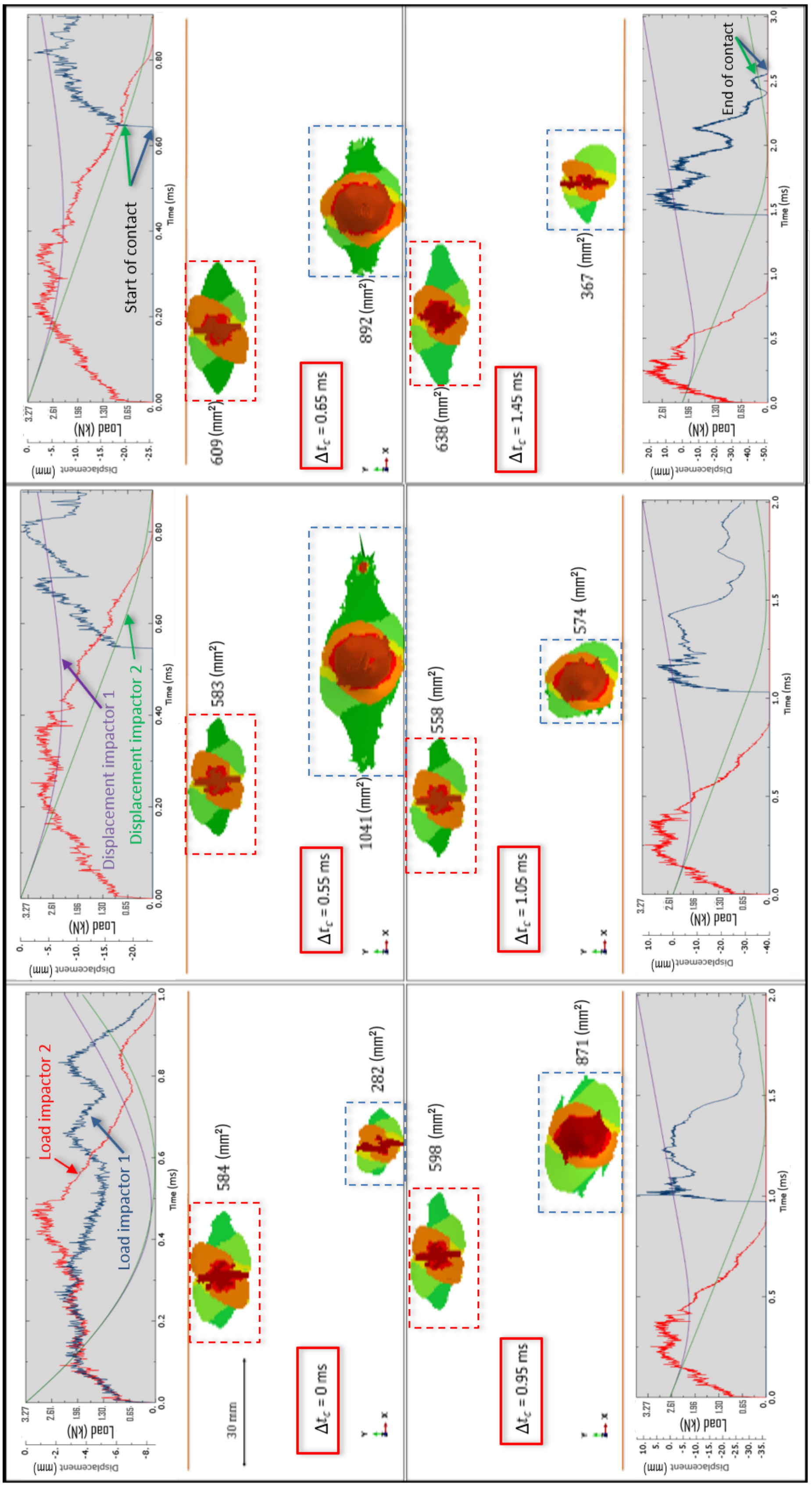

Figure 5.7 – Effect of time lag on delaminated area (DPM).

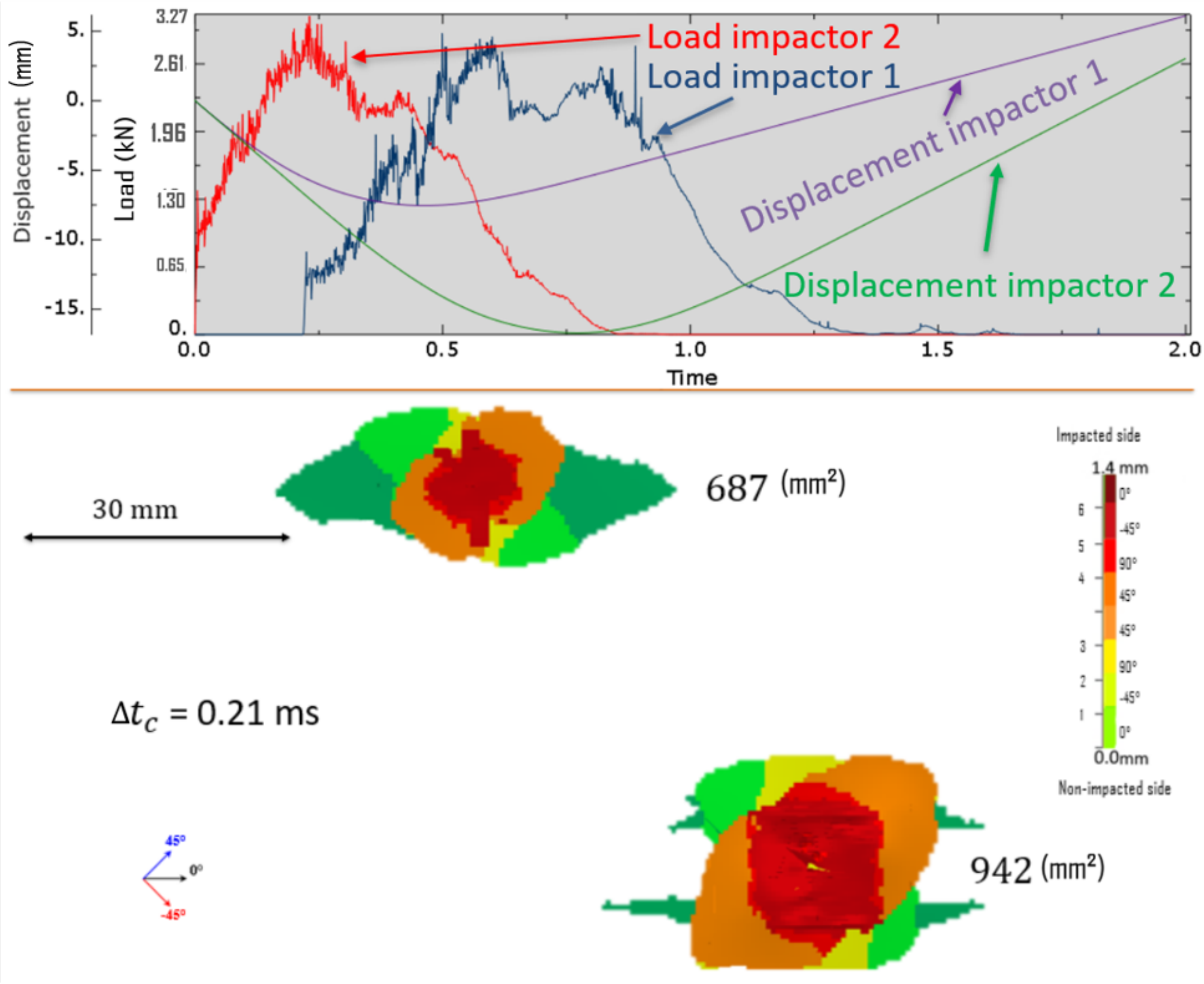

Figure 5.8 – Effect of time lag on delaminated area ($\Delta t_c = 0.21$ ms).

$= 0.21$ ms), the actual delaminated surface for the second impact can reach 1413 mm^2, resulting in a total delaminated surface of 2100 mm^2 (as a perspective to this point we can try replacing C3D8 elements with C3D8I in order to better reflect the bending behavior of a single element in the out-of-plane direction), confirming the same results as previously reported. Compared to this configuration ($\Delta t_c = 0.21$ ms), we notice that the greater the time lag between two impacts, the smaller the total delaminated area, see figure 5.9. It should be noted that the results of this figure are valid only for different values of Δt_c. For the case of two perfectly simultaneous impacts, we notice that it does not follow the law announced in the figure since the displacements are homogeneous and do not produce any particular case of extreme loading, see figure 5.7 at $\Delta t_c = 0$ ms.

Finally, it appears that time lag between the start of impactors movement is an essential multi-impacts parameter, but the time lag between the projectile/plate contact of two impacts is more crucial, which allows to take into account two parameters at the same time : the time lag between the start of impactors movement and plate

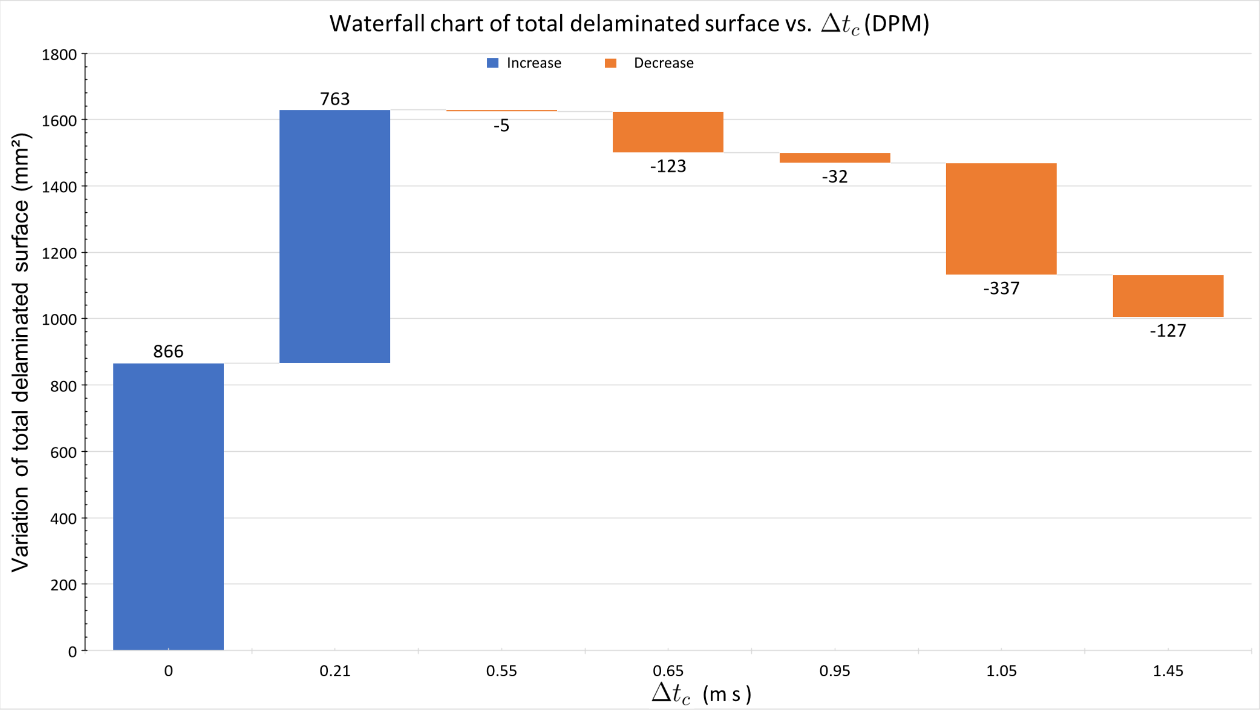

Figure 5.9 – Variation of delaminated area as a function of time lag.

vibration. Obviously, this depends on plate stiffness (thickness) and other impact parameters (energies, etc.), as shown in configurations at 30 J in total, where time lag and plate vibration are studied at low impact energies and where Δt_c plays no role at very low energies (see section 5.3.4. Five simultaneous impacts).

We can conclude that for two simultaneous impacts, if the value of Δt_c is strictly greater than 0 and less than 0.21 ms (which corresponds to the maximum effort in the case of a single impact), the more two impacts are delayed in time, the greater the delaminated surface due to the second impactor. If then Δt_c is strictly greater than 0.21 ms and less than 1 ms, the more two impacts are delayed in time, the smaller the delaminated area, see figure 5.9. This principle is repeated throughout the vibration of the plate. For perfectly simultaneous impacts, the second impactor generates the least delaminated surface. Note that this statement is only valid for the same distance between two impacts (or a distance of less than 160 mm in our case). If this is not the case, we may be in a situation where the multi-impact character does not play a supplementary role, and the time lag between impacts will not make any difference either.

5.3. Simultaneous impacts : number of impacts effect

5.3.1. Mono-impact and two simultaneous impacts

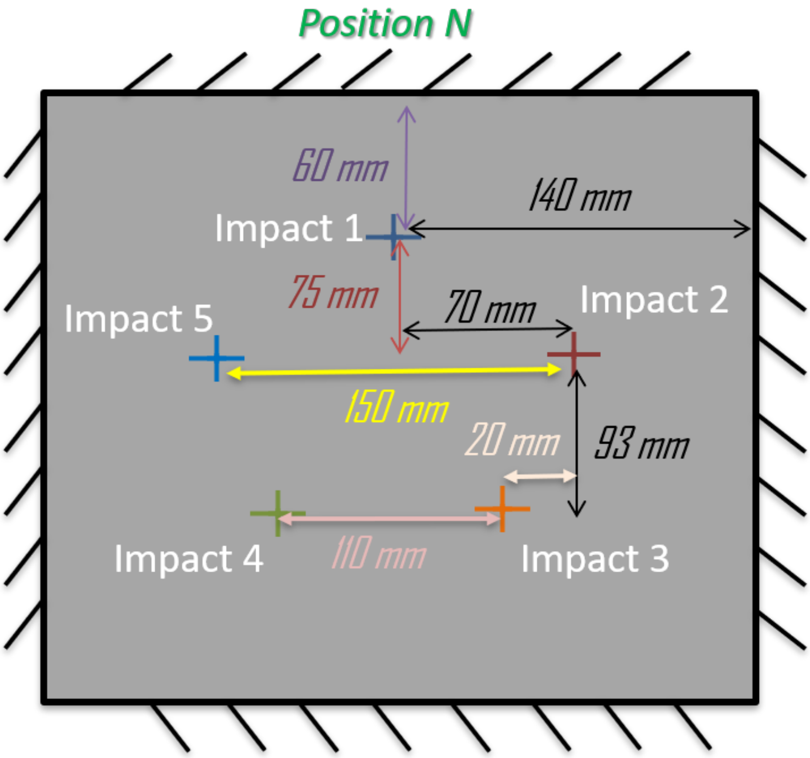

Figure 5.10 – Impact positions (N).

As previously stated, impact damage varies according to the distance between impacts, impact energy and projectile size, among other factors. Thus, to study only the effect of the number of impacts, we set the position of the impacts (see figure 5.10), with 20 mm diameter balls at an energy of 15 J simultaneously, the maximum time lag between the first and last ball arriving does not exceed 1 ms in all experimental cases. We decided to investigate only the simultaneous character, which is more critical than the sequential and more original for comparison with single-impact. Before proceeding with this study, we propose to summarize the influence of impact configuration and projectile size on the configurations already studied.

As shown in figure 5.11, where we rely on configurations Sq/⌀20/15J/Ba/M/2, Si/⌀20/15J/Ba/M/2 and M/⌀20/30/T/N/1 to fix and minimize the difference between the impact parameters. We note that the case of a single impact is the most critical, with 30 J dissipated instantaneously and locally on the composite structure (it is not totally dissipated, but it is energy taken from the ball, after perforation, the ball must still have residual kinetic energy), followed by two simultaneous impacts at a distance of 22 mm in the 0° direction, where we deliver 15 J per ball, which is equivalent to deliver 15 J per side with shared delaminated surface between the 2 impacts (union of the delaminated surface and not the sum), the damage generated

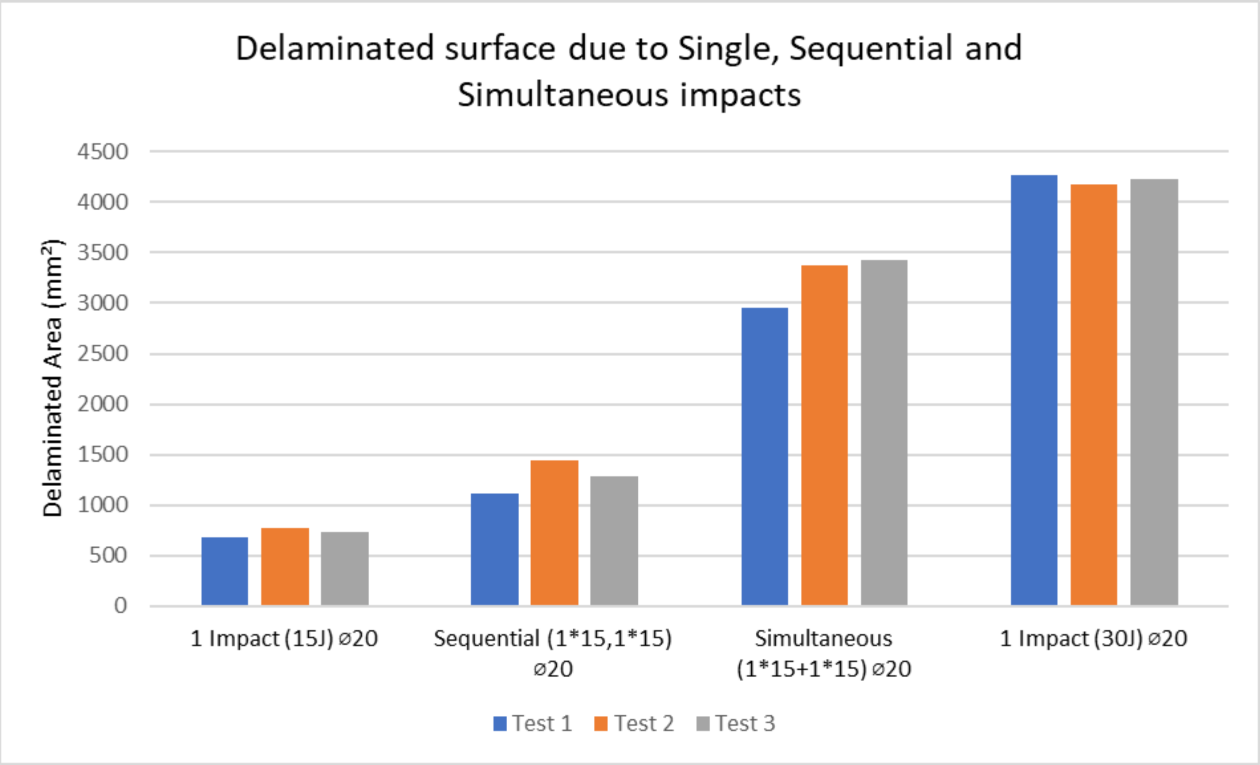

Figure 5.11 – Delaminated area due to mono-impact, sequential and simultaneous impacts.

locally represents that of an impact at 15 J (which is naturally less significant than that at 30 J and moreover shared between the two impact zones). We believe that the very large surface area delaminated in the case of a single impact is due to the phenomenon of delamination creation of interface 1 in the case of ball penetration, which is not only linked to matrix cracking but also to the direct contact between the ball and the last ply, which tears it off more than the delamination phenomenon linked to matrix cracking can do unaided. Then there is the sequential case, where only 15 J is dissipated instantaneously, which causes less damage. Finally, for a mono-impact at 15 J, only 15 J can be dissipated in total, so the least amount of damage is expected in the composite structure.

We now propose to summarize the effect of projectile size, taking into account configurations where the only parameter that changes is the size of the ball : configuration M/⌀20/15J/Ba/N/1, configuration Si/⌀20/15J/Ba/N/2, configuration M/⌀10/15J/Ba/N/1 and configuration Si/⌀10/15J/Ba/N/2. In all cases, impact with a 10 mm ball is more critical than impact with a 20 mm ball, see figure 5.12. In fact, damage is more localized in the case of the 10 mm ball and leads more easily to fiber breakage. This is particularly due to the velocity of the small ball (87 m/s), which is about 3 times greater than that of the 20 mm ball (30 m/s). The response of the composite structure is dominated by the propagation of a deformation wave through the thickness of the material, in which the structure does not have time to react, leading to localized damage. At the time of perforation initiation at the center of the impact, a smaller ball will perforate earlier than a larger ball (a small opening in the center

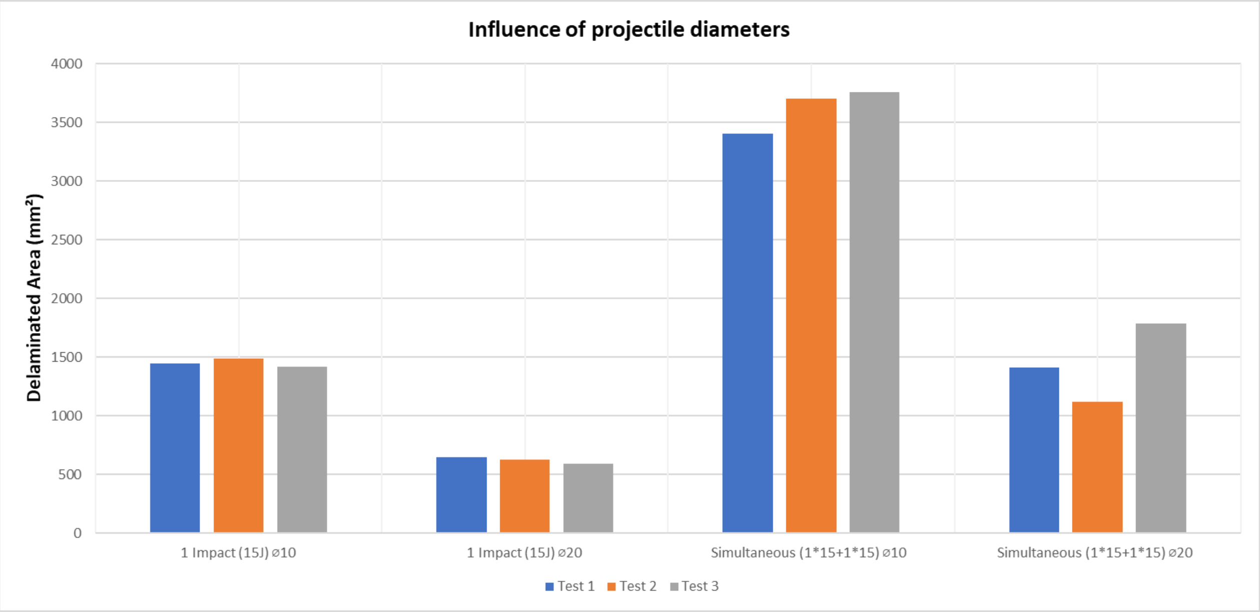

Figure 5.12 – The effect of projectile size on the multi-impact response of composite structures.

larger than its diameter will be sufficient), which has to wait for a larger defect to perforate the plate.

5.3.2. Three simultaneous impacts

In this configuration (Si/⌀20/15J/Ba/N/3), we perform 3 simultaneous impacts with 20 mm diameter balls at 15 J per ball (which corresponds to a velocity of 30 m/s per ball), the maximum time lag between the first and last ball arriving does not exceed 1 ms in all experimental case, the positions of impact are shown in figure 5.10. As we will discuss below, from 3 simultaneous impacts onwards, the vibratory character of the plate is strongly present and handles almost all the interactions between the different impacts. It is therefore important to monitor the plate's displacement during impact, as well as the time lag between the projectiles, in order to be able to follow and analyze the interactions.

As shown in the C-scans of figure 5.13, the delaminated area due to impactor 2 is 66% greater than that due to the first impactor, and the delaminated area due to impactor 3 is 77% greater than that due to the first impactor. This is partly explained by the extra energy dissipated when contact is re-established on the second and third impacts (figure 5.14). As illustrated in figure 5.14, an atypical force-displacement curve is found, reflecting the complexity of the phenomena involved in the case of 3 simultaneous impacts, the green hatched part of the curve indicates negative dissipated energy, i.e. energy released by the plate to the ball. We can predict that there will be another case where this vibration causes the ball and plate to come out of contact, but without contact being re-established. In this case, there will be less delamination

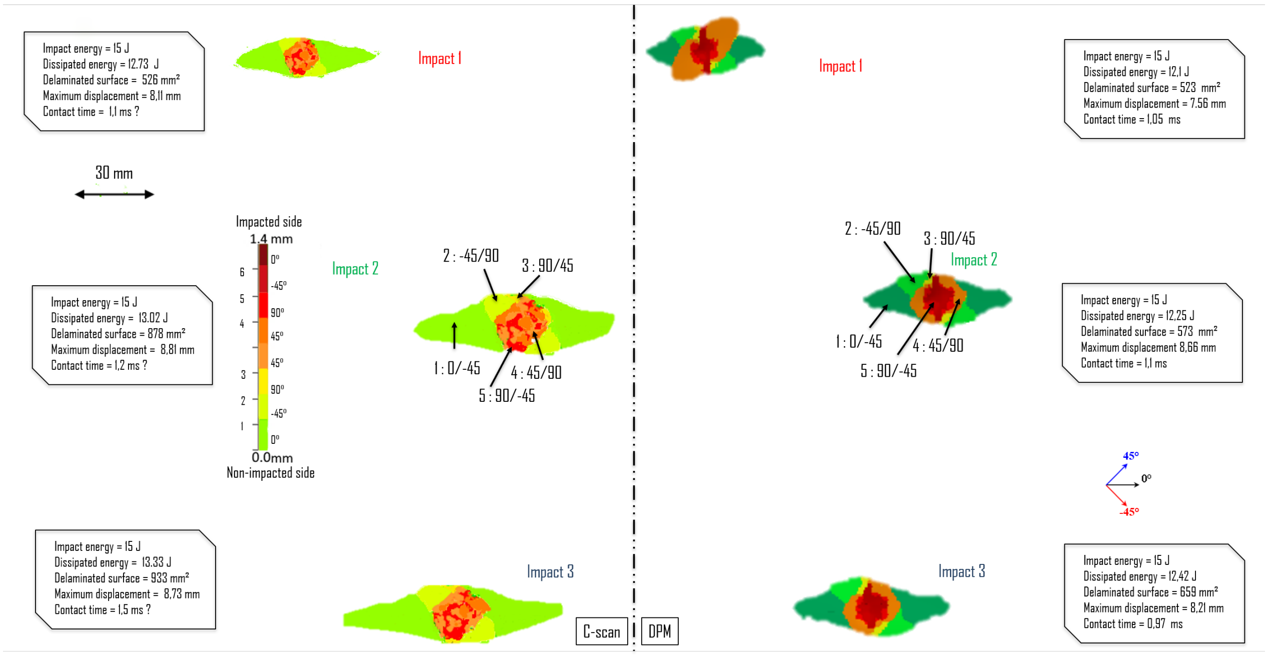

Figure 5.13 – C-scan of three simultaneous impacts : Experimental vs. DPM (configuration Si/⌀20/15J/Ba/N/3).

than in a single-impact case, since the force applied is lower and the energy dissipated is also lower.

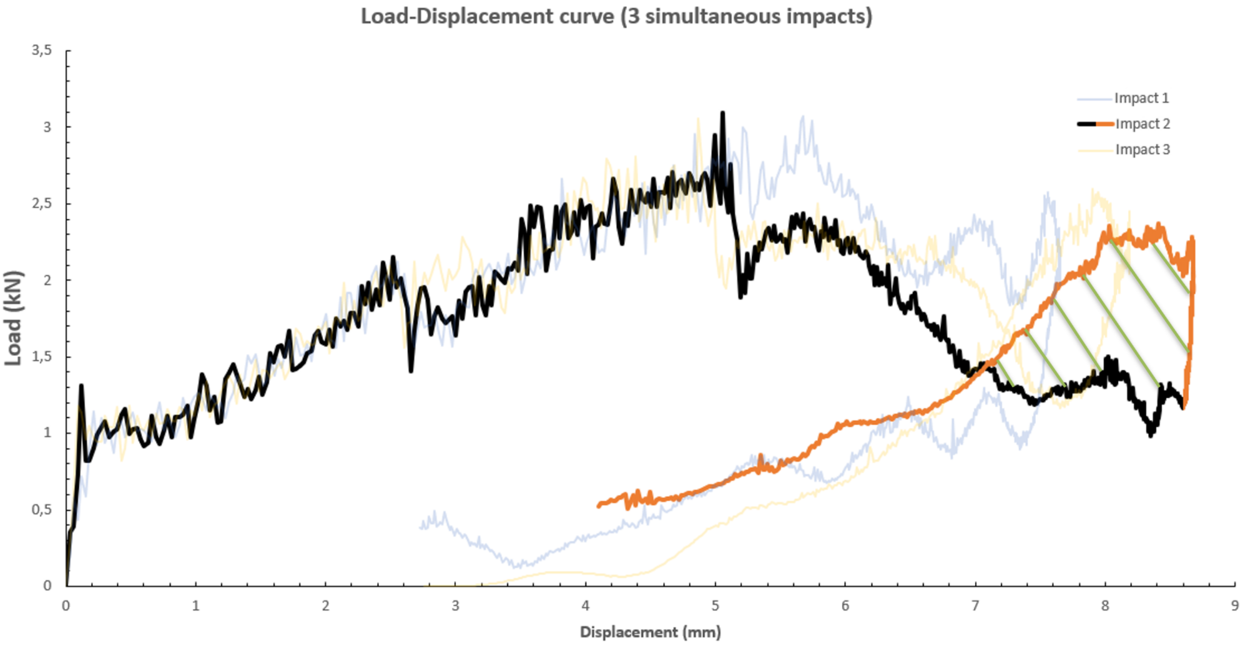

Figure 5.14 – Load-displacement curve for 3 simultaneous impacts, Si/⌀20/15J/Ba/N/3.

5.3.3. Four simultaneous impacts

In this configuration (Si/⌀20/15J/Ba/N/4), we perform 4 simultaneous impacts with 20 mm diameter balls at 15 J per ball (which corresponds to a velocity of 30 m/s per ball), the maximum time lag between the first and last ball arriving does not exceed 1 ms in all experimental cases, in the positions of impact shown in figure 5.10.

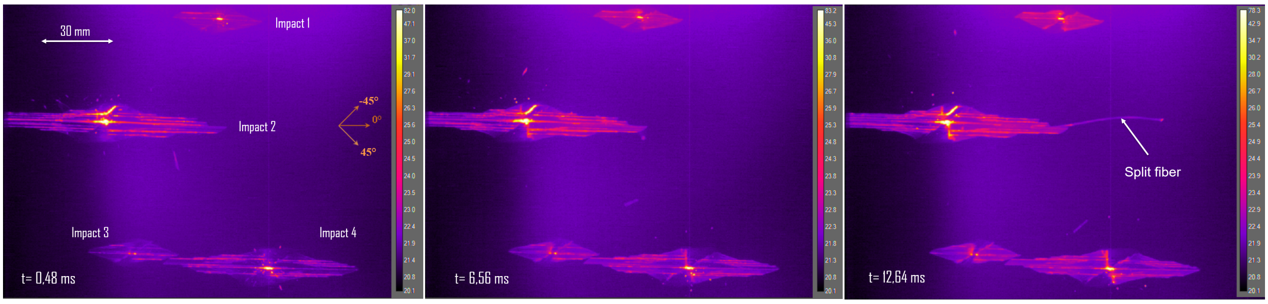

Figure 5.15 – Temperature variations during 4 simultaneous impacts (configuration Si/⌀20/15J/Ba/N/4).

As shown in the figure 5.15 (where the camera is placed behind the plate, on the non-impacted side), the temperature rises to values close to the plate perforation cases already treated (configuration M/⌀20/30J/Ba/K/1 for example, figure 3.35), we also see a split fiber at t = 12.64 ms, which means perforation may be imminent, we conclude that with the same energy per ball and on the same plate using the same classical impact parameters the damage created per impact zone can be completely different depending on the vibration of the plate at the moment of impact and so the multi-impact parameter (MIP) Δt_c. Compared with a single-impact case, we observe the same damage scenarios per impact zone. We note that, for impact 3 and 4, even though the damage caused by matrix cracking and delamination are very close, there was no interference. Moreover, with a higher acquisition frequency, we can measure the value of Δt_c by calculating the time delay between the appearance of the thermal signatures associated with the different impacts (which we were unable to do with precision, as the camera at our disposal is not fast enough).

Moving to the numerical model, for ($\Delta t_c = 0$ ms) the difference between the surfaces delaminated by impact is marginal, as shown in figure 5.16, compared to configurations with Δt_c different from zero, which are more critical, as shown in figure 5.15. Following energy dissipation in these cases in detail is complicated and only made possible by the use of a numerical model. To further enrich this study, we have chosen to carry out the perfectly simultaneous cases using the DPM (thanks to its reliability) and the delayed cases experimentally.

As shown in figure 5.17(a) several total loss/recovery of contact occurred after the classic impact time in a single-impact case (1 ms), implying that several overloads of force were applied to the plate. Before the 1 ms, for impact 3, we notice a drop in the force applied and then a recharge as there were two impacts of 15 J applied per

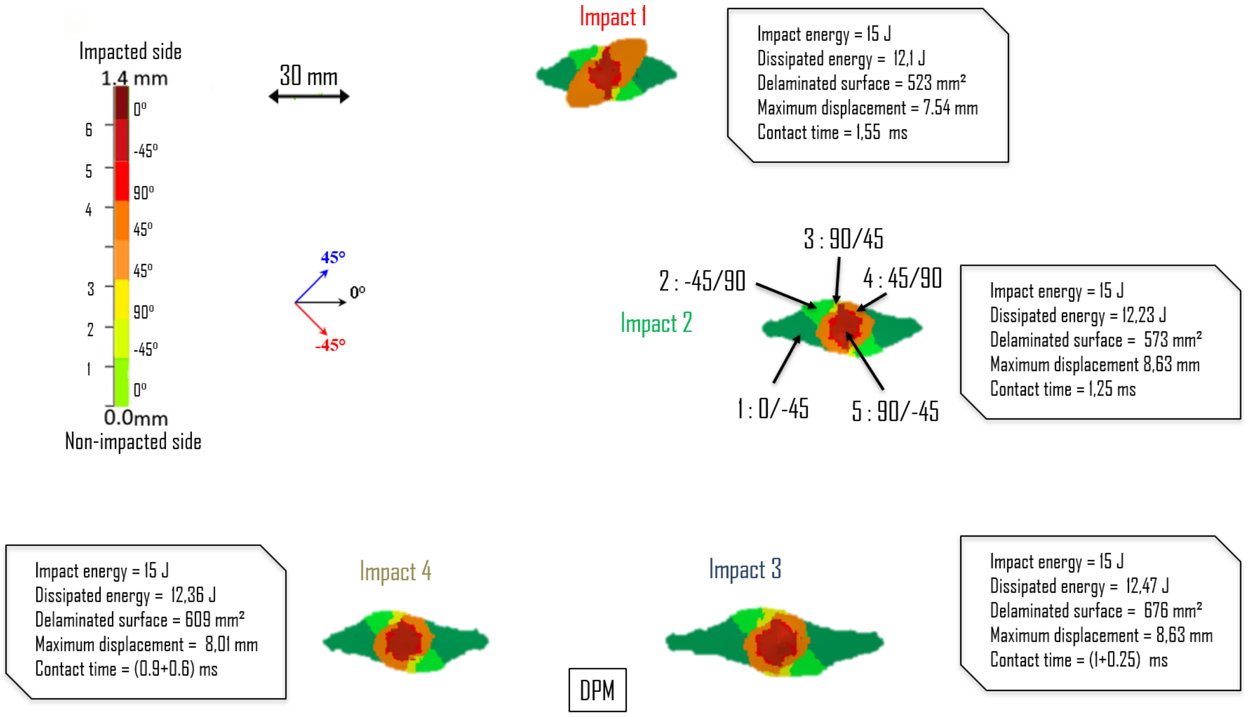

Impact energy = 15 J
Dissipated energy = 12,1 J
Delaminated surface = 523 mm²
Maximum displacement = 7.54 mm
Contact time = 1,55 ms

Impact energy = 15 J
Dissipated energy = 12,23 J
Delaminated surface = 573 mm²
Maximum displacement 8,63 mm
Contact time = 1,25 ms

Impact energy = 15 J
Dissipated energy = 12,36 J
Delaminated surface = 609 mm²
Maximum displacement = 8,01 mm
Contact time = (0.9+0.6) ms

Impact energy = 15 J
Dissipated energy = 12,47 J
Delaminated surface = 676 mm²
Maximum displacement = 8,63 mm
Contact time = (1+0.25) ms

Figure 5.16 – DPM C-scan of 4 simultaneous impacts ($\Delta t_c = 0$ms), Si/⌀20/15J/Ba/N/4.

duration of 0.5 ms (this partly explains why this is the impactor giving place to the largest delaminated surface). This is almost the case for impact 2, with less force generated by the delayed resumption of contact, which then generates less delaminated surface. For impact 1, there is a drop in force towards 0.75 ms (as opposed to 1 ms in the case of a single-impact impact), then there are several resumptions of contact, but these do not generate enough force on the plate, and therefore less surface delaminated than impact 3. For impact 4, contact was comparable to that in the case of a single impact (lasting 1 ms), except that the plate regained contact with the ball after 1 ms, generating more dissipated energy and therefore more delaminated surface compared with if contact has not been resumed. The only difference between the different impacts is their position, which is directly related to the vibration of the plate.

Impact 3 spends the least time in contact with the plate, but generates the most delaminated surface. This indicates that impact time plays an important role in dissipating more energy, but is not the primary factor ; more impact time for a vibrating plate that generates several start of contact losses will result in much less damage than a case with a relatively short contact time but with full contact between the ball and the plate or overload during the same time. Since in the figure 5.17(b), the energy that can be calculated is the sum of several energies stocked in the plate, so it is easier to use the load-time curve (5.17(a)) to simplify preliminary data analysis.

Figure 5.18 reveals the distribution of energy dissipated in the plate in fibers, matrix and delamination elements, the figure shows the accumulated damage at each maxi-

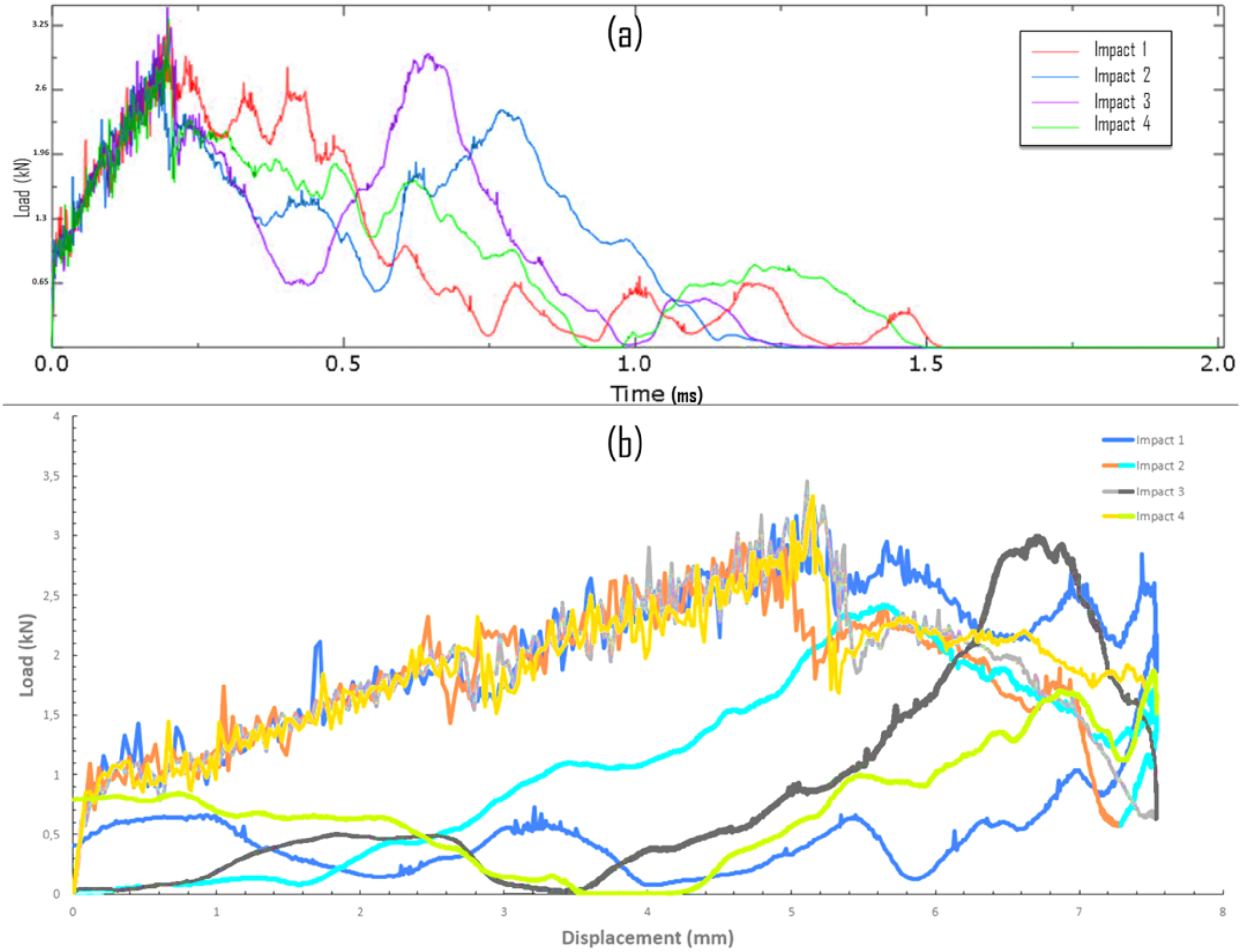

Figure 5.17 – Load-Time (a) and Load-displacement (b) curves for 4 simultaneous impacts (configuration Si/⌀20/15J/Ba/N/4).

mum force applied by one of the impactors, each maximum load reached by one of the impactors results in a new jump in damage dissipation energy (the dotted lines are drawn from the jumps observed on the damage dissipation). It is important to compare this figure with the case of a single impact (see figure 3.31). We note that the jumps in dissipated energy correspond more or less to the maximum forces measured in the impactors, giving rise to several fiber breaks and explaining the approach to perforation shown in the figure 5.15. This is also confirmed by the kinetic energy, where a greater proportion is recovered by the plate than in a mono-impact case. Finally, for damage energy, we count 11.67 times more energy dissipated compared to a mono-impact case, while the energy collected by the whole plate has only been multiplied by 4, which also explains the greater damage observed in this configuration. By energy type, the order of the proportions recovered by each type of element is the same, but the value of this proportion is much greater for the plate, which can lead to the total failure of a composite structure, given the primary role of fibers in mechanical characteristics.

To conclude this configuration, we have shown that the classical parameters involved

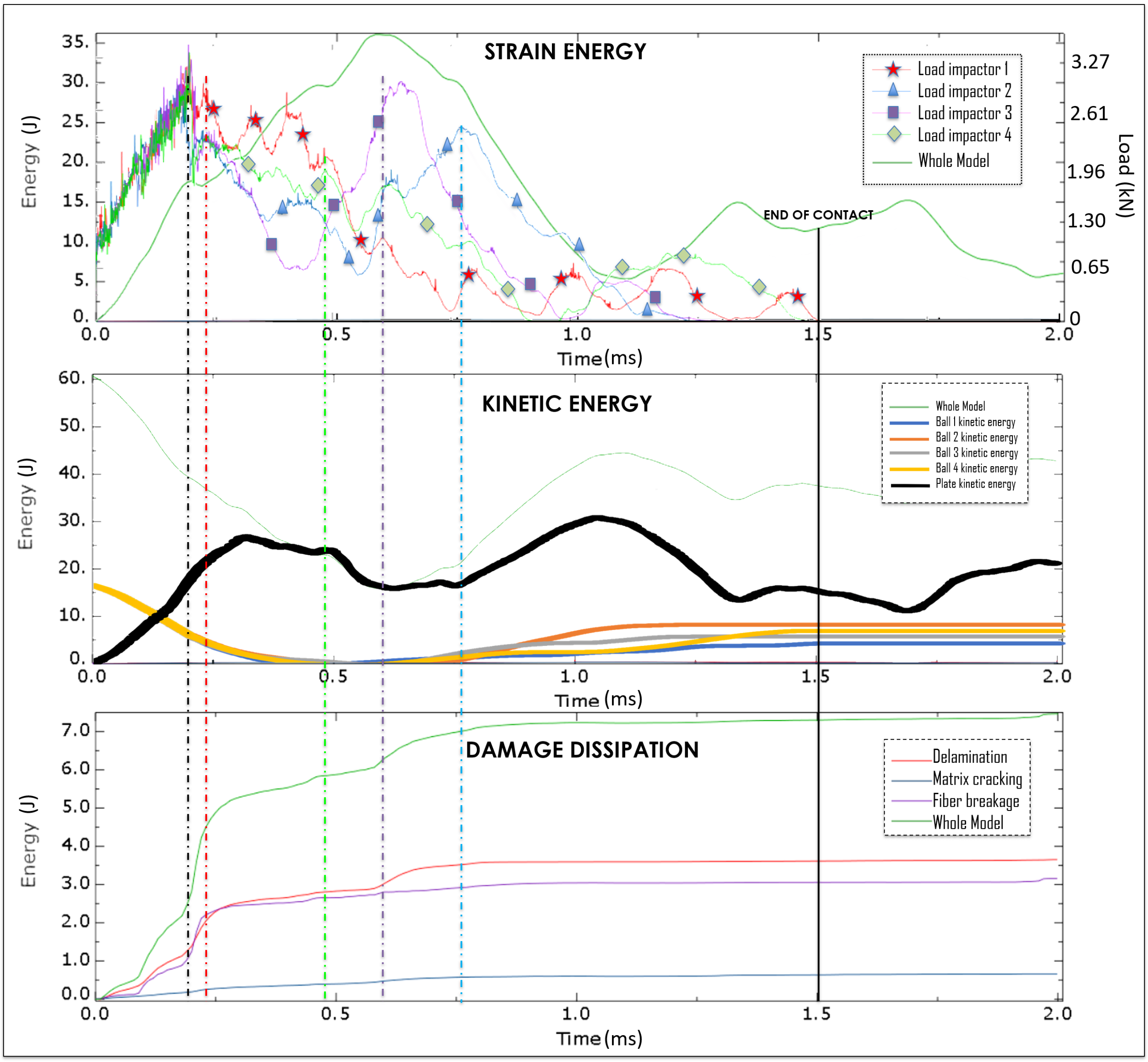

Figure 5.18 – Distribution of different types of energy in case of 4 simultaneous impacts.

in the single-impact case are important parameters that can alter the multi-impact behavior of composite structures. On the other hand, the Δt_c parameter together with the state of the plate vibration during a multi-impact case are two parameters that are more vivid and influential than the classical ones (except for energy, which will be studied in detail in configurations at 30 J in total).

5.3.4. Five simultaneous impacts

In this configuration (configuration Si/⌀20/15J/Ba/N/5), we perform 5 simultaneous impacts with 20 mm diameter balls at 15 J per ball (which corresponds to a velocity of 30 m/s per ball), the maximum time lag between the first and last ball arriving does not exceed 1 ms in all experimental cases, in the positions of impact shown in figure 5.10.

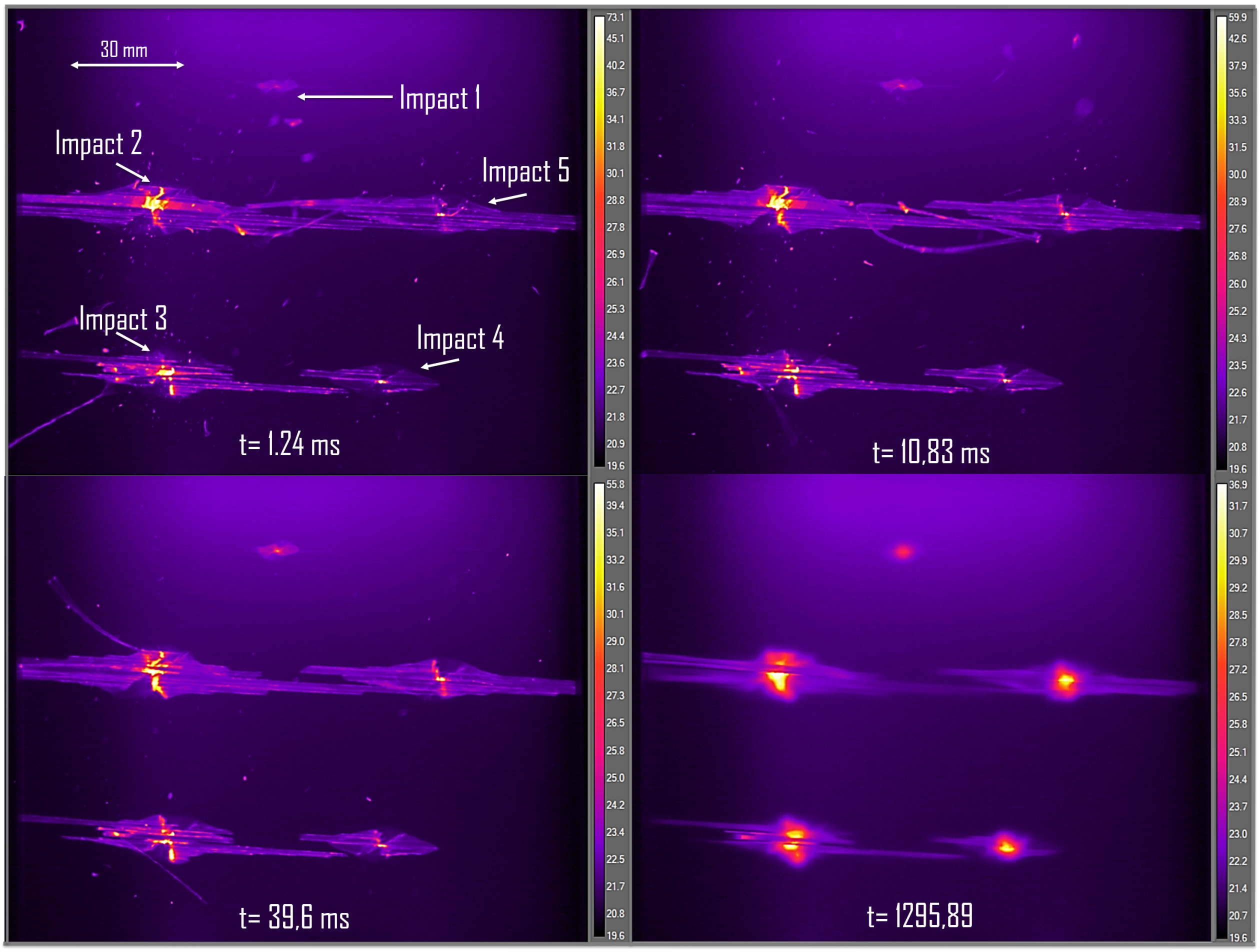

Figure 5.19 – Thermal film images produced during 5 simultaneous impacts.

The video recorded by the high-speed camera shows that ball 1 arrived last and was pushed back by the plate (due to the elastic energy stored by the plate and restored by the 4 balls arriving before ball 1) without damaging the plate significantly, i.e. it is a case of destructive interaction damage. The damage created by balls 2 and 5 arriving less than 0.4 ms behind balls 3 and 4 is excessive as a result of constructive interaction damage. Ball 4 arriving first causes damage comparable to that of a single impact. The second-arriving ball 3 creates more delamination than ball 4 and less than balls 2 and 5. On the other hand, we note that although the delamination created by ball 5 is greater than that created by ball 3, yet ball 3 produces several fiber breakages (we can see the fragments peeling off in figure 5.19), which is more dangerous as it indicates a close perforation of the plate in this area. This example shows that a large delaminated surface does not necessarily mean the most fiber breakages. The high-speed thermal camera gives more accurate information on multi-impact damage than the C-scan, in this multi-impact case, it highlights a greater risk in impact zone 3 than 5.

In a multi-impact case, it is essential to monitor the various load states on a case-

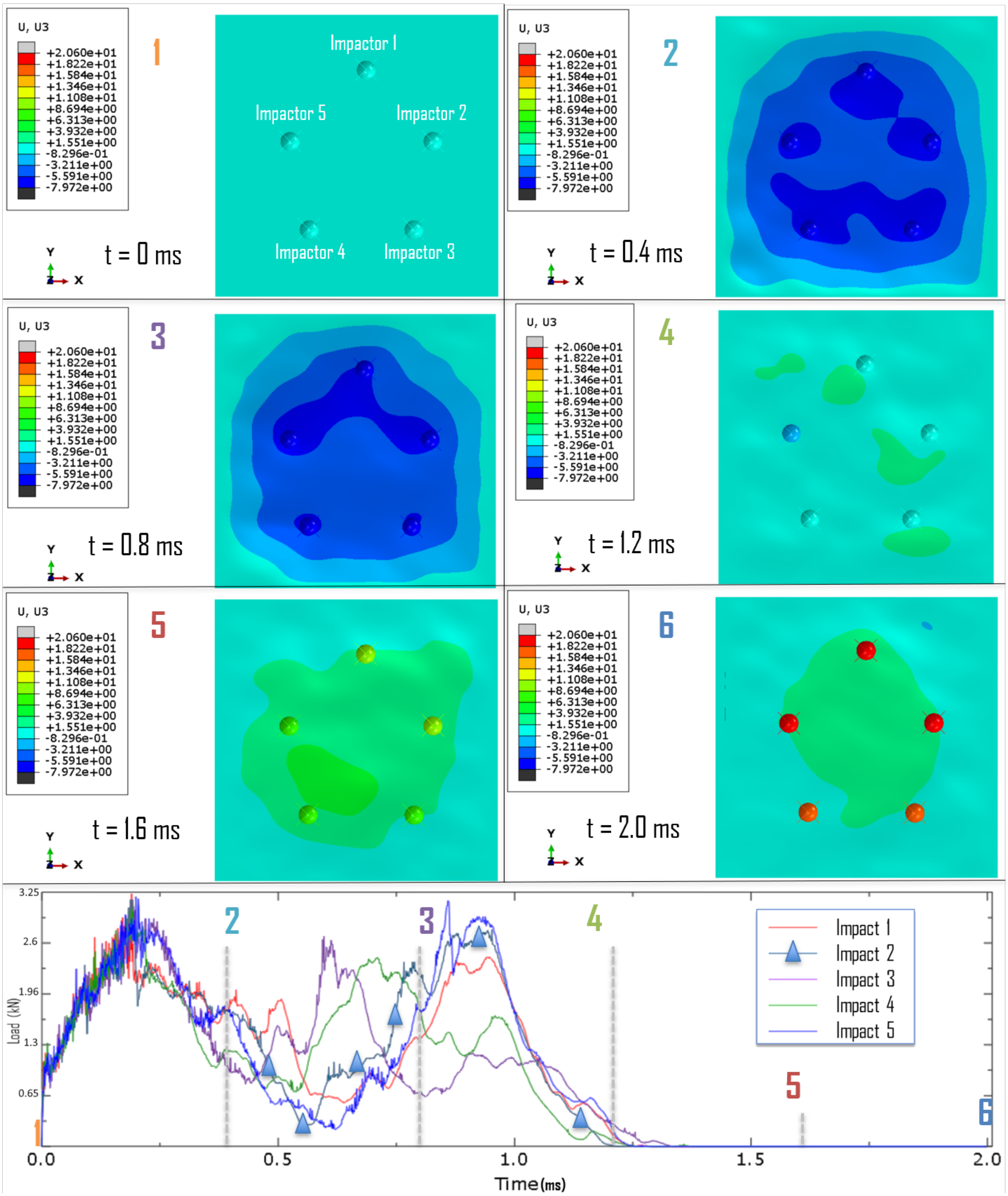

Figure 5.20 – Displacement along z due to 5 simultaneous impacts ($\Delta t_c = 0$ ms) and Load-Time curves.

by-case basis, starting with the parameter Δt_c and the vibration of the plate in the impact zone. This vibration obviously changes depending on the location of the other impactors. As shown in figure 5.20, the displacement of two impactors with the same impact parameters changes according to the position of the impact with respect to the others. For example, at t = 1.2 ms, impactors 2 and 5 (which are almost at the same position relative to the sides of the plate) have different movements, impactor 5 which is further apart from the others, generates more displacement of the plate, which partly explains why it generates the most delaminated surface, as shown in figure 5.21. The load-time curve (figure 5.20) also shows that impactor 2 generates the most load during the second contact with the plate.

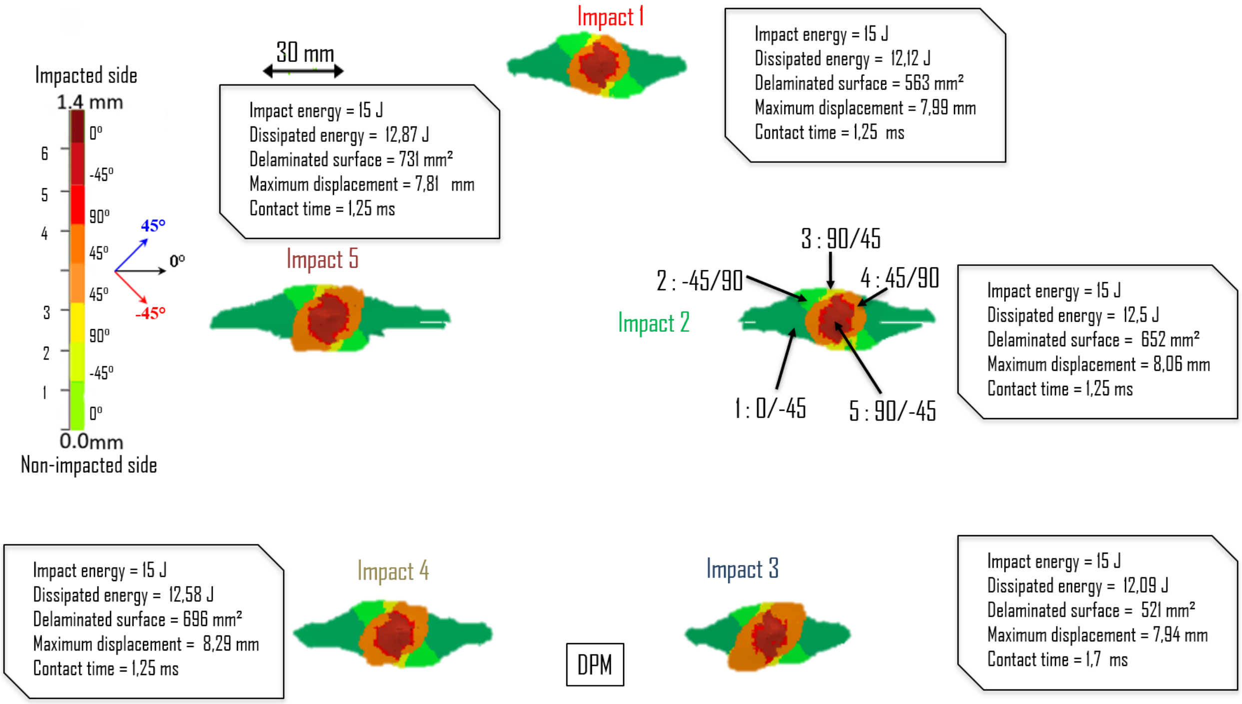

Figure 5.21 – DPM C-scan of 5 simultaneous impacts, Si/⌀20/15J/Ba/N/5.

By comparing the DPM C-scans (Δt_c = 0 ms, figure 5.21) of the 4 simultaneous impact configuration with those of the 5 simultaneous impact configuration, we can directly conclude that the order of the most delaminated surfaces is not the same, even though impactors 1 to 4 have exactly the same impact parameters in both configurations. This confirms the role played by the position of one impactor in relation to the others, which is directly linked to the vibration of the plate, which in turn is linked to the Δt_c parameter, thus managing the multi-impact character of composite structures. It should be noted that these results are increasingly greater in terms of total delaminated area, as the maximum time lag between the first and last arriving balls is not more than 1 ms (the usual contact time for a single impact configuration), creating a state of constructive interaction damage. If the time lag is greater, we can have a destructive interaction damage state, with less total delaminated surface in a case of 5 impacts than in one of 4 impacts, for example.

The load-time curve confirms all these previous results, see figure 5.22. Furthermore, in this configuration, there was no total loss of contact between the ball and the

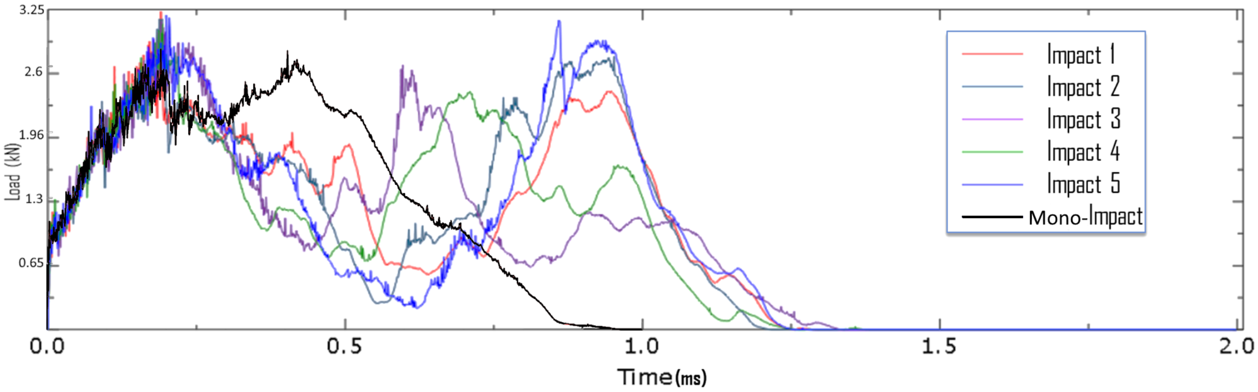

Figure 5.22 – Load-time curve of 5 simultaneous impacts.

plate. However, we note that the impact time is 50% longer than in a single-impact case, which might lead us to think that more time will be available to dissipate more energy. This is clearly not the case, as the longer impact time does not result in more energy being dissipated in the case of partial ball/plate contact losses. When dynamic effects are taken into account, in a multi-impact case, a longer impact time does not necessarily mean more damage. In this case, the impact time does not provide reliable information on the state of damage of composite structures. We must emphasize the important role played by the DPM in monitoring and understanding the phenomena involved in this type of complicated case.

Taking into account figure 5.22, we notice a first resumption of contact at all impactors at around 0.6 ms, resulting in a peak in the energy dissipated in the plate, which initially suggests a critical state of damage. However, as shown in figure 5.23, this peak was mainly observed in the strain energy, but did not lead to any significant change in the dissipated energy, confirming once again that perfectly simultaneous loading is less dangerous than simultaneous loading with a delay of less than 0.2 ms between impacts, which may lead to dissipated energy peaks and therefore more damage in composite structures.

To conclude on the effect of the number of simultaneous impacts at a constant energy per projectile, we have noted the strong influence of one more impact to change the load applied by another ball and the plate and the influence this can have on the amount of energy dissipated and which ultimately, whether it is important, leads to more damage on a composite structure. If we look at the total delaminated surface area, we see a positive trend in this area in relation to the number of impacts, the variation between the surface delaminated by a number of successive impactors is always increasing (between 1 and 4 impactors), but the gap tends to narrow towards an asymptote (between 4 and 5 simultaneous impacts), as shown in figure 5.24. However, we must note the more important role played by the Δt_c parameter, which at different values can result in more or less delaminated surfaces for the same number of simultaneous impacts.

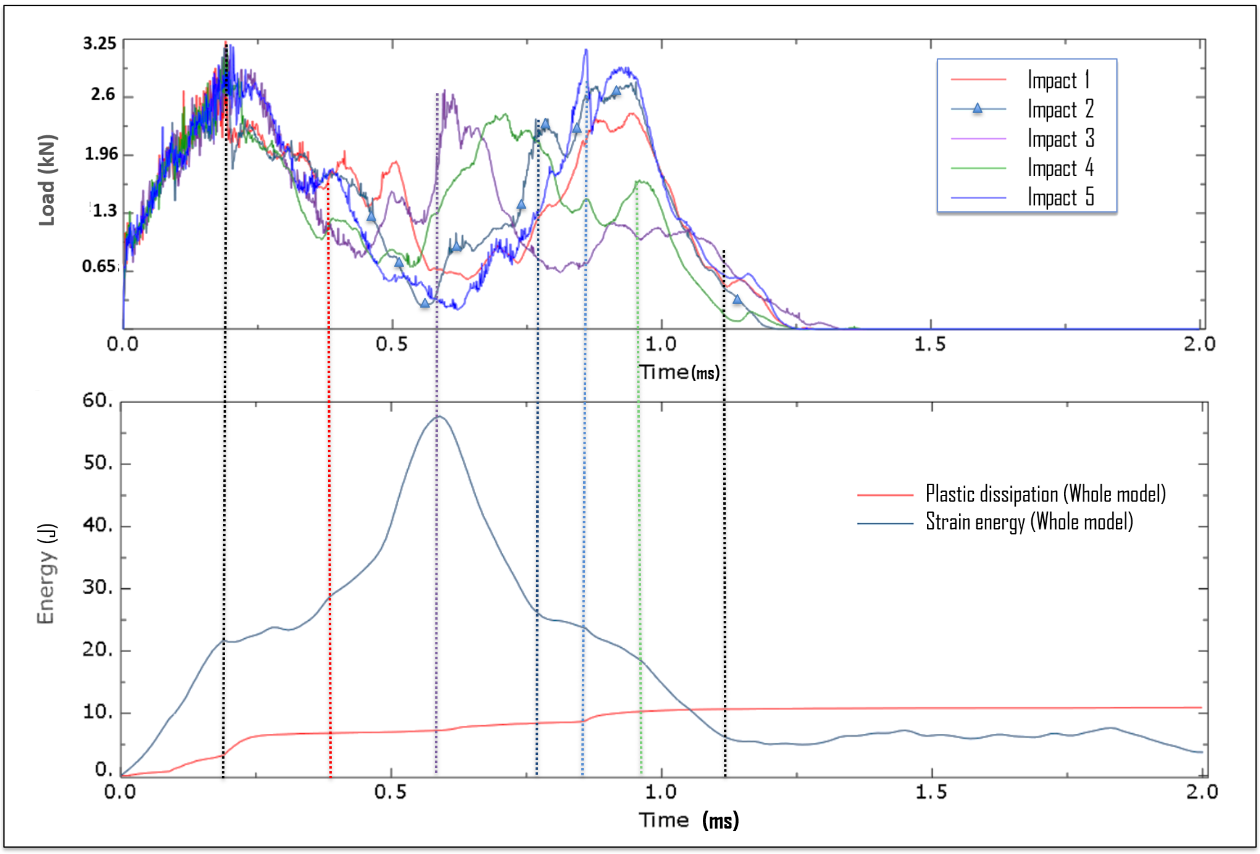

Figure 5.23 – Energy dissipation during 5 simultaneous impacts.

Figure 5.25 indicates that the ratio between the total delaminated surface and the number of impacts is not constant, the relationship between the total kinetic energy of projectiles launched simultaneously and the total surface area delaminated is non-linear. In fact, the ratio increases with the number of impacts, which may also be due to the constructive interaction damage conditions encountered during this experimental campaign.

5.4. Simultaneous impacts : effect of impact energy

In this section, we investigate the response of composite structures to multi-impacts at a constant total impact energy, which will allow us to highlight the effect of energy variation in the case of multi-impacts, going from 30 J per projectile to 6 J per projectile. For the latter configurations, the energy is increasingly lower to be able to re-study the effect of the different parameters of multi-impacts at lower energies, where interactions are more difficult to achieve and the effects are less significant. We adopt the same impact positions as before, see figure 5.10. Impacts are made with 20 mm-diameter steel balls.

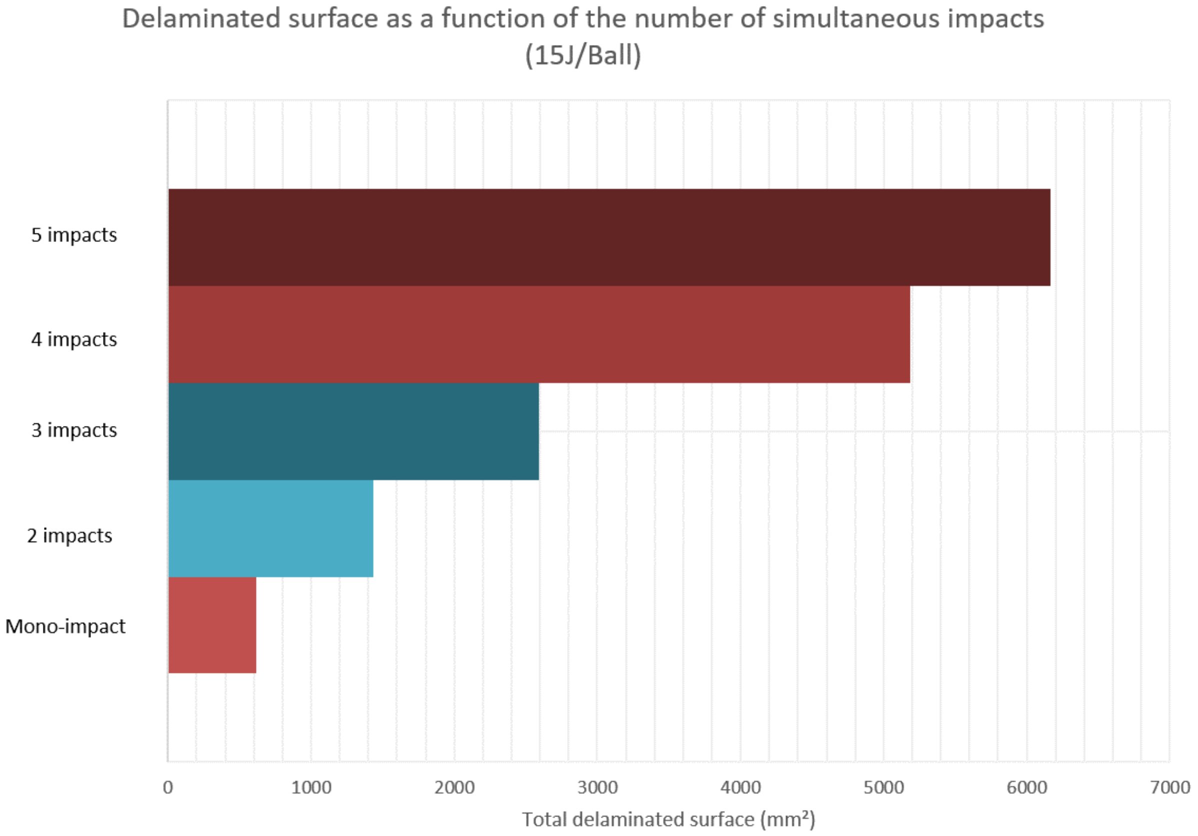

Figure 5.24 – Delaminated area as function of the number of simultaneous impacts (experimental results).

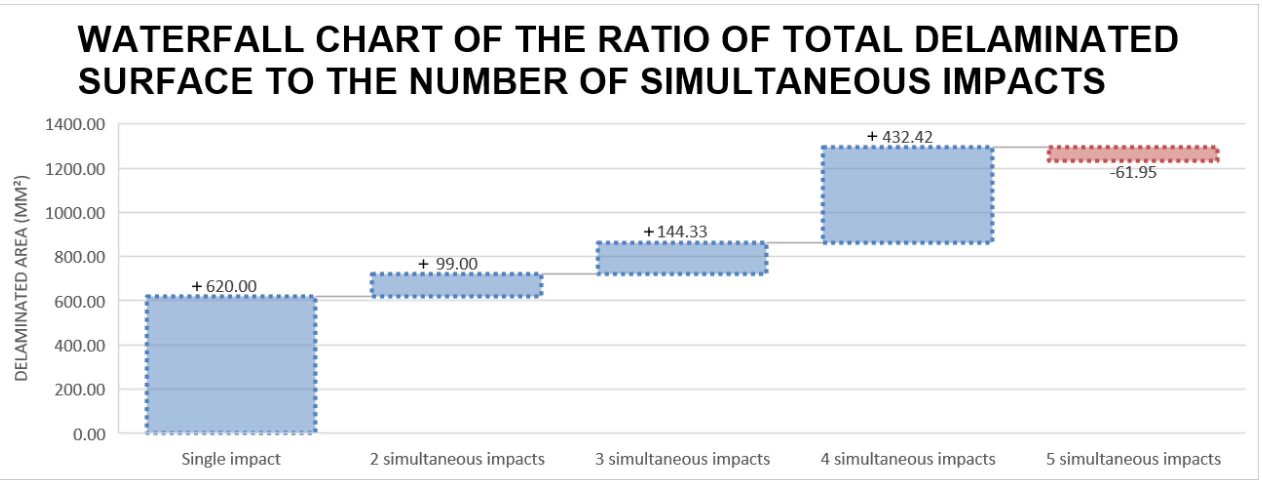

Figure 5.25 – Evolution of the ratio of delaminated area by the number of simultaneous impacts.

5.4.1. Mono-impact and two simultaneous impacts

To summarize the case of a single impact and 2 simultaneous impacts at different energies, we consider configuration M/⌀20/30J/T/N/1 , Configuration

Si/⌀20/15J/Ba/N/2, Configuration Si/⌀20/15J/Ba/L/2 and Configuration Si/⌀20/15J/Ba/M/2. In the case of a single impact at 30 J, the plate was perforated and the delaminated area is 230% greater than the total delaminated area in the case of two simultaneous impacts aligned in the 0° direction and close together (a distance of 22 mm between the impact centers). The union of delaminated surfaces in the case of two impacts generates less damage than two impacts not aligned along 0°. At 30 J, excessive delamination is largely due to direct contact between the ball at the moment of perforation and the last ply, as the ball detaches this ply and changes the classic delamination mechanism (due to matrix cracking). For two simultaneous impacts aligned in the 90° direction and 40 mm apart, we found 200% less delaminated surface compared with an impact at 30 J and 26% more compared with an impact aligned in the 0° direction. This difference is due to the fact that, in this case, the total delaminated surface takes into account the sum of the delamination created at the level of the 4 splinters and not the union between the common splinters. For two more distant impacts, the parameter Δt_c considerably changes the value of the total delaminated surface, the configurations being more critical if Δt_c is less than 0.2 ms and less critical afterwards until the end of the contact (1 ms). In our case, above a distance of 160 mm, the simultaneous character plays no significant role.

5.4.2. Three simultaneous impacts at 10J/projectile

In this configuration (configuration Si/⌀20/30J/T/N/3), we perform 3 simultaneous impacts with a maximum time lag between the first and the last impact of 1 ms. We used 20 mm diameter steel balls. Impacts are performed at an energy of 10 J per ball (corresponding to an impact velocity of 25 m/s), which is 2/3 of the energy typically used previously. However, as shown in figure 5.26, the surface area delaminated per impact is on average 214% lower than in the 15 J/ball cases. We also note that there is no significant difference between the delaminated areas even with $\Delta \mathrm{t}_c$ different from 0 experimentally and equal to zero in the numerical model. The multi-impact character is therefore less dominant at low energies and increasingly important at higher energies. We would like to point out that in the 3 tests carried out experimentally, the order of delaminated surfaces per impact is not the same, which shows that there is still a role played by the time lag between impacts, but this effect is so small and still negligible given the size of the damage generated.

We also notice that the impact time is greater than for the 15 J/ball configurations, whereas the delaminated surface is smaller in this case. Once again, this confirms that impact time is an important parameter, but should be treated with caution in relation to other parameters. It is unreliable to judge the criticality of damage to a composite structure solely on the basis of impact time. It should be noted that there were several drops in force applied to the plate for impactors 2 and 3, which partly explains the smaller delaminated area of these two impactors compared with impact 1. Note that the damage generated by these impacts is difficult to detect with a naked eye, but using the C-scan, we can detect delamination at all 6 interfaces of the material. This

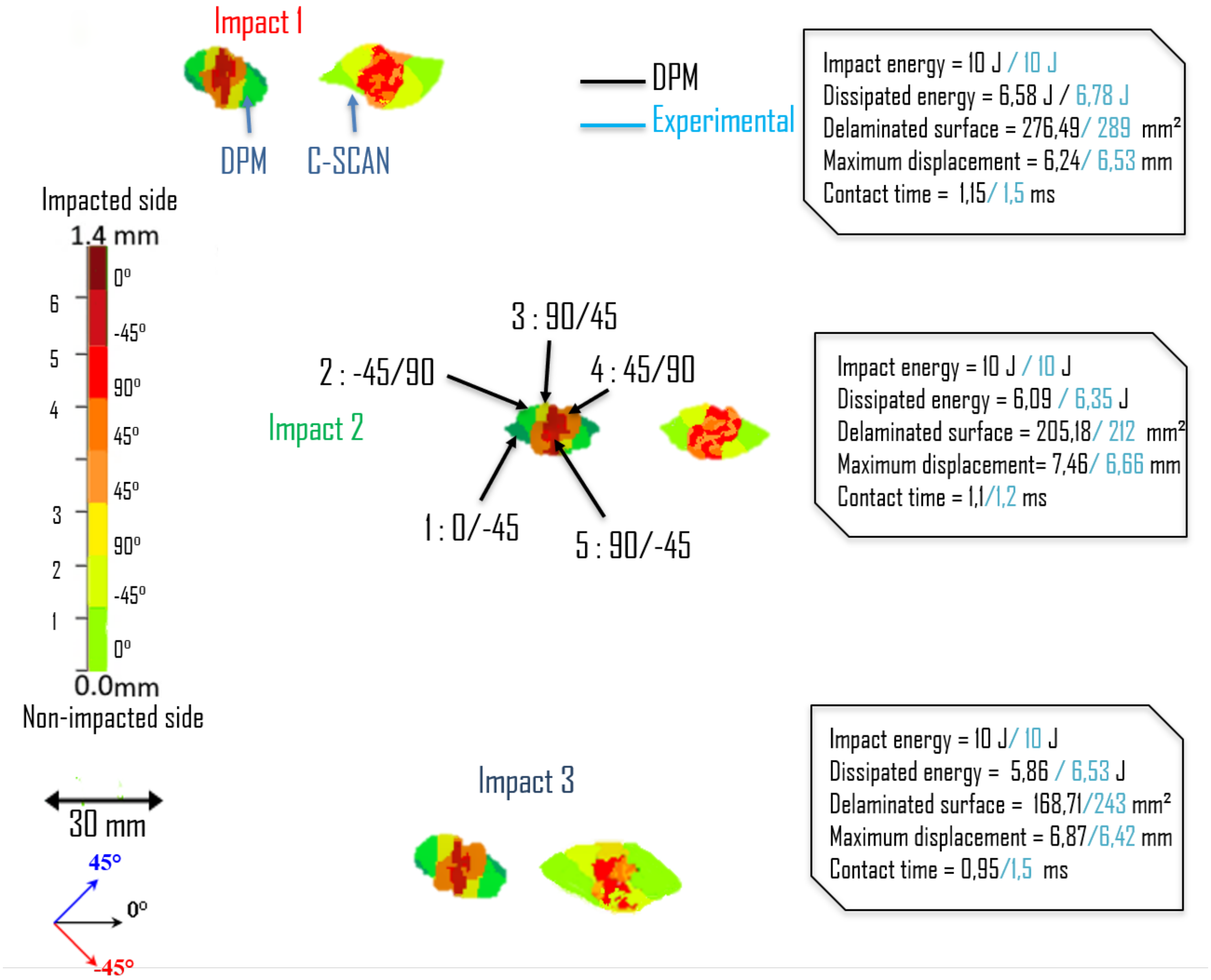

Figure 5.26 – C-scan of 3 simultaneous impacts at a total energy of 30 J : Experimental vs. DPM (configuration Si/⌀20/30J/T/N/3).

leads us back to the issue of barely visible impact damage (BVID), which can lead to a drop in the mechanical properties of composite structures without leaving a visible indentation on the surface.

5.4.3. Four simultaneous impacts at 7.5 J/projectile

In this configuration (configuration Si/⌀20/30J/T/N/4), we perform 4 simultaneous impacts with a maximum time lag between the first and the last impact of 1 ms. We used 20 mm diameter steel balls. Impacts are performed at an energy of 7.5 J per ball (corresponding to an impact velocity of 21.65 m/s), see figure 5.27. We find that the difference in the delaminated areas per impact becomes smaller as the impact energy decreases, and that the multi-impact character plays a smaller role, since whatever the parameter Δt_c there is little influence of the delayed impactor on the others. To explain this, we note on figure 5.28 that up to 67% of the balls' kinetic energy is transformed into elastic energy, and only a small amount is finally transformed into

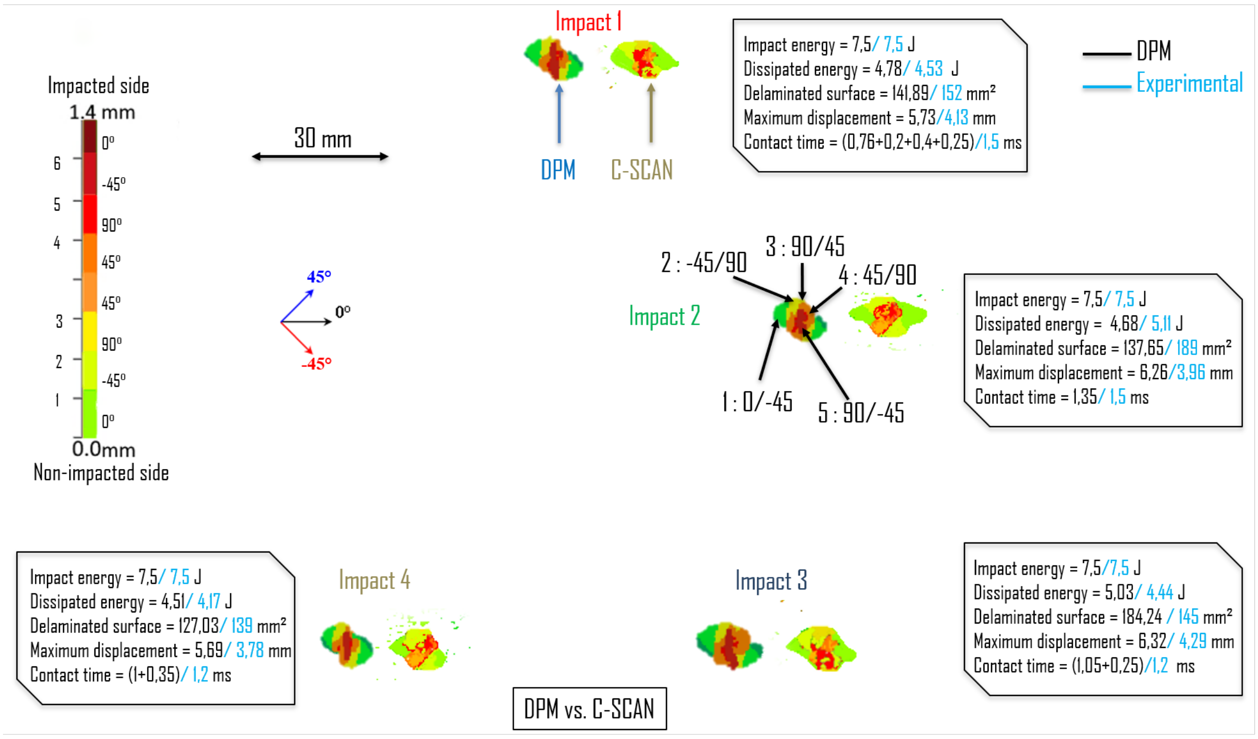

Figure 5.27 – C-scan of 4 simultaneous impacts at a total energy of 30 J : Experimental vs. DPM (configuration Si/⌀20/30J/T/N/4).

dissipated energy (< 1 J). Unlike the 15 J/ball cases, here the maximum impactor load does not directly imply a jump in dissipated energy, so fewer damages are noticeable, see figure 5.27. We also note that this part of dissipated energy increases slightly after 1 ms, which represents the end of contact for a single-impact case and corresponds here to a resumption of contact between several balls and the plate, see figure 5.28.

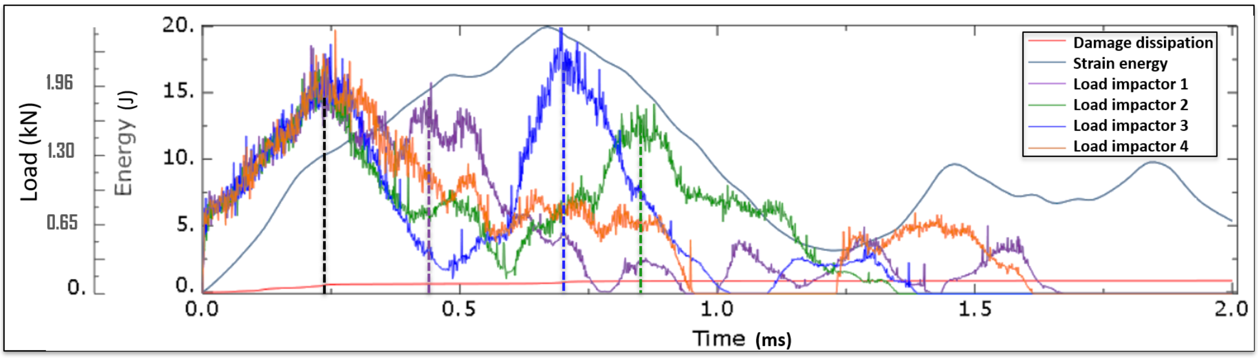

Figure 5.28 – Energy dissipation in a 4 simultaneous impacts at 30 J in total (DPM).

As shown in the figure, we exceeded 1.5 ms as impact time, while delamination was at its lowest throughout this work, demonstrating once again the irrelevance of considering impact time as the sole criterion for judging the severity of impact damage. Meanwhile, as in the case of multi-impact configurations at 15 J/ball, several partial losses and resumption of contact between the ball and the plate are observed. The effects of multi-impact are present, but their influence is minimal, since the energy dissipated is low, the difference between damage levels is also small, and the multi-impact character is not dominant. In the perfectly simultaneous cases (carried out under the DPM), the impact damage is slightly smaller than that obtained experimentally at Δt_c different from 0, but we cannot conclude beyond this, since even in the mono-impacts, we noticed a slightly smaller delaminated surface than experimentally.

In terms of analysis using the high speed IR camera, we lost considerable quality of the images obtained because of the use of a large recording window to capture the 4 impacts, the maximum frequency is lower (104 Hz) and does not allow us to track the damage during the impact time (1.5 ms), see figure 5.29. This is one of the main limitations of the used camera. We also note that the maximum temperature is very low, due to the fact that damage occurs at the depth of the material and the camera only detects what is transferred to the outer surface, which is low in this case given the low energy dissipated in the plate. This also shows that there are no fiber breakages on the plies close to the back of the plate. As temperature variations only represent delamination and matrix cracking (see chapter 3 for reference temperature variation values). Comparing thermal analysis results with C-scan,we observe that the C-scan is more precise in providing the shape of delaminations at low impact energies.

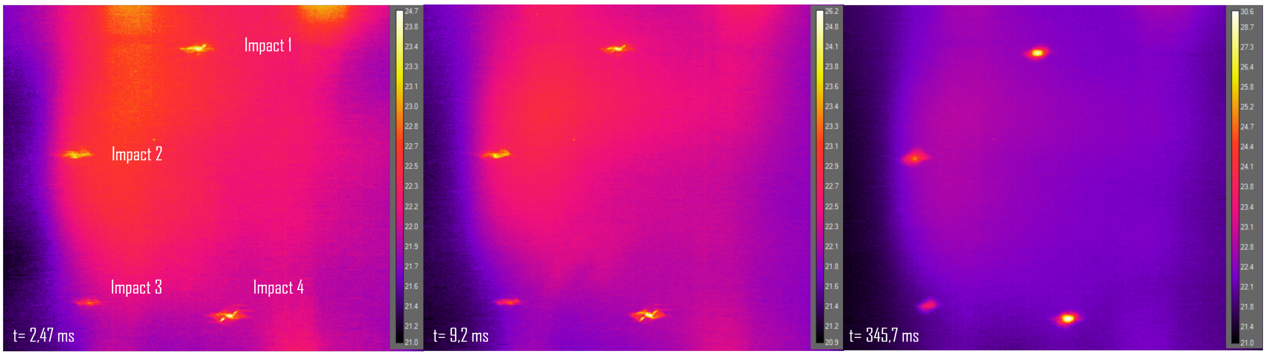

Figure 5.29 – Thermal film images of a 4 simultaneous impacts at 30 J in total.

5.4.4. Five simultaneous impacts at 6 J/projectile

In this configuration (configuration Si/⌀20/30J/T/N/5), we execute 5 simultaneous impacts with a maximum time lag between the first and the last impact of 1 ms. We used 20 mm diameter steel balls. Impacts are performed at an energy of 6 J per ball (corresponding to an impact velocity of 19.37 m/s), see figure 5.30. We do not notice any major difference in delaminated surfaces compared with the previous case (7.5 J/Ball). There is no great difference between the perfectly simultaneous configurations (DPM) and the configurations with Δt_c different from 0. As we explained in the previous configuration, the proportion of energy dissipated in the plate is low, the

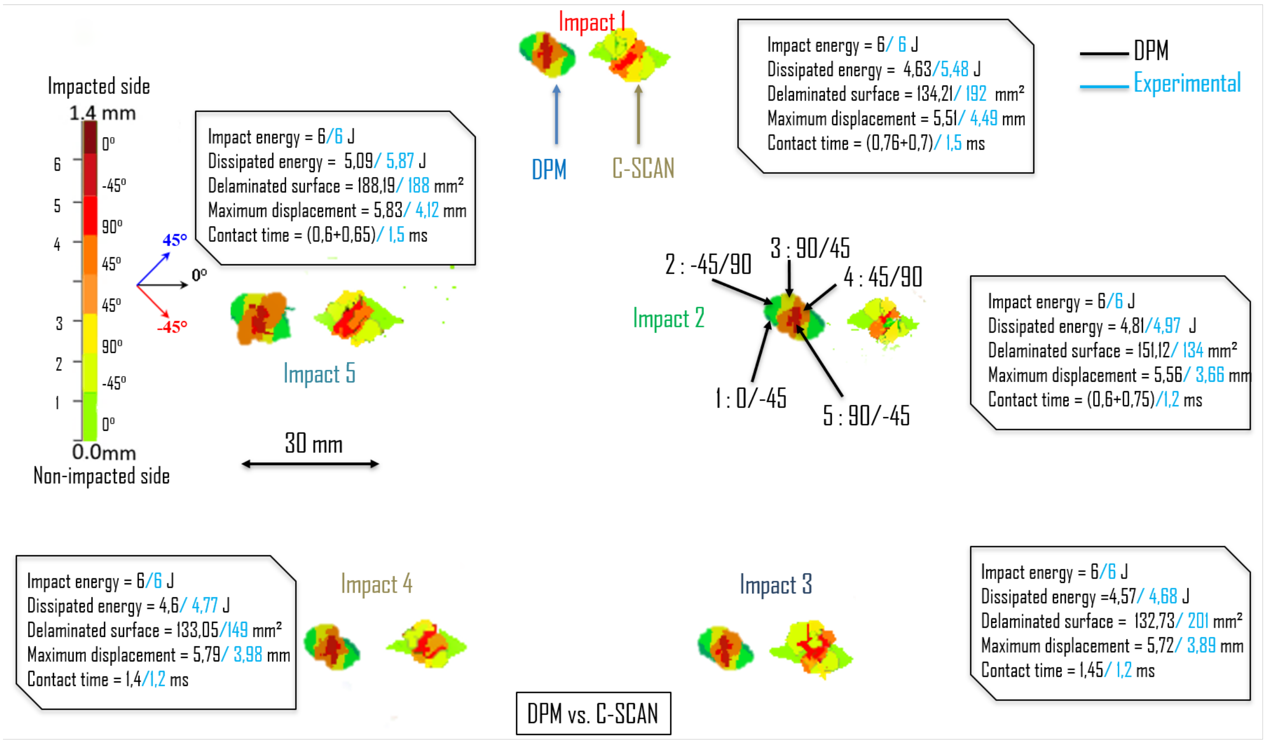

Figure 5.30 – C-scan of 5 simultaneous impacts at a total energy of 30 J : Experimental vs. DPM (configuration Si/⌀20/30J/T/N/5).

multi-impact character does not play a dominant role, and the structures are in any case slightly damaged.

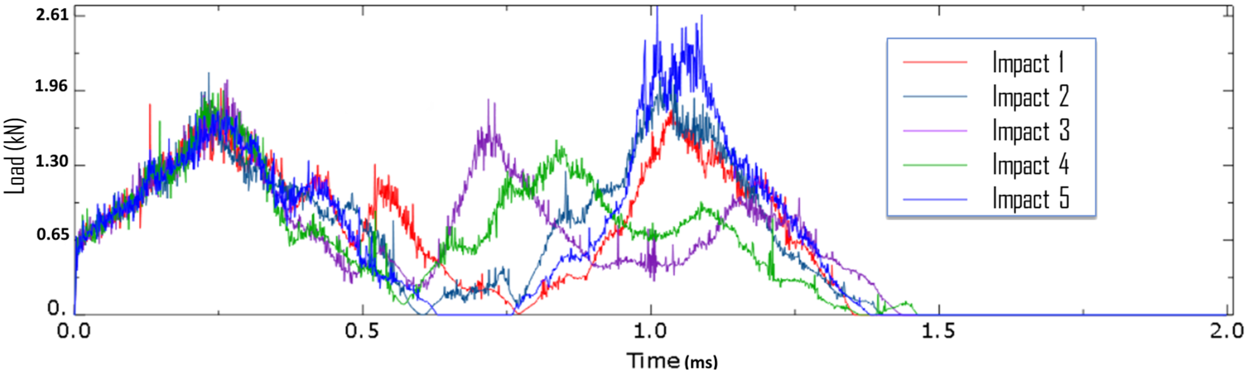

Figure 5.31 – Load-Time curve in a 5 simultaneous impacts at 30 J in total (DPM).

As shown in the figure 5.31, the multi-impact character is still present, with ball/plate drops and re-contacts and longer impact times, but given the low energy dissipated, this multi-impact character doesn't play a dominant role. Compared with the 4 simultaneous impacts configuration, we note here more effort drops and more disturbances at the various impacts. The impact time is shorter than that of the 4 simultaneous impacts configuration, but this doesn't make any real difference, as we explained earlier, due to drops and resumptions of contact.

To conclude this section on the effect of multi-impact energy, we note a different proportion of energy dissipated and delaminated area depending on the multi-impact configuration, the delaminated area is very low below 10 J and increases considerably for 15 and 30 J. It should be noted that a major reason for the excessive delamination at 30 J also lies in the perforation of the plate and the direct contact created between the ball and the last ply.

Comparing this configuration of 30 J in total with that of 15 J/ball (figure 5.32), we note the obvious result that increasing the number of impacts for a constant energy per ball generates greater damage than increasing the total energy applied to a composite structure. This is because the total energy between the two cases is not the same, and the energy dissipated is greater in 15 J/ball configuration, resulting in more extensive damage.

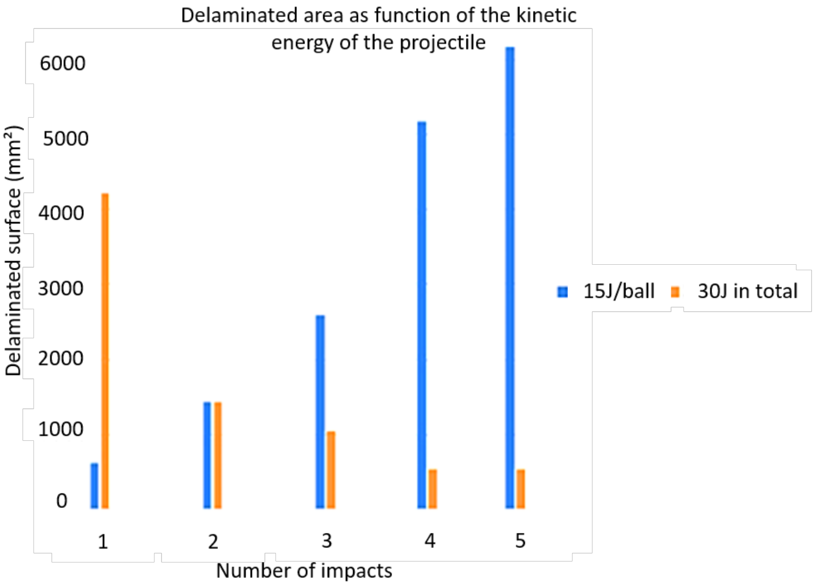

Figure 5.32 – Delaminated area as function of kinetic energy per projectile.

5.5. Repeated simultaneous impacts

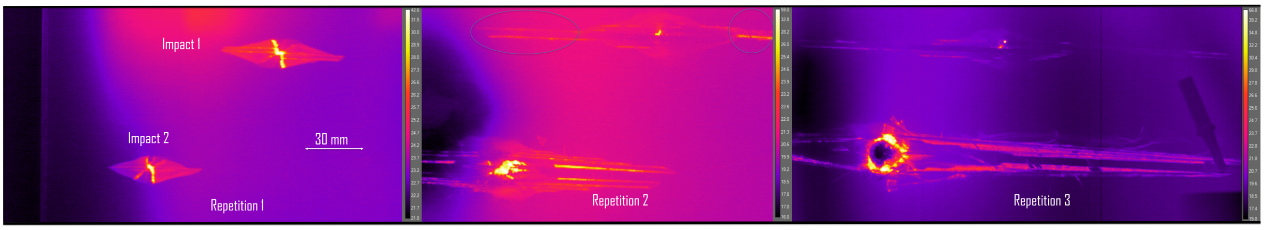

Figure 5.33 – Thermal film images of 2 repeated simultaneous impacts at 15 J/projectile.

In the literature, mono-impacts are widely studied, then an increasing number of publications are interested in repeated impacts. In this work, we have studied multi-impacts in detail, and in this section we follow up with the study of repeated simultaneous multi-impacts to track the evolution of multi-impacts over repetitions (2 simultaneous impacts repeated 3 times), see figure 5.33. The parameters used are the same as for configuration Si/⌀20/15J/Ba/N/2.

As shown in figure 5.33, the damage becomes increasingly severe from one repetition to the next, until the plate is perforated in impact zone 2.

Matrix cracking becomes increasingly pronounced, especially at the center of impact in the direction of the fibers in the lower ply (on the non-impacted face), and during the third repetition extends to the edges of the plate.

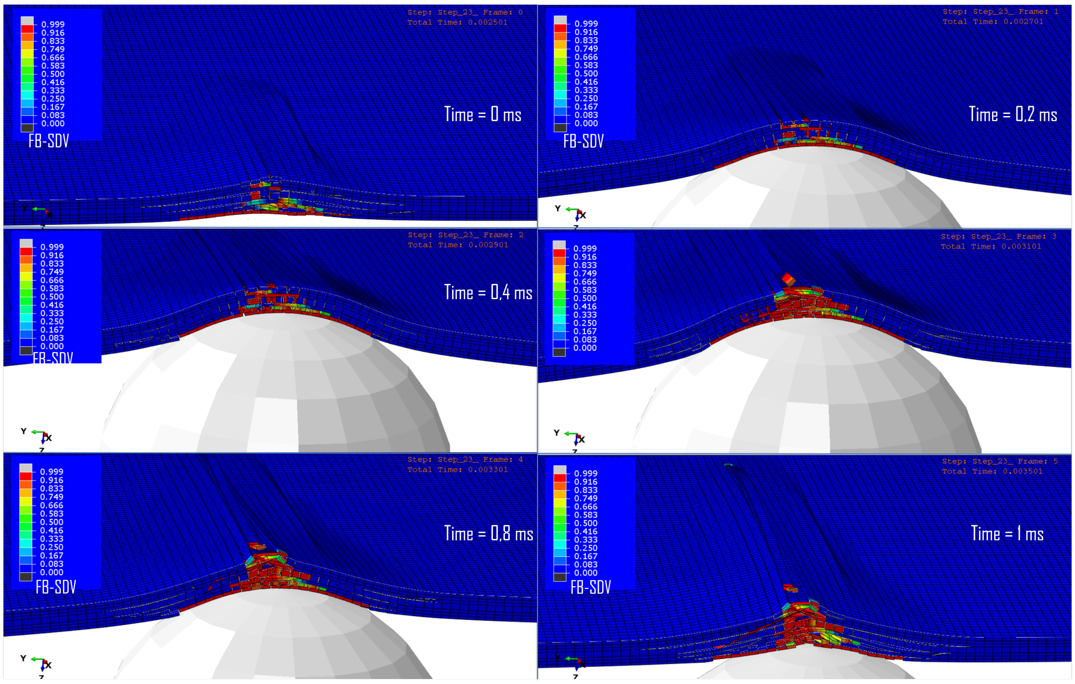

Figure 5.34 – Propagation of fiber breakages in the thickness of the material during the second repetition (DPM).

For fiber breakage, the area under the impactor contains the most fiber breakage, leading in the third repetition to perforation. To explain this, we use the numerical model to highlight the propagation of fiber breakage. Figure 5.34 shows that following the first impacts, most of the fiber breaks are located under the impactor on the impacted face (t = 0 ms). Then, following the breakage of all matrix cracking and delamination elements in the thickness of the material, the more fibers support the load applied by the impactor unaided, the more fiber breaks are observed from one ply to the one below, reaching the last ply in the third repetition. All elements under the impactor are fractured, the ball perforates then the plate. This test shows the criticality of repetition in producing fiber breaks in the thickness of the material, leading very quickly to complete perforation of the composite structure.

For delamination, we distinguish two different forms of evolution (figure 5.35) :

— Impact 1 (and impact 2 between the second and third repetition) : a basic delamination pattern remains the same (enlarging slightly) and it is just the splinters that delaminate sideways, this is because in the 90° direction the damage reaches its maximum, it is then blocked by the delamination on the outer "eye" shape. The delamination and matrix cracking in the center continue to propagate then creating long splinters on the sides.

— Impact 2 (between first and second repetition) : the entire shape expands over the course of the repetition. This is because the shape of the delamination in the first repetition has not yet reached its maximum, because of the MIP ($\Delta t_c = 1$ ms) the delamination created in zone 2 during the first repetition is less than that expected in the case of a mono-impact.

We then observe that, over several repetitions, the basic damage pattern seen in a simple simultaneous multi-impact case develops to its maximum, then delamination propagation and matrix cracking on the splinters continue at the same time as fiber breaks under the impactor in the thickness of the material. Finally, when all the elements under the impactor have broken, the projectile perforates the plate.

Figure 5.35 – Delaminated area as function of the number of repeated simultaneous impacts (experimental results).

Conclusion

In this chapter, we have explored the behavior and effects of simultaneous impacts versus repeated simultaneous impacts on composite structures. By conducting a comprehensive analysis of different impact configurations, we have gained valuable insights into the similarities, differences, and implications of these two types of multi-impact scenarios. It also gives us a more overall picture of the impact behavior of composite structures, including the various new multi-impact configurations presented throughout this work.

To conclude this chapter, it is relevant to consider simultaneous multi-impact cases as opposed to mono-impacts, repeated impacts and sequential multi-impacts, given the criticality of the damage generated in simultaneous cases, as well as the difference in damage-forming mechanisms that can, depending on the case, produce premature ruin of the composite structures. The MIP (Δt_c) and the plate vibration are the two most important elements to take into account when expecting a given pattern of damage. Other parameters such as impact time, impact energy and projectile size play an important role in multi-impact, except that they are always driven by the multi-impact parameter (MIP) in simultaneous cases. For tests with random impacts, critical configurations may be missed, as we have shown throughout this chapter, the time lag between impacts completely changes the state of damage created within composite structures.

The numerical model not only demonstrated its reliability in reproducing the response of composite structures in complex multi-impacts configurations, but was also a wand during the course of this work, helping to understand the phenomena involved and enabling us to track parameters that are difficult to measure experimentally, such as vibration at any point on the plate, load curves, multi-cut views without damaging any surface and so on.

Chapter 5

General conclusions and perspectives

The work carried out in this thesis initially enabled us to explore a new method for dimensioning composite structures in terms of tolerance to impact and multi-impact damage. This method is based on the use of the "compressed air cannon" machine developed during this thesis, which allows the phenomena between the plate and the impactor to be managed without forcing the impact direction, impact time or other impact parameters, which is more representative of real service conditions in many common cases. The use of IR high speed cameras has enabled us to validate the various damage scenarios involved, distinguishing between the different types of composite damage and their sequence and origins during impact.

The use of DPM in parallel with a Virtual Testing approach has enabled us to gain a better understanding of these phenomena, and to validate both experimental and numerical results in the case of an impact. The result has been a significant reduction in testing time and costs, and in some cases enabling the realization of certain configurations that are difficult to implement experimentally because of the order of accuracy required. These impact studies have been carried out on a structural scale, and not on a coupon scale or on uniaxial tests whose boundary conditions are not representative of the real life of a structure, as is the case with traditional sizing methods used in industry.

In this thesis, we have investigated and analyzed the multi-impact behavior of composite structures, aiming to enhance our understanding of their response to a general impact case and help improving their overall performance and durability. Through a combination of literature review, experimental investigations, and numerical simulations, several key findings and insights have emerged.

Firstly, the literature review provided a comprehensive overview of the impact behavior of composite structures, highlighting the various damage mechanisms that can occur and the degradation of structural performance over repetitive impacts. This literature review brought to light the need to study complicated multi-impact cases which are rarely covered in the literature.

Secondly, through experimental investigations using the Compressed Air Cannon, we were able to characterize the damage evolution and energy absorption of composite specimens subjected to all multi-impact cases, each time assessing the importance of each impact parameter. These experiments allowed us to understand the progressive damage accumulation and the influence of multiple loading events on the structural integrity of composites. We have also revealed the multi-impact parameter that drives the formation and criticality of damage in the case of multiple impacts.

Thirdly, numerical simulations, using the DPM, provided valuable insights into the stress distribution, failure mechanisms, and energy dissipation of composite structures under multi-impact conditions. In certain configurations, it has also overcome experimental limits, ensuring the desired precision of the various impact parameters. These simulations enabled us to optimize the design of composite structures for enhanced impact resistance and damage tolerance. By combining experimental and numerical approaches, we were able to achieve a better understanding of the various phenomena involved, and reduce both testing and calculation time/costs.

Subsequently, the thesis work removed the ambiguity of the terms used in the case of multiple impacts by distinguishing between different possible configurations with measurable parameters. This has allowed us to study each configuration side by side and distinguish the most critical ones. This work will provide the community interested in the study of the impact behavior of composite structures with a more general idea of the damage scenarios and the most influential parameters in the case of a single impact, and particularly in the different cases of multi-impact. The information provided in this manuscript on the distinction between the different impact cases will perhaps lead to the redesign of several test machines capable of more accurately reproducing real-life impact configurations without neglecting the essential parameters listed in the last three chapters. On the other hand, more attention has been paid to the instrumentation of the test benches, in order to obtain maximum information in the most complicated configurations. The use of the DPM in this part of our study was vital, given the complexity of the phenomena involved, due to the many interactions between the various projectiles. The DPM model allowed us to pinpoint the multi-impact parameter that drives the various multi-impact cases, and to go beyond our experimental limits, in particular to study the precise role of the multi-impact parameter (MIP).

As a result of this work, to compare two impact or multi-impact configurations, we need to be more precise about the test configuration in question : will the impacts be applied simultaneously or sequentially ? what is the time lag between them ? will they be in the same impact zone or staggered ? according to which direction ? what is the impactor size ? what is its energy ? By answering all these questions, with the information provided in this manuscript, we will be able to differentiate between the configurations in question and determine which is more critical, knowing exactly why. It can be concluded that the most critical time lag between 2 impacts is the one corresponding to the maximum effort of the first impact. Also, the delay between impacts plays a major role in the initiation and propagation of damage in a composite structure. Moreover, simultaneous damage appears to be more critical than sequential damage.

Finally, considering energies per ball seems more practical for the industry, as an impact at 30 J caused more delamination than all other configurations at 30 J in total applied. On the other hand, if we are interested in the phenomena that take place within impact configurations, multi-impact tests are richer and less predictable than single-impact tests. In fact, with the same parameters as for a single impact (energy, velocity, angle of impact, impactor position, etc.), the MIP changes the behavior of the plate and can cause damage many times greater (or smaller) than that expected in simple impact configurations.

Unfortunately, several elements remained unimproved. Firstly, time constraints have not allowed a complete characterization of the material and we have not been able to follow the mechanical test pyramid, a precise characterization should improve the numerical results and allow increasing the predictive performances of our model. Secondly, at the cannon level, the positions of the displacement sensors could have been optimized and placed directly behind the impact points (in configurations without plate perforation) to enable us to take advantage of the data from these sensors and compare them with the numerical model. Simultaneity control can be improved by further optimizing the cannon automation program, or by equipping the firing system with more precise electric actuators. The use of thermal imaging cameras is promising, but we must ensure greater acquisition frequency in order to track damage during impact with greater precision. It would also be important to calculate the heat transfer rate per ply, to enable us to get back to the exact time of the phenomena visualized on the non-impacted face. Finally, more effort can be given to DPM to improve the initiation of fiber breakage and coupling with matrix cracking, and more generally, the thermo-mechanical aspect needs to be modelled to obtain a model that predicts the temperature field, and then compare it with these results.

As an extension of this work, we can improve on the above points and extend the use of the cannon to other multi-impact configurations, by mixing balls of different dimensions, or using real gravel and gelatin or ice cubes to ensure these impacts, or test random impact configurations with impact probability laws to start feeding an AI-based model that can eventually predict the most critical configuration possible for a given material and stacking sequence. Independently of AI, DPM should now be used to refine which cases are the most critical ; and not only according to the criterion of delaminated surface but also of fiber breakage. In addition, the study detailed in this manuscript for a carbon/epoxy composite can be repeated using other materials (fiberglass, Kevlar, bio-composites, etc.). It would be also interesting to carry out a test campaign to evaluate the material's strain rate sensitivity in order to implement the DPM. To establish design criteria, CAI tests could be used to estimate the residual strength of multi-impacted plates. In this work, we focused on the delaminated surface, but this is not enough (even if it is a very interesting first step), we also need to do similar work on fiber breakage ; and finally, the residual strength which is the most important (as CAI is often the worst loading).

Bibliography

[1] Claire, T. (2020). Grêle : que couvre mon contrat d'assurance auto ?. `https://www.maif.fr/`, consulted on February 12, 2021.

[2] Tytelman, X. (2015). Tempête de grêle sur un avion : comment est-ce possible ?. `http://www.peuravion.fr/`, consulted on February 12, 2021.

[3] Cesari, F., Dal Re, V., Minak, G., Zucchelli, A. (2007). Damage and residual strength of laminated carbon–epoxy composite circular plates loaded at the centre. *Composites Part A : Applied Science and Manufacturing*, 38(5), 1163-1172.

[4] Caballero-Reynolds, A. (2017). Le péril aviaire est pris en compte par les constructeurs aéronautiques lors de la conception de leurs avions. `http://www.sudouest.fr/`, consulted on February 13, 2023.

[5] Abrate, S. (2011). *Impact Engineering of Composite Structures*, 526(1), 71-96.

[6] Wang, C., Yew, C. H. (1990). Impact damage in composite laminates. *Computers & Structures*, 37(6), 967-982.

[7] Xiao-Yu, S., Jian-Xin, T., Zheng, H., Xuan, G. (2018). A study on the failure mechanisms of composite laminates simultaneously impacted by two projectiles. *Advanced Composites Letters*, 27(3), 96-106.

[8] Davies, G. A. O., Olsson, R. (2004). Impact on composite structures. *The Aeronautical Journal*, 108(1080), 542-561.

[9] Cantwell, W. J., Worton, J. (1989). Comparison of the low and high velocity impact response of CFRP. *Composites Journal*, 20(6), 545-551.

[10] Mokhtar, H. B. (2012). Contribution to the study of impact damage on composite laminates : The effect of hygrothermal ageing and preloading. *Doctoral dissertation, University of Burgundy*, 76-89.

[11] Amouzou, A. S. E., Sicot, O., Chettah, A., Aivazzadeh, S. (2019). Experimental characterization of composite laminates under low-velocity multi-impact loading. *Journal of Composite Materials*, 53(15), 2025-2038.

[12] Amaro, A., Reis, P., Moura, M., Neto, M. (2013). Influence of multi-impacts on GRP composite Laminates. *Composites Part B : Engineering*, 46, 93-99.

[13] Bartus, S. D., Vaidya, U. K. (2007). Near-simultaneous and sequential multi-site impact response of S-2 glass/epoxy laminates. *16th International Conference on Composite Materials*, 1-4.

[14] Deka, L. J., Bartus, S. D., Vaidya, U. K. (2009). Multi-site impact response of S2-glass/epoxy composite laminates. *Composites Science and Technology*, 69(5), 725-735.

[15] Garzon-Hernandez, S., Garcia-Gonzalez, D., Arias, A. (2018). Multi-impact mechanical behaviour of short fibre reinforced composites. *Composite Structures*, 202, 241-252.

[16] Deconinck, P. (2014). Étude du comportement à l'impact de matériaux composites renforcés par tufting. *Doctoral dissertation, University of Lorraine*, 13-16.

[17] Hradecky, S. (2015). Incident : THY B738 at Nevsehir on May 5th 2015, bird strike. *http ://avherald.com/*, consulted on January 29, 2021.

[18] Mouritz, A.P. (2012). *Introduction to aerospace materials*, 4-32.

[19] Davies, G. A. O., Olsson, R. (2004). Impact on composite structures. *The Aeronautical Journal*, 542-561.

[20] AITM1-0010. (2005). Airbus Test Method : Determination of Compression Strength after Impact. *Airbus S.A.S Engineering Directorate*, 3.

[21] Boeing Specification Support Standard BSS 7260. (1988). Advanced Composite Compression Tests.

[22] SACMA Recommended Method SRM 2R-94. (1994). Compression After Impact Properties of Oriented Fiber-Resin Composites.

[23] ASTM D7137/D7137M. (2005). Standard Test Method for Compressive Residual Strength Properties of Damaged Polymer Matrix Composite Plates.

[24] Demuts, E., Whitehead, R. S., Deo, R. B. (1985). Assessment of Damage Tolerance in Composites. *Composites Structures*, 4, 45-58.

[25] De Luca, A., Caputo, F., Sharif Khodaei, Z., Aliabadi, M. H. (2018). Damage characterization of composite plates under low velocity impact using ultrasonic guided waves. *Composites Part B*, 138, 168-180.

[26] Amsc, N (2002). Composite Materials Handbook, MIL-HDBK-17E Polymer Matrix Composites, *Department of defense USA*, 1, 452-496.

[27] Hongkarnjanakul, N. (2007). Modélisation numérique pour la tolérance aux dommages d'impact sur stratifié composite : de l'impact à la résistance résiduelle en compression. *Doctoral dissertation, Compiègne University of Technology*, 67-102.

[28] De Freitas, M., Reis, L. (1998). Failure mechanisms on composite specimens subjected to compression after impact. *Composites Structures*, 42(4), 365-373.

[29] Baker, A., Dutton, S., Kelly, D. (2004). Composite materials for aircraft structures (2nd ed.).*American Institute of Aeronautics and Astronautics (AIAA)*, 68-82.

[30] Fawcett, A. J., Oakes, G. D. (2006). Boeing Composite Airframe Damage Tolerance and Service Experience. *Composite Damage Tolerance Maintenance Workshop*, 2-7.

[31] Dubary, N., Bouvet, C., Rivallant, S., Ratsifandrihana, L. (2017). Etude numérique du dimensionnement d'un stratifié composite aéronautique pour la tolérance aux dommages d'impact. *Journées Nationales sur les Composites 2017*, 1-10.

[32] Trousset, E. (2013). Prévision des dommages d'impact basse vitesse et basse énergie dans les composites à matrice organique stratifiés. *Doctoral dissertation, Ecole nationale supérieure d'arts et métiers - ENSAM*, 51-112.

[33] Léon-Dufour, J.-L. (2008). Composite structure certification and stress dossier.*Cours ISAE/ENSICA de Mécanique des Structures Stratifiées*, 1-7.

[34] Njionhou, K. A., Berthet, F., Castanié, B., Bouvet, C. (2012). Relationships Between LRI Process Parameters and Impact and Post-Impact Behaviour of Stitched and Unstitched NCF Laminates. *Applied Composite Materials*, 19(6), 3-16.

[35] Olsson, R. (2000). Mass criterion for wave controlled impact response of composite plates.*Composites Part A : Applied Science and Manufacturing*, 31(8), 879-887.

[36] Robinson, P., Davies, G.A.O. (1992). Impactor mass and specimen geometry effects in low velocity impact of laminated composites. *International Journal of Impact Engineering*, 12, 189-207.

[37] Parga-Landa, B., Vlegels, S., Hernández-Olivares, F., Clark, S. D. (1999). Analytical simulation of stress wave propagation in composite materials. *Composite Structures*, 45(2), 125-129.

[38] Yu, Z., Xue, P., Yao, P., Zahran, M. S. (2019). Analytical determination of the critical impact location for wing leading edge under birdstrike. *Latin American Journal of Solids and Structures*, 16(1), 152.

[39] Abrate, S. (1998). *Impact on composite structures*, 75-92.

[40] Cantwell, W. J., Worton, J. (1989). Comparison of the low and high velocity impact response of CFRP. *Open Journal of Composite Materials*, 7(1), 545–551.

[41] Hosur, M. V., Murthy, C. R. L., Ramamurthy, T. S., Shet, A. (1998). Estimation of impact-induced damage in CFRP laminates through ultrasonic imaging. *NDT E International*, 31(5), 359-374.

[42] Berthelot, J.-M. (2012). *Matériaux composites : comportement mécanique et analyse des structures (5th ed.)*, 10-18.

[43] Fuossa, E., Straznickya, P. V., Poon, C. (1998). Effects of stacking sequence on the impact resistance laminates - Part 1 : parametric study. *Composite Structures*, 41, 67-77.

[44] Mitrevski, T., Marshall, I. H., Thomson, R., Jones, R. (2006). Low-velocity impacts on preloaded GFRP specimens with various impactor shapes. *Composite Structures*, 76(2), 209-217.

[45] Cantwell, W.J., Morton, J. (1991). The impact resistance of composite materials – A review. *Composites Part A*, 22, 347–62.

[46] Ulven, C., Vaidya, U.K., Hosur, M.V. (2003). Effect of projectile shape during ballistic perforation of VARTM carbon/epoxy composite panels. *Composite Structures*, 61(1-2), 143-150.

[47] Caprino, G., Lopresto, V. (2000). Factors affecting the penetration energy of glass fibre reinforced plastics subjected to a concentrated transverse load. *Proceeding of European Conference on Composite Materials (ECCM 9)*, 4-7.

[48] Alcook, B. (2006). Low velocity impact performance of recyclable all-polypropylene composites. *Composites Science and Technology*, 66(8), 1030-1037.

[49] Herszberg, I., Weller, T. (2006). Impact damage resistance of buckled carbon/epoxy panels. *Composite Structures*, 73(2), 130-137.

[50] Bathias, C., coll. (2007). *Matériaux composites, Vieillissement physico-chimique des matériaux composites à matrice orgaique.* 2, 109-113.

[51] Wang, C., Roy, A., Silberschmidt, V.V., et al. (2017). Modelling of Damage Evolution in Braided Composites : Recent Developments. *Mech Adv Mater Mod Process*, 3(15).

[52] Whittingham, B., Marshall, I. H., Mitrevski, T., Jones, R. (2004). The response of composite structures with pre-stress subject to low velocity impact damage. *Composite Structures*, 66(1-4), 685-698.

[53] Eve, O. (1999). Etude du comportement des structures composites endommagées par un impact basse vitesse – Applications aux structures aéronautiques. *Doctoral dissertation, Université de Metz*, 211-215.

[54] Thomas, C. (2011). Étude des mécanismes d'endommagement des composites fibres de carbone / matrice polyamide : application à la réalisation de réservoirs de stockage de gaz sous haute pression de type IV (Doctoral dissertation, École Nationale Supérieure des Mines de Paris), 60-98.

[55] Bouvet, C. (2011). Dommages d'impact sur stratifié composite. *AMAC. 17èmes Journées Nationales sur les Composites (JNC17)*, 206.

[56] Chen, C. (2015). Contribution à la prise en compte des effets de l'environnement sur la tolérance aux dommages d'impact de stratifiés composites (Doctoral dissertation, university of Toulouse), 27-89.

[57] Dzenis, Y. A. (2001). Analysis of microdamage evolution histories in composites. *International Journal of Solids and Structures*, 38(10-13), 1831–1854.

[58] Richardson, M. O. W., Wisheart, M. J. (1996). Review of low-velocity impact properties of composite materials. *Composites, Part A : Applied Science and Manufacturing*, 27A(12), 1123-1131.

[59] Cantwell, W. J., Morton, J. (1989). Geometrical effects in the low velocity impact response of CFRP. *Composite Structures*, 12(1), 39–59.

[60] Choi, H. Y., Chang, F. K. (1992). A model for predicting damage in graphite epoxy laminated composites resulting from low-velocity point impact. *Journal of Composite Materials*, 26(14), 2134–2169.

[61] Abdulhamid, H. (2015). Étude de la tolérance aux dommages d'impact sur structure composite en zone de reprise de plis. *Doctoral dissertation, École Nationale Supérieure d'Arts et Métiers-ENSAM*, 73-130.

[62] Androuin, G. (2019). Caractérisation de la propagation de délaminage en fatigue : essais à résonance et sollicitation à amplitude variable. *Doctoral dissertation, Univesity of Toulouse*, 55-103.

[63] Davies, G. A. O., Zhang, X., Zhou, G., Watson, S. (1994). Numerical modelling of impact damage. *Composites*, 25(5), 342–350.

[64] Liu, D. (1988). Impact induced delamination a view of bending stiffness mismatching. *Journal of Composite Materials*, 22(7), 674–692.

[65] Wang, H., Vu-Khanh, T. (1995). Fracture mechanics and mechanisms of impact-induced delamination in laminated composites. *Journal of Composite Materials*, 29(2), 156–178.

[66] Abi Abdallah, E., Bouvet, C., Rivallant, S., Broll, B., Barrau, J. (2009). Experimental analysis of damage creation and permanent indentation on highly oriented plates. *Composites Science and Technology*, 69(7), 1238–1245.

[67] Shi, Y., Swait, T., Soutis, C. (2012). Modelling damage evolution in composite laminates subjected to low velocity impact. *Composite Structures*, 94(9), 2902–2913.

[68] Tan, S. C. (1991). A progressive failure model for composite laminates containing openings. *Journal of Composite Materials*, 25(5), 556–577.

[69] Chen, P., Shen, Z., Xiong, J., Yang, S., Fu, S., Ye, L. (2006). Failure mechanisms of laminated composites subjected to static indentation. *Composite structures*, 75(1), 489–495.

[70] Gómez-del Río, T., Zaera, R., Barbero, E., Navarro, C. (2005). Damage in CFRPs due to low velocity impact at low temperature. *Composites Part B*,36, 41-50.

[71] Reeder, J. R. (2006). 3D mixed-mode delamination fracture criteria - An experimentalist's perspective. *American Society for Composites 21st Annual Technical Conference*, 1-3.

[72] Chang, L. (1985).Impact fatigue of PPS/glass composites : Part I Theoretical analysis. *Journal of Materials Science Letters*, 4, 1221-1224.

[73] Roy, R., Sarkar, B.K., Bose, N.R. (2001). Impact fatigue of glass fibre–vinylester resin composites. *Composites Part A*, 32(6), 871-876.

[74] Jang, B.P., Kowbel, W., Jang, B.Z. (1992). Impact behavior and impact-fatigue testing of polymer composites. *Composites Science and Technology*, 44(2), 107-118.

[75] Niu, Y. F., Yan, Y., Yao, J. W. (2021). Hygrothermal aging mechanism of carbon fiber/epoxy resin composites based on quantitative characterization of interface structure. *Polymer Testing*, 94, 4-7.

[76] Mortaigne, B. (2005). *Vieillissement des Composites – Mécanismes et Méthodologie d'Etude*, 6-32.

[77] Kolopp, A., Rivallant, S., Bouvet, C. (2011). Impact Testing of Composite Sandwich Structures for Aircraft Armor Applications. *Comptes Rendus des JNC 17-Poitiers 2011*, 1-9.

[78] AITM1-0010. (2005). Airbus Test Method : Determination of Compression Strength after Impact.

[79] Bouvet, C., Castanie, B., Bizeul, M., Barrau, J. J. (2009). Low velocity impact modelling in laminate composite panels with discrete interface elements. *International Journal of Solids and Structures*, 46(22-23), 3820-3836.

[80] Trellu, A., Bouvet, C., Rivallant, S., Ratsifandrihana, L., Chardonneau, A. (2019). Simulation d'impact à moyenne vitesse et de compression ou cisaillement après impact sur grandes plaques composites stratifiées. *JNC21 (21ème Journées Nationales sur les Composites)*, 1-7.

[81] Passieux, J.C., Navarro, P., Périé, J.N., Marguet, S., Ferrero, J.F. (2014). A Digital Image Correlation Method For Tracking Planar Motions Of Rigid Spheres : Application To Medium Velocity Impacts. *Experimentals Mechanics*, 54, 1453-1466.

[82] Sultan, M.T.H., Basri, S., Rafie, A.S.M., Mustapha, F., Majid, D.L., Ajir, M.R. (2012). High velocity impact damage analysis for glass epoxy laminated plates. *Advanced Materials Research*, 399-401.

[83] Guillaud, N. (2015). Tolerance to Impact-Induced Damage in Thick Composite Structures : Application to Hyperbaric Composite Tanks. *Doctoral dissertation, École Nationale Supérieure d'Arts et Métiers*,67-98.

[84] Rezasefat, M., Beligni, A., Sbarufatti, C., Amico, S. C., Manes, A. (2023). Experimental and Numerical Study of the Influence of Pre-Existing Impact Damage on the Low-Velocity Impact Response of CFRP Panels. *Materials*, 16(5), 914.

[85] Kueh, A. B. H., Sabah, S. H. A., Qader, D. N., Drahman, S. H., Amran, M. (2023). Single and Repetitive Low-Velocity Impact Responses of Sandwich Composite Structures with Different Skin and Core Considerations : A Review. *Case Studies in Construction Materials*, 18.

[86] Huo, L., Kassapoglou, C., Alderliesten, R. C. (2023). Influence of Neighbouring Damage on Delamination Growth in Multiple Indented Composites. *Materials Design*, 227.

[87] Deka, L. J., Bartus, S. D., Vaidya, U. K. (2009). Multi-Site Impact Response of S2-Glass/Epoxy Composite Laminates. *Composites Science and Technology*, 69(6), 725-735.

[88] Vaidya, U. K., Deka, L. J. (2009). Single and Multisite Impact Response of S2-Glass/Epoxy Balsa Wood Core Sandwich Composites. *Major Accomplishments in Composite Materials and Sandwich Structures* (pp. 541-569). Springer Netherlands.

[89] Job, S. (2015). Why not composites in ships ? *Reinforced Plastics*, 59(2), 90-93.

[90] Abo Sabah, S. H., Kueh, A. B. H., Al-Fasih, M. Y. (2018). Bio-inspired vs. conventional sandwich beams : A low-velocity repeated impact behavior exploration. *Construction and Building Materials*, 169, 193-204.

[91] Merkisz, J., Bajerlein, M. (2011). Materiały kompozytowe stosowane we współczesnych statkach powietrznych. *Logistyka*, 6, 2829-2837.

[92] PORA, J. (2001). Airbus Large Aircraft Division, Composite Materials in the Airbus A380- From History to Future. *ICCM-13*, 1-10.

[93] Timmis, A.J., Hodzic, A., Koh, L., Bonner, M., Soutis, C., Schäfer, A.W., Dray, L. (2015). Environmental impact assessment of aviation emission reduction through the implementation of composite materials. *International Journal of Life Cycle Assessment*, 20(2), 233–243.

[94] Breuer, U.P. (2016). Requirements, Development and Certification Process. *Commercial Aircraft Composite Technology*, 25-44.

[95] Hosur, M.V., Murthy, C.R.L., Ramamurthy, T.S., Shet, A. (1998). Estimation of impact-induced damage in CFRP laminates through ultrasonic imaging. *NDT E International*, 31(5), 361-373.

[96] Le guen, H,. (1964). Etude des projections de gravillons par les véhicules automobiles. *Organisme national de sécurité routière*, 3-14.

[97] Daliri, A., Zhang, J., Wang, C.H. (2016). Hybrid polymer composites for high strain rate applications. In *Lightweight Composite Structures in Transport*, 121-163.

[98] Fangueiro, R., Rana, S. (Eds.). (2016). *Advanced Composite Materials for Aerospace Engineering Processing, Properties and Applications*.63-78.

[99] Elmarakbi, A. (Ed.). (2014). *Advanced Composite Materials for Automotive Applications : Structural Integrity and Crashworthiness*. 56-114.

[100] Gill, A., Robinson, P., Pinho, S. (2009). Effect of variation in fibre volume fraction on modes i and ii delamination behaviour of 5hs woven composites manufactured by rtm. *Composites Science and Technology*, 69(14), 2368-2375.

[101] Bisagni, C., Di Pietro, G., Fraschini, L., Terletti, D. (2005). Progressive crushing of fiber-reinforced composite structural components of a Formula One racing car. *Composites Structures*, 68(4), 491-503.

[102] Browning, K. A., Ludlam, F. H., Macklin, W. C. (1963). The density and structure of hailstones. *Quarterly Journal of the Royal Meteorological Society*, 379(9), 175-185.

[103] Lamb, A.J. (2007). Experimental investigation and numerical modelling of composite-honeycomb materials used in Formula 1 crash structures. *PhD dissertation, Cranfield University*, 11-63.

[104] Zhang, S., Zhu, X., Sun, H., Xiong, Y., Hou, H. (2012). Review of researches on composite marine propellers. *Advances in Mechanics*, 42(5), 620-633.

[105] Setvati, M.R., Mustaffa, Z., Shafiq, N., Syed, Z.I. (2014). A review on composite materials for offshore structures. In *Proceedings of the 33rd International Conference on Ocean*, 8-13.

[106] Shamsuddoha, M., Islam, M.M., Aravinthan, T., Manalo, A., Lau, K.-T. (2013). Effectiveness of using fibre-reinforced polymer composites for underwater steel pipeline repairs. *Composites Structures*, 100, 40-54.

[107] Olsson, R. (2010). Analytical model for delamination growth during small mass impact on plates. *International Journal of Solids and Structures*, 47(21), 2884-2892.

[108] Abrate, S. (2001). Modeling of impacts on composite structures. *Composite Structures*, 51(1), 129-138.

[109] Feraboli, P. (2006). Modified SDOF models for improved representation of the impact response of composite plates. *Journal of Composite Materials*, 40(19), 2235-2255.

[110] Lammerant, L., Verpoest, I. (1996). Modelling of the interaction between matrix cracks and delaminations during impact of composite plates. *Composites Science and Technology*, 56(10), 1171-1178.

[111] Renault, M. (1994). Compression après impact d'une plaque stratifiée carbone époxyde – Etude expérimentale et modélisation éléments finis associée. *Internal report EADS CCR.*

[112] Ilyas, M. (2010). Damage modeling of carbon epoxy laminated composites submitted to impact loading (Doctoral dissertation, Toulouse University), 43-89.

[113] Charrier, J.-S., Carrere, N., Laurin, F., Goncalves-Novo, E., Mahdi, S. (2011). Proposition d'une méthode d'analyse dédiée aux structures composites soumises à des sollicitations hors-plans. *17èmes Journées Nationales sur les Composites (JNC17).*

[114] Hashin, Z. (1980). Failure criteria for unidirectional fibre composites. *Journal of Applied Mechanics*, 47(6), 329-334.

[115] Puck, A., Schürmann, H. (2002). Failure analysis of FRP laminates by means of physically based phenomenological models. *Composites Science and Technology*, 62(12-13), 1633-1662.

[116] Tsai, S., Azzi, V. (1965). Anisotropic strength of composites. *Experimental Mechanics*, 5(9), 283-288.

[117] Tsai, S., Wu, E. (1971). A general theory of strength for anisotropic materials. *Journal of Composite Materials*, 5(1), 58-80.

[118] Hashin, Z., Rotem, A. (1973). Fatigue failure criterion for fiber reinforced materials. *Journal of Composites Materials*, 7(3), 448-464.

[119] JAAFAR, M. (2018). Étude expérimentale et simulation numérique de l'usinage des matériaux en nids d'abeilles. Application au fraisage des structures Nomex® et Aluminium. *Doctoral dissertation, Lorraine University*, 135-139.

[120] Beckelynck, B. (2016). Étude de la délamination sur des matériaux composites tissés taffetas : Essais de caractérisation et simulations numériques. *M.Sc. dissertation, Laval University*, 65-112.

[121] Hamitouche, L., Tarfaoui, M., Vautrin, A. (2009). Modélisation du délaminage par la méthode de la zone cohésive et problèmes d'instabilité - Modelling of delamination by the cohesive zone method and problems of instability. *JNC 16*, 1-10.

[122] Whitcomb, J. D. (1984). Analysis of instability-related growth of a through-width delamination. *NASA Technic Memo.-86301.*

[123] Andersson, M., Larsson, E. (2016). Benchmarking study of steel-composite structures in CAE crash applications (Master's thesis, Applied Mechanics),9-51.

[124] Kapadia, A. (2013). Non-Destructive Testing of Composite Materials. *National Composites Network*, 21-36.

[125] Chaibi, S. (2022). Prediction of damage induced by low velocity/low energy impact in latest generation carbon-epoxy laminated composites, *Doctoral dissertation, University of Toulouse*, 39-42.

[126] Garzon-Hernandez, S., Garcia-Gonzalez, D., Arias, A. (2018). Multi-Impact Mechanical Behaviour of Short Fibre Reinforced Composites. *Composite Structures*, 202, 241-252.

[127] Boyd, S. E., Emerson, R. P., Bogetti, T. A. (2013). Low-Velocity, Multi-Impact Durability Performance of Thick-Section 3WEAVE S2-Glass/SC-15 Composites Toughened With Thermoplastic Polyurethane Inter-Layer Films. *Army Research Laboratory TR-6547* , 5-13.

[128] Field, P.R., Hand, W., Cappelluti, G., McMillan, A., Foreman, A., Stubbs, D., Willows, M. (2008). Hail Threat Standardisation. *Met Office*, 85-90.

[129] Israr, H.A., Rivallant, S., Barrau, J.J. (2013). Experimental investigation on mean crushing stress characterization of carbon–epoxy plies under compressive crushing mode. *Composite structures*, 96, 357–364.

[130] Dassault Systèmes (2011). Abaqus Analysis User's Manual "Contact interaction analysis : overview". *Dassault Systèmes.*

[131] Ravi, C., Nistal, A., Falzon, B. G., Hawkins, S. C. (2017). Mode I Interlaminar Fracture Toughness of Carbon Nanotube Web-Modified Polymer Composites. *21st International Conference on Composite Materials (ICCM21).*

[132] Falzon, B. G., Hawkins, S. C., Huynh, C. P., Radjef, R., Brown, C. (2013). An investigation of Mode I and Mode II fracture toughness enhancement using aligned carbon nanotubes forests at the crack interface. *Composites Structures*, 106, 65-73.

[133] Leonardo, S. D., Nistal, A., Catalanotti, G., Hawkins, S. C., Falzon, B. G. (2019). Mode I interlaminar fracture toughness of thin-ply laminates with CNT webs at the crack interface. *Composites structures*, 225.

[134] Emery, T., Dulieu-Barton, J., Earl, J., Cunningham, P. (2008). A generalised approach to the calibration of orthotropic materials for thermoelastic stress analysis. *Composites Science and Technology*, 68(3-4), 743-752.

[135] Geubelle, P. H., Baylor, J. S. (1998). Impact-induced delamination of composites : a 2D simulation. *Composites Part B*, 29B, 589-602.

[136] Camacho, G. T., Ortiz, M. (1996). Computational modelling of impact damage in brittle materials. *Solids and Structures*, 33(20-22), 2899-2938.

[137] Lisle, T,. (2014). Analyse par thermographie infrarouge de l'endommagement des structures composites sous sollicitations quasi statiques. *Doctoral dissertation, University of Toulouse*, 79-96.

[138] Turon, A., Dávila, C. G., Camanho, P. P., Costa, J. (2007). An engineering solution for mesh size effects in the simulation of delamination using cohesive zone models. *Engineering Fracture Mechanics*, 74(10), 1665-1682.

[139] Vasilash, G. S. (2023). Lamborghini developments highlight continued focus on composites. `https://www.compositesworld.com/`, consulted on February 23, 2023.

[140] Chen, H., Guoyue, X., Xingmei, S., Chunming, S., Xiaoxing Y. (2010). The epoxy-siloxane/Al composite coatings with low infrared emissivity for high temperature applications. *Applied Surface Science*, 256(11), 3459-3463.

[141] Bayat, M., Safizadeh, M.S., Moradi, M. (2019). Numerical and experimental study for assessing stress in carbon epoxy composites using thermography. *Infrared Physics & Technology*, 98, 108-113.

[142] Pelzmann, T., Dupont, F., Sauté, B. (2023). Two-color pyrometry for backface temperature and emissivity measurement of burning materials. *International Journal of Thermal Sciences*, 184, 107894.

[143] Rittel, D. (1999). On the conversion of plastic work to heat during high strain rate deformation of glassy polymers. *Mechanics of Materials*, 31(2), 131-139.

A. Appendix : 3D view of the compressed air cannon test bench.

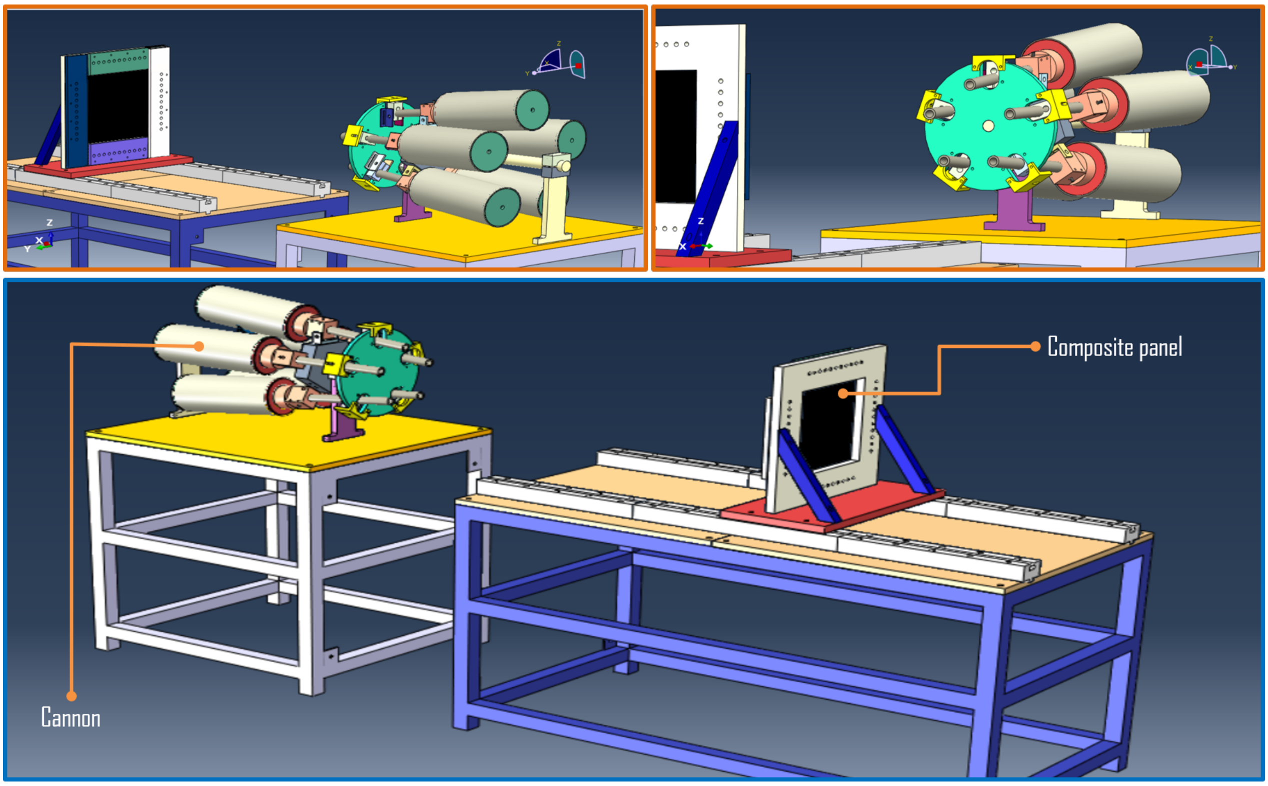

B. Appendix : Nomenclature of configurations

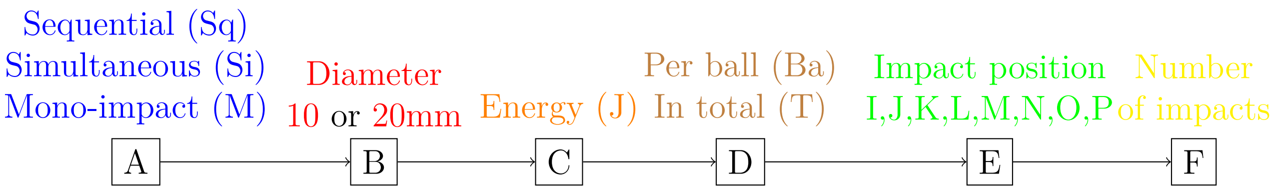

We will use the following nomenclature to distinguish the different configurations tested in this thesis : "configuration A/B/C/D/E/F*". Where A is either Sq to indicate sequential cases, Si to indicate simultaneous impacts or M to indicate a mono-impact case. B is either 10 to denote the use of 10 mm diameter balls or 20 to denote the use of 20 mm diameter balls. C specifies the projectile energy in J. If this energy is provided by each ball, then D is equal to Ba (per ball), and the energy value is specified in C. If D is T (in total), then the value of C represents the total energy with all the balls. Next, E denotes the impact position, generally explained in a schematic at the beginning of the following chapters to distinguish the different possible impact positions. F denotes the number of impacts in question, and finally, if "*" is added, it means that it is a configuration of repeated impacts. For example, the designation Configuration Si/⌀20/15J/Ba/O/2 means that it is a configuration of 2 simultaneous impacts with an energy of 15 J per ball using 20 mm diameter balls positioned at O-position, as shown in Figure 5.1.

C. Appendix : Configurations summary table

Main configuration	Nomenclature	Distance between impact centers (mm)	Type	Projectile diameter (mm)	Cannon
Sequential vs. simultaneous in undamaged areas	M/⌀20/15J/Ba/I/1	-	Mono	20	1
	Sq/⌀20/15J/Ba/L/2	40	Sequential		1
					2
	Si/⌀20/15J/Ba/L/2		Simultaneous		1
					2
Sequential vs. simultaneous in damaged areas	M/⌀20/15J/Ba/J/1	-	Mono		1
	Sq/⌀20/15J/Ba/M/2	22	Sequential		1
					2
	Si/⌀20/15J/Ba/M/2		Simultaneous		1
					2
Variable distance between impacts	Si/⌀20/15J/Ba/O/2	100	Simultaneous		1
					3
	Si/⌀20/15J/Ba/P/2	160			1
					4
15J per ball, varying the number of impacts	M/⌀20/15J/Ba/K/1	-	Mono		1
	Si/⌀20/15J/Ba/N/2	Position N	Simultaneous		1
					2
	Si/⌀20/15J/Ba/N/3				1
					2
					3
	Si/⌀20/15J/Ba/N/4				1
					2
					3
					4
	Si/⌀20/15J/Ba/N/5				1
					2
					3
					4
					5
30J in total, varying the number of impacts	M/⌀20/30J/Ba/K/1	-	Mono		1
	Si/⌀20/15J/Ba/N/2	Position N	Simultaneous		1
					2
	Si/⌀20/30J/T/N/3				1
					2
					3
	Si/⌀20/30J/T/N/4				1
					2
					3
					4
	Si/⌀20/30J/T/N/5				1
					2
					3
					4
					5
Ball 10mm	M/⌀10/15J/Ba/K/1	-	Mono	10	1
	Si/⌀10/15J/Ba/K/2	Position N	Simultaneous		1
					2
Simultaneous repeated impacts (cannon 1,2) (15J/B)	Si/⌀20/15J/Ba/N/2*		Repeated simultaneous	20	1
					2
					1
					2
					1
					2

D. Appendix : Summary of impact positions.

Position I

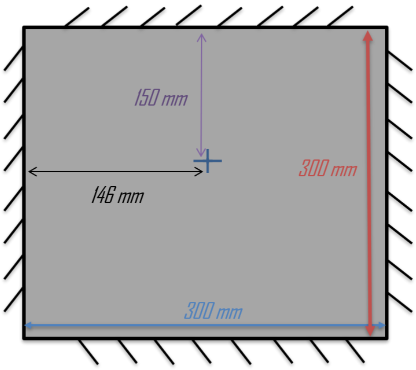

Position J

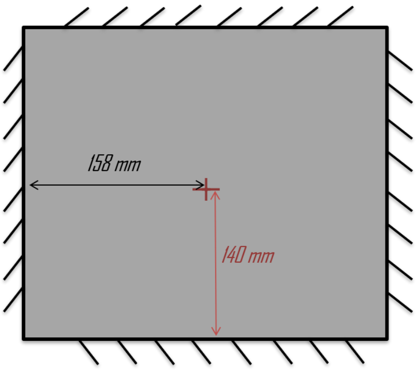

Position K

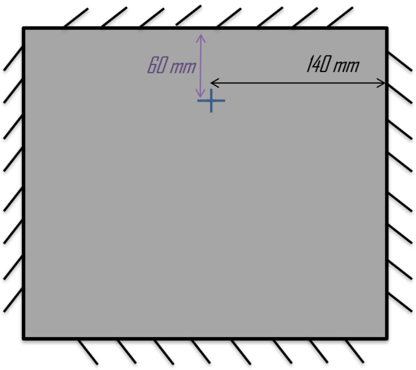

Position L

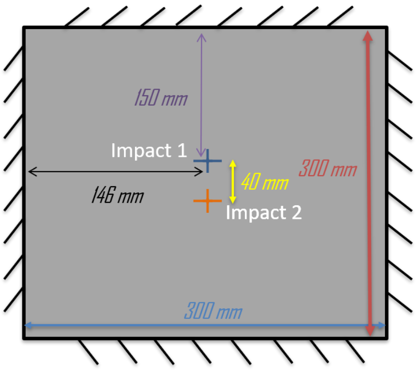

Position M

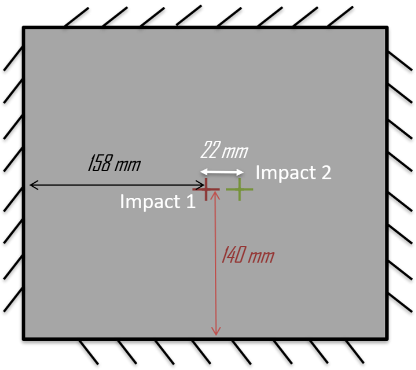

Position N

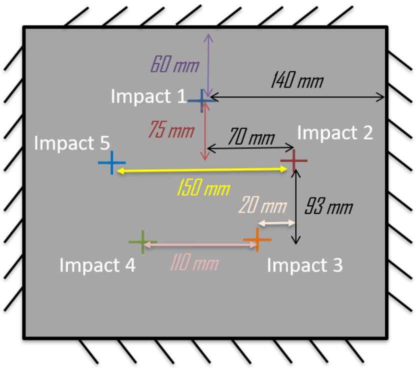

Position O

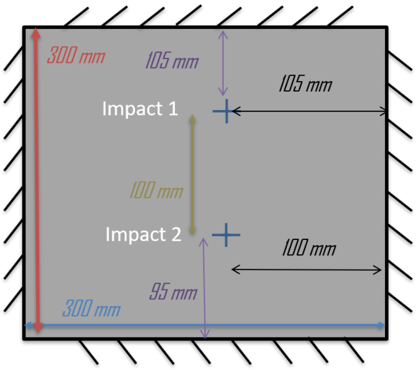

Position P

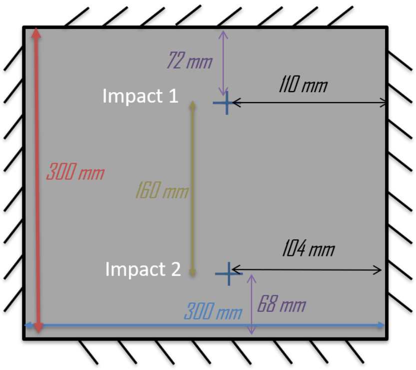

Titre : Comportement aux multi-impacts des structures composites : approche expérimentale et numérique.

Mots clés : Multi-impacts ; impact ; structures composites ; approche expérimentale et numérique ; canon à air comprimé ; discrete ply model.

Résumé : Les matériaux composites sont largement utilisés dans le domaine des transports en raison de leurs propriétés mécaniques spécifiques élevées. Cependant, au cours de leur cycle de vie, ils peuvent subir une dégradation significative de leurs propriétés mécaniques lorsqu'ils sont soumis à des chargements d'impacts. Les dommages induits par des impacts se manifestent sous différentes formes telles que la rupture des fibres, la fissuration matricielle, la décohésion fibres/matrice et le délaminage. L'étude du comportement aux impacts des structures composites a suscité une attention importante dans la littérature.

Cependant, ces études se rapportent généralement au cas d'un seul impact ou d'impacts répétés. Peu de travaux se sont intéressés au cas d'impacts multiples, même s'ils sont plus proches des conditions réelles de service, comme dans les cas de chute de grêlons ou de projection d'objets externes tels que les gravillons présents sur les routes, les impacts d'oiseaux, etc. Dans cette thèse, nous présentons des méthodes expérimentales et numériques robustes pour le suivi in-situ et post-mortem des endommagements suite aux différents cas d'impacts possibles : mono-impact, impacts répétés, séquentiels, simultanés, etc. Ce travail a consisté dans un premier temps à développer un banc d'essai unique « canon à air comprimé ». Ensuite, un dialogue (essais expérimentaux-calculs numériques) a été assuré afin de mieux comprendre les phénomènes en jeu dans les cas de multi-impacts, pour finalement atteindre les performances maximales des matériaux composites.

Title : Multi-impact behavior of composite structures : experimental and numerical approach.

Keywords : Multi-impact ; impact ; composite structures ; experimental and numerical approach ; compressed air cannon ; discrete ply model.

Abstract : Composite materials are widely used in the transportation field due to their high specific mechanical properties. However, during their life cycle, they can undergo significant degradation of their mechanical properties when subjected to impact loading. Impact-induced damage occurs in various forms, such as fiber breakage, matrix cracking, fiber/matrix decohesion and delamination. The study of the impact behavior of composite structures has attracted considerable attention in the literature. However, these studies generally relate to the case of a single impact or repeated impacts. Few studies have focused on the case of multiple impacts, even though these are closer to actual service conditions, as in the case of falling hailstones or the projection of external objects such as road gravels, bird strikes, etc. In this thesis, we present robust experimental and numerical methods for in-situ and post-mortem monitoring of damage following the various possible impact cases: single-impact, repeated, sequential, simultaneous impacts, etc. The first phase of the project involved the development of a unique "compressed air cannon" test bench. Then, a dialogue (experimental tests-numerical computations) was ensured to better understand the phenomena involved in multi-impact cases, to finally reach the maximum performance of composite materials.

Université Bourgogne Franche-Comté
32, avenue de l'Observatoire
25000 Besancon